T2R2 東京科学大学 リサーチリポジトリ
Science Tokyo Research Repository

論文 / 著書情報
Article / Book Information

題目(和文)	
Title(English)	Development of numerical model for complex flows on unstructured grids using multi-moment finite volume formulations
著者(和文)	XieBin
Author(English)	Bin Xie
出典(和文)	学位:博士（理学）, 学位授与機関:東京工業大学, 報告番号:甲第9960号, 授与年月日:2015年9月25日, 学位の種別:課程博士, 審査員:肖　鋒,奥野　喜裕,青木　尊之,末包　哲也,長崎　孝夫
Citation(English)	Degree:Doctor (Science), Conferring organization: Tokyo Institute of Technology, Report number:甲第9960号, Conferred date:2015/9/25, Degree Type:Course doctor, Examiner:,,,,
学位種別(和文)	博士論文
Type(English)	Doctoral Thesis

Powered by T2R2 (Science Tokyo Research Repository)

Development of numerical model for complex flows on unstructured grids using multi-moment finite volume formulations

A Dissertation Submitted to Tokyo Institute of Technology in Partial Fulfillment of the Requirement for the Degree of Doctor of Science

by

Bin Xie
Department of Energy Sciences
Tokyo Institute of Technology

June 2015

Abstract

Numerical simulation of interfacial multi-phase flows in complex geometrical configurations is one of the most challenging research areas in modern computational fluid dynamics (CFD). Development of numerical model for this sort of phenomena relies on some crucial numerical techniques, such as spatial discretizations in presence of complex geometry, capturing (or tracking) moving interfaces which may have topological changes, as well as efficient solver for flows of wide range Mach numbers, among others. As a matter of fact, numerical schemes of high practical value, which are usually expected to possess simultaneously adequate numerical accuracy, reliable computational robustness and computational efficiency, are far from well established. In this study, some novel unstructured numerical formulations have been devised and verified toward constructing a practical numerical model for complex interfacial multiphase flow simulations. The numerical schemes are designed so that the numerical solution quality is well-balanced with the algorithmic complexity and computational cost. The resulting numerical model is thus of great practical significance. The major efforts in this study have been made in the following four aspects.

1. Two variants of the multi-moment finite volume method, i.e. volume-integrated average and point value based multi-moment (VPM) method and multi-moment constrained finite volume (MCV) method, have been proposed on unstructured grids of arbitrary element shapes in 2 and 3 dimensions. These methods treat the point values at each vertex of the grid element as new computational variables in addition to the volume average value in the conventional finite volume method, thus allow generating high-order reconstructions on compact stencils. Both VPM and MCV methods show quite significant improvement in numerical accuracy and robustness at a modest increase in computational complexity and cost.

2. An algebraic interface capturing scheme, so-called THINC (tangent of hyperbola for interface capturing) scheme, has been extended to unstructured grids of arbitrary elements in 2 and 3 dimensions. This scheme makes use of the multi-dimensional hyperbolic tangent function for approximating the volume of fluid (VOF) filled in multiphase flows. THINC scheme is able to capture moving interfaces with accuracy

comparable to the Piecewise-Linear Interface Calculation (PLIC) type geometrical VOF schemes. Without geometrical interface reconstruction which involves great deal of algorithmic complexity and computational cost, this type method finds very few implementations in unstructured grids, the THINC scheme is much superior in simplicity and can be used for unstructured grids straightforwardly.

3. A fully conservative pressure projection formulation for solving flows of all Mach numbers has been constructed on unstructured grids. It assures the rigorous numerical conservativeness for all mass, momentum and total energy. A total variation diminishing (TVD) limiting scheme has been devised based on the unstructured multi-moment spatial reconstructions, which effectively suppresses unphysical oscillations associated with discontinuous solutions without introducing excessive numerical dissipation. This formulation applies robustly to all Mach-number flows from highly compressible flow to completely incompressible flow.

4. Integrating the basic numerical approaches mentioned above, a numerical model for multi-phase interfacial fluid dynamics has been constructed. Particular attention has been paid to devise reliable numerical formulation for surface tension computation, where the THINC scheme is used for rescaling the interface transition layer to get physics-compatible representation of fluid property.

All the numerical formulations have been extensively verified and validated by a wide range of benchmark tests, including analysis of errors and convergence rates, evaluation of robustness and computational cost, as well as the reliability of the numerical model for real-case applications. The numerical results show that the present model is well balanced among accuracy, robustness, efficiency, complexity and cost. It is thus can be expected as a reliable and practical framework for numerical simulations for complex flows in real-case applications.

Acknowledgements

All I would like to express my gratitude to my supervisor Dr. Feng Xiao for his supervision, help and guidance during my PHD study. When I began my study in this laboratory, I was extremely lack of knowledge in mathematics, physics and computer science. Everything seems difficult for me and I even don't know how to catch up. Thanks for my supervisor's patient explanation, enthusiastic help and continuous encouragement, finally I mastered most of related knowledge and began to enjoy the research journey. I also would like to acknowledge to all the members in our laboratory. For example, Dr. Ii who is my OB, provided most pioneering researches of my present studies and always replied my detailed questions rapidly. Dr. Ikebata who is expert of computer science and has rich working experience, always gave me valuable advices and the helpful discussions. Dr. Sun is in mathematical background and usually touch me a lot of related knowledge. Dr. Che who comes from meteorologic bureau, is of strong capability and finished the arranged work excellently. I really enjoyed the time with Mr. Murakami, and hope him to be able to make even great achievements in research. Mr. Inaba, a serious guy, not only outstandingly makes progress in research, but also often helps others to manage network system and organize activities like welcome party, year-end party and so on. Mr. Nakayama, a happy guy, who always makes the laboratory bright. I really hope he can make great job with my new numerical model. Mr. Deng and Mr. Jin, two hard working guys, assisted me a lot with verification and validation. Mr. Kondo, Tsubone and Wang, the truely new driving force of laboratory, should be able to make even big contributions, I have to stop here but by no mean stop extending my gratitude to everyone in the laboratory for their support, discussion and nice time we have enjoyed together.

Besides, I'd like to acknowledge Japan Society for the Promotion of Science (JSPS) which provides Doctoral Course (DC2) scholarship and research grant for my doctoral studies.

Last, I want to thank my family. After all, you are the ones who makes everything worthwhile. I also thank for accompany of my girl friend who always inspires me to struggle, and concentrate on my study.

Contents

Abstract **1**

Declaration **3**

1 Introduction **18**

1.1 Background 18

1.2 Previous and related studies 19

1.2.1 Reconstruction for spatial discretisation 19

1.2.2 Interface capturing in multiphase flow 21

1.2.3 Mach uniform model and oscillation suppression procedure in compressible flow 22

1.3 Purpose of present study 23

1.4 Thesis outline 24

2 Reconstructions based on multi-moments and multi-moment constraints on unstructured grids **26**

2.1 Definition of multi-moments on unstructured grids 26

2.2 Mapping of grid element 27

2.3 High order reconstructions using volume-average/point-values 31

2.4 High order reconstructions using multi-moment constraints 42

2.5 Numerical approximation for derivatives and integrals 53

2.5.1 First order derivatives at cell vertices as well as surface center 54

2.5.2 Integral average quantity on cell surface 54

2.5.3 First order derivatives on cell surface 59

2.6 Summary of chapter 2 62

3 Numerical models for Navier-stokes equations using VPM and MCV **63**

3.1 Governing equation in conservation form 63

3.2 Mach uniform solution procedure based on projection method 64

3.3 Time integration method 66

3.4 Time Evolution converting formulation 68

3.5 Spatial discretization of advection term 70
3.5.1 The piecewise reconstruction polynomial 70
3.5.2 The advection flux in (3.37) 72
3.5.3 The gradient operator in the advection term in (3.35) 73
3.6 Slope limiting projection 73
3.7 Spatial discretization of diffusion term 75
3.7.1 The explicit scheme for diffusion equation 75
3.7.2 The implicit scheme for diffusion equation 77
3.8 Spatial discretization of Poisson equation for pressure field 79
3.8.1 Projection of the velocity field 82
3.9 Summary of solution procedures 84
3.10 Verification tests 85
3.10.1 Advection of sine wave 85
3.10.2 Solid rotation of 2D cone 86
3.10.3 Advection transport of discontinuities 89
3.10.4 TEC formulation 92
3.10.5 Elliptic equation for Poisson problem 93
3.10.6 Taylor vortex problem 94
3.10.7 Lid driven square cavity problem 99
3.10.8 Lid driven forward-step cavity problem 101
3.10.9 Lid driven skew cavity problem 102
3.10.10 Lid driven semi-circular cavity problem 102
3.10.11 3D lid driven cubic cavity problem 103
3.10.12 2D circular explosion shock tests 105
3.10.13 Mach 3 wind tunnel with a step 107
3.10.14 NACA 0012 airfoil 113
3.10.15 Square cavity flow with wide range of Reynolds number 113
3.10.16 Isosceles triangular lid driven cavity flow 117
3.10.17 Equilateral triangular lid driven cavity flow 122
3.10.18 2D viscous flow around a circular cylinder 123
3.10.19 Viscous flow in a channel with a backward-facing step 124
3.10.20 Viscous flows passing a sphere with different Reynolds numbers . . . 126
3.10.21 Flow over a circular cylinder with Reynolds number of 3900 128
3.11 Summary of chapter 3 135

4 Algebraic interface capturing scheme on unstructured grid 136
4.1 Algebraic numerical approaches for moving interface in multiphase flow . . 136
4.2 Governing equation for volume fraction function 137

4.3 Multi-dimensional THINC scheme on unstructured grid 138
4.3.1 Reconstruction polynomial of multi-dimensional THINC formulation 138
4.3.2 The normal vector and curvature of the interface 141
4.3.3 The THINC reconstruction function 143
4.4 Verification tests 161
4.4.1 Interface reconstructions for a circular shape 161
4.4.2 Zalesak body rotation on quadrilateral mesh 163
4.4.3 Shearing flow on quadrilateral mesh 166
4.4.4 Zalesak solid rotation on hexahedral mesh 170
4.4.5 Shearing flow on hexahedral mesh 171
4.5 Summary of chapter 4 174

5 Numerical model for incompressible interfacial multiphase flow 175
5.1 Governing equations 175
5.2 Smoothed volume fraction and fluid property 176
5.3 Surface tension formulation 177
5.4 Solution procedure for equation system 180
5.5 Validation tests 181
5.5.1 2D Dambreak without obstacle 181
5.5.2 A circular droplet in static fluid 181
5.5.3 Two dimensional bubble rising 185
5.5.4 Three dimensional dambreak problem with obstacle 186
5.5.5 Single bubble rising in a wide range of Reynolds and Bond number . 189
5.5.6 Motion of microdropelet passing through ratchet structure 191
5.6 Summary of chapter 5 196

6 Conclusions and future work 197
6.1 Major contributions of present study 198
6.2 Impact of present study on related research field 199
6.3 Future work 200

Appendix 1: Interpolation from cell center to vertex by least square method 202

Appendix 2: Analytical expression for a quartic equation in the present method 204

Reference 205

List of Figures

2.1 The two-dimensional grid elements: triangular(left) and quadrilateral(right) element. . . . 26
2.2 The arbitrary unstructured grid element. From left to right is quadrilateral, tetrahedral, hexahedral, prismatic and pyramidal element. . . . 27
2.3 The two-dimensional grid elements: triangular(left) and quadrilateral(right) element. . . . 27
2.4 The arbitrary unstructured grid element. From left to right is quadrilateral, tetrahedral, hexahedral, prismatic and pyramidal element. . . . 28
2.5 The moment for gradient reconstruction across two face adjacent cells (left) and reconstruction stencils for boundary cell(right). . . . 59
2.6 The moment for gradient reconstruction across two face adjacent cells of 3D arbitrary unstructured elements. . . . 61

3.1 TEC formulation for mapping VIA to PV. . . . 69
3.2 Reconstruction stencil for gradient approximation . . . 71
3.3 Point gradient operator in the advection term. . . . 72
3.4 Schematic diagram of indicator function. . . . 74
3.5 TVD monotonicity region of present limiter on Sweby‘s diagram. . . . 74
3.6 Point Laplace operator in the diffusion term. . . . 76
3.7 Gradient reconstruction for orthogonal the boundary edge. . . . 77
3.8 Numerical error for MCV/VPM scheme with and without flux limiter function and compared with conventional FVM scheme. . . . 87
3.9 The computational meshes for advection test. Left (grid A): a mesh generated by Delaunay algorithm. Right (grid B): a mesh where a region has heavily distorted triangular elements of bad conditions in orthogonality, skewness and uniformity. . . . 88
3.10 The numerical results of VPM/MCV scheme for the solid rotation advection tests on grid A (left) and grid B (right). . . . 89
3.11 Same as Fig. 3.10 but by the QUICK scheme. . . . 89
3.12 Same as Fig. 3.10 but by the superbee TVD scheme. . . . 90

3.13 Same as Fig. 3.10 but by the MUSCL scheme. 90
3.14 Bird's eye view of square pulse advected after one revolution by VPM/MCV (left) and QUICK(right) on unstructured quadrilateral grid. 91
3.15 Bird's eye view of Zalesak profile advected after one revolution by VPM/MCV scheme equipped with TVD limiter. Left: initial profile, Right: profile after one revolution. 91
3.16 X-Z plane view of Zalesak profile advected after one revolution by VPM/MCV scheme equipped with TVD limiter. Left: initial profile, Right: profile after one revolution. 92
3.17 The computational meshes for Poisson equation test. Left (grid A): a mesh generated by Delaunay algorithm. Right (grid B): a mesh where a region has heavily distorted triangular elements with bad conditions in orthogonality, skewness and uniformity. 93
3.18 The numerical errors and convergence rates for velocity (left) and pressure (right). 96
3.19 Pressure contour profile computed on Grid B by QUICK, VPM/MCV-RK, VPM/MCV-BDF method respectively(left to right). The red solid line is for exact solution and black dot line is for present results. 98
3.20 The kinetic energy for inviscid simulation of Taylor vortex problem with time step 0.001. Left: results of VPM/MCV-RK computed on different grid resolution. Right: results of VPM/MCV-BDF computed on different grid resolution. 99
3.21 Convergence rate of dissipation rate. 100
3.22 Numerical results of square cavity flow problem. Displayed are stream line on a 5612-cell mesh (left), u profiles along $x = 0.5$ line (middle) and v profiles along $y = 0.5$ line (right) on grids of different resolutions. 101
3.23 Numerical results of square cavity flow problem on a 5612-cell mesh. Displayed are the u profile along $x = 0.5$ line (left) and v profile along $y = 0.5$ line (right). 102
3.24 Numerical results of square cavity flow problem. Displayed are computational grid (top-left), stream line on a 4523-cell mesh (top-right), u profiles along $x = 0.5$ line (bottom-left) and v profiles along $y = 0.5$ line (bottom-right) on grids of different resolutions. 103
3.25 Numerical results of forward-step cavity flow problem. Displayed are stream line on a 7538-cell mesh (left), u profile along $x = 0.75$ line (middle) and v profile along $y = 0.75$ line (right). 104

3.26 Numerical results of forward-step cavity flow problem. Displayed are computational grid (top-left), stream line on a 7722-cell mesh (top-right), u profiles along $x = 0.75$ line (bottom-left) and v profiles along $y = 0.75$ line (bottom-right) on grids of different resolutions. 105
3.27 Numerical results of a 30° inclined skew cavity flow problem. Displayed are stream line on a 1872-cell mesh (left), u profile along $y = \tan(30^o)(x - 0.5)$ line (middle) and v profile along $y = \tan(30^o)/2$ line (right). 106
3.28 Numerical results of a 45° inclined skew cavity flow problem. Displayed are stream line on a 7352-cell mesh (left), u profile along $y = \tan(45^o)(x - 0.5)$ line (middle) and v profile along $y = \tan(45^o)/2$ line (right). 107
3.29 Numerical results of semi-circular cavity flow problem. Displayed are stream line on a 2266-cell mesh (left), u profile along $x = 0.5$ line (middle) and v profile along $y = -0.25$ line (right). 108
3.30 Numerical results of semi-circular cavity flow problem. Displayed are computational grid (top-left), stream line on a 4089-cell mesh (top-right), u profiles along $x = 0.5$ line (bottom-left) and v profiles along $y = -0.25$ line (bottom-right) on grids of different resolutions. 108
3.31 Grids used for the 3D lid driven cubic cavity flows. Left: regular Cartesian grid; Right: irregular hexahedral grid. 109
3.32 Numerical results on Cartesian grid for the 3D lid driven cavity flow. Displayed are v profile along centerline $(x, 0, 0)$ (left) and u profile along centerline $(0, y, 0)$ (right). The reference results of [5] was computed by a Chebyshev-collocation method with $96 \times 96 \times 64$ Gauss-Lobatto points. 109
3.33 Same as Fig. 3.32 but using the irregular hexahedral grid. 110
3.34 Pressure contours (left) and stream lines (right) on $z = 0$ cross-section of the 3D lid-driven cavity flow. 110
3.35 Same as Fig. 3.34 but on $y = 0$ cross-section. 111
3.36 Same as Fig. 3.34 but on $x = 0$ cross-section. 111
3.37 Bird's eye views of the density (left) and pressure (right) of the circular explosion test with condition of (3.98) at time of 0.25. 111
3.38 Bird's eye views of the density (left) and pressure (right) of the circular explosion test with condition of (3.99) at time of 0.00012. 112
3.39 Numerical results showing the contour plots of density for the flow past a step test. 112
3.40 Computational structure and grids used in NACA 0012 airfoil test case. . . 113
3.41 Pressure coefficient C_p distribution along boundary of NACA 0012 airfoil. . 114
3.42 Computational grid and nomenclature of vortices for square lid driven cavity flow. 115

3.43 Streamline of square cavity flow for Reynolds number of 100, 1000, 5000 (left to right). 115
3.44 Vorticity contours of square cavity flow for Reynolds number of 100, 1000, 5000 (left to right). 115
3.45 Vertical and horizontal velocity profiles along centre lines of square cavity for Reynolds number of 100, 1000, 5000 (left to right). 116
3.46 Geometry and computational grid of isosceles triangular lid driven cavity flow. 118
3.47 Experiment photographs[44] and numerical simulation for isosceles triangular cavity flow. 119
3.48 Streamline contours of isosceles triangular cavity flow for Reynolds number of 100, 500, 1000 (left to right). 120
3.49 Vorticity contours of isosceles triangular cavity flow for Reynolds number of 100, 500, 1000 (left to right). 120
3.50 Horizontal velocity(u) along the line joining the center of EG and FG(left) and the line from G to the center of EF(right). 120
3.51 Vertical velocity(v) along the line joining the center of EG and FG(left) and the line from G to the center of EF(right). 121
3.52 Vorticity(ω) along the line joining the center of EG and FG(left) and the line from G to the center of EF(right). 121
3.53 Geometry and computational grid of equilateral triangular lid driven cavity flow. 122
3.54 Streamline contours of equilateral triangular cavity flow for Reynolds number of 100, 200, 500 (left to right). 122
3.55 Vorticity contours of equilateral triangular cavity flow for Reynolds number of 100, 200, 500 (left to right). 123
3.56 Vertical and horizontal velocity profiles along centre lines of equilateral triangular cavity for Reynolds number of 100, 200, 500 (left to right). . . . 123
3.57 Geometry and boundary conditions for case of circular cylinder. 124
3.58 The physical fields at the instant when the lift force becomes largest. Displayed are velocity norm (top), pressure (middle) and vorticity (bottom) fields. 125
3.59 Time history of drag and lift coefficient. 126
3.60 Zoomed view of time history of drag (left) and lift (right) coefficient. . . . 126
3.61 Geometry and computational grid for case of backward-facing step. 127
3.62 Numerical results of the back-facing step channel flow test on the 800×40 grid. Displayed are stream line, pressure contour, vorticity contour and velocity magnitude respectively from top to bottom. 127

3.63 Magnitude of velocity and vorticity profile across the channel $x = 7$ and $x = 15$ for finest grid. 128
3.64 Geometry and computational grid for viscous flows passing a sphere. . . . 129
3.65 Streamlines on the central cross section of flows passing a sphere. Displayed are the steady cases with Reynolds numbers of 50 (top-left), 100 (top-right), 150 (bottom-left) and 200 (bottom-right). 129
3.66 Flow geometry as a function of the Reynolds number. Displayed are the polar separation angle Θ_s (top-left), the separation length x_s (top-right), the vortex position (x_c, y_c) (bottom-left) and the drag coefficient C_d(bottom-right). See Fig. 4 and 5 in [78] as well as the references therein for the reproduced data. 130
3.67 The contours of ω_z at Re=300 for a quarter period on xy-plane at $\phi = 0$ (top-left), $\phi = \pi/2$ (top-right), $\phi = \pi$ (bottom-left) and $\phi = 3\pi/2$ (bottom-right). Contours are drawn at 0.5 increment with the solid and dot lines for positive and negative values respectively. 131
3.68 Cross-section of grids used in the circular cylinder simulation. 132
3.69 Streamwise velocity on the center line in the wake of a circular cylinder. . . 132
3.70 Streamwise velocity and cross-flow velocity at three locations in the wake of a circular cylinder. 132
3.71 Isocontour maps of the mean streamwise velocity $\langle u \rangle$ normalized with U_c(left column, present result; right column, PIV in [120]). 133
3.72 Isocontour maps of the mean cross-flow velocity $\langle v \rangle$ normalized with U_c(left column, present result; right column, PIV in [120]). 133
3.73 Isocontour maps of the variance of streamwise velocity fluctuations $\left\langle u'u' \right\rangle$ normalized with U_c^2(left column, present result; right column, PIV in [120]). 133
3.74 Isocontour maps of the variance of cross-flow velocity fluctuations $\left\langle v'v' \right\rangle$ normalized with U_c^2(left column, present result; right column, PIV in [120]). 134
3.75 Isocontour maps of the covariance of the velocity fluctuations $\left\langle u'v' \right\rangle$ normalized with U_c^2(left column, present result; right column, PIV in [120]). . . 134

4.1 Interface reconstructions for a circular shape with exact unit normal vector. Left (grid A): a structured quadrilateral mesh. Right (grid B): a unstructured quadrilateral mesh. 162
4.2 The computational meshes for advection test. Left (grid A): a structured quadrilateral mesh. Right (grid B): a unstructured quadrilateral mesh. . . 164

4.3 Numerical results of Zalesak slotted-cylinder test problems. Left (grid A): enlarged view of 0.05,0.5,0.95 contour on 10000 structured quadrilateral grids. Right (grid B): enlarged view of 0.05,0.5,0.95 contour on 10056 unstructured quadrilateral grids. 165
4.4 Numerical results of Zalesak slotted-cylinder test problems. Left (grid A): interface(contour 0.5) on 10000 structured quadrilateral grids. Right (grid B): interface(contour 0.5) on 10056 unstructured quadrilateral grids. 166
4.5 Numerical results for T=2 of time-dependent single vortex flow test problem on a Cartesian grid of 128×128 cells (left) and an unstructured quadrilateral grid of 16395 cells (right). The red lines indicate the numerical solutions at $T/2$ and T. The black dot line represents the initial profile (exact solution). 167
4.6 Same as Fig. 4.5, but for $T = 8$. 168
4.7 Contours of 0.05, 0.5, 0.95 of the volume fraction fields at $T = 8$. 168
4.8 The computational meshes for Zalesak 3D rotation test. Left (grid A): a structured hexahedral mesh. Right (grid B): a unstructured hexahedral mesh. 170
4.9 Numerical results for Zalesak 3D rotation test problems on structured hexahedral grids at $t = 2\pi$ with exact (Left), 100^3 (Middle), 200^3 (Right). . . . 171
4.10 Numerical results for Zalesak 3D rotation test problems on unstructured hexahedral grids at $t = 2\pi$ with exact (Left), 995200(Middle), 8068200 (Right). 172
4.11 The computational meshes for shear 3D test. Left (grid A): a Cartesian grid. Right (grid B): an unstructured hexahedral grid. 172
4.12 Numerical results for time-dependent 3D vortical deformation flow test on 128^3 Cartesian grid. Displayed are the iso-surface of contour 0.5 of the instantaneous solutions at time $t = 0,\ \frac{T}{2},\ T$ with $T = 3$. 173
4.13 Same as Fig. 4.12, but on a unstructured hexahedral grid of 2166400 cells. 173

5.1 Thickness of jump transition can be effectively controlled by parameter β. 177
5.2 Definition of two dimensional dambreak test without obstacle. 181
5.3 Snapshots of the water column for time 0.1(left) and 0.2(right). 182
5.4 Snapshots of the water column for time 0.3(left) and 0.4(right). 182
5.5 Air-water interface horizontal(left) and vertical(right) positions as a function of time in non-dimensional units. 182
5.6 Convergence behavior for pressure jump after one time step with exact curvature($\kappa = 4$) and numerical curvature. 184
5.7 Bird's eye views of pressure jump computed with numerical curvature on different grid resolution. 185

5.8 Profile along x axis of pressure jump computed with numerical curvature on different grid resolution. 186
5.9 The evolution of the total kinetic energy in the drop oscillation problem. The left figure shows the results on grid of 14412 elements and 57518 elements for time [1,100]. The right figure shows the convergence behavior on grid of 57518 elements for long time computation. 187
5.10 The VOF reaches steady state at time of $t = 250$. The left figure shows the profile of VOF value(ϕ) of 0.05, 0.5 and 0.95 and exact interface($\phi = 0.5$) is also plotted by red line. The right figure shows the pressure distribution in bird's eye views. 187
5.11 Left: initial condition; Right: bubble shape indicated by $\phi = 0.5$ for time 0s and 3s. 188
5.12 Time history of rising position and velocity for bubble. 188
5.13 Left: the region filled with bad mesh elements. Right: bubble shape at end time for good mesh(black line) and bad mesh(red line). 188
5.14 Configuration of the dam-break test (left), the measurement position for pressure(right). 189
5.15 Snapshot of simulation for dambreak with an obstacle at instant of time 0.48s, 0.96s, 1.92s and 2.4s. 190
5.16 Pressure time histories at probe P1 and P3 on the vertical boundary of obstacle. 191
5.17 Pressure time histories at probe P5 and P7 on the horizontal boundary of obstacle. 191
5.18 Computational grid across section(left) and bubble shape as well as streamline based on the bubble rise velocity(right). 192
5.19 Comparisons of the bubble shape and streamline based on the bubble rise velocity. The left side and right side of each panel indicate the present result and experiment/other simulation results as Hnat and Buckmaster[57](left), Gueyffier et al.[42](middle) and Ii et al.[66](right). 192
5.20 Time histories of bubble rising velocity(left) and position(right). 193
5.21 Schematic of investigated microfluidic ratchet structure. 194
5.22 Comparison of pressure drop under different flow rate between numerical solution and experimental data(left). Periodical behavior of pressure drop as well as bubble shapes(right). 195

List of Tables

2.1 Mapping for triangular and quadrilateral element. 29
2.2 Mapping for tetrahedral, hexahedral, prismatic and pyramidal element. . . 30
2.3 Coefficients of reconstruction function in VPM scheme for different element shapes. 31
2.4 Constraint conditions and basis functions for triangular element. 33
2.5 Constraint conditions and basis functions for quadrilateral element. 34
2.6 Constraint conditions and basis functions for tetrahedral element. 36
2.7 Constraint conditions and basis functions for hexahedral element. 37
2.8 Constraint conditions and basis functions for prismatic element. 39
2.9 Constraint conditions and basis functions for pyramidal element. 41
2.10 Approximated formulations of PV at cell center for all type of unstructured grid elements for VPM scheme. 42
2.11 Coefficients of reconstruction function in MCV scheme for different element shapes. 43
2.12 Constraint conditions and basis functions for triangular element. 44
2.13 Constraint conditions and basis functions for quadrilateral element. 45
2.14 Constraint conditions and basis functions for tetrahedral element. 47
2.15 Constraint conditions and basis functions for hexahedral element. 49
2.16 Constraint conditions and basis functions for prismatic element. 50
2.17 Constraint conditions and basis functions for pyramidal element. 52
2.18 Multi-moment constrained conditions for all type of unstructured grid elements for MCV scheme. 53
2.19 First order derivatives of VPM scheme at random position in local cell (ξ_i, η_i, ζ_i) for each unstructured elements. 55
2.20 First order derivatives of MCV scheme at random position in local cell (ξ_i, η_i, ζ_i) for each unstructured elements. 56
2.21 The integral average quantities for VPM scheme on different unstructured element shapes. 57
2.22 The integral average quantities for MCV scheme on different unstructured element shapes. 58

3.1 Comparison of L_1 errors and convergence rates of different advection schemes. 85
3.2 Computational cost estimation for advection calculation of VPM/MCV in comparison with the QUICK scheme. 86
3.3 Comparison of L_1 errors and convergence rates for different gradient moments as well as TVD limiter. 87
3.4 Numerical errors on different grids and degradation rate. 88
3.5 Maximum and minimum values in the numerical solutions. 91
3.6 Numerical errors and convergence orders of least square TEC scheme. . . . 92
3.7 Numerical errors of the least square TEC scheme. 92
3.8 Numerical errors and convergence orders of Poisson equation. 93
3.9 Degradation error for Poisson equation computed by MCV, FVM and FEM methods. 94
3.10 Numerical errors and convergence rates of VPM and conventional FVM models for Taylor vortex problem. 95
3.11 Computation cost and numerical accuracy for incompressible fluid solvers. . 96
3.12 L_2 error and convergence rate for incompressible solvers and compared with FVM(QUICK) and VPM method. 97
3.13 Degradation error for shear vortex problem computed by FVM(QUICK), VPM/MCV-RK and VPM/MCV-BDF method. 98
3.14 Kinetic variation and related dissipation rate. 98
3.15 Computation cost for advection of QUICK and VPM schemes. 106
3.16 Comparison of maximum streamfunction value, the vorticity value and location of primary vortex, for Reynolds number of 1000. 116
3.17 Property of primary and secondary vortices for Reynolds number of 5000; streamfunction ψ and vorticity value ω, locations (x, y). 117
3.18 Comparison characteristics of the primary vortex for different Reynolds numbers; streamfunction ψ_p and vorticity value ω_p, locations (ξ_p, η_p). . . . 121
3.19 Comparison characteristics of the primary vortex for different Reynolds numbers; streamfunction ψ_p and vorticity value ω_p, locations (ξ_p, η_p). . . . 124
3.20 Comparison between the present solution and the reference solutions. 125
3.21 Numerical results of backward-facing step channel flow and comparison with existing studies. 128
3.22 Numerical results of viscous flows over a sphere. 131
3.23 Comparison of statistics around circular cylinder at Reynolds number of 3900. St, U_{min}, θ_{sep}, L_{rec} denotes Strouhat number, minimum mean streamwise velocity, separation angle and length of recirculation region, respectively. 134

4.1 Coefficients of multi-dimensional THINC reconstruction formulation for different type elements. 140
4.2 Unit normal vector at cell center for each element type. 142
4.3 Curvature tensor at the cell center for each element type. 142
4.4 Numerical error for interface reconstruction with exact and numerical unit normal vector. 163
4.5 Numerical errors of modified Zalesak slotted cylinder test. 164
4.6 Numerical results of Zalesak slotted-cylinder test problems on grid A and grid B with resolution of $1/100$ and $1/200$. 167
4.7 Numerical errors and convergence orders of Zalesak solid rotation on grid A and grid B comparison with THINC type schemes. 169
4.8 Numerical errors and convergence rates of UMTHINC/QHQ schemes on comparison with other existing PLIC VOF schemes for the time-dependent single vortex test[126] at $T = 2$. We use the numerical results as well as the names of different PLIC schemes reported in [126, 54] and [134]. 169
4.9 Same as Table 4.8, but for $T = 8$. 170
4.10 Numerical errors and convergence orders of UMTHINC/QHQ in the Zalesak 3D solid rotational flow on grid A and grid B. 171
4.11 Numerical errors and convergence orders for the time-dependent 3D vortical deformation flow test. 173

5.1 Reconstruction function for calculation of nodal curvature κ_{ik}. 179
5.2 Convergence behavior for pressure jump after one time step with exact curvature($\kappa = 4$) and numerical curvature. 184
5.3 Sensitivity for spurious current with different tolerance $\varepsilon_{\text{pressure}}$ in pressure Poison equation after one time step. 184
5.4 Quantitative comparison for results computed on good mesh and bad mesh. 186
5.5 Comparison of terminal bubble shapes observed in experiments and predicted in simulation under Reynolds and Bond number. 193
5.6 Comparison of droplet shape between the present numerical solution and referred experimental data [102]. 194

Nomenclature

γ specific heat capacity ratio

κ curvature of interface

ϕ point value of any scalar quantity

$\mathbf{m}$ momentum vector with three component denoted by m_x, m_y, m_z

ν kinetic viscosity

Ω_i control volume of grid element i

$\overline{\phi}$ integrated average of any scalar quantity

ρ density

Γ_{ij} surface segment j of grid element i

E total energy

$H(\mathbf{x})$ hyperbolic tangent function for interface capturing

J Jacobian matrix

p pressure

$\mathbf{u}$ velocity vector with three component denoted by u, v, w

ξ, η, ζ component of three dimensional local coordinate

t time

x, y, z component of three dimensional Cartesian coordinate

Chapter 1

Introduction

1.1 Background

Multi-phase complex flows cover a wide spectrum of problems in industrial applications including engine combustion, hydraulic pump, floating wind turbine and so on. These problems involve not only complex geometry but also complicated physical phenomena such as high Reynolds number turbulent flows, multiphase interfacial flows, and compressible flows, all of which are very challenging research issues in both science and engineering. Numerical simulation for complex flow has been widely accepted as an indispensable measure due to its great superiority over experiments to extract data and optimize design within affordable expense.

Computational Fluid Dynamics (CFD) provides the methods for numerical simulation of complex flows. In spite of the fact that there are a dozen of methodologies and numerous schemes available for CFD analysis, it is still far from requirement for accurately reproducing most physical phenomena in complex flows. The difficulties for simulation mainly lie in following issues:

- Complex geometric structure: The applications for industries are always associated with complex geometric structures such as blade of water turbine, spray nozzle in the engine, spacecraft and so on. In this situation, unstructured grid is required due to its flexibility and generality for elements splitting procedure and simplicity for specification of boundary condition. Not limited to triangular and tetrahedral elements, quadrilateral, hexahedral prismatic and pyramidal elements are also required particularly for resolving boundary layer in high Reynolds flows. However, unstructured grid brings in a series of difficulties in the algorithmic complexity, rapidly increases computational cost and solution dependency on grid quality.

- Adequate solution accuracy: The solution with adequate accuracy is difficult to achieve on unstructured grid due to its geometrical and topological complexity of

computational grid. Higher numerical reconstruction involving more degree of freedoms (DOFs) cannot be carried out as straightforwardly as structured grid. Moreover, the elimination or alleviation for accuracy degradation by mesh quality is also one of the major difficulties for practical applications.

- Applicable complexity and computational cost: Organization of geometrical and topological relations on unstructured grids lead to significant increase in both processor calculation and memory usage. The algorithmic formulation based on unstructured grid needs extra effort to adopt flexible grid information. This extra cost increases rapidly and even becomes prohibitive due to the fact that it usually associates with dense matrix manipulation within each reconstruction stencil. Thus, the algorithmic complexity and computational cost should be paid adequate attention for ensuring practicality for real applications.

In this study, against these difficulties, we will propose novel methodologies and develop practical numerical model on unstructured grids for the simulation of complex flows. In the next section, an overview of the subjects is presented, covering the relevant studies concerning the reconstruction for spatial discretisation, interface capturing in multiphase flow and Mach uniform model as well as oscillation suppression procedure in compressible flow.

1.2 Previous and related studies

1.2.1 Reconstruction for spatial discretisation

In the past few decades, there have been numerous studies of spatial discretisation in order to obtain adequate solution. Among these studies, the finite volume method (FVM) has gained a great popularity in computational fluid dynamics (CFD) because of its better conservativeness and flexibility to adapt to arbitrary unstructured grids. Nearly all commercial CFD codes are based on the "FVM + unstructured grid" prevailing paradigm. However, developing high-order finite volume model on unstructured grids is not a trivial task. For example, the essentially non-oscillatory (ENO)[53, 1, 143] finite volume scheme proposed by Harten firstly utilized high-order finite-volume discretization based on adaptive stencil strategy in order to choose "smoothest" reconstruction stencil. In addition, weighted ENO (WENO)[36, 59, 76, 30, 153] schemes have been developed by devising an effective indicator function to evaluate "smoothness" of each stencil. Some other schemes as well as their variants construction high-order reconstruction formulation based on k-exact least-square method[10, 11, 114, 115, 112, 110]. The major challenges in these cases are primarily related to stencil selection. As mentioned in [36], particular attention must be paid to choose the admissible stencils and there is not a simple rule to guide this pro-

cedure for reconstructions higher than first order. Additionally, the wide reconstruction stencils give rise to difficulties with specification of boundary condition and parallel implementation. As a matter of fact, most operational codes, including the major commercial codes, are limited to the second order on unstructured grids, where a linear reconstruction such as the MUSCL (Monotone Upstream-centered Schemes for Conservation Laws) scheme [159, 160] is used.

The numerical schemes with compact stencil, on the other hand, add the degree of freedoms (DOFs) locally on each cell for high order reconstructions, and are more flexible and easier to implement on unstructured meshes. The representative methods of this sort are the discontinuous Galerkin (DG) method [21, 22, 23, 24], the spectral finite volume (SV) and spectral difference (SD) method [162, 163, 164, 103]. The DG, SV and SD methods share many similarities and the major difference is related to how to determine and update the DOFs in selected reconstruction stencils. These high order schemes generally make use of the Riemann solvers to get the numerical fluxes across cell boundaries where the reconstructed physical fields are allowed to be discontinuous, and have proven to gain great success in solving advection-dominated flows. However, as mentioned in [90], these type of high order version of schemes suffer from : (i) more restrictive time step for stability and further exacerbated with order increasing; (ii)relative high computational cost and storage cost, particularly for implicit solution procedure. Furthermore, not as many as implementations of these methods are found for the incompressible Navier-Stokes equations where one has substantial difficulty because of the singularity in the hyperbolic system as the sound speed can be infinite.

As related studies indicate, both FVM and the existing high-order local reconstruction based methods have not be able to fully meet different requirements for industrial applications. Being an approach different from the aforementioned ones, a class of schemes, known as the CIP (cubic interpolated pseudo-particle method or constrained interpolation profile) method, were proposed and developed by Yabe and co-workers [180, 6, 70, 183, 170, 148, 182, 71, 169]. The underlying idea of CIP is to make use of multiple types of discrete quantities, which are in fact the different moments of the physical field, as the prognostic variables. The successive studies under the multi-moment concept have shown a new path out of the numerical framework to develop practical models [172, 174, 175, 3, 64, 63, 20]. Among others, the multi-moment finite volume method (MM-FVM) and multi-moment constrained finite volume method(MCV) demonstrate great potential for real-case applications as a good trade-off between computational efficiency and numerical accuracy. The extension of MM-FVM and MCV to unstructured grids has been investigated by adding point values at both cell vertices and edges. These approaches are only limited to two dimensional triangular element and complicated to realize on three dimensional grids for real-case applications. Following the studies of

[4, 63, 65], we will simplify the original unstructured MM-FVM and MCV and extend toward arbitrary unstructured grids for establishment of a practical CFD model for complex flows.

1.2.2 Interface capturing in multiphase flow

The one-fluid model [152] has achieved a great progress in the past decades and now is widely used in the simulations of multi-phase fluid dynamics. The interface capturing method plays a key role in a one-fluid model for identifying two physically immiscible fluids. Eulerian type formulation that solves a field function in a fixed grid has been proven powerful and robust for the multiphase flow analyses involving topological changes in the moving interfaces separating different fluids. Among the widely used methods of this kind, the volume of fluid (VOF) method is of particular interest because of its rigorous numerical conservation. Following the underlying concept in [61], more sophisticated algorithms for reconstructing the interface have been proposed in the successive studies [8, 54, 122, 123, 126, 130, 134, 189, 190].

A VOF method makes use of the volume fraction function to identify the moving interface which is updated through a finite volume formulation. So, the key issue is how to calculate the numerical fluxes. To this end, piecewise reconstructions must be built over the grid cells where the interface falls in. The most popular reconstruction in the VOF method is the piecewise linear interface calculation (PLIC) method found in [189, 190] and its advanced variants in [8, 54, 122, 123, 126, 130, 134], where a Heaviside function is defined by explicitly creating the interface with a line (2D) or a plane (3D) based on geometric representations which are usually complicated, even some efforts have been made to simplify the numerical procedure in the PLIC algorithm [133]. A more comprehensive survey of the geometric type VOF method is found in [152].

Above mentioned methods are essentially established on a Cartesian coordinate mesh, and there are a few existing works in the literature to extend the PLIC reconstruction to unstructured grids with triangular element [137, 185] and tetrahedral element [185]. The reason behind is that a geometric reconstruction for an interface in a triangular or tetrahedral grid including the interface advection is not a trivial task, which involves much more complicated numerical procedure compared to the cases in the Cartesian grid. Furthermore, the algorithmic complexity will be significantly increased when higher order approximation, e.g. quadratic surface, is used to represent the interface. To our knowledge, numerical model for interfacial flows with PLIC VOF method in tetrahedral grid has not been well-established. From the point of real-case application, a reliable and efficient interface-capturing scheme for unstructured triangular/tetrahedral grid is highly demanded.

Based on another strategy different from the conventional PLIC VOF schemes, an al-

gebraic type method, so-called tangent of hyperbola interface capturing (THINC) method [174], has been proposed by utilizing a hyperbolic tangent function for the reconstruction. Some variants have been so far developed [186, 176, 187] to improve the multidimensional solutions when using the 1D solver as the basic building block. These THINC schemes are very simple and can be used as normal advection schemes. In spite of the simplicity, these schemes can give high-quality numerical solutions comparable to the conventional PLIC VOF methods. Using a continuous analytical function, a THINC scheme uniquely retrieves the interface from given volume fraction values. The geometric manipulations in the PLIC algorithm are not required here, which largely simplifies the numerical procedure and allows the multidimensional extension to be conducted in a straightforward way. A sophisticated scheme, so-called MTHINC (multidimensional THINC) method [66], has been proposed by using a multidimensional hyperbolic tangent function for reconstruction. The numerical accuracy is remarkably improved due to the multi-dimensional reconstruction, and moreover, higher-order interface approximation, like the quadratic interface, can be formulated straightforwardly under the THINC framework.

Following previous studies of MTHINC method, we will develop unstructured multi-dimensional THINC (UMTHINC) formulation which gives accurate solution comparable to PLIC type VOF schemes, and is easy to implement on arbitrary unstructured grids and robust enough to deal with distorted grid elements.

1.2.3 Mach uniform model and oscillation suppression procedure in compressible flow

The complex flows in industrial applications usually involve variation in wide range of Mach number from incompressible to compressible flows. The standard density and Riemann solver based methods encounter substantial difficulty to deal with the singularity in the case of small Mach number, which makes the pressure extremely sensitive to even a tiny change in density and results in severely restricted CFL condition due to computational stability. The remedy for this type of numerical methods to be applicable for low Mach flow has to resort to preconditioning the density-based explicit method [46, 87, 157, 156, 165].

As an alternative approach to this problem, the pressure-based unified projection formulation enables simulations involving compressible and incompressible flows with a unified formulation. The pressure projection method was pioneered by Harlow et al. and Chorin[49, 50, 51, 19] where the incompressibility is realized by the procedure of projecting the final velocity onto a subspace that satisfies divergence free condition. The pressure projection method can be easily modified to compute compressible flow by including the compressibility in the mass continuity equation when deriving the implicit pressure Poisson equation. The researches in this direction can be found in [72, 141, 80, 107, 13, 181, 180, 172, 175, 91, 93] among others. Most of these researches

use structured grids with staggered moment arrangement, which has been proven to be more effective for velocity and pressure coupling. Further efforts regarding extending this type of methods to unstructured grids to develop practical models of adequate numerical accuracy and robustness are still required.

Another issue for compressible fluid dynamics is how to suppress or eliminate unphysical oscillation in the region with soltuion discontinuities. In last decades, sustained efforts have been made for the sort of total variational diminishing (TVD) schemes which stablize the computation of discontinuities and are widely used due to its efficient implementation. After the theoretical basis work of Harten [52], many researches, such as [147, 18, 92, 127, 128], have been carried out which facilitated the TVD method to be widely accepted as a main-stream solver for aerodynamics and other CFD applications. According to Darwish's study[26], the TVD limiter has been extend to arbitrary unstructured grids. A TVD limiting formulation compatible with MM-FVM/MCV schemes has been devised on unstructured grids in this study to remove unphysical oscillations in compressible flow simulations.

1.3 Purpose of present study

The purpose of present study is to develop unstructured numerical model for complex flow based on finite volume formulation. The present model needs to inherit full flexibility of FVM to adopt both structured and unstructured grids including triangular, quadrilateral elements for 2D and tetrahedral, hexahedral, prismatic and pyramidal elements for 3D. Compared with conventional FVM, this model is aimed at significantly improving the numerical accuracy at expense of minimized extra computational cost. At meanwhile, it should reduce or even remove the degradation error due to the distorted elements. In this study, we put effort to make improvements concerning spatial discretization method, interface capturing scheme, TVD limiting approaches which constitute major ingredients of numerical model for incompressible/compressible flow, multiphase flow and high Reynolds number flow.

- We will propose a novel numerical formulation for spatial discretization and apply it to solve incompressible unsteady Navier–Stokes equations. Compared with conventional FVM, additional DOFs are defined at cell vertices and treated as independent variables. These DOFs facilitate to make more accurate and robust reconstruction within compact stencils. Without large increase in algorithmic complexity and computational cost, the targeted numerical model should achieve significant improvements in (1) the convergence rate in advection computation, (2) the accuracy of the whole fluid solver in terms of numerical errors and (3) the robustness to the computational mesh.

- We will extend the multi-dimensional THINC formulation[66] for interface capturing to arbitrary unstructured grids, which leads to an accurate and practical interface-capturing method well-suitable for simulation of interfacial multiphase flow involving complex geometry. Using multi-dimensional hyperbolic tangent function, the new scheme, unstructured MTHINC (UMTHINC) method piecewisely reconstructs the interface in each grid cell. In additional to linear approximation, the UMTHINC scheme can even fit the interface by a quadratic surface in quadrilateral (2D) and hexahedral (3D) elements. As expected, the present UMTHINC scheme shows competitive accuracy in both numerical error and convergence behavior in comparison with other VOF interface-capturing schemes.

- We will develop Mach uniform pressure based solver and TVD limiting approaches for compressible flow. Solving with conservative quantities like density, momentum and total energy based on finite volume method, the present model can ensure exact conservation. With implicitly formulated pressure Poisson equation, the restriction of Mach number and CFL condition of stability held by density based method can be removed unconditionally. We will also devise TVD limiter compatible for MM-FVM/MCV scheme which effectively eliminates numerical oscillation in region of the discontinuities without introducing excessive diffusion. Numerical accuracy in term of both error and convergence should be ensured superiority to conventional FVM schemes. The performance will be confirmed by a sequence of numerical examples which reveal that present numerical model can accurately resolve compressible flow in wide range of Mach numbers.

1.4 Thesis outline

Chapter 2 primarily introduces novel reconstruction procedure of MM-FVM and MCV formulation on unstructured grids based on multi-moment concept. In addition to the volume integrated average (VIA) that is the only computational variable in the conventional FVM, we add the point value (PV) at the cell vertices as a new DOF. The present method is called volume integrated average and point value based multi-moment (VPM) method, in which the VIA moment is computed by a finite volume formulation of flux form, and thus exactly conservative, while the PV moment is point-wisely updated by a differential form that can be computed very efficiently in unstructured grids. The reconstruction stencil is compact, and more importantly there is no arbitrariness in choosing the stencil for reconstruction. This method can be equivalently expressed as multi-moment constrained finite volume method(MCV) by approximating VIA in term of PVs at cell vertices as well as cell center. Both VPM and MCV has been extended to arbitrary unstructured grids including triangular, quadrilateral elements for 2D and tetrahedral, hexahedral, prismatic

and pyramidal elements for 3D.

Chapter 3 demonstrates the governing equations and numerical models for incompressible flow and Mach uniform compressible flow. Both VPM and MCV methods are applied with pressure solution procedure. Given the solution variable ϕ^n at time n, the Navier-Stokes equations are integrated to time $n+1$ by using a sequence of fraction steps. Either Runge-Kuta or back-difference formula (BDF) is used as time integration scheme to bridge three decomposed operators. In order to remove non-physical oscillation near the solution discontinuities, TVD limiter with higher order is devised to make full use of multi-moments or moment-constraints for VPM/MCV schemes. As shown in verification tests, the present numerical models show significant improvement in accuracy, robustness and reliability for incompressible flow, Mach uniform compressible flow as well as high Reynolds number flow.

Chapter 4 presents novel unstructured MTHINC (UMTHINC) method to capture or track moving interface for multiphase flow. In order to identify the different fluids, volume fraction value is defined and reconstructed by multi-dimensional hyperbolic tangent function in each grid cell. Despite of different integral quadrature approaches with each element type, the reconstruction formulation can be represented in the unified form as

$$\widehat{H}(\mathbf{X}) = \frac{1}{2}\left(1 + \tanh\left(\beta\left(P(\mathbf{X}) + d\right)\right)\right),$$

where $\mathbf{X}$ is local coordinate, $P(\mathbf{X})$ is a surface function in two or three dimensions, and parameter β is for controlling the sharpness of the function $\widehat{H}(\mathbf{X})$. The performance of UMTHINC scheme is verified by numerous benchmark tests, which reveals that both accuracy and convergence rate is competitive to PLIC type VOF schemes within only several algebraic calculations.

As both incompressible flow solver and interface capturing scheme have been developed, the multiphase interfacial flow will be integrated and illustrated in Chapter 5. In order to identify immiscible fluids, VOF is defined in each cell and updated by UMTHINC scheme at each time step. Referring to the work of [187, 188], we proposed techniques for VOF smoothing based on THINC formulation and calculation of geometrical property of interface like curvature and unit normal vector. Numerical tests carried out in the subsequent studies indicate that the present numerical model is of high performance in accuracy, robustness and sufficient reliability in resolving surface tension force for multiphase flow.

Chapter 6 summarizes present study and offers some conclusion regarding the major contributions and impact on related studies. We also mention some deficiencies and provide suggestions for future research.

Chapter 2

Reconstructions based on multi-moments and multi-moment constraints on unstructured grids

2.1 Definition of multi-moments on unstructured grids

The computational domain is divided into elements Ω_i $(i = 1, ..., I)$ of different types.

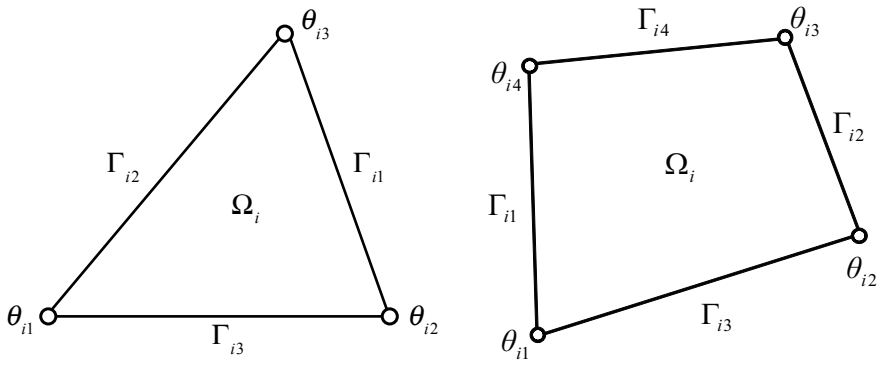


Figure 2.1: The two-dimensional grid elements: triangular(left) and quadrilateral(right) element.

Shown in Fig. 2.1, we consider triangular and quadrilateral elements in two dimensions. We denote the vertices by θ_{ik} with $k = 1, 2, \cdots, K$ and $K = 3$ for triangular element and $K = 4$ for quadrilateral element. The locations of the vertices are (x_{ik}, y_{ik}) respectively, and the boundary line segments of element Ω_i are denoted by Γ_{ij} as shown Fig. 2.1. We also denote the middle points and the outward normal unit vector of segment Γ_{ij} by $\tilde{\theta}_{ij}$ and $\mathbf{n}_{ij} = (n_{xij}, n_{yij})$ respectively. The mass center (x_{ic}, y_{ic}) of the element is denoted by θ_{ic}. For three dimensions, we consider four types of elements used in this study, i.e. tetrahedron, hexahedron, prism and pyramid. In the same symbol and notation, the cell

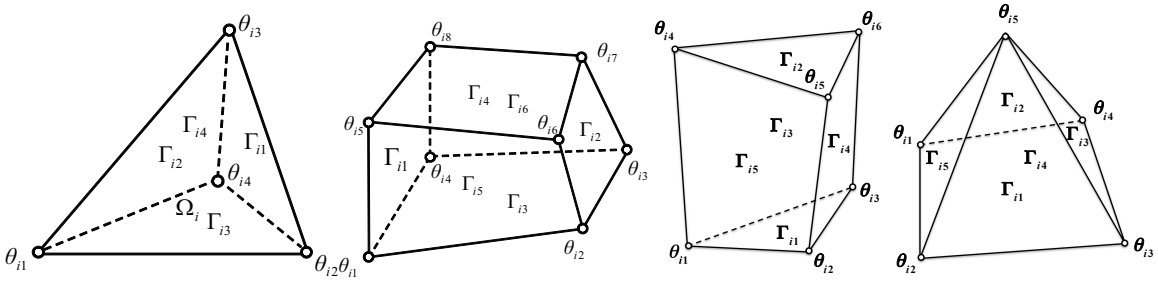


Figure 2.2: The arbitrary unstructured grid element. From left to right is quadrilateral, tetrahedral, hexahedral, prismatic and pyramidal element.

vertices θ_{ik}, boundary surface segments Γ_{ij} as well as normal unit vector $\mathbf{n}_{ij}$ are denoted as shown in Fig. 2.2. The vertices are connected by boundary segments Γ_{ij} which are either a straight line (2D) or a plane (3D) separating elements Ω_i and Ω_{ij}, where the cell index "ij" is re-numbered in respect to the target cell Ω_i. The topological relation with its global index is realized through a connection table.

2.2 Mapping of grid element

In order to simplify the reconstruction, mesh cell Ω_i is transformed from global coordinate system $x-y-z$ to a canonical reference coordinate system $\xi-\eta-\zeta$ as shown in Fig. 2.3 and 2.4. For 2D, component in third dimension is discarded by default.

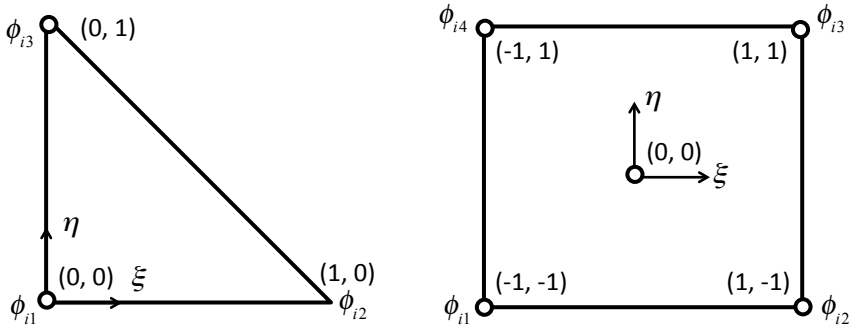


Figure 2.3: The two-dimensional grid elements: triangular(left) and quadrilateral(right) element.

The mapping formulation for both two and three dimensional elements can be generalized in the form of:

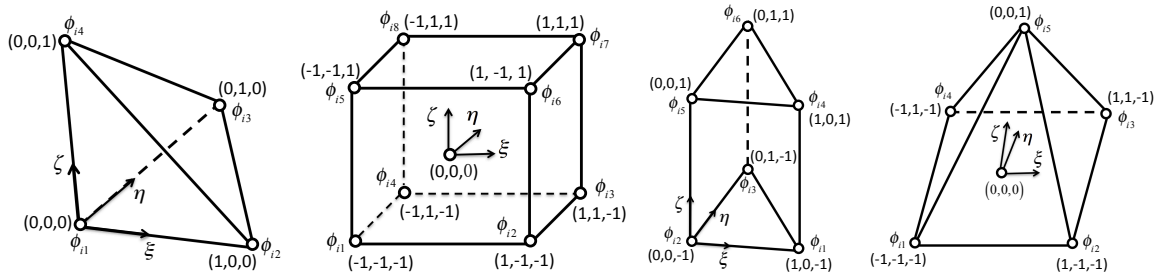


Figure 2.4: The arbitrary unstructured grid element. From left to right is quadrilateral, tetrahedral, hexahedral, prismatic and pyramidal element.

$$\begin{bmatrix} 1 \\ x \\ y \\ z \\ \phi \end{bmatrix} = \begin{bmatrix} 1 & 1 & \cdots & 1 & 1 \\ x_{i1} & x_{i2} & \cdots & x_{iK-1} & x_{iK} \\ y_{i1} & y_{i2} & \cdots & y_{iK-1} & y_{iK} \\ z_{i1} & z_{i2} & \cdots & z_{iK-1} & z_{iK} \\ \phi_{i1} & \phi_{i2} & \cdots & \phi_{iK-1} & \phi_{iK} \end{bmatrix} \begin{bmatrix} \mathcal{N}_1 \\ \mathcal{N}_2 \\ \vdots \\ \mathcal{N}_{K-1} \\ \mathcal{N}_K \end{bmatrix}$$

where ϕ represents any possible quantity located on random coordinate (x, y, z) in each grid element, (x_{ik}, y_{ik}, z_{ik}) stands for coordinate of cell vertices and $\mathcal{N}_k$ for corresponding basis function on related vertices. Another important issue is to map first order derivatives from global coordinate to local coordinate and vice versa. The derivatives transformed between global and local coordinate are expressed in the form of (2.1) and (2.2).

$$\begin{aligned}
\Phi_{i\xi}(\xi_i,\eta_i,\zeta_i) &= x_{\xi i}(x_i,y_i,z_i)\,\Phi_{ix}(x_i,y_i,z_i) + y_{\xi i}(x_i,y_i,z_i)\,\Phi_{iy}(x_i,y_i,z_i) + z_{\xi i}(x_i,y_i,z_i)\,\Phi_{iz}(x_i,y_i,z_i), \\
\Phi_{i\eta}(\xi_i,\eta_i,\zeta_i) &= x_{\eta i}(x_i,y_i,z_i)\,\Phi_{ix}(x_i,y_i,z_i) + y_{\eta i}(x_i,y_i,z_i)\,\Phi_{iy}(x_i,y_i,z_i) + z_{\eta i}(x_i,y_i,z_i)\,\Phi_{iz}(x_i,y_i,z_i), \\
\Phi_{i\zeta}(\xi_i,\eta_i,\zeta_i) &= x_{\zeta i}(x_i,y_i,z_i)\,\Phi_{iy}(x_i,y_i,z_i) + y_{\zeta i}(x_i,y_i,z_i)\,\Phi_{iy}(x_i,y_i,z_i) + z_{\zeta i}(x_i,y_i,z_i)\,\Phi_{iz}(x_i,y_i,z_i).
\end{aligned} \tag{2.1}$$

$$\begin{aligned}
\Phi_{ix}(x_i,y_i,z_i) &= \xi_{xi}(\xi_i,\eta_i,\zeta_i)\,\Phi_{i\xi}(\xi_i,\eta_i,\zeta_i) + \eta_{xi}(\xi_i,\eta_i,\zeta_i)\,\Phi_{i\eta}(\xi_i,\eta_i,\zeta_i) + \zeta_{xi}(\xi_i,\eta_i,\zeta_i)\,\Phi_{i\zeta}(\xi_i,\eta_i,\zeta_i), \\
\Phi_{iy}(x_i,y_i,z_i) &= \xi_{yi}(\xi_i,\eta_i,\zeta_i)\,\Phi_{i\xi}(\xi_i,\eta_i,\zeta_i) + \eta_{yi}(\xi_i,\eta_i,\zeta_i)\,\Phi_{i\eta}(\xi_i,\eta_i,\zeta_i) + \zeta_{yi}(\xi_i,\eta_i,\zeta_i)\,\Phi_{i\zeta}(\xi_i,\eta_i,\zeta_i), \\
\Phi_{iz}(x_i,y_i,z_i) &= \xi_{zi}(\xi_i,\eta_i,\zeta_i)\,\Phi_{i\xi}(\xi_i,\eta_i,\zeta_i) + \eta_{zi}(\xi_i,\eta_i,\zeta_i)\,\Phi_{i\eta}(\xi_i,\eta_i,\zeta_i) + \zeta_{zi}(\xi_i,\eta_i,\zeta_i)\,\Phi_{i\zeta}(\xi_i,\eta_i,\zeta_i).
\end{aligned} \tag{2.2}$$

These transformation formulations can be equivalently expressed in matrix form (2.4) by Jacobian operator J as well as inverse Jacobian operator J^{-1}. More details for different element shapes are shown in Table 2.1 and 2.2.

	Triangular element	Quadrilateral element
mapping formulation	$\mathcal{N}_1 = 1-\xi-\eta,$ $\mathcal{N}_2 = \xi,$ $\mathcal{N}_3 = \eta.$	$\mathcal{N}_n = \frac{1}{4}(1+\xi_n\xi)(1+\eta_n\eta)$ $n = 1,2,3,4$
basis function for mapping	$x_{\xi i} = x_{i2} - x_{i1},$ $x_{\eta i} = x_{i3} - x_{i1},$ $y_{\xi i} = y_{i2} - y_{i1},$ $y_{\eta i} = y_{i3} - y_{i1}.$	$x_{\xi i} = \frac{1}{4}(-x_{i1} + x_{i2} + x_{i3} - x_{i4} + A_x\eta)$ $x_{\eta i} = \frac{1}{4}(-x_{i1} - x_{i2} + x_{i3} + x_{i4} + A_x\xi)$ $y_{\xi i} = \frac{1}{4}(-y_{i1} + y_{i2} + y_{i3} - y_{i4} + A_y\eta)$ $y_{\eta i} = \frac{1}{4}(-y_{i1} - y_{i2} + y_{i3} + y_{i4} + A_y\xi)$ $A_\alpha = \alpha_{i1} - \alpha_{i2} + \alpha_{i3} - \alpha_{i4},\ \alpha = x \text{ or } y$
derivative from global to local	$\begin{bmatrix} \phi_{\xi i}(x,y) \\ \phi_{\eta i}(x,y) \end{bmatrix} = \begin{bmatrix} x_{\xi i} & y_{\xi i} \\ x_{\eta i} & y_{\eta i} \end{bmatrix} \begin{bmatrix} \frac{\partial \phi_i(x,y)}{\partial x} \\ \frac{\partial \phi_i(x,y)}{\partial y} \end{bmatrix}$	
derivative from local to global	$\begin{bmatrix} \phi_{xi}(\xi,\eta) \\ \phi_{yi}(\xi,\eta) \end{bmatrix} = \begin{bmatrix} \xi_{xi} & \eta_{xi} \\ \xi_{yi} & \eta_{yi} \end{bmatrix} \begin{bmatrix} \frac{\partial \phi_i(\xi,\eta)}{\partial \xi} \\ \frac{\partial \phi_i(\xi,\eta)}{\partial \eta} \end{bmatrix}$	
Jacobian matrix	$J = \begin{bmatrix} x_{\xi i} & y_{\xi i} \\ x_{\eta i} & y_{\eta i} \end{bmatrix},\ J^{-1} = \begin{bmatrix} \xi_{xi} & \eta_{xi} \\ \xi_{yi} & \eta_{yi} \end{bmatrix}$	

Table 2.1: Mapping for triangular and quadrilateral element.

$$\begin{bmatrix} \Phi_{i\xi}(\xi_i,\eta_i,\zeta_i) \\ \Phi_{i\eta}(\xi_i,\eta_i,\zeta_i) \\ \Phi_{i\zeta}(\xi_i,\eta_i,\zeta_i) \end{bmatrix} = \begin{bmatrix} x_{\xi i} & y_{\xi i} & z_{\xi i} \\ x_{\eta i} & y_{\eta i} & z_{\eta i} \\ x_{\zeta i} & y_{\zeta i} & z_{\zeta i} \end{bmatrix} \begin{bmatrix} \Phi_{ix}(x_i,y_i,z_i) \\ \Phi_{iy}(x_i,y_i,z_i) \\ \Phi_{iz}(x_i,y_i,z_i) \end{bmatrix} = J \cdot \begin{bmatrix} \Phi_{ix}(x_i,y_i,z_i) \\ \Phi_{iy}(x_i,y_i,z_i) \\ \Phi_{iz}(x_i,y_i,z_i) \end{bmatrix} \tag{2.3}$$

$$\begin{bmatrix} \Phi_{ix}(x_i,y_i,z_i) \\ \Phi_{iy}(x_i,y_i,z_i) \\ \Phi_{iz}(x_i,y_i,z_i) \end{bmatrix} = \begin{bmatrix} \xi_{xi} & \eta_{xi} & \zeta_{xi} \\ \xi_{yi} & \eta_{yi} & \zeta_{yi} \\ \xi_{zi} & \eta_{zi} & \zeta_{zi} \end{bmatrix} \begin{bmatrix} \Phi_{i\xi}(\xi_i,\eta_i,\zeta_i) \\ \Phi_{i\eta}(\xi_i,\eta_i,\zeta_i) \\ \Phi_{i\zeta}(\xi_i,\eta_i,\zeta_i) \end{bmatrix} = J^{-1} \cdot \begin{bmatrix} \Phi_{i\xi}(\xi_i,\eta_i,\zeta_i) \\ \Phi_{i\eta}(\xi_i,\eta_i,\zeta_i) \\ \Phi_{i\zeta}(\xi_i,\eta_i,\zeta_i) \end{bmatrix} \tag{2.4}$$

	Tetrahedral element	Hexahedral element	Prismatic element	Pyramidal element
mapping formulation	$\mathcal{N}_1 = 1-\xi-\eta-\zeta,$ $\mathcal{N}_2 = \xi,$ $\mathcal{N}_3 = \eta,$ $\mathcal{N}_4 = \zeta.$	$\mathcal{N}_n = \frac{1}{8}(1+\xi_n\xi)(1+\eta_n\eta)(1+\zeta_n\zeta)$ $n = 1,2,3,4,5,6,7,8$	$\mathcal{N}_1 = \frac{1}{2}(1-\xi-\eta)(1-\zeta),$ $\mathcal{N}_2 = \frac{1}{2}\xi(1-\zeta),$ $\mathcal{N}_3 = \frac{1}{2}\eta(1-\zeta),$ $\mathcal{N}_4 = \frac{1}{2}(1-\xi-\eta)(1+\zeta),$ $\mathcal{N}_5 = \frac{1}{2}\xi(1+\zeta),$ $\mathcal{N}_6 = \frac{1}{2}\eta(1+\zeta),$	$\mathcal{N}_1 = \frac{1}{8}(1-\zeta) - \frac{1}{4}(\xi+\eta+\xi\eta\zeta),$ $\mathcal{N}_2 = \frac{1}{8}(1-\zeta) + \frac{1}{4}(\xi-\eta+\xi\eta\zeta),$ $\mathcal{N}_3 = \frac{1}{8}(1-\zeta) + \frac{1}{4}(\xi+\eta-\xi\eta\zeta),$ $\mathcal{N}_4 = \frac{1}{8}(1-\zeta) - \frac{1}{4}(\xi-\eta-\xi\eta\zeta),$ $\mathcal{N}_5 = \frac{1}{2} + \frac{1}{2}\zeta,$
basis function for mapping	$x_{\xi i} = \sum x_{ik}\left(\partial\mathcal{N}_j/\partial\xi\right), \quad x_{\eta i} = \sum y_{ik}\left(\partial\mathcal{N}_j/\partial\xi\right), \quad x_{\zeta i} = \sum z_{ik}\left(\partial\mathcal{N}_j/\partial\xi\right),$ $y_{\xi i} = \sum x_{ik}\left(\partial\mathcal{N}_j/\partial\eta\right), \quad y_{\eta i} = \sum y_{ik}\left(\partial\mathcal{N}_j/\partial\eta\right), \quad y_{\zeta i} = \sum z_{ik}\left(\partial\mathcal{N}_j/\partial\eta\right),$ $z_{\xi i} = \sum x_{ik}\left(\partial\mathcal{N}_j/\partial\zeta\right), \quad z_{\eta i} = \sum y_{ik}\left(\partial\mathcal{N}_j/\partial\zeta\right), \quad z_{\zeta i} = \sum z_{ik}\left(\partial\mathcal{N}_j/\partial\zeta\right).$			
derivative from global to local	$\begin{bmatrix} \phi_{\xi i}(x,y,z) \\ \phi_{\eta i}(x,y,z) \\ \phi_{\zeta i}(x,y,z) \end{bmatrix} = \begin{bmatrix} x_{\xi i} & y_{\xi i} & z_{\xi i} \\ x_{\eta i} & y_{\eta i} & z_{\eta i} \\ x_{\zeta i} & y_{\zeta i} & z_{\zeta i} \end{bmatrix} \begin{bmatrix} \frac{\partial\phi_i(x,y,z)}{\partial x} \\ \frac{\partial\phi_i(x,y,z)}{\partial y} \\ \frac{\partial\phi_i(x,y,z)}{\partial z} \end{bmatrix}$			
derivative from local to global	$\begin{bmatrix} \phi_{xi}(\xi,\eta,\zeta) \\ \phi_{yi}(\xi,\eta,\zeta) \\ \phi_{zi}(\xi,\eta,\zeta) \end{bmatrix} = \begin{bmatrix} \xi_{xi} & \eta_{xi} & \zeta_{xi} \\ \xi_{yi} & \eta_{yi} & \zeta_{yi} \\ \xi_{zi} & \eta_{zi} & \zeta_{zi} \end{bmatrix} \begin{bmatrix} \frac{\partial\phi_i(\xi,\eta,\zeta)}{\partial\xi} \\ \frac{\partial\phi_i(\xi,\eta,\zeta)}{\partial\eta} \\ \frac{\partial\phi_i(\xi,\eta,\zeta)}{\partial\zeta} \end{bmatrix}$			
Jacobian matrix	$J = \begin{bmatrix} x_{\xi i} & y_{\xi i} & z_{\xi i} \\ x_{\eta i} & y_{\eta i} & z_{\eta i} \\ x_{\zeta i} & y_{\zeta i} & z_{\zeta i} \end{bmatrix}, \; J^{-1} = \begin{bmatrix} \xi_{xi} & \eta_{xi} & \zeta_{xi} \\ \xi_{yi} & \eta_{yi} & \zeta_{yi} \\ \xi_{zi} & \eta_{zi} & \zeta_{zi} \end{bmatrix}$			

Table 2.2: Mapping for tetrahedral, hexahedral, prismatic and pyramidal element.

Element Type	Reconstruction Type
Triangular element	$A_1 = 1,\ B_1 = 0,\ A_2 = 0,\ B_2 = 0$
Quadrilateral element	$A_1 = 1,\ B_1 = 0,\ A_2 = 1,\ B_2 = 0$
Tetrahedral element	$A_1 = 1,\ B_1 = 1,\ A_2 = 0,\ B_2 = 0$
Hexahedral element	$A_1 = 1,\ B_1 = 1,\ A_2 = 1,\ B_2 = 1$
Prismatic element	$A_1 = 1,\ B_1 = 1,\ A_2 = 0,\ B_2 = 1$
Pyramidal element	$A_1 = 1,\ B_1 = 1,\ A_2 = 1,\ B_2 = 0$

Table 2.3: Coefficients of reconstruction function in VPM scheme for different element shapes.

2.3 High order reconstructions using volume-average/point-values

The present VPM method employs volume integrated average (VIA) and point value (PV) located at the cell vertices $(\theta_{ik}, k = 1, 2, \cdots, K)$ as prognostic variables for each element. For a physical variable $\phi(x, y, z, t)$ the VIA and PV are defined as

$$\phi_{ik}(t) \equiv \phi(x_{ik}, y_{ik}, z_{ik}, t),\ k = 1, 2, \cdots, K; \tag{2.5}$$

$$\overline{\phi}_i(t) \equiv \frac{1}{|\Omega_i|} \int_{\Omega_i} \phi(x, y, t) d\Omega. \tag{2.6}$$

In addition to prognostic VIA and PV, the $(\phi_{\xi i}, \phi_{\eta i}, \phi_{\zeta i})$ and $\left(\phi_{\xi^2 i}, \phi_{\eta^2 i}, \phi_{\zeta^2 i}\right)$ at barycenter θ_{ic} are defined as first order and second derivatives respectively for higher order reconstruction. The piecewise reconstruction polynomial is constructed on the local coordinate in the form of:

$$\Phi_i(\xi, \eta) = \sum_{k=1}^{k=K} \psi_{ik}\phi_{ik} + \overline{\psi}\,\overline{\phi}_i + A_1(\psi_\xi \phi_{\xi i} + \psi_\eta \phi_{\eta i}) + B_1 \psi_\zeta \phi_{\zeta i} + A_2(\psi_{\xi^2}\phi_{\xi^2 i} + \psi_{\eta^2}\phi_{\eta^2 i}) + B_2 \psi_{\zeta^2}\phi_{\zeta^2 i}, \tag{2.7}$$

The related coefficients A_1, A_2, B_1, B_2 vary for different element shapes as given in

Table 2.3, and unknown coefficients can be uniquely determined by following constraint conditions (2.8) in terms of both prognostic and interpolated variables in each step. It is noteworthy that $(\phi_{\xi i}, \phi_{\eta i}, \phi_{\zeta i})$ and $\left(\phi_{\xi^2 i}, \phi_{\eta^2 i}, \phi_{\zeta^2 i}\right)$ are computed intermediately from surrounding DOFs and $\left(\phi_{\xi^2 i}, \phi_{\eta^2 i}, \phi_{\zeta^2 i}\right)$ is not always necessary in some type of elements. The more details of VPM are clarified for each element shape separately.

$$\begin{cases} \Phi_i(\xi_{ik}, \eta_{ik}, \zeta_{ik}) = \phi_{ij} & k = 1, 2, \cdots, K \\ \frac{1}{|\omega|} \iint_\omega \Phi_i(\xi, \eta, \zeta) = \overline{\phi}_i \\ \dfrac{\partial \Phi_i(\xi, \eta, \zeta)}{\partial \xi}\Big|_{(x_{ic}, y_{ic}, z_{ic})} = \phi_{\xi i} \\ \dfrac{\partial \Phi_i(\xi, \eta, \zeta)}{\partial \eta}\Big|_{(x_{ic}, y_{ic}, z_{ic})} = \phi_{\eta i} \\ \dfrac{\partial \Phi_i(\xi, \eta, \zeta)}{\partial \zeta}\Big|_{(x_{ic}, y_{ic}, z_{ic})} = \phi_{\zeta i} \\ \dfrac{\partial^2 \Phi_i(\xi, \eta, \zeta)}{\partial \xi^2}\Big|_{(x_{ic}, y_{ic}, z_{ic})} = \phi_{\xi^2 i} \\ \dfrac{\partial^2 \Phi_i(\xi, \eta, \zeta)}{\partial \eta^2}\Big|_{(x_{ic}, y_{ic}, z_{ic})} = \phi_{\eta^2 i} \\ \dfrac{\partial \Phi_i^2(\xi, \eta, \zeta)}{\partial \zeta^2}\Big|_{(x_{ic}, y_{ic}, z_{ic})} = \phi_{\zeta^2 i} \quad . \end{cases} \tag{2.8}$$

- For triangular element

The reconstruction function for unstructured triangular element Ω_i is built up on the canonical reference coordinate with nodes $\theta_{i1}\,(0,0)$, $\theta_{i2}\,(1,0)$ and $\theta_{i3}\,(0,1)$ as shown in Fig. 2.3. The three boundary line segments of element Ω_i are denoted by $\Gamma_{i1} = \overline{\theta_{i2}\theta_{i3}}$, $\Gamma_{i2} = \overline{\theta_{i3}\theta_{i1}}$ and $\Gamma_{i3} = \overline{\theta_{i1}\theta_{i2}}$. The reconstruction function can be determined from constraint conditions and expressed in basis function form as Table 2.4.

From reconstruction function, PV at cell center is derived straightforwardly as (2.9)

$$\phi_{i4} = \frac{4}{3}\overline{\phi}_i - \frac{1}{9}\left(\phi_{i1} + \phi_{i2} + \phi_{i3}\right). \tag{2.9}$$

- For quadrilateral element

The reconstruction function for unstructured quadrilateral element Ω_i is built up on the canonical reference coordinate with nodes $\theta_{i1}\,(-1,-1)$, $\theta_{i2}\,(1,-1)$, $\theta_{i3}\,(1,1)$ and $\theta_{i4}\,(-1,1)$ as shown in Fig. 2.3. The four boundary line segments of element Ω_i are denoted by $\Gamma_{i1} = \overline{\theta_{i4}\theta_{i1}}$, $\Gamma_{i2} = \overline{\theta_{i2}\theta_{i3}}$, $\Gamma_{i3} = \overline{\theta_{i1}\theta_{i2}}$ and $\Gamma_{i4} = \overline{\theta_{i3}\theta_{i4}}$. The reconstruction function can be determined from constraint conditions and expressed in basis function form as Table 2.5.

From reconstruction function, we can derive PV at cell center in form of

$$\phi_{i5} = \frac{9}{8}\overline{\phi}_i - \frac{1}{32}\left(\phi_{i1} + \phi_{i2} + \phi_{i3} + \phi_{i4}\right) - \frac{1}{8}\left(\phi_{\xi^2 i} + \phi_{\eta^2 i}\right). \tag{2.10}$$

$$\Phi_i(\xi,\eta) \quad = \quad \Phi_i(\xi,\eta) = \psi_1\phi_{i1} + \psi_2\phi_{i2} + \psi_3\phi_{i3} + \overline{\psi}\ \overline{\phi}_i + \psi_\xi\phi_{\xi i} + \psi_\eta\phi_{\eta i},$$

$$\text{constraint conditions} \quad \begin{cases} \Phi_i(0,0) = \phi_{i1} \\ \Phi_i(1,0) = \phi_{i2} \\ \Phi_i(0,1) = \phi_{i3} \\ \iint_\omega \Phi_i(\xi,\eta)d\xi d\eta = \overline{\phi}_i/2 \\ \dfrac{\partial\Phi_i(\xi,\eta)}{\partial\xi}\Big|_{(\frac{1}{3},\frac{1}{3})} = \phi_{\xi i} \\ \dfrac{\partial\Phi_i(\xi,\eta)}{\partial\eta}\Big|_{(\frac{1}{3},\frac{1}{3})} = \phi_{\eta i} \end{cases}$$

$$\text{basis functions} \quad \begin{cases} \psi_1 = 1 - \frac{10}{3}\xi - \frac{10}{3}\eta + \frac{16}{3}\xi\eta + \frac{7}{3}\xi^2 + \frac{7}{3}\eta^2 \\ \psi_2 = \frac{2}{3}\eta - \frac{4}{3}\xi - \frac{2}{3}\xi\eta + \frac{7}{3}\xi^2 - \frac{2}{3}\eta^2 \\ \psi_3 = \frac{2}{3}\xi - \frac{4}{3}\eta - \frac{2}{3}\xi\eta - \frac{2}{3}\xi^2 + \frac{7}{3}\eta^2 \\ \overline{\psi} = 4\xi + 4\eta - 4\xi\eta - 4\xi^2 - 4\eta^2 \\ \psi_\xi = \xi - 2\eta + 2\xi\eta - \xi^2 + 2\eta^2 \\ \psi_\eta = \eta - 2\xi + 2\xi\eta + 2\xi^2 - \eta^2 \end{cases}$$

Table 2.4: Constraint conditions and basis functions for triangular element.

In order to determine $\left(\phi_{\xi^2 i}, \phi_{\eta^2 i}\right)$ in each grid cell, a piecewise reconstruction polynomial $\Psi_i\left(\xi,\eta\right) = c_0 + c_1\xi + c_2\eta + c_3\xi^2 + c_4\eta^2 + c_5\xi\eta$ is constructed. The coefficients are determined by DOFs on local coordinate in each single cell as (2.11)

$$\begin{cases} \Psi_i - 1, -1) = \phi_{i1} \\ \Psi_i(1,-1) = \phi_{i2} \\ \Psi_i(1,1) = \phi_{i3} \\ \Psi_i(-1,1) = \phi_{i4} \\ \iint_{\Omega_i} \Psi_i(\xi,\eta)d\xi d\eta = \overline{\phi}_i \\ \dfrac{\partial\Psi_i(\xi,\eta)}{\partial\xi}\Big|_{(0,0)} = \phi_{\xi i} \\ \dfrac{\partial\Psi_i(\xi,\eta)}{\partial\eta}\Big|_{(0,0)} = \phi_{\eta i} \end{cases} . \tag{2.11}$$

The resulted over-determined matrix system can be solved by least square method. $\left(\phi_{\xi^2 i}, \phi_{\eta^2 i}\right)$ then is expressed by (2.12)

$$
\begin{aligned}
\Phi_i(\xi,\eta) &= \psi_1\phi_{i1} + \psi_2\phi_{i2} + \psi_3\phi_{i3} + \psi_4\phi_{i4} + \psi_5\phi_{i5} + \psi_\xi\phi_{\xi i} + \psi_\eta\phi_{\eta i} \\
&+ \psi_{\xi^2}\phi_{\xi^2 i} + \psi_{\eta^2}\phi_{\eta^2 i},
\end{aligned}
$$

constraint conditions

$$
\begin{cases}
\Phi_i(-1,-1) = \phi_{i1} \\
\Phi_i(1,-1) = \phi_{i2} \\
\Phi_i(1,1) = \phi_{i3} \\
\Phi_i(-1,1) = \phi_{i4} \\
\iint_{\omega} \Phi_i(\xi,\eta)d\xi d\eta = 4\overline{\phi}_i \\
\dfrac{\partial\Phi_i(\xi,\eta)}{\partial\xi}\Big|_{(0,0)} = \phi_{\xi i} \\
\dfrac{\partial\Phi_i(\xi,\eta)}{\partial\eta}\Big|_{(0,0)} = \phi_{\eta i} \\
\dfrac{\partial^2\Phi_i(\xi,\eta)}{\partial^2\xi}\Big|_{(0,0)} = \phi_{\xi^2 i} \\
\dfrac{\partial\Phi_i^2(\xi,\eta)}{\partial^2\eta}\Big|_{(0,0)} = \phi_{\eta^2 i}
\end{cases}
$$

basis functions

$$
\begin{cases}
\psi_1 = -\frac{1}{4}\xi^2\eta - \frac{1}{4}\xi\eta^2 + \frac{1}{4}\xi\eta + \frac{9}{32}\xi^2\eta^2 - \frac{1}{32} \\
\psi_2 = -\frac{1}{4}\xi^2\eta + \frac{1}{4}\xi\eta^2 - \frac{1}{4}\xi\eta + \frac{9}{32}\xi^2\eta^2 - \frac{1}{32} \\
\psi_3 = \frac{1}{4}\xi^2\eta + \frac{1}{4}\xi\eta^2 + \frac{1}{4}\xi\eta + \frac{9}{32}\xi^2\eta^2 - \frac{1}{32} \\
\psi_4 = \frac{1}{4}\xi^2\eta - \frac{1}{4}\xi\eta^2 - \frac{1}{4}\xi\eta + \frac{9}{32}\xi^2\eta^2 - \frac{1}{32} \\
\overline{\psi} = \frac{9}{8} - \frac{9}{8}\xi^2\eta^2 \\
\psi_\xi = \xi - \xi\eta^2 \\
\psi_\eta = \eta - \xi^2\eta \\
\psi_{\xi^2} = \frac{1}{2}\xi^2 - \frac{3}{8}\xi^2\eta^2 - \frac{1}{8} \\
\psi_{\eta^2} = \frac{1}{2}\eta^2 - \frac{3}{8}\xi^2\eta^2 - \frac{1}{8}
\end{cases}
$$

Table 2.5: Constraint conditions and basis functions for quadrilateral element.

$$\begin{aligned}\phi_{\xi^2 i} &= \frac{3}{8}\left(\phi_{i1}+\phi_{i2}+\phi_{i3}+\phi_{i4}\right)-\frac{3}{2}\overline{\phi}_i,\\ \phi_{\eta^2 i} &= \frac{3}{8}\left(\phi_{i1}+\phi_{i2}+\phi_{i3}+\phi_{i4}\right)-\frac{3}{2}\overline{\phi}_i.\end{aligned} \tag{2.12}$$

Substitute into (2.10), we can obtain final form of constrained condition (2.13) for quadrilateral element

$$\phi_{i5}=\frac{3}{2}\overline{\phi}_i-\frac{1}{8}\left(\phi_{i1}+\phi_{i2}+\phi_{i3}+\phi_{i4}\right). \tag{2.13}$$

- For tetrahedral element

The reconstruction function for unstructured tetrahedral element Ω_i is built up on the canonical reference coordinate with nodes $\theta_{i1}\,(0,0,0)$, $\theta_{i2}\,(1,0,0)$, $\theta_{i3}\,(0,1,0)$ and $\theta_{i4}\,(0,0,1)$ as show in Fig. 2.3. The four boundary surfaces of element Ω_i are denoted by $\Gamma_{i1}=\overline{(\theta_{i3},\theta_{i2},\theta_{i4})}$, $\Gamma_{i2}=\overline{(\theta_{i4},\theta_{i1},\theta_{i3})}$, $\Gamma_{i3}=\overline{(\theta_{i1},\theta_{i4},\theta_{i2})}$, and $\Gamma_{i4}=\overline{(\theta_{i2},\theta_{i3},\theta_{i1})}$. The reconstruction function can be determined from constraint conditions and expressed in basis function form as Table 2.6.

In the same manner, PV at cell center is derived as (2.14)

$$\phi_{i5}=\frac{5}{4}\overline{\phi}_i-\frac{1}{16}\left(\phi_{i1}+\phi_{i2}+\phi_{i3}+\phi_{i4}\right). \tag{2.14}$$

- For hexahedral element

The reconstruction function for unstructured hexahedral element Ω_i is built up on the canonical reference coordinate with nodes $\theta_{i1}\,(-1,-1,-1)$, $\theta_{i2}\,(1,-1,-1)$, $\theta_{i3}\,(1,1,-1)$, $\theta_{i4}\,(-1,1,-1)$, $\theta_{i5}\,(-1,-1,1)$, $\theta_{i6}\,(1,-1,1)$, $\theta_{i7}\,(1,1,1)$ and $\theta_{i8}\,(-1,1,1)$ as shown in Fig. 2.4. The six cell surfaces of element Ω_i are denoted by $\Gamma_{i1}=\overline{(\theta_{i1},\theta_{i5},\theta_{i8},\theta_{i4})}$, $\Gamma_{i2}=\overline{(\theta_{i2},\theta_{i3},\theta_{i7},\theta_{i6})}$, $\Gamma_{i3}=\overline{(\theta_{i1},\theta_{i4},\theta_{i3},\theta_{i2})}$, $\Gamma_{i4}=\overline{(\theta_{i5},\theta_{i6},\theta_{i7},\theta_{i8})}$,$\Gamma_{i5}=\overline{(\theta_{i1},\theta_{i2},\theta_{i6},\theta_{i5})}$ and $\Gamma_{i6}=\overline{(\theta_{i3},\theta_{i4},\theta_{i8},\theta_{i7})}$. The reconstruction function can be determined from constraint conditions and expressed in basis function form as Table 2.7.

From reconstruction function, we can derive PV at cell center in the form as

$$\phi_{i9}=\frac{27}{26}\overline{\phi}_i-\frac{1}{208}\left(\phi_{i1}+\phi_{i2}+\phi_{i3}+\phi_{i4}+\phi_{i5}+\phi_{i6}+\phi_{i7}+\phi_{i8}\right)-\frac{2}{13}\left(\phi_{\xi^2 i}+\phi_{\eta^2 i}+\phi_{\zeta^2 i}\right).$$

From piecewise reconstruction polynomial $\Psi_i\left(\xi,\eta,\zeta\right)=c_0+c_1\xi+c_2\eta+c_3\zeta+c_4\xi^2+c_5\eta^2+c_6\zeta^2+c_7\xi\eta+c_8\eta\zeta+c_9\zeta\xi$, the $\left(\phi_{\xi^2 i},\phi_{\eta^2 i},\phi_{\zeta^2 i}\right)$ is determined as (2.15)

$$\Phi_i(\xi,\eta,\zeta) \;=\; \psi_1\phi_{i1}+\psi_2\phi_{i2}+\psi_3\phi_{i3}+\psi_4\phi_{i4}+\psi_5\phi_{i5}+\psi_\xi\phi_{\xi i}+\psi_\eta\phi_{\eta i}+\psi_\zeta\phi_{\zeta i},$$

constraint conditions

$$\begin{cases}
\Phi_i(0,0,0)=\phi_{i1}\\
\Phi_i(1,0,0)=\phi_{i2}\\
\Phi_i(0,1,0)=\phi_{i3}\\
\Phi_i(0,0,1)=\phi_{i4}\\
\iiint_\omega \Phi_i(\xi,\eta,\zeta)d\xi d\eta d\zeta=\overline{\phi}_i/6_i\\
\dfrac{\partial\Phi_i(\xi,\eta,\zeta)}{\partial\xi}\Big|_{(\frac14,\frac14,\frac14)}=\phi_{\xi i}\\
\dfrac{\partial\Phi_i(\xi,\eta,\zeta)}{\partial\eta}\Big|_{(\frac14,\frac14,\frac14)}=\phi_{\eta i}\\
\dfrac{\partial\Phi_i(\xi,\eta,\zeta)}{\partial\eta}\Big|_{(\frac14,\frac14,\frac14)}=\phi_{\zeta i},
\end{cases}$$

basis functions

$$\begin{cases}
\psi_1=1-\frac{17}{6}(\xi+\eta+\zeta)+\frac{23}{6}(\xi\eta+\xi\zeta+\eta\zeta)+\frac{11}{6}(\xi^2+\eta^2+\zeta^2)\\
\psi_2=\frac16(\eta+\zeta-5\xi)-\frac16(\xi\eta+\xi\zeta+\eta\zeta)+\frac16(11\xi^2-\eta^2-\zeta^2)\\
\psi_3=\frac16(\xi+\zeta-5\eta)-\frac16(\xi\eta+\xi\zeta+\eta\zeta)+\frac16(11\eta^2-\xi^2-\zeta^2)\\
\psi_4=\frac16(\xi+\eta-5\zeta)-\frac16(\xi\eta+\xi\zeta+\eta\zeta)+\frac16(11\zeta^2-\xi^2-\eta^2)\\
\overline{\psi}=\frac{10}{3}(\xi+\eta+\zeta)-\frac{10}{3}(\xi\eta+\xi\zeta+\eta\zeta)-\frac{10}{3}(\xi^2+\eta^2+\zeta^2)\\
\psi_\xi=\xi-\eta-\zeta+\xi\eta+\xi\zeta+\eta\zeta-\xi^2+\eta^2+\zeta^2\\
\psi_\eta=\eta-\xi-\zeta+\xi\eta+\xi\zeta+\eta\zeta+\xi^2-\eta^2+\zeta^2\\
\psi_\zeta=\zeta-\xi-\eta+\xi\eta+\xi\zeta+\eta\zeta+\xi^2+\eta^2-\zeta^2.
\end{cases}$$

Table 2.6: Constraint conditions and basis functions for tetrahedral element.

$$
\begin{aligned}
\Phi_i(\xi,\eta,\zeta) &= \psi_1\phi_{i1}+\psi_2\phi_{i2}+\psi_3\phi_{i3}+\psi_4\phi_{i4}+\psi_5\phi_{i5}+\psi_6\phi_{i6}+\psi_7\phi_{i7}+\psi_8\phi_{i8} \\
&+ \psi_9\phi_{i9}+\psi_\xi\phi_{\xi i}+\psi_\eta\phi_{\eta i}+\psi_\zeta\phi_{\zeta i}+\psi_{\xi^2}\phi_{\xi^2 i}+\psi_{\eta^2}\phi_{\eta^2 i}+\psi_{\zeta^2}\phi_{\zeta^2 i},
\end{aligned}
$$

constraint conditions

$$
\begin{cases}
\Phi_i(-1,-1,-1)=\phi_{i1} \\
\Phi_i(1,-1,-1)=\phi_{i2} \\
\Phi_i(1,1,-1)=\phi_{i3} \\
\Phi_i(-1,1,-1)=\phi_{i4} \\
\Phi_i(-1,-1,1)=\phi_{i5} \\
\Phi_i(1,-1,1)=\phi_{i6} \\
\Phi_i(1,1,1)=\phi_{i7} \\
\Phi_i(-1,1,1)=\phi_{i8} \\
\iint_{\omega}\Phi_i(\xi,\eta,\zeta)d\xi d\eta d\zeta = 8\overline{\phi}_i \\
\dfrac{\partial\Phi_i(\xi,\eta,\zeta)}{\partial\xi}\Big|_{(0,0,0)}=\phi_{\xi i} \\
\dfrac{\partial\Phi_i(\xi,\eta,\zeta)}{\partial\eta}\Big|_{(0,0,0)}=\phi_{\eta i} \\
\dfrac{\partial\Phi_i(\xi,\eta,\zeta)}{\partial\zeta}\Big|_{(0,0,0)}=\phi_{\zeta i}, \\
\dfrac{\partial^2\Phi_i(\xi,\eta,\zeta)}{\partial\xi^2}\Big|_{(0,0,0)}=\phi_{\xi^2 i} \\
\dfrac{\partial^2\Phi_i(\xi,\eta,\zeta)}{\partial\eta}\Big|_{(0,0,0)}=\phi_{\eta^2 i} \\
\dfrac{\partial\Phi_i^2(\xi,\eta,\zeta)}{\partial\zeta^2}\Big|_{(0,0,0)}=\phi_{\zeta^2 i},
\end{cases}
$$

basis functions

$$
\begin{cases}
\psi_1=\frac{1}{8}(\xi\eta+\eta\zeta+\zeta\xi)-\frac{1}{16}(\xi^2\eta+\xi\eta^2+\eta^2\zeta+\eta\zeta^2+\xi^2\zeta+\xi\zeta^2)-\frac{1}{8}\xi\eta\zeta+\frac{27}{208}\xi^2\eta^2\zeta^2-\frac{1}{208} \\
\psi_2=\frac{1}{8}(\eta\zeta-\xi\eta-\zeta\xi)-\frac{1}{16}(3(\eta^2\zeta+\eta\zeta^2)-\xi^2\eta-\xi\eta^2-\xi^2\zeta-\xi\zeta^2)+\frac{1}{8}\xi\eta\zeta+\frac{27}{208}\xi^2\eta^2\zeta^2-\frac{1}{208} \\
\psi_3=\frac{1}{8}(\xi\eta-\zeta\xi-\eta\zeta)+\frac{1}{16}(3(\xi^2\eta+\xi\eta^2)-\eta^2\zeta-\eta\zeta^2-\xi^2\zeta-\xi\zeta^2)-\frac{1}{8}\xi\eta\zeta+\frac{27}{208}\xi^2\eta^2\zeta^2-\frac{1}{208} \\
\psi_4=\frac{1}{8}(\zeta\xi-\xi\eta-\eta\zeta)-\frac{1}{16}(3(\xi^2\zeta+\xi\zeta^2)-\xi^2\eta-\xi\eta^2-\eta^2\zeta-\eta\zeta^2)+\frac{1}{8}\xi\eta\zeta+\frac{27}{208}\xi^2\eta^2\zeta^2-\frac{1}{208} \\
\psi_5=\frac{1}{8}(\xi\eta-\zeta\xi-\eta\zeta)-\frac{1}{16}(3(\xi^2\eta+\xi\eta^2)-\eta^2\zeta-\eta\zeta^2-\xi^2\zeta-\xi\zeta^2)+\frac{1}{8}\xi\eta\zeta+\frac{27}{208}\xi^2\eta^2\zeta^2-\frac{1}{208} \\
\psi_6=\frac{1}{8}(\zeta\xi-\xi\eta-\eta\zeta)-\frac{1}{16}(3(\xi^2\zeta+\xi\zeta^2)-\xi^2\eta-\xi\eta^2-\eta^2\zeta-\eta\zeta^2)-\frac{1}{8}\xi\eta\zeta+\frac{27}{208}\xi^2\eta^2\zeta^2-\frac{1}{208} \\
\psi_7=\frac{1}{8}(\xi\eta+\zeta\xi+\eta\zeta)+\frac{1}{16}(\xi^2\eta+\xi\eta^2+\eta^2\zeta+\eta\zeta^2+\xi^2\zeta+\xi\zeta^2)+\frac{1}{8}\xi\eta\zeta+\frac{27}{208}\xi^2\eta^2\zeta^2-\frac{1}{208} \\
\psi_8=\frac{1}{8}(\eta\zeta-\xi\eta-\zeta\xi)-\frac{1}{16}(3(\eta^2\zeta+\eta\zeta^2)-\xi^2\eta-\xi\eta^2-\xi^2\zeta-\xi\zeta^2)-\frac{1}{8}\xi\eta\zeta+\frac{27}{208}\xi^2\eta^2\zeta^2-\frac{1}{208} \\
\overline{\psi}=\frac{27}{26}-\frac{27}{26}\xi^2\eta^2\zeta^2 \\
\psi_\xi=\frac{1}{2}(\eta^2\zeta+\eta\zeta^2-\xi^2\eta-\xi\eta^2-\xi^2\zeta-\xi\zeta^2)+\xi \\
\psi_\eta=\frac{1}{2}(\xi^2\zeta+\xi\zeta^2-\eta^2\zeta-\eta\zeta^2-\xi^2\eta-\xi\eta^2)+\eta \\
\psi_\zeta=\frac{1}{2}(\xi^2\eta-\xi\eta^2-\xi^2\zeta-\xi\zeta^2-\eta^2\zeta-\eta\zeta^2)+\zeta \\
\psi_{\xi^2}=\frac{1}{2}\xi^2-\frac{9}{26}\xi^2\eta^2\zeta^2-\frac{2}{13} \\
\psi_{\eta^2}=\frac{1}{2}\eta^2-\frac{9}{26}\xi^2\eta^2\zeta^2-\frac{2}{13} \\
\psi_{\zeta^2}=\frac{1}{2}\zeta^2-\frac{9}{26}\xi^2\eta^2\zeta^2-\frac{2}{13}
\end{cases}
$$

Table 2.7: Constraint conditions and basis functions for hexahedral element.

$$\begin{aligned}
\phi_{\xi^2 i} &= \frac{1}{8}\left(\phi_{i1}+\phi_{i2}+\phi_{i3}+\phi_{i4}+\phi_{i5}+\phi_{i6}+\phi_{i7}+\phi_{i8}\right)-\overline{\phi}_i, \\
\phi_{\eta^2 i} &= \frac{1}{8}\left(\phi_{i1}+\phi_{i2}+\phi_{i3}+\phi_{i4}+\phi_{i5}+\phi_{i6}+\phi_{i7}+\phi_{i8}\right)-\overline{\phi}_i, \\
\phi_{\zeta^2 i} &= \frac{1}{8}\left(\phi_{i1}+\phi_{i2}+\phi_{i3}+\phi_{i4}+\phi_{i5}+\phi_{i6}+\phi_{i7}+\phi_{i8}\right)-\overline{\phi}_i.
\end{aligned} \tag{2.15}$$

Thus PV at cell center is approximated in the final form of (2.16)

$$\phi_{i9}=\frac{39}{26}\overline{\phi}_i-\frac{13}{208}\left(\phi_{i1}+\phi_{i2}+\phi_{i3}+\phi_{i4}+\phi_{i15}+\phi_{i6}+\phi_{i7}+\phi_{i8}\right). \tag{2.16}$$

- For prismatic element

The reconstruction function for unstructured prismatic element Ω_i is built up on the canonical reference coordinate with nodes $\theta_{i1}\left(1,0,-1\right)$, $\theta_{i2}\left(0,0,-1\right)$, $\theta_{i3}\left(0,1,-1\right)$, $\theta_{i4}\left(1,0,1\right)$, $\theta_{i5}\left(0,0,1\right)$ and $\theta_{i6}\left(0,1,1\right)$ as shown in Fig. 2.4. The five cell surfaces of element Ω_i are denoted by $\Gamma_{i1}=\overline{(\theta_{i1},\theta_{i2},\theta_{i3})}$, $\Gamma_{i2}=\overline{(\theta_{i4},\theta_{i5},\theta_{i6})}$, $\Gamma_{i3}=\overline{(\theta_{i1},\theta_{i3},\theta_{i6},\theta_{i4})}$, $\Gamma_{i4}=\overline{(\theta_{i3},\theta_{i2},\theta_{i5},\theta_{i6})}$ and $\Gamma_{i5}=\overline{(\theta_{i2},\theta_{i1},\theta_{i4},\theta_{i5})}$. The reconstruction function can be determined from constraint conditions and expressed in basis function form as Table 2.8.

From reconstruction function, we can derive PV at cell center as

$$\phi_{i7}=\frac{4}{3}\overline{\phi}_i-\frac{1}{18}\left(\phi_{i1}+\phi_{i2}+\phi_{i3}+\phi_{i4}+\phi_{i5}+\phi_{i6}\right)-\frac{1}{18}\phi_{\zeta^2 i}.$$

The first order derivatives are first derived from linear reconstruction polynomial $\Lambda_i\left(\xi,\eta,\zeta\right)=c_0+c_1\xi+c_2\eta+c_3\zeta$, and $(\phi_{\xi i},\phi_{\eta i},\phi_{\zeta i})$ are determined as (2.17)

$$\begin{aligned}
\phi_{\xi i} &= \frac{1}{2}\left(\phi_{i1}+\phi_{i4}-\phi_{i2}-\phi_{i5}\right), \\
\phi_{\eta i} &= \frac{1}{2}\left(\phi_{i3}+\phi_{i6}-\phi_{i2}-\phi_{i5}\right), \\
\phi_{\zeta i} &= \frac{1}{6}\left(\phi_{i3}+\phi_{i4}+\phi_{i5}-\phi_{i1}-\phi_{i2}-\phi_{i3}\right).
\end{aligned} \tag{2.17}$$

In the same manner, from higher order reconstruction polynomial $\Psi_i\left(\xi,\eta,\zeta\right)=c_0+c_1\xi+c_2\eta+c_3\zeta+c_4\zeta^2+c_5\xi\eta+c_6\eta\zeta+c_7\zeta\xi$, $\phi_{\zeta^2 i}$ then is derived as (2.18)

$$\begin{aligned}
\phi_{\zeta^2 i} &= \tfrac{1}{16}\left(5\left(\phi_{i1}+\phi_{i3}+\phi_{i4}+\phi_{i6}\right)+14\left(\phi_{i2}+\phi_{i5}\right)\right)-3\overline{\phi}_i+\tfrac{3}{8}\left(\phi_{\xi i}+\phi_{\eta i}\right) \\
&= \tfrac{1}{2}\left(\phi_{i1}+\phi_{i3}+\phi_{i4}+\phi_{i6}+\phi_{i2}+\phi_{i5}\right)-3\overline{\phi}_i.
\end{aligned} \tag{2.18}$$

$$\begin{aligned}\Phi_i(\xi,\eta,\zeta) &= \psi_1\phi_{i1}+\psi_2\phi_{i2}+\psi_3\phi_{i3}+\psi_4\phi_{i4}+\psi_5\phi_{i5}+\psi_6\phi_{i6}+\psi_7\phi_{i7}+\psi_\xi\phi_{\xi i}\\ &+ \psi_\eta\phi_{\eta i}+\psi_\zeta\phi_{\zeta i}+\psi_{\zeta^2}\phi_{\zeta^2 i}.\end{aligned}$$

constraint conditions

$$\begin{cases}\Phi_i(1,0,-1)=\phi_{i1}\\ \Phi_i(0,0,-1)=\phi_{i2}\\ \Phi_i(0,1,-1)=\phi_{i3}\\ \Phi_i(1,0,1)=\phi_{i4}\\ \Phi_i(0,0,1)=\phi_{i5}\\ \Phi_i(0,1,1)=\phi_{i6}\\ \iint_{\tilde{\omega}}\Phi_i(\xi,\eta,\zeta)d\xi d\eta d\zeta=\overline{\phi}_i\\ \dfrac{\partial\Phi_i(\xi,\eta,\zeta)}{\partial\xi}\Big|_{(\frac{1}{3},\frac{1}{3},0)}=\phi_{\xi i}\\ \dfrac{\partial\Phi_i(\xi,\eta,\zeta)}{\partial\eta}\Big|_{(\frac{1}{3},\frac{1}{3},0)}=\phi_{\eta i}\\ \dfrac{\partial\Phi_i(\xi,\eta,\zeta)}{\partial\zeta}\Big|_{(\frac{1}{3},\frac{1}{3},0)}=\phi_{\zeta i}\\ \dfrac{\partial^2\Phi_i(\xi,\eta,\zeta)}{\partial\zeta^2}\Big|_{(\frac{1}{3},\frac{1}{3},0)}=\phi_{\zeta^2 i},\end{cases}$$

basis functions

$$\begin{cases}\psi_1=-\frac{2}{3}\xi+\frac{1}{3}\eta+\frac{7}{6}\xi^2-\frac{1}{3}\eta^2-\frac{1}{3}\xi\eta-\frac{1}{2}\zeta\xi+\frac{3}{2}\xi\eta\zeta\\ \psi_2=\frac{1}{2}-\frac{5}{3}\xi-\frac{5}{3}\eta-\frac{1}{2}\zeta+\frac{7}{6}\xi^2+\frac{7}{6}\eta^2+\frac{8}{3}\xi\eta+\frac{1}{2}\eta\zeta+\frac{1}{2}\zeta\xi+\frac{3}{2}\xi\eta\zeta\\ \psi_3=-\frac{2}{3}\eta+\frac{1}{3}\xi+\frac{7}{6}\eta^2-\frac{1}{3}\xi^2-\frac{1}{3}\xi\eta-\frac{1}{2}\eta\zeta+\frac{3}{2}\xi\eta\zeta\\ \psi_4=-\frac{2}{3}\xi+\frac{1}{3}\eta+\frac{7}{6}\xi^2-\frac{1}{3}\eta^2-\frac{1}{3}\xi\eta+\frac{1}{2}\zeta\xi-\frac{3}{2}\xi\eta\zeta\\ \psi_5=\frac{1}{2}-\frac{5}{3}\xi-\frac{5}{3}\eta+\frac{1}{2}\zeta+\frac{7}{6}\xi^2+\frac{7}{6}\eta^2+\frac{8}{3}\xi\eta-\frac{1}{2}\eta\zeta-\frac{1}{2}\zeta\xi-\frac{3}{2}\xi\eta\zeta\\ \psi_6=-\frac{2}{3}\eta+\frac{1}{3}\xi+\frac{7}{6}\eta^2-\frac{1}{3}\xi^2-\frac{1}{3}\xi\eta+\frac{1}{2}\eta\zeta-\frac{3}{2}\xi\eta\zeta\\ \overline{\psi}=4\xi+4\eta-4\xi^2-4\eta^2-4\xi\eta\\ \psi_\xi=\xi-2\eta-\xi^2+2\eta^2+2\xi\eta\\ \psi_\eta=\eta-2\xi-\eta^2+2\xi^2+2\xi\eta\\ \psi_\zeta=9\xi\eta\zeta\\ \psi_{\zeta^2}=-\frac{1}{2}+\frac{4}{3}\xi+\frac{4}{3}\eta-\frac{4}{3}\xi^2-\frac{4}{3}\eta^2+\frac{1}{2}\zeta^2-\frac{4}{3}\xi\eta\end{cases}$$

Table 2.8: Constraint conditions and basis functions for prismatic element.

Thus PV at cell center is approximated in the final form of(2.19)

$$\phi_{i7} = \frac{3}{2}\overline{\phi}_i - \frac{1}{12}\left(\phi_{i1} + \phi_{i2} + \phi_{i3} + \phi_{i4} + \phi_{i5} + \phi_{i6}\right). \tag{2.19}$$

- For pyramidal element

The reconstruction function for unstructured pyramidal element Ω_i is built up on the canonical reference coordinate with nodes $\theta_{i1}\left(-1,-1,-1\right)$, $\theta_{i2}\left(1,-1,-1\right)$, $\theta_{i3}\left(1,1,-1\right)$, $\theta_{i4}\left(-1,1,-1\right)$ and $\theta_{i5}\left(0,0,1\right)$ as shown in Fig. 2.4. The five cell surfaces of element Ω_i are denoted by $\Gamma_{i1} = \overline{(\theta_{i1},\theta_{i2},\theta_{i3},\theta_{i4})}$, $\Gamma_{i2} = \overline{(\theta_{i1},\theta_{i4},\theta_{i5})}$, $\Gamma_{i3} = \overline{(\theta_{i4},\theta_{i3},\theta_{i5})}$, $\Gamma_{i4} = \overline{(\theta_{i3},\theta_{i2},\theta_{i5})}$ and $\Gamma_{i5} = \overline{(\theta_{i2},\theta_{i1},\theta_{i5})}$. The reconstruction function can be determined from constraint conditions and expressed in basis function form as Table 2.9.

From reconstruction function, we can derive the constrained condition as

$$\phi_{i6} = \frac{945}{842}\overline{\phi}_i - \frac{1}{3368}\left(45\left(\phi_{i1} + \phi_{i2} + \phi_{i3} + \phi_{i4}\right) + 116\phi_{i5}\right) + \frac{129}{1684}\phi_{\zeta i} - \frac{36}{421}\left(\phi_{\xi^2 i} + \phi_{\eta^2 i}\right).$$

The first order derivatives are first derived from linear reconstruction polynomial $\Lambda_i\left(\xi,\eta,\zeta\right) = c_0 + c_1\xi + c_2\eta + c_3\zeta$, and $(\phi_{\xi i}, \phi_{\eta i}, \phi_{\zeta i})$ are determined as (2.20)

$$\begin{aligned}
\phi_{\xi i} &= \frac{1}{2}\left(\phi_{i2} + \phi_{i3} - \phi_{i1} - \phi_{i4}\right), \\
\phi_{\eta i} &= \frac{1}{2}\left(\phi_{i3} + \phi_{i4} - \phi_{i1} - \phi_{i2}\right), \\
\phi_{\zeta i} &= \frac{2}{77}\overline{\phi}_i + \frac{38}{77}\phi_{i5} - \frac{10}{77}\left(\phi_{i1} + \phi_{i2} + \phi_{i3} + \phi_{i4}\right).
\end{aligned} \tag{2.20}$$

In the same manner, from higher order piecewise reconstruction polynomial $\Psi_i\left(\xi,\eta,\zeta\right) = c_0 + c_1\xi + c_2\eta + c_3\zeta + c_4\xi^2 + c_5\eta^2 + c_6\xi\eta$, $\left(\phi_{\xi^2 i}, \phi_{\eta^2 i}\right)$ can be obtained as (2.21)

$$\begin{aligned}
\phi_{\xi^2 i} &= \frac{1}{1144}\left(345\left(\phi_{i1} + \phi_{i2} + \phi_{i3} + \phi_{i4}\right) - 200\phi_{i5}\right) - \frac{295}{286}\overline{\phi}_i + \frac{45}{52}\phi_{\zeta i}, \\
\phi_{\eta^2 i} &= \frac{1}{1144}\left(345\left(\phi_{i1} + \phi_{i2} + \phi_{i3} + \phi_{i4}\right) - 200\phi_{i5}\right) - \frac{295}{286}\overline{\phi}_i + \frac{45}{52}\phi_{\zeta i}.
\end{aligned} \tag{2.21}$$

Thus PV at cell center is approximated in the final form of (2.22)

$$\phi_{i6} = \frac{546531}{421421}\overline{\phi}_i - \frac{187665}{3371368}\left(\phi_{i1} + \phi_{i2} + \phi_{i3} + \phi_{i4}\right) - \frac{62555}{842842}\phi_{i5}. \tag{2.22}$$

For convenience, approximated formulations of PV at cell center for all type of unstructured grid elements are summarized in Table 2.10.

$$
\begin{aligned}
\Phi_i(\xi,\eta,\zeta) &= \psi_1\phi_{i1} + \psi_2\phi_{i2} + \psi_3\phi_{i3} + \psi_4\phi_{i4} + \psi_5\phi_{i5} + \psi_6\phi_{i6} + \psi_\xi\phi_{\xi i} + \psi_\eta\phi_{\eta i} \\
&+ \psi_\zeta\phi_{\zeta i} + \psi_{\xi^2}\phi_{\xi^2 i} + \psi_{\eta^2}\phi_{\eta^2 i},
\end{aligned}
$$

constraint conditions

$$
\begin{cases}
\Phi_i(-1,-1,-1) = \phi_{i1} \\
\Phi_i(1,-1,-1) = \phi_{i2} \\
\Phi_i(1,1,-1) = \phi_{i3} \\
\Phi_i(-1,1,-1) = \phi_{i4} \\
\Phi_i(0,0,1) = \phi_{i5} \\
\iint_{\omega} \Phi_i(\xi,\eta,\zeta)d\xi d\eta d\zeta = 8\overline{\phi}_i/3 \\
\dfrac{\partial\Phi_i(\xi,\eta,\zeta)}{\partial\xi}\Big|_{(0,0,-\frac{1}{2})} = \phi_{\xi i} \\
\dfrac{\partial\Phi_i(\xi,\eta,\zeta)}{\partial\eta}\Big|_{(0,0,-\frac{1}{2})} = \phi_{\eta i} \\
\dfrac{\partial\Phi_i(\xi,\eta,\zeta)}{\partial\zeta}\Big|_{(0,0,-\frac{1}{2})} = \phi_{\zeta i} \\
\dfrac{\partial^2\Phi_i(\xi,\eta,\zeta)}{\partial\xi^2}\Big|_{(0,0,-\frac{1}{2})} = \phi_{\xi^2 i} \\
\dfrac{\partial^2\Phi_i(\xi,\eta,\zeta)}{\partial\eta}\Big|_{(0,0,-\frac{1}{2})} = \phi_{\eta^2 i},
\end{cases}
$$

basis functions

$$
\begin{cases}
\psi_1 = -\frac{1}{4}(\xi^2\eta + \xi\eta^2) + \frac{441}{1684}\xi^2\eta^2 - \frac{1}{4}\xi\eta\zeta + \frac{5}{842}\left(\zeta^2 + \zeta - 2\right) \\
\psi_2 = -\frac{1}{4}(\xi^2\eta - \xi\eta^2) + \frac{441}{1684}\xi^2\eta^2 + \frac{1}{4}\xi\eta\zeta + \frac{5}{842}\left(\zeta^2 + \zeta - 2\right) \\
\psi_3 = \frac{1}{4}(\xi^2\eta + \xi\eta^2) + \frac{441}{1684}\xi^2\eta^2 - \frac{1}{4}\xi\eta\zeta + \frac{5}{842}\left(\zeta^2 + \zeta - 2\right) \\
\psi_4 = \frac{1}{4}(\xi^2\eta - \xi\eta^2) + \frac{441}{1684}\xi^2\eta^2 + \frac{1}{4}\xi\eta\zeta + \frac{5}{842}\left(\zeta^2 + \zeta - 2\right) \\
\psi_5 = \frac{21}{421} + \frac{200}{421}\zeta + \frac{200}{421}\zeta^2 - \frac{21}{421}\xi^2\eta^2 \\
\overline{\psi} = \frac{8}{9} - \frac{4}{9}\zeta - \frac{4}{9}\zeta^2 - \frac{8}{9}\xi^2\eta^2 \\
\psi_\xi = \xi - \xi\eta^2 \\
\psi_\eta = \eta - \xi^2\eta \\
\psi_\zeta = \frac{169}{421} + \frac{126}{421}\zeta - \frac{295}{421}\zeta^2 + \frac{252}{421}\xi^2\eta^2 \\
\psi_{\xi^2} = \frac{1}{2}\xi^2 - \frac{1}{2}\xi^2\eta^2 + \frac{16}{421}\left(\zeta^2 + \zeta - 2\right) \\
\psi_{\eta^2} = \frac{1}{2}\eta^2 - \frac{1}{2}\xi^2\eta^2 + \frac{16}{421}\left(\zeta^2 + \zeta - 2\right)
\end{cases}
$$

Table 2.9: Constraint conditions and basis functions for pyramidal element.

Element Type	Approximated formulations of PV at cell center
Triangular element	$\phi_{i4} = \frac{4}{3}\overline{\phi}_i - \frac{1}{9}\left(\phi_{i1} + \phi_{i2} + \phi_{i3}\right)$
Quadrilateral element	$\phi_{i5} = \frac{3}{2}\overline{\phi}_i - \frac{1}{8}\left(\phi_{i1} + \phi_{i2} + \phi_{i3} + \phi_{i4}\right)$
Tetrahedral element	$\phi_{i5} = \frac{5}{4}\overline{\phi}_i - \frac{1}{16}\left(\phi_{i1} + \phi_{i2} + \phi_{i3} + \phi_{i4}\right)$
Hexahedral element	$\phi_{i9} = \frac{39}{26}\overline{\phi}_i - \frac{13}{208}\left(\phi_{i1} + \phi_{i2} + \phi_{i3} + \phi_{i4} + \phi_{i15} + \phi_{i6} + \phi_{i7} + \phi_{i8}\right)$
Prismatic element	$\phi_{i7} = \frac{3}{2}\overline{\phi}_i - \frac{1}{12}\left(\phi_{i1} + \phi_{i2} + \phi_{i3} + \phi_{i4} + \phi_{i5} + \phi_{i6}\right)$
Pyramidal element	$\phi_{i6} = \frac{546531}{421421}\overline{\phi}_i - \frac{187665}{3371368}\left(\phi_{i1} + \phi_{i2} + \phi_{i3} + \phi_{i4}\right) - \frac{62555}{842842}\phi_{i5}$

Table 2.10: Approximated formulations of PV at cell center for all type of unstructured grid elements for VPM scheme.

2.4 High order reconstructions using multi-moment constraints

The present MCV method locates the solution points at the mass center (θ_{ic}) and vertices ($\theta_{ik}, k = 1, 2, \cdots, K$) for each element, and the PVs at these solution points need to be updated in time at every step. For a physical variable $\phi(x, y, z, t)$ the computational variables are defined as

$$\phi_{ik}(t) \equiv \phi(x_{ik}, y_{ik}, z_{ik}, t),\ k = 1, 2, \cdots, K; \tag{2.23}$$

$$\phi_{i(K+1)}(t) \equiv \phi(x_{ic}, y_{ic}, z_{ic}, t). \tag{2.24}$$

With provisional variables $(\phi_{\xi i}, \phi_{\eta i}, \phi_{\zeta i})$ and $\left(\phi_{\xi^2 i}, \phi_{\eta^2 i}, \phi_{\zeta^2 i}\right)$ defined at barycenter θ_{ic}, piecewise reconstruction polynomial on the local coordinate is formulated with higher order as:

$$\Phi_i(\xi, \eta) = \sum_{k=1}^{k=K+1} \psi_{ik}\phi_{ik} + A_1(\psi_\xi\phi_{\xi i} + \psi_\eta\phi_{\eta i}) + B_1\psi_\zeta\phi_{\zeta i} + A_2(\psi_{\xi^2}\phi_{\xi^2 i} + \psi_{\eta^2}\phi_{\eta^2 i}) + B_2\psi_{\zeta^2}\phi_{\zeta^2 i}, \tag{2.25}$$

The A_1, A_2, B_1, B_2 are coefficients vary for different element shapes as given in Table

Element Type	Reconstruction Type
Triangular element	$A_1 = 1,\ B_1 = 0,\ A_2 = 0,\ B_2 = 0$
Quadrilateral element	$A_1 = 1,\ B_1 = 0,\ A_2 = 1,\ B_2 = 0$
Tetrahedral element	$A_1 = 1,\ B_1 = 1,\ A_2 = 0,\ B_2 = 0$
Hexahedral element	$A_1 = 1,\ B_1 = 1,\ A_2 = 1,\ B_2 = 1$
Prismatic element	$A_1 = 1,\ B_1 = 1,\ A_2 = 0,\ B_2 = 1$
Pyramidal element	$A_1 = 1,\ B_1 = 1,\ A_2 = 1,\ B_2 = 0$

Table 2.11: Coefficients of reconstruction function in MCV scheme for different element shapes.

2.11, and unknown coefficients can be uniquely determined in the same way with VPM scheme by the constraint conditions (2.26). Separately, we derive MCV reconstruction for each element shape as below.

$$\begin{cases} \Phi_i(\xi_{ik}, \eta_{ik}, \zeta_{ik}) = \phi_{ik} & k = 1, 2, \cdots, K \\ \Phi_i(\xi_{ic}, \eta_{ic}, \zeta_{ic}) = \phi_{i(K+1)} \\ \dfrac{\partial \Phi_i(\xi,\eta,\zeta)}{\partial \xi}\Big|_{(x_{ic},y_{ic},z_{ic})} = \phi_{\xi i} \\ \dfrac{\partial \Phi_i(\xi,\eta,\zeta)}{\partial \eta}\Big|_{(x_{ic},y_{ic},z_{ic})} = \phi_{\eta i} \\ \dfrac{\partial \Phi_i(\xi,\eta,\zeta)}{\partial \zeta}\Big|_{(x_{ic},y_{ic},z_{ic})} = \phi_{\zeta i} \\ \dfrac{\partial^2 \Phi_i(\xi,\eta,\zeta)}{\partial \xi^2}\Big|_{(x_{ic},y_{ic},z_{ic})} = \phi_{\xi^2 i} \\ \dfrac{\partial^2 \Phi_i(\xi,\eta,\zeta)}{\partial \eta^2}\Big|_{(x_{ic},y_{ic},z_{ic})} = \phi_{\eta^2 i} \\ \dfrac{\partial \Phi_i^2(\xi,\eta,\zeta)}{\partial \zeta^2}\Big|_{(x_{ic},y_{ic},z_{ic})} = \phi_{\zeta^2 i} \quad . \end{cases} \tag{2.26}$$

- For triangular element

The reconstruction function for unstructured triangular element Ω_i is built up on the

$$\Phi_i(\xi,\eta) \quad = \quad \Phi_i(\xi,\eta) = \psi_1\phi_{i1} + \psi_2\phi_{i2} + \psi_3\phi_{i3} + \overline{\psi}\ \overline{\phi}_i + \psi_\xi\phi_{\xi i} + \psi_\eta\phi_{\eta i},$$

$$\text{constraint conditions} \begin{cases} \Phi_i(0,0) = \phi_{i1} \\ \Phi_i(1,0) = \phi_{i2} \\ \Phi_i(0,1) = \phi_{i3} \\ \Phi_i(\frac{1}{3},\frac{1}{3}) = \phi_{i4} \\ \dfrac{\partial\Phi_i(\xi,\eta)}{\partial\xi}\Big|_{(\frac{1}{3},\frac{1}{3})} = \phi_{\xi i} \\ \dfrac{\partial\Phi_i(\xi,\eta)}{\partial\eta}\Big|_{(\frac{1}{3},\frac{1}{3})} = \phi_{\eta i} \end{cases}$$

$$\text{basis functions} \begin{cases} \psi_1 = 1 - 3\xi - 3\eta + 5\xi\eta + 2\xi^2 + 2\eta^2 \\ \psi_2 = \eta - \xi - \xi\eta + 2\xi^2 - \eta^2 \\ \psi_3 = \xi - \eta - \xi\eta - \xi^2 + 2\eta^2 \\ \psi_4 = 3\xi + 3\eta - 3\xi\eta - 3\xi^2 - 3\eta^2 \\ \psi_\xi = \xi - 2\eta + 2\xi\eta - \xi^2 + 2\eta^2 \\ \psi_\eta = \eta - 2\xi + 2\xi\eta + 2\xi^2 - \eta^2 \end{cases}$$

Table 2.12: Constraint conditions and basis functions for triangular element.

canonical reference coordinate with nodes $\theta_{i1}\,(0,0)$, $\theta_{i2}\,(1,0)$ and $\theta_{i3}\,(0,1)$ as shown in Fig. 2.3. The three boundary line segments of element Ω_i are denoted by $\Gamma_{i1} = \overline{\theta_{i2}\theta_{i3}}$, $\Gamma_{i2} = \overline{\theta_{i3}\theta_{i1}}$ and $\Gamma_{i3} = \overline{\theta_{i1}\theta_{i2}}$. The reconstruction function can be determined from constraint conditions and expressed in basis function form as Table 2.12.

From reconstruction function, we can derive multi-moment constrained condition as (2.27)

$$\overline{\phi}_i = \iint_{\Omega_i} \Phi_i(\xi,\eta)d\xi d\eta = \frac{1}{12}\left(\phi_{i1} + \phi_{i2} + \phi_{i3} + 9\phi_{i4}\right). \tag{2.27}$$

- For quadrilateral element

The reconstruction function for unstructured quadrilateral element Ω_i is built up on the canonical reference coordinate with nodes $\theta_{i1}\,(-1,-1)$, $\theta_{i2}\,(1,-1)$, $\theta_{i3}\,(1,1)$ and $\theta_{i4}\,(-1,1)$ as shown in Fig. 2.3. The four boundary line segments of element Ω_i are denoted by $\Gamma_{i1} = \overline{\theta_{i4}\theta_{i1}}$, $\Gamma_{i2} = \overline{\theta_{i2}\theta_{i3}}$, $\Gamma_{i3} = \overline{\theta_{i1}\theta_{i2}}$ and $\Gamma_{i4} = \overline{\theta_{i3}\theta_{i4}}$. The reconstruction function can be determined from constraint conditions and expressed in basis function form as Table 2.13.

$$
\begin{aligned}
\Phi_i(\xi,\eta) &= \psi_1\phi_{i1} + \psi_2\phi_{i2} + \psi_3\phi_{i3} + \psi_4\phi_{i4} + \psi_5\phi_{i5} + \psi_\xi\phi_{\xi i} + \psi_\eta\phi_{\eta i} \\
&+ \psi_{\xi^2}\phi_{\xi^2 i} + \psi_{\eta^2}\phi_{\eta^2 i},
\end{aligned}
$$

constraint conditions

$$
\begin{cases}
\Phi_i(-1,-1) = \phi_{i1} \\
\Phi_i(1,-1) = \phi_{i2} \\
\Phi_i(1,1) = \phi_{i3} \\
\Phi_i(-1,1) = \phi_{i4} \\
\Phi_i(0,0) = \phi_{i5} \\
\dfrac{\partial\Phi_i(\xi,\eta)}{\partial\xi}\Big|_{(0,0)} = \phi_{\xi i} \\
\dfrac{\partial\Phi_i(\xi,\eta)}{\partial\eta}\Big|_{(0,0)} = \phi_{\eta i} \\
\dfrac{\partial^2\Phi_i(\xi,\eta)}{\partial^2\xi}\Big|_{(0,0)} = \phi_{\xi^2 i} \\
\dfrac{\partial\Phi_i^2(\xi,\eta)}{\partial^2\eta}\Big|_{(0,0)} = \phi_{\eta^2 i}
\end{cases}
$$

basis functions

$$
\begin{cases}
\psi_1 = -\frac{1}{4}\xi^2\eta - \frac{1}{4}\xi\eta^2 + \frac{1}{4}\xi\eta + \frac{1}{4}\xi^2\eta^2 \\
\psi_2 = -\frac{1}{4}\xi^2\eta + \frac{1}{4}\xi\eta^2 - \frac{1}{4}\xi\eta + \frac{1}{4}\xi^2\eta^2 \\
\psi_3 = \frac{1}{4}\xi^2\eta + \frac{1}{4}\xi\eta^2 + \frac{1}{4}\xi\eta + \frac{1}{4}\xi^2\eta^2 \\
\psi_4 = \frac{1}{4}\xi^2\eta - \frac{1}{4}\xi\eta^2 - \frac{1}{4}\xi\eta + \frac{1}{4}\xi^2\eta^2 \\
\psi_5 = 1 - \xi^2\eta^2 \\
\psi_\xi = \xi - \xi\eta^2 \\
\psi_\eta = \eta - \xi^2\eta \\
\psi_{\xi^2} = \frac{1}{2}\xi^2 - \frac{1}{2}\xi^2\eta^2 \\
\psi_{\eta^2} = \frac{1}{2}\eta^2 - \frac{1}{2}\xi^2\eta^2
\end{cases}
$$

Table 2.13: Constraint conditions and basis functions for quadrilateral element.

From reconstruction function, we can derive the constrained condition as

$$\overline{\phi}_i = \iint_{\Omega_i} \Phi_i(\xi,\eta)d\xi d\eta = \frac{1}{36}\left(32\phi_{i5} + \phi_{i1} + \phi_{i2} + \phi_{i3} + \phi_{i4} + 4\phi_{\xi^2 i} + 4\phi_{\eta^2 i}\right). \tag{2.28}$$

In order to determine $\left(\phi_{\xi^2 i}, \phi_{\eta^2 i}\right)$, a piecewise reconstruction polynomial $\Psi_i\left(\xi,\eta\right) = c_0 + c_1\xi + c_2\eta + c_3\xi^2 + c_4\eta^2 + c_5\xi\eta$ is constructed. The coefficients are determined by DOFs on local coordinate in each single cell as (2.29)

$$\begin{cases} \Psi_i - 1, -1) = \phi_{i1} \\ \Psi_i(1,-1) = \phi_{i2} \\ \Psi_i(1,1) = \phi_{i3} \\ \Psi_i(-1,1) = \phi_{i4} \\ \Psi_i(0,0) = \phi_{i5} \\ \dfrac{\partial \Psi_i(\xi,\eta)}{\partial \xi}\Big|_{(0,0)} = \phi_{\xi i} \\ \dfrac{\partial \Psi_i(\xi,\eta)}{\partial \eta}\Big|_{(0,0)} = \phi_{\eta i} \quad . \end{cases} \tag{2.29}$$

The resulted over-determined matrix system is solved by the least square method. $\left(\phi_{\xi^2 i}, \phi_{\eta^2 i}\right)$ then can be expressed by (2.30)

$$\begin{aligned} \phi_{\xi^2 i} &= \frac{1}{4}\left(\phi_{i1} + \phi_{i2} + \phi_{i3} + \phi_{i4}\right) - \phi_{i5}, \\ \phi_{\eta^2 i} &= \frac{1}{4}\left(\phi_{i1} + \phi_{i2} + \phi_{i3} + \phi_{i4}\right) - \phi_{i5}. \end{aligned} \tag{2.30}$$

Substitute into (2.28), we can obtain final form of multi-moment constrained condition (2.31) for quadrilateral element

$$\overline{\phi}_i = \iint_{\Omega_i} \Phi_i(\xi,\eta)d\xi d\eta = \frac{1}{12}\left(\phi_{i1} + \phi_{i2} + \phi_{i3} + \phi_{i4} + 8\phi_{i5}\right). \tag{2.31}$$

- For tetrahedral element

The reconstruction function for unstructured tetrahedral element Ω_i is built up on the canonical reference coordinate with nodes $\theta_{i1}\left(0,0,0\right)$, $\theta_{i2}\left(1,0,0\right)$, $\theta_{i3}\left(0,1,0\right)$ and $\theta_{i4}\left(0,0,1\right)$ as shown in Fig. 2.4. The four boundary surfaces of element Ω_i are denoted by $\Gamma_{i1} = \overline{(\theta_{i3},\theta_{i2},\theta_{i4})}$, $\Gamma_{i2} = \overline{(\theta_{i4},\theta_{i1},\theta_{i3})}$, $\Gamma_{i3} = \overline{(\theta_{i1},\theta_{i4},\theta_{i2})}$, and $\Gamma_{i4} = \overline{(\theta_{i2},\theta_{i3},\theta_{i1})}$. The reconstruction function can be determined from constraint conditions and expressed in basis function form as Table 2.14.

$$\Phi_i(\xi,\eta,\zeta) \;=\; \psi_1\phi_{i1}+\psi_2\phi_{i2}+\psi_3\phi_{i3}+\psi_4\phi_{i4}+\psi_5\phi_{i5}+\psi_\xi\phi_{\xi i}+\psi_\eta\phi_{\eta i}+\psi_\zeta\phi_{\zeta i},$$

constraint conditions

$$\begin{cases}
\Phi_i(0,0,0)=\phi_{i1}\\
\Phi_i(1,0,0)=\phi_{i2}\\
\Phi_i(0,1,0)=\phi_{i3}\\
\Phi_i(0,0,1)=\phi_{i4}\\
\Phi_i(\frac{1}{4},\frac{1}{4},\frac{1}{4})=\phi_{i5}\\
\dfrac{\partial\Phi_i(\xi,\eta,\zeta)}{\partial\xi}\Big|_{(\frac{1}{4},\frac{1}{4},\frac{1}{4})}=\phi_{\xi i}\\
\dfrac{\partial\Phi_i(\xi,\eta,\zeta)}{\partial\eta}\Big|_{(\frac{1}{4},\frac{1}{4},\frac{1}{4})}=\phi_{\eta i}\\
\dfrac{\partial\Phi_i(\xi,\eta,\zeta)}{\partial\eta}\Big|_{(\frac{1}{4},\frac{1}{4},\frac{1}{4})}=\phi_{\zeta i},
\end{cases}$$

basis functions

$$\begin{cases}
\psi_1=1-\frac{8}{3}(\xi+\eta+\zeta)+\frac{11}{3}(\xi\eta+\xi\zeta+\eta\zeta)+\frac{5}{3}(\xi^2+\eta^2+\zeta^2)\\
\psi_2=\frac{1}{3}(\eta+\zeta-2\xi)-\frac{1}{3}(\xi\eta+\xi\zeta+\eta\zeta)+\frac{1}{3}(5\xi^2-\eta^2-\zeta^2)\\
\psi_3=\frac{1}{3}(\xi+\zeta-2\eta)-\frac{1}{3}(\xi\eta+\xi\zeta+\eta\zeta)+\frac{1}{3}(5\eta^2-\xi^2-\zeta^2)\\
\psi_4=\frac{1}{3}(\xi+\eta-2\zeta)-\frac{1}{3}(\xi\eta+\xi\zeta+\eta\zeta)+\frac{1}{3}(5\zeta^2-\xi^2-\eta^2)\\
\psi_5=\frac{8}{3}(\xi+\eta+\zeta)-\frac{8}{3}(\xi\eta+\xi\zeta+\eta\zeta)-\frac{8}{3}(\xi^2+\eta^2+\zeta^2)\\
\psi_\xi=\xi-\eta-\zeta+\xi\eta+\xi\zeta+\eta\zeta-\xi^2+\eta^2+\zeta^2\\
\psi_\eta=\eta-\xi-\zeta+\xi\eta+\xi\zeta+\eta\zeta+\xi^2-\eta^2+\zeta^2\\
\psi_\zeta=\zeta-\xi-\eta+\xi\eta+\xi\zeta+\eta\zeta+\xi^2+\eta^2-\zeta^2.
\end{cases}$$

Table 2.14: Constraint conditions and basis functions for tetrahedral element.

The multi-moment constrained condition can be directly derived as (2.32)

$$\overline{\phi}_i = \frac{1}{20}\left(\phi_{i1} + \phi_{i2} + \phi_{i3} + \phi_{i4} + 16\phi_{i5}\right). \tag{2.32}$$

- For hexahedral element

The reconstruction function for unstructured hexahedral element Ω_i is built up on the canonical reference coordinate with nodes $\theta_{i1}\,(-1,-1,-1)$, $\theta_{i2}\,(1,-1,-1)$, $\theta_{i3}\,(1,1,-1)$, $\theta_{i4}\,(-1,1,-1)$, $\theta_{i5}\,(-1,-1,1)$, $\theta_{i6}\,(1,-1,1)$, $\theta_{i7}\,(1,1,1)$ and $\theta_{i8}\,(-1,1,1)$ as shown in Fig. 2.4. The six cell surfaces of element Ω_i are denoted by $\Gamma_{i1} = \overline{(\theta_{i1},\theta_{i5},\theta_{i8},\theta_{i4})}$, $\Gamma_{i2} = \overline{(\theta_{i2},\theta_{i3},\theta_{i7},\theta_{i6})}$, $\Gamma_{i3} = \overline{(\theta_{i1},\theta_{i4},\theta_{i3},\theta_{i2})}$, $\Gamma_{i4} = \overline{(\theta_{i5},\theta_{i6},\theta_{i7},\theta_{i8})}$,$\Gamma_{i5} = \overline{(\theta_{i1},\theta_{i2},\theta_{i6},\theta_{i5})}$ and $\Gamma_{i6} = \overline{(\theta_{i3},\theta_{i4},\theta_{i8},\theta_{i7})}$. The reconstruction function can be determined from constraint conditions and expressed in basis function form as Table 2.15.

From reconstruction function, we can derive the constrained condition as

$$\overline{\phi}_i = \frac{1}{216}\left(\phi_{i1} + \phi_{i2} + \phi_{i3} + \phi_{i4} + \phi_{i5} + \phi_{i6} + \phi_{i7} + \phi_{i8}\right) + \frac{26}{27}\phi_{i9} + \frac{4}{27}\left(\phi_{\xi^2 i} + \phi_{\eta^2 i} + \phi_{\zeta^2 i}\right).$$

From piecewise reconstruction polynomial $\Psi_i\,(\xi,\eta,\zeta) = c_0 + c_1\xi + c_2\eta + c_3\zeta + c_4\xi^2 + c_5\eta^2 + c_6\zeta^2 + c_7\xi\eta + c_8\eta\zeta + c_9\zeta\xi$, the $\left(\phi_{\xi^2 i}, \phi_{\eta^2 i}, \phi_{\zeta^2 i}\right)$ is determined as (2.33)

$$\begin{aligned}
\phi_{\xi^2 i} &= \frac{1}{12}\left(\phi_{i1} + \phi_{i2} + \phi_{i3} + \phi_{i4} + \phi_{i5} + \phi_{i6} + \phi_{i7} + \phi_{i8}\right) - \frac{2}{3}\phi_{i9}, \\
\phi_{\eta^2 i} &= \frac{1}{12}\left(\phi_{i1} + \phi_{i2} + \phi_{i3} + \phi_{i4} + \phi_{i5} + \phi_{i6} + \phi_{i7} + \phi_{i8}\right) - \frac{2}{3}\phi_{i9}, \\
\phi_{\zeta^2 i} &= \frac{1}{12}\left(\phi_{i1} + \phi_{i2} + \phi_{i3} + \phi_{i4} + \phi_{i5} + \phi_{i6} + \phi_{i7} + \phi_{i8}\right) - \frac{2}{3}\phi_{i9}.
\end{aligned} \tag{2.33}$$

The multi-moment constrained condition is finally determined as (2.34)

$$\overline{\phi}_i = \frac{1}{24}\left(\phi_{i1} + \phi_{i2} + \phi_{i3} + \phi_{i4} + \phi_{i5} + \phi_{i6} + \phi_{i7} + \phi_{i8} + 16\phi_{i9}\right). \tag{2.34}$$

- For prismatic element

The reconstruction function for unstructured prismatic element Ω_i is built up on the canonical reference coordinate with nodes $\theta_{i1}\,(1,0,-1)$, $\theta_{i2}\,(0,0,-1)$, $\theta_{i3}\,(0,1,-1)$, $\theta_{i4}\,(1,0,1)$, $\theta_{i5}\,(0,0,1)$ and $\theta_{i6}\,(0,1,1)$ as shown in Fig. 2.4. The five cell surfaces of element Ω_i are denoted by $\Gamma_{i1} = \overline{(\theta_{i1},\theta_{i2},\theta_{i3})}$, $\Gamma_{i2} = \overline{(\theta_{i4},\theta_{i5},\theta_{i6})}$, $\Gamma_{i3} = \overline{(\theta_{i1},\theta_{i3},\theta_{i6},\theta_{i4})}$, $\Gamma_{i4} = \overline{(\theta_{i3},\theta_{i2},\theta_{i5},\theta_{i6})}$ and $\Gamma_{i5} = \overline{(\theta_{i2},\theta_{i1},\theta_{i4},\theta_{i5})}$. The reconstruction function can be determined from constraint conditions and expressed in basis function form as Table 2.16.

From reconstruction function, we can derive the constrained condition as

$$\overline{\phi}_i = \frac{1}{24}\left(\phi_{i1} + \phi_{i2} + \phi_{i3} + \phi_{i4} + \phi_{i5} + \phi_{i6}\right) + \frac{3}{4}\phi_{i7} + \frac{1}{24}\phi_{\zeta^2 i}.$$

$$
\begin{aligned}
\Phi_i(\xi,\eta,\zeta) &= \psi_1\phi_{i1} + \psi_2\phi_{i2} + \psi_3\phi_{i3} + \psi_4\phi_{i4} + \psi_5\phi_{i5} + \psi_6\phi_{i6} + \psi_7\phi_{i7} + \psi_8\phi_{i8} \\
&+ \psi_9\phi_{i9} + \psi_\xi\phi_{\xi i} + \psi_\eta\phi_{\eta i} + \psi_\zeta\phi_{\zeta i} + \psi_{\xi^2}\phi_{\xi^2 i} + \psi_{\eta^2}\phi_{\eta^2 i} + \psi_{\zeta^2}\phi_{\zeta^2 i},
\end{aligned}
$$

constraint conditions

$$
\begin{cases}
\Phi_i(-1,-1,-1) = \phi_{i1} \\
\Phi_i(1,-1,-1) = \phi_{i2} \\
\Phi_i(1,1,-1) = \phi_{i3} \\
\Phi_i(-1,1,-1) = \phi_{i4} \\
\Phi_i(-1,-1,1) = \phi_{i5} \\
\Phi_i(1,-1,1) = \phi_{i6} \\
\Phi_i(1,1,1) = \phi_{i7} \\
\Phi_i(-1,1,1) = \phi_{i8} \\
\Phi_i(0,0,0) = \phi_{i9} \\
\frac{\partial\Phi_i(\xi,\eta,\zeta)}{\partial\xi}\Big|_{(0,0,0)} = \phi_{\xi i} \\
\frac{\partial\Phi_i(\xi,\eta,\zeta)}{\partial\eta}\Big|_{(0,0,0)} = \phi_{\eta i} \\
\frac{\partial\Phi_i(\xi,\eta,\zeta)}{\partial\zeta}\Big|_{(0,0,0)} = \phi_{\zeta i}, \\
\frac{\partial^2\Phi_i(\xi,\eta,\zeta)}{\partial\xi^2}\Big|_{(0,0,0)} = \phi_{\xi^2 i} \\
\frac{\partial^2\Phi_i(\xi,\eta,\zeta)}{\partial\eta}\Big|_{(0,0,0)} = \phi_{\eta^2 i} \\
\frac{\partial\Phi_i^2(\xi,\eta,\zeta)}{\partial\zeta^2}\Big|_{(0,0,0)} = \phi_{\zeta^2 i},
\end{cases}
$$

basis functions

$$
\begin{cases}
\psi_1 = \frac{1}{8}(\xi\eta+\eta\zeta+\zeta\xi) - \frac{1}{16}(\xi^2\eta+\xi\eta^2+\eta^2\zeta+\eta\zeta^2+\xi^2\zeta+\xi\zeta^2) - \frac{1}{8}\xi\eta\zeta + \frac{1}{8}\xi^2\eta^2\zeta^2 \\
\psi_2 = \frac{1}{8}(\eta\zeta-\xi\eta-\zeta\xi) - \frac{1}{16}(3(\eta^2\zeta+\eta\zeta^2)-\xi^2\eta-\xi\eta^2-\xi^2\zeta-\xi\zeta^2) + \frac{1}{8}\xi\eta\zeta + \frac{1}{8}\xi^2\eta^2\zeta^2 \\
\psi_3 = \frac{1}{8}(\xi\eta-\zeta\xi-\eta\zeta) + \frac{1}{16}(3(\xi^2\eta+\xi\eta^2)-\eta^2\zeta-\eta\zeta^2-\xi^2\zeta-\xi\zeta^2) - \frac{1}{8}\xi\eta\zeta + \frac{1}{8}\xi^2\eta^2\zeta^2 \\
\psi_4 = \frac{1}{8}(\zeta\xi-\xi\eta-\eta\zeta) - \frac{1}{16}(3(\xi^2\zeta+\xi\zeta^2)-\xi^2\eta-\xi\eta^2-\eta^2\zeta-\eta\zeta^2) + \frac{1}{8}\xi\eta\zeta + \frac{1}{8}\xi^2\eta^2\zeta^2 \\
\psi_5 = \frac{1}{8}(\xi\eta-\zeta\xi-\eta\zeta) - \frac{1}{16}(3(\xi^2\eta+\xi\eta^2)-\eta^2\zeta-\eta\zeta^2-\xi^2\zeta-\xi\zeta^2) + \frac{1}{8}\xi\eta\zeta + \frac{1}{8}\xi^2\eta^2\zeta^2 \\
\psi_6 = \frac{1}{8}(\zeta\xi-\xi\eta-\eta\zeta) - \frac{1}{16}(3(\xi^2\zeta+\xi\zeta^2)-\xi^2\eta-\xi\eta^2-\eta^2\zeta-\eta\zeta^2) - \frac{1}{8}\xi\eta\zeta + \frac{1}{8}\xi^2\eta^2\zeta^2 \\
\psi_7 = \frac{1}{8}(\xi\eta+\zeta\xi+\eta\zeta) + \frac{1}{16}(\xi^2\eta+\xi\eta^2+\eta^2\zeta+\eta\zeta^2+\xi^2\zeta+\xi\zeta^2) + \frac{1}{8}\xi\eta\zeta + \frac{1}{8}\xi^2\eta^2\zeta^2 \\
\psi_8 = \frac{1}{8}(\eta\zeta-\xi\eta-\zeta\xi) - \frac{1}{16}(3(\eta^2\zeta+\eta\zeta^2)-\xi^2\eta-\xi\eta^2-\xi^2\zeta-\xi\zeta^2) - \frac{1}{8}\xi\eta\zeta + \frac{1}{8}\xi^2\eta^2\zeta^2 \\
\psi_9 = 1-\xi^2\eta^2\zeta^2 \\
\psi_\xi = \frac{1}{2}(\eta^2\zeta+\eta\zeta^2-\xi^2\eta-\xi\eta^2-\xi^2\zeta-\xi\zeta^2) + \xi \\
\psi_\eta = \frac{1}{2}(\xi^2\zeta+\xi\zeta^2-\eta^2\zeta-\eta\zeta^2-\xi^2\eta-\xi\eta^2) + \eta \\
\psi_\zeta = \frac{1}{2}(\xi^2\eta-\xi\eta^2-\xi^2\zeta-\xi\zeta^2-\eta^2\zeta-\eta\zeta^2) + \zeta \\
\psi_{\xi^2} = \frac{1}{2}\xi^2 - \frac{1}{2}\xi^2\eta^2\zeta^2 \\
\psi_{\eta^2} = \frac{1}{2}\eta^2 - \frac{1}{2}\xi^2\eta^2\zeta^2 \\
\psi_{\zeta^2} = \frac{1}{2}\zeta^2 - \frac{1}{2}\xi^2\eta^2\zeta^2
\end{cases}
$$

Table 2.15: Constraint conditions and basis functions for hexahedral element.

$$\begin{aligned}\Phi_i(\xi,\eta,\zeta) &= \psi_1\phi_{i1}+\psi_2\phi_{i2}+\psi_3\phi_{i3}+\psi_4\phi_{i4}+\psi_5\phi_{i5}+\psi_6\phi_{i6}+\psi_7\phi_{i7}+\psi_\xi\phi_{\xi i}\\ &+ \psi_\eta\phi_{\eta i}+\psi_\zeta\phi_{\zeta i}+\psi_{\zeta^2}\phi_{\zeta^2 i}.\end{aligned}$$

constraint conditions

$$\begin{cases}\Phi_i(1,0,-1)=\phi_{i1}\\ \Phi_i(0,0,-1)=\phi_{i2}\\ \Phi_i(0,1,-1)=\phi_{i3}\\ \Phi_i(1,0,1)=\phi_{i4}\\ \Phi_i(0,0,1)=\phi_{i5}\\ \Phi_i(0,1,1)=\phi_{i6}\\ \Phi_i(\frac{1}{3},\frac{1}{3},0)=\phi_{i7}\\ \dfrac{\partial\Phi_i(\xi,\eta,\zeta)}{\partial\xi}\Big|_{(\frac{1}{3},\frac{1}{3},0)}=\phi_{\xi i}\\ \dfrac{\partial\Phi_i(\xi,\eta,\zeta)}{\partial\eta}\Big|_{(\frac{1}{3},\frac{1}{3},0)}=\phi_{\eta i}\\ \dfrac{\partial\Phi_i(\xi,\eta,\zeta)}{\partial\zeta}\Big|_{(\frac{1}{3},\frac{1}{3},0)}=\phi_{\zeta i}\\ \dfrac{\partial^2\Phi_i(\xi,\eta,\zeta)}{\partial\zeta^2}\Big|_{(\frac{1}{3},\frac{1}{3},0)}=\phi_{\zeta^2 i},\end{cases}$$

basis functions

$$\begin{cases}\psi_1=-\frac{1}{2}\xi+\frac{1}{2}\eta+\xi^2-\frac{1}{2}\eta^2-\frac{1}{2}\xi\eta-\frac{1}{2}\zeta\xi+\frac{3}{2}\xi\eta\zeta\\ \psi_2=\frac{1}{2}-\frac{3}{2}\xi-\frac{3}{2}\eta-\frac{1}{2}\zeta+\xi^2+\eta^2+\frac{5}{2}\xi\eta+\frac{1}{2}\eta\zeta+\frac{1}{2}\zeta\xi+\frac{3}{2}\xi\eta\zeta\\ \psi_3=-\frac{1}{2}\eta+\frac{1}{2}\xi+\eta^2-\frac{1}{2}\xi^2-\frac{1}{2}\xi\eta-\frac{1}{2}\eta\zeta+\frac{3}{2}\xi\eta\zeta\\ \psi_4=-\frac{1}{2}\xi+\frac{1}{2}\eta+\xi^2-\frac{1}{2}\eta^2-\frac{1}{2}\xi\eta+\frac{1}{2}\zeta\xi-\frac{3}{2}\xi\eta\zeta\\ \psi_5=\frac{1}{2}-\frac{3}{2}\xi-\frac{3}{2}\eta+\frac{1}{2}\zeta+\xi^2+\eta^2+\frac{5}{2}\xi\eta-\frac{1}{2}\eta\zeta-\frac{1}{2}\zeta\xi-\frac{3}{2}\xi\eta\zeta\\ \psi_6=-\frac{1}{2}\eta+\frac{1}{2}\xi+\eta^2-\frac{1}{2}\xi^2-\frac{1}{2}\xi\eta+\frac{1}{2}\eta\zeta-\frac{3}{2}\xi\eta\zeta\\ \psi_7=3\xi+3\eta-3\xi^2-3\eta^2-3\xi\eta\\ \psi_\xi=\xi-2\eta-\xi^2+2\eta^2+2\xi\eta\\ \psi_\eta=\eta-2\xi-\eta^2+2\xi^2+2\xi\eta\\ \psi_\zeta=9\xi\eta\zeta\\ \psi_{\zeta^2}=-\frac{1}{2}+\frac{3}{2}\xi+\frac{3}{2}\eta-\frac{3}{2}\xi^2-\frac{3}{2}\eta^2+\frac{1}{2}\zeta^2-\frac{3}{2}\xi\eta\end{cases}$$

Table 2.16: Constraint conditions and basis functions for prismatic element.

The first order derivative is first derived from linear reconstruction polynomial $\Lambda_i(\xi,\eta,\zeta) = c_0 + c_1\xi + c_2\eta + c_3\zeta$ and $(\phi_{\xi i}, \phi_{\eta i}, \phi_{\zeta i})$ are determined as (2.35)

$$\begin{aligned} \phi_{\xi i} &= \frac{1}{2}\left(\phi_{i1} + \phi_{i4} - \phi_{i2} - \phi_{i5}\right), \\ \phi_{\eta i} &= \frac{1}{2}\left(\phi_{i3} + \phi_{i6} - \phi_{i2} - \phi_{i5}\right), \\ \phi_{\zeta i} &= \frac{1}{6}\left(\phi_{i3} + \phi_{i4} + \phi_{i5} - \phi_{i1} - \phi_{i2} - \phi_{i3}\right). \end{aligned} \tag{2.35}$$

In the same manner, from higher order reconstruction polynomial $\Psi_i(\xi,\eta,\zeta) = c_0 + c_1\xi + c_2\eta + c_3\zeta + c_4\zeta^2 + c_5\xi\eta + c_6\eta\zeta + c_7\zeta\xi$, $\phi_{\zeta^2 i}$ can be determined as (2.36)

$$\begin{aligned} \phi_{\zeta^2 i} &= \tfrac{1}{6}\left(\phi_{i1} + \phi_{i3} + \phi_{i4} + \phi_{i6} + 4\left(\phi_{i2} + \phi_{i5}\right)\right) - 2\phi_{i7} + \tfrac{1}{3}\left(\phi_{\xi i} + \phi_{\eta i}\right) \\ &= \tfrac{1}{3}\left(\phi_{i1} + \phi_{i3} + \phi_{i4} + \phi_{i6} + \phi_{i2} + \phi_{i5}\right) - 2\phi_{i7}. \end{aligned} \tag{2.36}$$

The multi-moment constrained condition of prismatic element is determined as (2.37)

$$\overline{\phi}_i = \frac{1}{18}\left(\phi_{i1} + \phi_{i2} + \phi_{i3} + \phi_{i4} + \phi_{i5} + \phi_{i6}\right) + \frac{2}{3}\phi_{i7}. \tag{2.37}$$

- For pyramidal element

The reconstruction function for unstructured pyramidal element Ω_i is built up on the canonical reference coordinate with nodes $\theta_{i1}(-1,-1,-1)$, $\theta_{i2}(1,-1,-1)$, $\theta_{i3}(1,1,-1)$, $\theta_{i4}(-1,1,-1)$ and $\theta_{i5}(0,0,1)$ as shown in Fig. 2.4. The five cell surfaces of element Ω_i are denoted by $\Gamma_{i1} = \overline{(\theta_{i1},\theta_{i2},\theta_{i3},\theta_{i4})}$, $\Gamma_{i2} = \overline{(\theta_{i1},\theta_{i4},\theta_{i5})}$, $\Gamma_{i3} = \overline{(\theta_{i4},\theta_{i3},\theta_{i5})}$, $\Gamma_{i4} = \overline{(\theta_{i3},\theta_{i2},\theta_{i5})}$ and $\Gamma_{i5} = \overline{(\theta_{i2},\theta_{i1},\theta_{i5})}$. The reconstruction function can be determined from constraint conditions and expressed in basis function form as Table 2.17.

From reconstruction function, we can derive the constrained condition as

$$\overline{\phi}_i = \frac{1}{84}\left(\phi_{i1} + \phi_{i2} + \phi_{i3} + \phi_{i4}\right) + \frac{58}{945}\phi_{i5} + \frac{842}{945}\phi_{i6} - \frac{43}{630}\phi_{\zeta i} + \frac{8}{105}\left(\phi_{\xi^2 i} + \phi_{\eta^2 i}\right).$$

The first order derivative is first derived from linear reconstruction polynomial $\Lambda_i(\xi,\eta,\zeta) = c_0 + c_1\xi + c_2\eta + c_3\zeta$ and $(\phi_{\xi i}, \phi_{\eta i}, \phi_{\zeta i})$ are determined as (2.38)

$$\begin{aligned} \phi_{\xi i} &= \frac{1}{2}\left(\phi_{i2} + \phi_{i3} - \phi_{i1} - \phi_{i4}\right), \\ \phi_{\eta i} &= \frac{1}{2}\left(\phi_{i3} + \phi_{i4} - \phi_{i1} - \phi_{i2}\right), \\ \phi_{\zeta i} &= \frac{2}{77}\phi_{i6} + \frac{38}{77}\phi_{i5} - \frac{10}{77}\left(\phi_{i1} + \phi_{i2} + \phi_{i3} + \phi_{i4}\right). \end{aligned} \tag{2.38}$$

$$\begin{aligned}\Phi_i(\xi,\eta,\zeta) &= \psi_1\phi_{i1}+\psi_2\phi_{i2}+\psi_3\phi_{i3}+\psi_4\phi_{i4}+\psi_5\phi_{i5}+\psi_6\phi_{i6}+\psi_\xi\phi_{\xi i}+\psi_\eta\phi_{\eta i}\\ &+ \psi_\zeta\phi_{\zeta i}+\psi_{\xi^2}\phi_{\xi^2 i}+\psi_{\eta^2}\phi_{\eta^2 i},\end{aligned}$$

constraint conditions

$$\begin{cases}\Phi_i(-1,-1,-1)=\phi_{i1}\\ \Phi_i(1,-1,-1)=\phi_{i2}\\ \Phi_i(1,1,-1)=\phi_{i3}\\ \Phi_i(-1,1,-1)=\phi_{i4}\\ \Phi_i(0,0,1)=\phi_{i5}\\ \Phi_i(0,0,-\frac{1}{2})=\phi_{i6}\\ \dfrac{\partial\Phi_i(\xi,\eta,\zeta)}{\partial\xi}\Big|_{(0,0,-\frac{1}{2})}=\phi_{\xi i}\\ \dfrac{\partial\Phi_i(\xi,\eta,\zeta)}{\partial\eta}\Big|_{(0,0,-\frac{1}{2})}=\phi_{\eta i}\\ \dfrac{\partial\Phi_i(\xi,\eta,\zeta)}{\partial\zeta}\Big|_{(0,0,-\frac{1}{2})}=\phi_{\zeta i}\\ \dfrac{\partial^2\Phi_i(\xi,\eta,\zeta)}{\partial\xi^2}\Big|_{(0,0,-\frac{1}{2})}=\phi_{\xi^2 i}\\ \dfrac{\partial^2\Phi_i(\xi,\eta,\zeta)}{\partial\eta}\Big|_{(0,0,-\frac{1}{2})}=\phi_{\eta^2 i},\end{cases}$$

basis functions

$$\begin{cases}\psi_1=-\frac{1}{4}(\xi^2\eta+\xi\eta^2)+\frac{1}{4}\xi^2\eta^2-\frac{1}{4}\xi\eta\zeta\\ \psi_2=-\frac{1}{4}(\xi^2\eta-\xi\eta^2)+\frac{1}{4}\xi^2\eta^2+\frac{1}{4}\xi\eta\zeta\\ \psi_3=\frac{1}{4}(\xi^2\eta+\xi\eta^2)+\frac{1}{4}\xi^2\eta^2-\frac{1}{4}\xi\eta\zeta\\ \psi_4=\frac{1}{4}(\xi^2\eta-\xi\eta^2)+\frac{1}{4}\xi^2\eta^2+\frac{1}{4}\xi\eta\zeta\\ \psi_5=\frac{1}{9}+\frac{4}{9}\zeta+\frac{4}{9}\zeta^2-\frac{1}{9}\xi^2\eta^2\\ \psi_6=\frac{8}{9}-\frac{4}{9}\zeta-\frac{4}{9}\zeta^2-\frac{8}{9}\xi^2\eta^2\\ \psi_\xi=\xi-\xi\eta^2\\ \psi_\eta=\eta-\xi^2\eta\\ \psi_\zeta=\frac{1}{3}+\frac{1}{3}\zeta-\frac{2}{3}\zeta^2+\frac{2}{3}\xi^2\eta^2\\ \psi_{\xi^2}=\frac{1}{2}\xi^2-\frac{1}{2}\xi^2\eta^2\\ \psi_{\eta^2}=\frac{1}{2}\eta^2-\frac{1}{2}\xi^2\eta^2\end{cases}$$

Table 2.17: Constraint conditions and basis functions for pyramidal element.

Element Type	Multi-moment constrained conditions
Triangular element	$\overline{\phi}_i = \frac{1}{12}\left(\phi_{i1} + \phi_{i2} + \phi_{i3} + 9\phi_{i4}\right)$
Quadrilateral element	$\overline{\phi}_i = \frac{1}{12}\left(\phi_{i1} + \phi_{i2} + \phi_{i3} + \phi_{i4} + 8\phi_{i5}\right)$
Tetrahedral element	$\overline{\phi}_i = \frac{1}{20}\left(\phi_{i1} + \phi_{i2} + \phi_{i3} + \phi_{i4} + 16\phi_{i5}\right)$
Hexahedral element	$\overline{\phi}_i = \frac{1}{24}\left(\phi_{i1} + \phi_{i2} + \phi_{i3} + \phi_{i4} + \phi_{i5} + \phi_{i6} + \phi_{i7} + \phi_{i8} + 16\phi_{i9}\right)$
Prismatic element	$\overline{\phi}_i = \frac{1}{18}\left(\phi_{i1} + \phi_{i2} + \phi_{i3} + \phi_{i4} + \phi_{i5} + \phi_{i6}\right) + \frac{2}{3}\phi_{i7}$
Pyramidal element	$\overline{\phi}_i = \frac{77887}{1649340}\left(\phi_{i1} + \phi_{i2} + \phi_{i3} + \phi_{i4}\right) + \frac{77887}{1237005}\phi_{i5} + \frac{925457}{1237005}\phi_{i6}$

Table 2.18: Multi-moment constrained conditions for all type of unstructured grid elements for MCV scheme.

In the same manner, from reconstruction polynomial $\Psi_i\left(\xi,\eta,\zeta\right) = c_0 + c_1\xi + c_2\eta + c_3\zeta + c_4\xi^2 + c_5\eta^2 + c_6\xi\eta$, $\left(\phi_{\xi^2 i}, \phi_{\eta^2 i}\right)$ can be obtained as (2.39)

$$\begin{aligned} \phi_{\xi^2 i} &= \frac{1}{4}\left(\phi_{i1} + \phi_{i2} + \phi_{i3} + \phi_{i4}\right) - \frac{1}{17}\phi_{i5} - \frac{16}{17}\phi_{i6} + \frac{10}{17}\phi_{\zeta i}, \\ \phi_{\eta^2 i} &= \frac{1}{4}\left(\phi_{i1} + \phi_{i2} + \phi_{i3} + \phi_{i4}\right) - \frac{1}{17}\phi_{i5} - \frac{16}{17}\phi_{i6} + \frac{10}{17}\phi_{\zeta i}. \end{aligned} \tag{2.39}$$

The multi-moment constrained condition of pyramidal element then is determined as (2.40)

$$\overline{\phi}_i = \frac{77887}{1649340}\left(\phi_{i1} + \phi_{i2} + \phi_{i3} + \phi_{i4}\right) + \frac{77887}{1237005}\phi_{i5} + \frac{925457}{1237005}\phi_{i6}. \tag{2.40}$$

As conclusion, the multi-moment constrained condition for all type of unstructured grid elements are given in Table 2.18.

2.5 Numerical approximation for derivatives and integrals

Since the reconstruction function is determined, we can immediately compute the quantities such as first order derivatives at vertices as well as surface center and integral average quantity on cell surface.

2.5.1 First order derivatives at cell vertices as well as surface center

The first order derivatives on local coordinate (ξ_i, η_i, ζ_i) are defined as:

$$\begin{aligned}
\Phi_{i\xi}\left(\xi_i, \eta_i, \zeta_i\right) &= \left.\frac{\partial \Phi(\xi,\eta,\zeta)}{\partial \xi}\right|_{\xi=\xi_i,\eta=\eta_i,\zeta=\zeta_i} \\
\Phi_{i\eta}\left(\xi_i, \eta_i, \zeta_i\right) &= \left.\frac{\partial \Phi(\xi,\eta,\zeta)}{\partial \eta}\right|_{\xi=\xi_i,\eta=\eta_i,\zeta=\zeta_i} \\
\Phi_{i\zeta}\left(\xi_i, \eta_i, \zeta_i\right) &= \left.\frac{\partial \Phi(\xi,\eta,\zeta)}{\partial \zeta}\right|_{\xi=\xi_i,\eta=\eta_i,\zeta=\zeta_i}
\end{aligned} \quad .$$

As reconstruction function has been determined in Section 2.3 and 2.4, the first order derivatives at random position in local cell (ξ_i, η_i, ζ_i) can be derived straightforwardly. As the basis functions are frequently used afterwards, the formulations of derivatives for arbitrary unstructured grids for both VPM and MCV are give in Table 2.19 and 2.20.

With specifying the coordinate (ξ_i, η_i, ζ_i) by cell vertices $(\xi_{ik}, \eta_{ik}, \zeta_{ik})$ or surface center $(\xi_{ij}, \eta_{ij}, \zeta_{ij})$, we can compute derivatives at required position in the form of local coordinate. Using the formulation of (2.2) or (2.4), we can transform derivatives to global coordinate at cell vertices $(\Phi_{x_{ik}}, \Phi_{y_{ik}}, \Phi_{z_{ik}})$ or surface centroids $\left(\Phi_{x_{ij}}, \Phi_{y_{ij}}, \Phi_{z_{ij}}\right)$.

2.5.2 Integral average quantity on cell surface

The integral average quantity on cell surface can be computed from reconstruction function on the local coordinate directly in the form of:

$$\overline{\phi}_{\Gamma ij} = \frac{1}{|\Gamma|}\int_{\Gamma} \Phi_i\left(\xi, \eta, \zeta\right) d\Gamma$$

The integral average quantities for VPM scheme on unstructured grid are summarized in the form of DOFs as Table 2.21.

Similarly, the integral average quantities for MCV scheme on unstructured grid are summarized in the form of DOFs as Table 2.22.

Element Type	First order derivatives $(\Phi_{i\xi}, \Phi_{i\eta}, \Phi_{i\zeta})$ at arbitrary vertex in local cell (ξ_i, η_i, ζ_i)
Triangular element	$\Phi_{i\xi}(\xi_i,\eta_i) = \frac{1}{3}\left(-10\phi_{i1}-4\phi_{i2}+2\phi_{i3}+12\overline{\phi}_i+3\phi_{\xi i}-6\phi_{\eta i}\right)+\frac{2}{3}\left(7\phi_{i1}+7\phi_{i2}-2\phi_{i3}-12\overline{\phi}_i-3\phi_{\xi i}+6\phi_{\eta i}\right)\xi$ $+ \frac{1}{3}\left(16\phi_{i1}-2\phi_{i2}-2\phi_{i3}-12\overline{\phi}_i+6\phi_{\xi i}+6\phi_{\eta i}\right)\eta$ $\Phi_{i\eta}(\xi_i,\eta_i) = \frac{1}{3}\left(-10\phi_{i1}-4\phi_{i3}+2\phi_{i2}+12\overline{\phi}_i+3\phi_{\eta i}-6\phi_{\xi i}\right)+\frac{2}{3}\left(7\phi_{i1}+7\phi_{i3}-2\phi_{i2}-12\overline{\phi}_i-3\phi_{\eta i}+6\phi_{\xi i}\right)\eta$ $+ \frac{1}{3}\left(16\phi_{i1}-2\phi_{i2}-2\phi_{i3}-12\overline{\phi}_i+6\phi_{\xi i}+6\phi_{\eta i}\right)\xi$
Quadrilateral element	$\Phi_{i\xi}(\xi_i,\eta_i) = \frac{1}{4}\left(\phi_{i1}-\phi_{i2}+\phi_{i3}-\phi_{i4}\right)\eta+\frac{1}{2}\left(-\phi_{i1}-\phi_{i2}+\phi_{i3}+\phi_{i4}-4\phi_{\eta i}\right)\xi\eta+\left(-\phi_{i1}+\phi_{i2}+\phi_{i3}-\phi_{i4}-4\phi_{\xi i}\right)\eta^2$ $+ \frac{1}{16}\left(9\left(\phi_{i1}+\phi_{i2}+\phi_{i3}+\phi_{i4}\right)-36\overline{\phi}_i-12\phi_{\xi^2 i}-12\phi_{\eta^2 i}\right)\xi\eta^2+\phi_{\xi i}+\xi\phi_{\xi^2 i}$ $\Phi_{i\eta}(\xi_i,\eta_i) = \frac{1}{4}\left(\phi_{i1}-\phi_{i2}+\phi_{i3}-\phi_{i4}\right)\xi+\frac{1}{2}\left(-\phi_{i1}-\phi_{i2}+\phi_{i3}+\phi_{i4}-4\phi_{\eta i}\right)\xi^2+\left(-\phi_{i1}+\phi_{i2}+\phi_{i3}-\phi_{i4}-4\phi_{\xi i}\right)\xi\eta$ $+ \frac{1}{16}\left(9\left(\phi_{i1}+\phi_{i2}+\phi_{i3}+\phi_{i4}\right)-36\overline{\phi}_i-12\phi_{\xi^2 i}-12\phi_{\eta^2 i}\right)\xi^2\eta+\phi_{\eta i}+\eta\phi_{\eta^2 i}$
Tetrahedral element	$\Phi_{i\xi}(\xi_i,\eta_i,\zeta_i) = \frac{1}{6}\left(-17\phi_{i1}-5\phi_{i2}+\phi_{i3}+\phi_{i4}+20\overline{\phi}_i+6\phi_{\xi i}-6\phi_{\eta i}-6\phi_{\zeta i}\right)$ $+ \frac{1}{3}\left(11\phi_{i1}+11\phi_{i2}-\phi_{i3}-\phi_{i4}-20\overline{\phi}_i-6\phi_{\xi i}+6\phi_{\eta i}+6\phi_{\zeta i}\right)\xi$ $+ \frac{1}{6}\left(23\phi_{i1}-\phi_{i2}-\phi_{i3}-\phi_{i4}-20\overline{\phi}_i+6\phi_{\xi i}+6\phi_{\eta i}+6\phi_{\zeta i}\right)(\eta+\zeta)$ $\Phi_{i\eta}(\xi_i,\eta_i,\zeta_i) = \frac{1}{6}\left(-17\phi_{i1}-5\phi_{i3}+\phi_{i2}+\phi_{i4}+20\overline{\phi}_i+6\phi_{\eta i}-6\phi_{\xi i}-6\phi_{\zeta i}\right)$ $+ \frac{1}{3}\left(11\phi_{i1}+11\phi_{i3}-\phi_{i2}-\phi_{i4}-20\overline{\phi}_i-6\phi_{\eta i}+6\phi_{\xi i}+6\phi_{\zeta i}\right)\eta$ $+ \frac{1}{6}\left(23\phi_{i1}-\phi_{i2}-\phi_{i3}-\phi_{i4}-20\overline{\phi}_i+6\phi_{\xi i}+6\phi_{\eta i}+6\phi_{\zeta i}\right)(\xi+\zeta)$ $\Phi_{i\zeta}(\xi_i,\eta_i,\zeta_i) = \frac{1}{6}\left(-17\phi_{i1}-5\phi_{i4}+\phi_{i2}+\phi_{i3}+20\overline{\phi}_i+6\phi_{\zeta i}-6\phi_{\xi i}-6\phi_{\eta i}\right)$ $+ \frac{1}{3}\left(11\phi_{i1}+11\phi_{i4}-\phi_{i2}-\phi_{i3}-20\overline{\phi}_i-6\phi_{\zeta i}+6\phi_{\xi i}+6\phi_{\eta i}\right)\zeta$ $+ \frac{1}{6}\left(23\phi_{i1}-\phi_{i2}-\phi_{i3}-\phi_{i4}-20\overline{\phi}_i+6\phi_{\xi i}+6\phi_{\eta i}+6\phi_{\zeta i}\right)(\xi+\eta)$
Hexahedral element	$\Phi_{i\xi}(\xi_i,\eta_i,\zeta_i) = \frac{1}{104}\left(27\left(\phi_{i1}+\phi_{i2}+\phi_{i3}+\phi_{i4}+\phi_{i5}+\phi_{i6}+\phi_{i7}+\phi_{i8}\right)-216\overline{\phi}_i-72\left(\phi_{\xi^2 i}+\phi_{\eta^2 i}+\phi_{\zeta^2 i}\right)\right)\xi\eta^2\zeta^2$ $+ \frac{1}{16}\left(\phi_{i2}+3\phi_{i3}+\phi_{i4}+\phi_{i7}-\phi_{i1}-3\phi_{i5}-\phi_{i6}-\phi_{i8}-8\phi_{\xi i}-8\phi_{\eta i}+8\phi_{\zeta i}\right)\left(2\xi\eta+\eta^2\right)$ $+ \frac{1}{16}\left(\phi_{i2}+\phi_{i5}+3\phi_{i6}+\phi_{i7}-\phi_{i1}-\phi_{i3}-3\phi_{i4}-\phi_{i8}-8\phi_{\xi i}-8\phi_{\zeta i}+8\phi_{\eta i}\right)\left(2\xi\zeta+\zeta^2\right)$ $+ \frac{1}{8}\left(\phi_{i1}+\phi_{i3}+\phi_{i5}+\phi_{i7}-\phi_{i2}-\phi_{i4}-\phi_{i6}-\phi_{i8}\right)\eta+\frac{1}{8}\left(\phi_{i1}+\phi_{i4}+\phi_{i6}+\phi_{i7}-\phi_{i2}-\phi_{i3}-\phi_{i5}-\phi_{i8}\right)\zeta$ $+ \frac{1}{8}\left(\phi_{i2}+\phi_{i4}+\phi_{i5}+\phi_{i7}-\phi_{i1}-\phi_{i3}-\phi_{i6}-\phi_{i8}\right)\eta\zeta+\phi_{\xi i}+\xi\phi_{\xi^2 i}$ $\Phi_{i\eta}(\xi_i,\eta_i,\zeta_i) = \frac{1}{104}\left(27\left(\phi_{i1}+\phi_{i2}+\phi_{i3}+\phi_{i4}+\phi_{i5}+\phi_{i6}+\phi_{i7}+\phi_{i8}\right)-216\overline{\phi}_i-72\left(\phi_{\xi^2 i}+\phi_{\eta^2 i}+\phi_{\zeta^2 i}\right)\right)\xi\eta^2\zeta^2$ $+ \frac{1}{16}\left(\phi_{i2}+3\phi_{i3}+\phi_{i4}+\phi_{i7}-\phi_{i1}-3\phi_{i5}-\phi_{i6}-\phi_{i8}-8\phi_{\xi i}-8\phi_{\eta i}+8\phi_{\zeta i}\right)\left(2\xi\eta+\eta^2\right)$ $+ \frac{1}{16}\left(\phi_{i2}+\phi_{i5}+3\phi_{i6}+\phi_{i7}-\phi_{i1}-\phi_{i3}-3\phi_{i4}-\phi_{i8}-8\phi_{\xi i}-8\phi_{\zeta i}+8\phi_{\eta i}\right)\left(2\xi\zeta+\zeta^2\right)$ $+ \frac{1}{8}\left(\phi_{i1}+\phi_{i3}+\phi_{i5}+\phi_{i7}-\phi_{i2}-\phi_{i4}-\phi_{i6}-\phi_{i8}\right)\eta+\frac{1}{8}\left(\phi_{i1}+\phi_{i4}+\phi_{i6}+\phi_{i7}-\phi_{i2}-\phi_{i3}-\phi_{i5}-\phi_{i8}\right)\zeta$ $+ \frac{1}{8}\left(\phi_{i2}+\phi_{i4}+\phi_{i5}+\phi_{i7}-\phi_{i1}-\phi_{i3}-\phi_{i6}-\phi_{i8}\right)\eta\zeta+\phi_{\eta i}+\eta\phi_{\eta^2 i}$ $\Phi_{i\zeta}(\xi_i,\eta_i,\zeta_i) = \frac{1}{104}\left(27\left(\phi_{i1}+\phi_{i2}+\phi_{i3}+\phi_{i4}+\phi_{i5}+\phi_{i6}+\phi_{i7}+\phi_{i8}\right)-216\overline{\phi}_i-72\left(\phi_{\xi^2 i}+\phi_{\eta^2 i}+\phi_{\zeta^2 i}\right)\right)\xi\eta^2\zeta^2$ $+ \frac{1}{16}\left(\phi_{i2}+3\phi_{i3}+\phi_{i4}+\phi_{i7}-\phi_{i1}-3\phi_{i5}-\phi_{i6}-\phi_{i8}-8\phi_{\xi i}-8\phi_{\eta i}+8\phi_{\zeta i}\right)\left(2\xi\eta+\eta^2\right)$ $+ \frac{1}{16}\left(\phi_{i2}+\phi_{i5}+3\phi_{i6}+\phi_{i7}-\phi_{i1}-\phi_{i3}-3\phi_{i4}-\phi_{i8}-8\phi_{\xi i}-8\phi_{\zeta i}+8\phi_{\eta i}\right)\left(2\xi\zeta+\zeta^2\right)$ $+ \frac{1}{8}\left(\phi_{i1}+\phi_{i3}+\phi_{i5}+\phi_{i7}-\phi_{i2}-\phi_{i4}-\phi_{i6}-\phi_{i8}\right)\eta+\frac{1}{8}\left(\phi_{i1}+\phi_{i4}+\phi_{i6}+\phi_{i7}-\phi_{i2}-\phi_{i3}-\phi_{i5}-\phi_{i8}\right)\zeta$ $+ \frac{1}{8}\left(\phi_{i2}+\phi_{i4}+\phi_{i5}+\phi_{i7}-\phi_{i1}-\phi_{i3}-\phi_{i6}-\phi_{i8}\right)\eta\zeta+\phi_{\zeta i}+\zeta\phi_{\zeta^2 i}$
Prismatic element	$\Phi_{i\xi}(\xi_i,\eta_i,\zeta_i) = \frac{1}{3}\left(-2\phi_{i1}-5\phi_{i2}+\phi_{i3}-2\phi_{i4}-5\phi_{i5}+\phi_{i6}+12\overline{\phi}_i+3\phi_{\xi i}-6\phi_{\eta i}+4\phi_{\zeta^2 i}\right)$ $+ \frac{1}{3}\left(7\left(\phi_{i1}+\phi_{i2}+\phi_{i4}+\phi_{i5}\right)-2\left(\phi_{i3}+\phi_{i6}\right)-24\overline{\phi}_i-6\phi_{\xi i}+12\phi_{\eta i}-8\phi_{\zeta^2 i}\right)\xi$ $+ \frac{1}{3}\left(8\left(\phi_{i2}+\phi_{i5}\right)-\left(\phi_{i1}+\phi_{i3}+\phi_{i4}+\phi_{i6}\right)-12\overline{\phi}_i+6\phi_{\xi i}+6\phi_{\eta i}-4\phi_{\zeta^2 i}\right)\eta$ $+ \frac{1}{2}\left(-\phi_{i1}+\phi_{i2}+\phi_{i4}-\phi_{i5}\right)\zeta+\frac{3}{2}\left(\phi_{i1}+\phi_{i2}+\phi_{i3}-\phi_{i4}-\phi_{i5}-\phi_{i6}+6\phi_{\zeta i}\right)\eta\zeta$ $\Phi_{i\eta}(\xi_i,\eta_i,\zeta_i) = \frac{1}{3}\left(\phi_{i1}-5\phi_{i2}-2\phi_{i3}+2\phi_{i4}-5\phi_{i5}-2\phi_{i6}+12\overline{\phi}_i+3\phi_{\eta i}-6\phi_{\xi i}+4\phi_{\zeta^2 i}\right)$ $+ \frac{1}{3}\left(7\left(\phi_{i2}+\phi_{i3}+\phi_{i5}+\phi_{i6}\right)-2\left(\phi_{i1}+\phi_{i4}\right)-24\overline{\phi}_i-6\phi_{\eta i}+12\phi_{\xi i}-8\phi_{\zeta^2 i}\right)\eta$ $+ \frac{1}{3}\left(8\left(\phi_{i2}+\phi_{i5}\right)-\left(\phi_{i1}+\phi_{i3}+\phi_{i4}+\phi_{i6}\right)-12\overline{\phi}_i+6\phi_{\xi i}+6\phi_{\eta i}-4\phi_{\zeta^2 i}\right)\xi$ $+ \frac{1}{2}\left(\phi_{i2}-\phi_{i3}-\phi_{i5}+\phi_{i6}\right)\zeta+\frac{3}{2}\left(\phi_{i1}+\phi_{i2}+\phi_{i3}-\phi_{i4}-\phi_{i5}-\phi_{i6}+6\phi_{\zeta i}\right)\xi\zeta$ $\Phi_{i\zeta}(\xi_i,\eta_i,\zeta_i) = \frac{1}{2}\left(\phi_{i2}-\phi_{i3}-\phi_{i5}+\phi_{i6}\right)\eta+\frac{1}{2}\left(-\phi_{i1}+\phi_{i2}+\phi_{i4}-\phi_{i5}\right)\xi+\frac{1}{2}\phi_{i5}-\frac{1}{2}\phi_{i2}+\zeta\phi_{\zeta^2 i}$ $+ \frac{3}{2}\left(\phi_{i1}+\phi_{i2}+\phi_{i3}-\phi_{i4}-\phi_{i5}-\phi_{i6}+6\phi_{\zeta i}\right)\xi\eta$
Pyramidal element	$\Phi_{i\xi}(\xi_i,\eta_i,\zeta_i) = \frac{1}{842}\left(441\left(\phi_{i1}+\phi_{i2}+\phi_{i3}+\phi_{i4}\right)-84\phi_{i5}-1680\overline{\phi}_i+1008\phi_{\zeta i}-714\left(\phi_{\xi^2 i}+\phi_{\eta^2 i}\right)\right)\xi\eta^2+\phi_{\xi i}+\xi\phi_{\xi^2 i}$ $+ \frac{1}{4}\left(-\phi_{i1}-\phi_{i2}+\phi_{i3}+\phi_{i4}-4\phi_{\eta i}\right)\xi\eta+\frac{1}{4}\left(-\phi_{i1}+\phi_{i2}+\phi_{i3}-\phi_{i4}-4\phi_{\xi i}\right)\eta^2+\frac{1}{4}\left(-\phi_{i1}+\phi_{i2}-\phi_{i3}+\phi_{i4}\right)\eta\zeta$ $\Phi_{i\eta}(\xi_i,\eta_i,\zeta_i) = \frac{1}{842}\left(441\left(\phi_{i1}+\phi_{i2}+\phi_{i3}+\phi_{i4}\right)-84\phi_{i5}-1680\overline{\phi}_i+1008\phi_{\zeta i}-714\left(\phi_{\xi^2 i}+\phi_{\eta^2 i}\right)\right)\xi^2\eta+\phi_{\eta i}+\eta\phi_{\eta^2 i}$ $+ \frac{1}{4}\left(-\phi_{i1}-\phi_{i2}+\phi_{i3}+\phi_{i4}-4\phi_{\eta i}\right)\xi^2+\frac{1}{4}\left(-\phi_{i1}+\phi_{i2}+\phi_{i3}-\phi_{i4}-4\phi_{\xi i}\right)\xi\eta+\frac{1}{4}\left(-\phi_{i1}+\phi_{i2}-\phi_{i3}+\phi_{i4}\right)\xi\zeta$ $\Phi_{i\zeta}(\xi_i,\eta_i,\zeta_i) = \frac{1}{421}\left(5\left(\phi_{i1}+\phi_{i2}+\phi_{i3}+\phi_{i4}\right)+400\phi_{i5}-420\overline{\phi}_i+590\phi_{\zeta i}-32\left(\phi_{\xi^2 i}+\phi_{\eta^2 i}\right)\right)\zeta+\frac{1}{4}\left(-\phi_{i1}+\phi_{i2}-\phi_{i3}+\phi_{i4}\right)\xi\eta$ $+ \frac{1}{842}\left(5\left(\phi_{i1}+\phi_{i2}+\phi_{i3}+\phi_{i4}\right)+400\phi_{i5}-420\overline{\phi}_i+252\phi_{\zeta i}+32\left(\phi_{\xi^2 i}+\phi_{\eta^2 i}\right)\right)$

Table 2.19: First order derivatives of VPM scheme at random position in local cell (ξ_i, η_i, ζ_i) for each unstructured elements.

Element Type	First order derivatives $(\Phi_{i\xi}, \Phi_{i\eta}, \Phi_{i\zeta})$ at arbitrary vertex in local cell (ξ_i, η_i, ζ_i)
Triangular element	$\Phi_{i\xi}(\xi_i,\eta_i) = (-3\phi_{i1}-\phi_{i2}+\phi_{i3}+3\phi_{i4}+\phi_{\xi i}-2\phi_{\eta i})+2(2\phi_{i1}+2\phi_{i2}-\phi_{i3}-3\phi_{i4}-\phi_{\xi i}+2\phi_{\eta i})\xi$ $+ (5\phi_{i1}-\phi_{i2}-\phi_{i3}-3\phi_{i4}+2\phi_{\xi i}+2\phi_{\eta i})\eta$ $\Phi_{i\eta}(\xi_i,\eta_i) = (-3\phi_{i1}-\phi_{i3}+\phi_{i2}+3\phi_{i4}+\phi_{\eta i}-2\phi_{\xi i})+2(2\phi_{i1}+2\phi_{i3}-\phi_{i2}-3\phi_{i4}-\phi_{\eta i}+2\phi_{\xi i})\eta$ $+ (5\phi_{i1}-\phi_{i2}-\phi_{i3}-3\phi_{i4}+2\phi_{\xi i}+2\phi_{\eta i})\xi$
Quadrilateral element	$\Phi_{i\xi}(\xi_i,\eta_i) = \frac{1}{4}(\phi_{i1}-\phi_{i2}+\phi_{i3}-\phi_{i4})\eta+\frac{1}{2}(-\phi_{i1}-\phi_{i2}+\phi_{i3}+\phi_{i4}-4\phi_{\eta i})\xi\eta+(-\phi_{i1}+\phi_{i2}+\phi_{i3}-\phi_{i4}-4\phi_{\xi i})\eta^2$ $+ \frac{1}{4}(\phi_{i1}+\phi_{i2}+\phi_{i3}+\phi_{i4}-4\phi_{i5}-2\phi_{\xi^2 i}-2\phi_{\eta^2 i})\xi\eta^2+\phi_{\xi i}+\xi\phi_{\xi^2 i}$ $\Phi_{i\eta}(\xi_i,\eta_i) = \frac{1}{4}(\phi_{i1}-\phi_{i2}+\phi_{i3}-\phi_{i4})\xi+\frac{1}{2}(-\phi_{i1}-\phi_{i2}+\phi_{i3}+\phi_{i4}-4\phi_{\eta i})\xi^2+(-\phi_{i1}+\phi_{i2}+\phi_{i3}-\phi_{i4}-4\phi_{\xi i})\xi\eta$ $+ \frac{1}{4}(\phi_{i1}+\phi_{i2}+\phi_{i3}+\phi_{i4}-4\phi_{i5}-2\phi_{\xi^2 i}-2\phi_{\eta^2 i})\xi^2\eta+\phi_{\eta i}+\eta\phi_{\eta^2 i}$
Tetrahedral element	$\Phi_{i\xi}(\xi_i,\eta_i,\zeta_i) = \frac{1}{3}(-8\phi_{i1}-2\phi_{i2}+\phi_{i3}+\phi_{i4}+8\phi_{i5}+3\phi_{\xi i}-3\phi_{\eta i}-3\phi_{\zeta i})$ $+ \frac{2}{3}(5\phi_{i1}+5\phi_{i2}-\phi_{i3}-\phi_{i4}-8\phi_{i5}-3\phi_{\xi i}+3\phi_{\eta i}+3\phi_{\zeta i})\xi$ $+ \frac{1}{3}(11\phi_{i1}-\phi_{i2}-\phi_{i3}-\phi_{i4}-8\phi_{i5}+3\phi_{\xi i}+3\phi_{\eta i}+3\phi_{\zeta i})(\eta+\zeta)$ $\Phi_{i\eta}(\xi_i,\eta_i,\zeta_i) = \frac{1}{3}(-8\phi_{i1}-2\phi_{i3}+\phi_{i2}+\phi_{i4}+8\phi_{i5}+3\phi_{\eta i}-3\phi_{\xi i}-3\phi_{\zeta i})$ $+ \frac{2}{3}(5\phi_{i1}+5\phi_{i3}-\phi_{i2}-\phi_{i4}-8\phi_{i5}-3\phi_{\eta i}+3\phi_{\xi i}+3\phi_{\zeta i})\eta$ $+ \frac{1}{3}(11\phi_{i1}-\phi_{i2}-\phi_{i3}-\phi_{i4}-8\phi_{i5}+3\phi_{\xi i}+3\phi_{\eta i}+3\phi_{\zeta i})(\xi+\zeta)$ $\Phi_{i\zeta}(\xi_i,\eta_i,\zeta_i) = \frac{1}{3}(-8\phi_{i1}-2\phi_{i4}+\phi_{i2}+\phi_{i3}+8\phi_{i5}+6\phi_{\zeta i}-6\phi_{\xi i}-6\phi_{\eta i})$ $+ \frac{2}{3}(5\phi_{i1}+5\phi_{i4}-\phi_{i2}-\phi_{i3}-8\phi_{i5}-2\phi_{\zeta i}+2\phi_{\xi i}+2\phi_{\eta i})\zeta$ $+ \frac{1}{3}(11\phi_{i1}-\phi_{i2}-\phi_{i3}-\phi_{i4}-8\phi_{i5}+2\phi_{\xi i}+2\phi_{\eta i}+2\phi_{\zeta i})(\xi+\eta)$
Hexahedral element	$\Phi_{i\xi}(\xi_i,\eta_i,\zeta_i) = \frac{1}{4}(\phi_{i1}+\phi_{i2}+\phi_{i3}+\phi_{i4}+\phi_{i5}+\phi_{i6}+\phi_{i7}+\phi_{i8}-8\phi_{i9}-4(\phi_{\xi^2 i}+\phi_{\eta^2 i}+\phi_{\zeta^2 i}))\xi\eta^2\zeta^2$ $+ \frac{1}{16}(\phi_{i2}+3\phi_{i3}+\phi_{i4}+\phi_{i7}-\phi_{i1}-3\phi_{i5}-\phi_{i6}-\phi_{i8}-8\phi_{\xi i}-8\phi_{\eta i}+8\phi_{\zeta i})(2\xi\eta+\eta^2)$ $+ \frac{1}{16}(\phi_{i2}+\phi_{i5}+3\phi_{i6}+\phi_{i7}-\phi_{i1}-\phi_{i3}-3\phi_{i4}-\phi_{i8}-8\phi_{\xi i}-8\phi_{\zeta i}+8\phi_{\eta i})(2\xi\zeta+\zeta^2)$ $+ \frac{1}{8}(\phi_{i1}+\phi_{i3}+\phi_{i5}+\phi_{i7}-\phi_{i2}-\phi_{i4}-\phi_{i6}-\phi_{i8})\eta+\frac{1}{8}(\phi_{i1}+\phi_{i4}+\phi_{i6}+\phi_{i7}-\phi_{i2}-\phi_{i3}-\phi_{i5}-\phi_{i8})\zeta$ $+ \frac{1}{8}(\phi_{i2}+\phi_{i4}+\phi_{i5}+\phi_{i7}-\phi_{i1}-\phi_{i3}-\phi_{i6}-\phi_{i8})\eta\zeta+\phi_{\xi i}+\xi\phi_{\xi^2 i}$ $\Phi_{i\eta}(\xi_i,\eta_i,\zeta_i) = \frac{1}{4}(\phi_{i1}+\phi_{i2}+\phi_{i3}+\phi_{i4}+\phi_{i5}+\phi_{i6}+\phi_{i7}+\phi_{i8}-8\phi_{i9}-4(\phi_{\xi^2 i}+\phi_{\eta^2 i}+\phi_{\zeta^2 i}))\xi\eta^2\zeta^2$ $+ \frac{1}{16}(\phi_{i2}+3\phi_{i3}+\phi_{i4}+\phi_{i7}-\phi_{i1}-3\phi_{i5}-\phi_{i6}-\phi_{i8}-8\phi_{\xi i}-8\phi_{\eta i}+8\phi_{\zeta i})(2\xi\eta+\eta^2)$ $+ \frac{1}{16}(\phi_{i2}+\phi_{i5}+3\phi_{i6}+\phi_{i7}-\phi_{i1}-\phi_{i3}-3\phi_{i4}-\phi_{i8}-8\phi_{\xi i}-8\phi_{\zeta i}+8\phi_{\eta i})(2\xi\zeta+\zeta^2)$ $+ \frac{1}{8}(\phi_{i1}+\phi_{i3}+\phi_{i5}+\phi_{i7}-\phi_{i2}-\phi_{i4}-\phi_{i6}-\phi_{i8})\eta+\frac{1}{8}(\phi_{i1}+\phi_{i4}+\phi_{i6}+\phi_{i7}-\phi_{i2}-\phi_{i3}-\phi_{i5}-\phi_{i8})\zeta$ $+ \frac{1}{8}(\phi_{i2}+\phi_{i4}+\phi_{i5}+\phi_{i7}-\phi_{i1}-\phi_{i3}-\phi_{i6}-\phi_{i8})\eta\zeta+\phi_{\eta i}+\eta\phi_{\eta^2 i}$ $\Phi_{i\zeta}(\xi_i,\eta_i,\zeta_i) = \frac{1}{4}(\phi_{i1}+\phi_{i2}+\phi_{i3}+\phi_{i4}+\phi_{i5}+\phi_{i6}+\phi_{i7}+\phi_{i8}-8\phi_{i9}-4(\phi_{\xi^2 i}+\phi_{\eta^2 i}+\phi_{\zeta^2 i}))\xi\eta^2\zeta^2$ $+ \frac{1}{16}(\phi_{i2}+3\phi_{i3}+\phi_{i4}+\phi_{i7}-\phi_{i1}-3\phi_{i5}-\phi_{i6}-\phi_{i8}-8\phi_{\xi i}-8\phi_{\eta i}+8\phi_{\zeta i})(2\xi\eta+\eta^2)$ $+ \frac{1}{16}(\phi_{i2}+\phi_{i5}+3\phi_{i6}+\phi_{i7}-\phi_{i1}-\phi_{i3}-3\phi_{i4}-\phi_{i8}-8\phi_{\xi i}-8\phi_{\zeta i}+8\phi_{\eta i})(2\xi\zeta+\zeta^2)$ $+ \frac{1}{8}(\phi_{i1}+\phi_{i3}+\phi_{i5}+\phi_{i7}-\phi_{i2}-\phi_{i4}-\phi_{i6}-\phi_{i8})\eta+\frac{1}{8}(\phi_{i1}+\phi_{i4}+\phi_{i6}+\phi_{i7}-\phi_{i2}-\phi_{i3}-\phi_{i5}-\phi_{i8})\zeta$ $+ \frac{1}{8}(\phi_{i2}+\phi_{i4}+\phi_{i5}+\phi_{i7}-\phi_{i1}-\phi_{i3}-\phi_{i6}-\phi_{i8})\eta\zeta+\phi_{\zeta i}+\zeta\phi_{\zeta^2 i}$
Prismatic element	$\Phi_{i\xi}(\xi_i,\eta_i,\zeta_i) = \frac{1}{2}(-\phi_{i1}-3\phi_{i2}+\phi_{i3}-\phi_{i4}-3\phi_{i5}+\phi_{i6}+6\phi_{i7}+2\phi_{\xi i}-4\phi_{\eta i}+3\phi_{\zeta^2 i})$ $+ (2(\phi_{i1}+\phi_{i2}+\phi_{i4}+\phi_{i5})-(\phi_{i3}+\phi_{i6})-6\phi_{i7}-2\phi_{\xi i}+4\phi_{\eta i}-3\phi_{\zeta^2 i})\xi$ $+ \frac{1}{2}(5(\phi_{i2}+\phi_{i5})-(\phi_{i1}+\phi_{i3}+\phi_{i4}+\phi_{i6})-6\phi_{i7}+4\phi_{\xi i}+4\phi_{\eta i}-3\phi_{\zeta^2 i})\eta$ $+ \frac{1}{2}(-\phi_{i1}+\phi_{i2}+\phi_{i4}-\phi_{i5})\zeta+\frac{3}{2}(\phi_{i1}+\phi_{i2}+\phi_{i3}-\phi_{i4}-\phi_{i5}-\phi_{i6}+6\phi_{\zeta i})\eta\zeta$ $\Phi_{i\eta}(\xi_i,\eta_i,\zeta_i) = \frac{1}{2}(\phi_{i1}-3\phi_{i2}-\phi_{i3}+\phi_{i4}-3\phi_{i5}-\phi_{i6}+6\phi_{i7}+2\phi_{\eta i}-4\phi_{\xi i}+3\phi_{\zeta^2 i})$ $+ (2(\phi_{i2}+\phi_{i3}+\phi_{i5}+\phi_{i6})-(\phi_{i1}+\phi_{i4})-6\phi_{i7}-2\phi_{\eta i}+4\phi_{\xi i}-3\phi_{\zeta^2 i})\eta$ $+ \frac{1}{2}(5(\phi_{i2}+\phi_{i5})-(\phi_{i1}+\phi_{i3}+\phi_{i4}+\phi_{i6})-6\phi_{i7}+2\phi_{\xi i}+4\phi_{\eta i}-3\phi_{\zeta^2 i})\xi$ $+ \frac{1}{2}(\phi_{i2}-\phi_{i3}-\phi_{i5}+\phi_{i6})\zeta+\frac{3}{2}(\phi_{i1}+\phi_{i2}+\phi_{i3}-\phi_{i4}-\phi_{i5}-\phi_{i6}+6\phi_{\zeta i})\xi\zeta$ $\Phi_{i\zeta}(\xi_i,\eta_i,\zeta_i) = \frac{1}{2}(\phi_{i2}-\phi_{i3}-\phi_{i5}+\phi_{i6})\eta+\frac{1}{2}(-\phi_{i1}+\phi_{i2}+\phi_{i4}-\phi_{i5})\xi+\frac{1}{2}\phi_{i5}-\frac{1}{2}\phi_{i2}+\zeta\phi_{\zeta^2 i}$ $+ \frac{3}{2}(\phi_{i1}+\phi_{i2}+\phi_{i3}-\phi_{i4}-\phi_{i5}-\phi_{i6}+6\phi_{\zeta i})\xi\eta$
Pyramidal element	$\Phi_{i\xi}(\xi_i,\eta_i,\zeta_i) = 2(\frac{1}{4}(\phi_{i1}+\phi_{i2}+\phi_{i3}+\phi_{i4})-\frac{1}{9}\phi_{i5}-\frac{8}{9}\phi_{i6}+\frac{2}{3}\phi_{\zeta i}-\frac{1}{2}(\phi_{\xi^2 i}+\phi_{\eta^2 i}))\xi\eta^2+\phi_{\xi i}+\xi\phi_{\xi^2 i}$ $+ \frac{1}{4}(-\phi_{i1}-\phi_{i2}+\phi_{i3}+\phi_{i4}-4\phi_{\eta i})\xi\eta+\frac{1}{4}(-\phi_{i1}+\phi_{i2}+\phi_{i3}-\phi_{i4}-4\phi_{\xi i})\eta^2+\frac{1}{4}(-\phi_{i1}+\phi_{i2}-\phi_{i3}+\phi_{i4})\eta\zeta$ $\Phi_{i\eta}(\xi_i,\eta_i,\zeta_i) = 2(\frac{1}{4}(\phi_{i1}+\phi_{i2}+\phi_{i3}+\phi_{i4})-\frac{1}{9}\phi_{i5}-\frac{8}{9}\phi_{i6}+\frac{2}{3}\phi_{\zeta i}-\frac{1}{2}(\phi_{\xi^2 i}+\phi_{\eta^2 i}))\xi^2\eta+\phi_{\eta i}+\eta\phi_{\eta^2 i}$ $+ \frac{1}{4}(-\phi_{i1}-\phi_{i2}+\phi_{i3}+\phi_{i4}-4\phi_{\eta i})\xi^2+\frac{1}{4}(-\phi_{i1}+\phi_{i2}+\phi_{i3}-\phi_{i4}-4\phi_{\xi i})\xi\eta+\frac{1}{4}(-\phi_{i1}+\phi_{i2}-\phi_{i3}+\phi_{i4})\xi\zeta$ $\Phi_{i\zeta}(\xi_i,\eta_i,\zeta_i) = \frac{2}{9}(2\phi_{i5}-2\phi_{i6}-3\phi_{\zeta i})\zeta+\frac{1}{4}(-\phi_{i1}+\phi_{i2}-\phi_{i3}+\phi_{i4})\xi\eta+\frac{2}{9}(2\phi_{i5}-2\phi_{i6}+3\phi_{\zeta i})$

Table 2.20: First order derivatives of MCV scheme at random position in local cell (ξ_i, η_i, ζ_i) for each unstructured elements.

Element Type	Integral average quantity
Triangular element	$\overline{\phi}_{\Gamma_{i1}} = \frac{1}{9}\phi_{i1} + \frac{1}{9}\phi_{i2} + \frac{1}{9}\phi_{i3} + \frac{2}{3}\overline{\phi}_i + \frac{1}{6}\phi_{\xi i} - \frac{1}{3}\phi_{\eta i}$, $\overline{\phi}_{\Gamma_{i2}} = \frac{1}{9}\phi_{i1} + \frac{1}{9}\phi_{i2} + \frac{1}{9}\phi_{i3} + \frac{2}{3}\overline{\phi}_i - \frac{1}{3}\phi_{\xi i} + \frac{1}{6}\phi_{\eta i}$, $\overline{\phi}_{\Gamma_{i3}} = \frac{1}{9}\phi_{i2} + \frac{1}{9}\phi_{i1} + \frac{1}{9}\phi_{i3} + \frac{2}{3}\overline{\phi}_i + \frac{1}{6}\phi_{\xi i} + \frac{1}{6}\phi_{\eta i}$.
Quadrilateral element	$\overline{\phi}_{\Gamma_{i1}} = \frac{7}{48}\phi_{i1} - \frac{1}{48}\phi_{i2} - \frac{1}{48}\phi_{i3} + \frac{7}{48}\phi_{i4} + \frac{3}{4}\overline{\phi}_i - \frac{2}{3}\phi_{\xi i} + \frac{1}{4}\phi_{\xi^2 i} - \frac{1}{12}\phi_{\eta^2 i}$ $\overline{\phi}_{\Gamma_{i2}} = \frac{7}{48}\phi_{i2} - \frac{1}{48}\phi_{i1} - \frac{1}{48}\phi_{i4} + \frac{7}{48}\phi_{i3} + \frac{3}{4}\overline{\phi}_i + \frac{2}{3}\phi_{\xi i} + \frac{1}{4}\phi_{\xi^2 i} - \frac{1}{12}\phi_{\eta^2 i}$ $\overline{\phi}_{\Gamma_{i3}} = \frac{7}{48}\phi_{i1} - \frac{1}{48}\phi_{i3} - \frac{1}{48}\phi_{i4} + \frac{7}{48}\phi_{i2} + \frac{3}{4}\overline{\phi}_i - \frac{2}{3}\phi_{\eta i} + \frac{1}{4}\phi_{\eta^2 i} - \frac{1}{12}\phi_{\xi^2 i}$ $\overline{\phi}_{\Gamma_{i4}} = \frac{7}{48}\phi_{i3} - \frac{1}{48}\phi_{i1} - \frac{1}{48}\phi_{i2} + \frac{7}{48}\phi_{i4} + \frac{3}{4}\overline{\phi}_i + \frac{2}{3}\phi_{\eta i} + \frac{1}{4}\phi_{\eta^2 i} - \frac{1}{12}\phi_{\xi^2 i}$
Tetrahedral element	$\overline{\phi}_{\Gamma_{i1}} = \frac{1}{24}(\phi_{i1} + \phi_{i2} + \phi_{i3} + \phi_{i4}) + \frac{5}{6}\overline{\phi}_i + \frac{1}{12}\phi_{\xi i} + \frac{1}{12}\phi_{\eta i} - \frac{1}{4}\phi_{\zeta i}$ $\overline{\phi}_{\Gamma_{i2}} = \frac{1}{24}(\phi_{i1} + \phi_{i2} + \phi_{i3} + \phi_{i4}) + \frac{5}{6}\overline{\phi}_i + \frac{1}{12}\phi_{\xi i} + \frac{1}{12}\phi_{\zeta i} - \frac{1}{4}\phi_{\eta i}$ $\overline{\phi}_{\Gamma_{i3}} = \frac{1}{24}(\phi_{i1} + \phi_{i2} + \phi_{i3} + \phi_{i4}) + \frac{5}{6}\overline{\phi}_i + \frac{1}{12}\phi_{\eta i} + \frac{1}{12}\phi_{\zeta i} - \frac{1}{4}\phi_{\xi i}$ $\overline{\phi}_{\Gamma_{i4}} = \frac{1}{24}(\phi_{i1} + \phi_{i2} + \phi_{i3} + \phi_{i4}) + \frac{5}{6}\overline{\phi}_i + \frac{1}{12}\phi_{\xi i} + \frac{1}{12}\phi_{\eta i} + \frac{1}{12}\phi_{\zeta i}$
Hexahedral element	$\overline{\phi}_{\Gamma_{i1}} = \frac{1}{156}(8(\phi_{i1} + \phi_{i4} + \phi_{i5} + \phi_{i8}) - 5(\phi_{i2} + \phi_{i3} + \phi_{i6} + \phi_{i7})) + \frac{12}{13}\overline{\phi}_i - \frac{2}{3}\phi_{\xi i} + \frac{1}{39}(12\phi_{\xi^2 i} - \phi_{\eta^2 i} - \phi_{\zeta^2 i})$ $\overline{\phi}_{\Gamma_{i2}} = \frac{1}{156}(8(\phi_{i2} + \phi_{i3} + \phi_{i6} + \phi_{i7}) - 5(\phi_{i1} + \phi_{i4} + \phi_{i5} + \phi_{i8})) + \frac{12}{13}\overline{\phi}_i + \frac{2}{3}\phi_{\xi i} + \frac{1}{39}(12\phi_{\xi^2 i} - \phi_{\eta^2 i} - \phi_{\zeta^2 i})$ $\overline{\phi}_{\Gamma_{i3}} = \frac{1}{156}(8(\phi_{i1} + \phi_{i2} + \phi_{i5} + \phi_{i6}) - 5(\phi_{i3} + \phi_{i4} + \phi_{i7} + \phi_{i8})) + \frac{12}{13}\overline{\phi}_i - \frac{2}{3}\phi_{\eta i} + \frac{1}{39}(12\phi_{\eta^2 i} - \phi_{\xi^2 i} - \phi_{\zeta^2 i})$ $\overline{\phi}_{\Gamma_{i4}} = \frac{1}{156}(8(\phi_{i3} + \phi_{i4} + \phi_{i7} + \phi_{i8}) - 5(\phi_{i1} + \phi_{i2} + \phi_{i5} + \phi_{i6})) + \frac{12}{13}\overline{\phi}_i + \frac{2}{3}\phi_{\eta i} + \frac{1}{39}(12\phi_{\eta^2 i} - \phi_{\xi^2 i} - \phi_{\zeta^2 i})$ $\overline{\phi}_{\Gamma_{i5}} = \frac{1}{156}(8(\phi_{i1} + \phi_{i2} + \phi_{i3} + \phi_{i4}) - 5(\phi_{i5} + \phi_{i6} + \phi_{i7} + \phi_{i8})) + \frac{12}{13}\overline{\phi}_i - \frac{2}{3}\phi_{\zeta i} + \frac{1}{39}(12\phi_{\zeta^2 i} - \phi_{\xi^2 i} - \phi_{\eta^2 i})$ $\overline{\phi}_{\Gamma_{i6}} = \frac{1}{156}(8(\phi_{i5} + \phi_{i6} + \phi_{i7} + \phi_{i8}) - 5(\phi_{i1} + \phi_{i2} + \phi_{i3} + \phi_{i4})) + \frac{12}{13}\overline{\phi}_i + \frac{2}{3}\phi_{\zeta i} + \frac{1}{39}(12\phi_{\zeta^2 i} - \phi_{\xi^2 i} - \phi_{\eta^2 i})$
Prismatic element	$\overline{\phi}_{\Gamma_{i1}} = \frac{1}{24}((\phi_{i1} + \phi_{i2} + \phi_{i3}) - (\phi_{i4} + \phi_{i5} + \phi_{i6})) + \overline{\phi}_i - \frac{3}{4}\phi_{\zeta i} + \frac{1}{3}\phi_{\zeta^2 i}$ $\overline{\phi}_{\Gamma_{i2}} = \frac{1}{24}((\phi_{i4} + \phi_{i5} + \phi_{i6}) - (\phi_{i1} + \phi_{i2} + \phi_{i3})) + \overline{\phi}_i + \frac{3}{4}\phi_{\zeta i} + \frac{1}{3}\phi_{\zeta^2 i}$ $\overline{\phi}_{\Gamma_{i3}} = \frac{1}{18}(\phi_{i1} + \phi_{i2} + \phi_{i3} + \phi_{i4} + \phi_{i5} + \phi_{i6}) + \frac{2}{3}\overline{\phi}_i + \frac{1}{6}\phi_{\xi i} + \frac{1}{6}\phi_{\eta i} - \frac{1}{9}\phi_{\zeta^2 i}$ $\overline{\phi}_{\Gamma_{i4}} = \frac{1}{18}(\phi_{i1} + \phi_{i2} + \phi_{i3} + \phi_{i4} + \phi_{i5} + \phi_{i6}) + \frac{2}{3}\overline{\phi}_i - \frac{1}{3}\phi_{\xi i} + \frac{1}{6}\phi_{\eta i} - \frac{1}{9}\phi_{\zeta^2 i}$ $\overline{\phi}_{\Gamma_{i5}} = \frac{1}{18}(\phi_{i1} + \phi_{i2} + \phi_{i3} + \phi_{i4} + \phi_{i5} + \phi_{i6}) + \frac{2}{3}\overline{\phi}_i + \frac{1}{6}\phi_{\xi i} - \frac{1}{3}\phi_{\eta i} - \frac{1}{9}\phi_{\zeta^2 i}$
Pyramidal element	$\overline{\phi}_{\Gamma_{i1}} = \frac{1}{1684}(29(\phi_{i1} + \phi_{i2} + \phi_{i3} + \phi_{i4}) - 56\phi_{i5}) + \frac{1120}{1263}\overline{\phi}_i - \frac{224}{421}\phi_{\zeta i} + \frac{55}{1263}\phi_{\xi^2 i} + \frac{55}{1263}\phi_{\eta^2 i}$ $\overline{\phi}_{\Gamma_{i2}} = \frac{1}{25260}(1277(\phi_{i1} + \phi_{i4}) - 407(\phi_{i2} + \phi_{i3}) + 1120\phi_{i5}) + \frac{1120}{1263}\overline{\phi}_i - \frac{8}{15}\phi_{\xi i} + \frac{170}{1263}\phi_{\zeta i} + \frac{641}{5052}\phi_{\xi^2 i} - \frac{67}{1684}\phi_{\eta^2 i}$ $\overline{\phi}_{\Gamma_{i3}} = \frac{1}{25260}(1277(\phi_{i1} + \phi_{i2}) - 407(\phi_{i3} + \phi_{i4}) + 1120\phi_{i5}) + \frac{1120}{1263}\overline{\phi}_i - \frac{8}{15}\phi_{\eta i} + \frac{170}{1263}\phi_{\zeta i} + \frac{641}{5052}\phi_{\eta^2 i} - \frac{67}{1684}\phi_{\xi^2 i}$ $\overline{\phi}_{\Gamma_{i4}} = \frac{1}{25260}(1277(\phi_{i2} + \phi_{i3}) - 407(\phi_{i1} + \phi_{i4}) + 1120\phi_{i5}) + \frac{1120}{1263}\overline{\phi}_i + \frac{8}{15}\phi_{\xi i} + \frac{170}{1263}\phi_{\zeta i} + \frac{641}{5052}\phi_{\xi^2 i} - \frac{67}{1684}\phi_{\eta^2 i}$ $\overline{\phi}_{\Gamma_{i5}} = \frac{1}{25260}(1277(\phi_{i3} + \phi_{i4}) - 407(\phi_{i1} + \phi_{i2}) + 1120\phi_{i5}) + \frac{1120}{1263}\overline{\phi}_i + \frac{8}{15}\phi_{\eta i} + \frac{170}{1263}\phi_{\zeta i} + \frac{641}{5052}\phi_{\eta^2 i} - \frac{67}{1684}\phi_{\xi^2 i}$

Table 2.21: The integral average quantities for VPM scheme on different unstructured element shapes.

Element Type	Integral average quantity
Triangular element	$\overline{\phi}_{\Gamma_{i1}} = \frac{1}{6}\phi_{i1} + \frac{1}{6}\phi_{i2} + \frac{1}{6}\phi_{i3} + \frac{1}{2}\phi_{i4} + \frac{1}{6}\phi_{\xi i} - \frac{1}{3}\phi_{\eta i},$ $\overline{\phi}_{\Gamma_{i2}} = \frac{1}{6}\phi_{i1} + \frac{1}{6}\phi_{i2} + \frac{1}{6}\phi_{i3} + \frac{1}{2}\phi_{i4} - \frac{1}{3}\phi_{\xi i} + \frac{1}{6}\phi_{\eta i},$ $\overline{\phi}_{\Gamma_{i3}} = \frac{1}{6}\phi_{i1} + \frac{1}{6}\phi_{i2} + \frac{1}{6}\phi_{i3} + \frac{1}{2}\phi_{i4} + \frac{1}{6}\phi_{\xi i} + \frac{1}{6}\phi_{\eta i}.$
Quadrilateral element	$\overline{\phi}_{\Gamma_{i1}} = \frac{1}{6}\phi_{i1} + \frac{1}{6}\phi_{i4} + \frac{2}{3}\phi_{i5} - \frac{2}{3}\phi_{\xi i} + \frac{1}{3}\phi_{\xi^2 i}$ $\overline{\phi}_{\Gamma_{i2}} = \frac{1}{6}\phi_{i2} + \frac{1}{6}\phi_{i3} + \frac{2}{3}\phi_{i5} + \frac{2}{3}\phi_{\xi i} + \frac{1}{3}\phi_{\xi^2 i}$ $\overline{\phi}_{\Gamma_{i3}} = \frac{1}{6}\phi_{i1} + \frac{1}{6}\phi_{i2} + \frac{2}{3}\phi_{i5} - \frac{2}{3}\phi_{\eta i} + \frac{1}{3}\phi_{\eta^2 i}$ $\overline{\phi}_{\Gamma_{i4}} = \frac{1}{6}\phi_{i3} + \frac{1}{6}\phi_{i4} + \frac{2}{3}\phi_{i5} + \frac{2}{3}\phi_{\eta i} + \frac{1}{e}\phi_{\eta^2 i}$
Tetrahedral element	$\overline{\phi}_{\Gamma_{i1}} = \frac{1}{12}\left(\phi_{i1} + \phi_{i2} + \phi_{i3} + \phi_{i4}\right) + \frac{2}{3}\phi_{i5} + \frac{1}{12}\phi_{\xi i} + \frac{1}{12}\phi_{\eta i} - \frac{1}{4}\phi_{\zeta i}$ $\overline{\phi}_{\Gamma_{i2}} = \frac{1}{12}\left(\phi_{i1} + \phi_{i2} + \phi_{i3} + \phi_{i4}\right) + \frac{2}{3}\phi_{i5} + \frac{1}{12}\phi_{\xi i} + \frac{1}{12}\phi_{\zeta i} - \frac{1}{4}\phi_{\eta i}$ $\overline{\phi}_{\Gamma_{i3}} = \frac{1}{12}\left(\phi_{i1} + \phi_{i2} + \phi_{i3} + \phi_{i4}\right) + \frac{2}{3}\phi_{i5} + \frac{1}{12}\phi_{\eta i} + \frac{1}{12}\phi_{\zeta i} - \frac{1}{4}\phi_{\xi i}$ $\overline{\phi}_{\Gamma_{i4}} = \frac{1}{12}\left(\phi_{i1} + \phi_{i2} + \phi_{i3} + \phi_{i4}\right) + \frac{2}{3}\phi_{i5} + \frac{1}{12}\phi_{\xi i} + \frac{1}{24}\phi_{\eta i} + \frac{1}{12}\phi_{\zeta i}$
Hexahedral element	$\overline{\phi}_{\Gamma_{i1}} = \frac{1}{36}\left(2\left(\phi_{i1} + \phi_{i4} + \phi_{i5} + \phi_{i8}\right) - \left(\phi_{i2} + \phi_{i3} + \phi_{i6} + \phi_{i7}\right)\right) + \frac{8}{9}\phi_{i9} - \frac{2}{3}\phi_{\xi i} + \frac{1}{9}\left(4\phi_{\xi^2 i} - \phi_{\eta^2 i} - \phi_{\zeta^2 i}\right)$ $\overline{\phi}_{\Gamma_{i2}} = \frac{1}{36}\left(2\left(\phi_{i2} + \phi_{i3} + \phi_{i6} + \phi_{i7}\right) - \left(\phi_{i1} + \phi_{i4} + \phi_{i5} + \phi_{i8}\right)\right) + \frac{8}{9}\phi_{i9} + \frac{2}{3}\phi_{\xi i} + \frac{1}{9}\left(4\phi_{\xi^2 i} - \phi_{\eta^2 i} - \phi_{\zeta^2 i}\right)$ $\overline{\phi}_{\Gamma_{i3}} = \frac{1}{36}\left(2\left(\phi_{i1} + \phi_{i2} + \phi_{i5} + \phi_{i6}\right) - \left(\phi_{i3} + \phi_{i4} + \phi_{i7} + \phi_{i8}\right)\right) + \frac{8}{9}\phi_{i9} - \frac{2}{3}\phi_{\eta i} + \frac{1}{9}\left(4\phi_{\eta^2 i} - \phi_{\xi^2 i} - \phi_{\zeta^2 i}\right)$ $\overline{\phi}_{\Gamma_{i4}} = \frac{1}{36}\left(2\left(\phi_{i3} + \phi_{i4} + \phi_{i7} + \phi_{i8}\right) - \left(\phi_{i1} + \phi_{i2} + \phi_{i5} + \phi_{i6}\right)\right) + \frac{8}{9}\phi_{i9} + \frac{2}{3}\phi_{\eta i} + \frac{1}{9}\left(4\phi_{\eta^2 i} - \phi_{\xi^2 i} - \phi_{\zeta^2 i}\right)$ $\overline{\phi}_{\Gamma_{i5}} = \frac{1}{36}\left(2\left(\phi_{i1} + \phi_{i2} + \phi_{i3} + \phi_{i4}\right) - \left(\phi_{i5} + \phi_{i6} + \phi_{i7} + \phi_{i8}\right)\right) + \frac{8}{9}\phi_{i9} - \frac{2}{3}\phi_{\zeta i} + \frac{1}{9}\left(4\phi_{\zeta^2 i} - \phi_{\xi^2 i} - \phi_{\eta^2 i}\right)$ $\overline{\phi}_{\Gamma_{i6}} = \frac{1}{36}\left(2\left(\phi_{i5} + \phi_{i6} + \phi_{i7} + \phi_{i8}\right) - \left(\phi_{i1} + \phi_{i2} + \phi_{i3} + \phi_{i4}\right)\right) + \frac{8}{9}\phi_{i9} + \frac{2}{3}\phi_{\zeta i} + \frac{1}{9}\left(4\phi_{\zeta^2 i} - \phi_{\xi^2 i} - \phi_{\eta^2 i}\right)$
Prismatic element	$\overline{\phi}_{\Gamma_{i1}} = \frac{1}{12}\left(\phi_{i1} + \phi_{i2} + \phi_{i3}\right) + \frac{3}{4}\phi_{i7} - \frac{3}{4}\phi_{\zeta i} + \frac{3}{8}\phi_{\zeta^2 i}$ $\overline{\phi}_{\Gamma_{i2}} = \frac{1}{12}\left(\phi_{i4} + \phi_{i5} + \phi_{i6}\right) + \frac{3}{4}\phi_{i7} + \frac{3}{4}\phi_{\zeta i} + \frac{3}{8}\phi_{\zeta^2 i}$ $\overline{\phi}_{\Gamma_{i3}} = \frac{1}{12}\left(\phi_{i1} + \phi_{i2} + \phi_{i3} + \phi_{i4} + \phi_{i5} + \phi_{i6}\right) + \frac{1}{2}\phi_{i7} + \frac{1}{6}\phi_{\xi i} + \frac{1}{6}\phi_{\eta i} - \frac{1}{12}\phi_{\zeta^2 i}$ $\overline{\phi}_{\Gamma_{i4}} = \frac{1}{12}\left(\phi_{i1} + \phi_{i2} + \phi_{i3} + \phi_{i4} + \phi_{i5} + \phi_{i6}\right) + \frac{1}{2}\phi_{i7} - \frac{1}{3}\phi_{\xi i} + \frac{1}{6}\phi_{\eta i} - \frac{1}{12}\phi_{\zeta^2 i}$ $\overline{\phi}_{\Gamma_{i5}} = \frac{1}{12}\left(\phi_{i1} + \phi_{i2} + \phi_{i3} + \phi_{i4} + \phi_{i5} + \phi_{i6}\right) + \frac{1}{2}\phi_{i7} + \frac{1}{6}\phi_{\xi i} - \frac{1}{3}\phi_{\eta i} - \frac{1}{12}\phi_{\zeta^2 i}$
Pyramidal element	$\overline{\phi}_{\Gamma_{i1}} = \frac{1}{36}\left(\phi_{i1} + \phi_{i2} + \phi_{i3} + \phi_{i4}\right) + \frac{8}{81}\phi_{i5} + \frac{64}{81}\phi_{i6} - \frac{16}{27}\phi_{\zeta i} + \frac{1}{9}\phi_{\xi^2 i} + \frac{1}{9}\phi_{\eta^2 i}$ $\overline{\phi}_{\Gamma_{i2}} = \frac{1}{180}\left(11\left(\phi_{i1} + \phi_{i4}\right) - \left(\phi_{i2} + \phi_{i3}\right)\right) + \frac{8}{81}\phi_{i5} + \frac{64}{81}\phi_{i6} - \frac{8}{15}\phi_{\xi i} + \frac{2}{27}\phi_{\zeta i} + \frac{7}{36}\phi_{\xi^2 i} + \frac{1}{36}\phi_{\eta^2 i}$ $\overline{\phi}_{\Gamma_{i3}} = \frac{1}{180}\left(11\left(\phi_{i1} + \phi_{i2}\right) - \left(\phi_{i3} + \phi_{i4}\right)\right) + \frac{8}{81}\phi_{i5} + \frac{64}{81}\phi_{i6} - \frac{8}{15}\phi_{\eta i} + \frac{2}{27}\phi_{\zeta i} + \frac{7}{36}\phi_{\eta^2 i} + \frac{1}{36}\phi_{\xi^2 i}$ $\overline{\phi}_{\Gamma_{i4}} = \frac{1}{180}\left(11\left(\phi_{i2} + \phi_{i3}\right) - \left(\phi_{i1} + \phi_{i4}\right)\right) + \frac{8}{81}\phi_{i5} + \frac{64}{81}\phi_{i6} + \frac{8}{15}\phi_{\xi i} + \frac{2}{27}\phi_{\zeta i} + \frac{7}{36}\phi_{\xi^2 i} + \frac{1}{36}\phi_{\eta^2 i}$ $\overline{\phi}_{\Gamma_{i5}} = \frac{1}{180}\left(11\left(\phi_{i3} + \phi_{i4}\right) - \left(\phi_{i1} + \phi_{i2}\right)\right) + \frac{8}{81}\phi_{i5} + \frac{64}{81}\phi_{i6} + \frac{8}{15}\phi_{\eta i} + \frac{2}{27}\phi_{\zeta i} + \frac{7}{36}\phi_{\eta^2 i} + \frac{1}{36}\phi_{\xi^2 i}$

Table 2.22: The integral average quantities for MCV scheme on different unstructured element shapes.

2.5.3 First order derivatives on cell surface

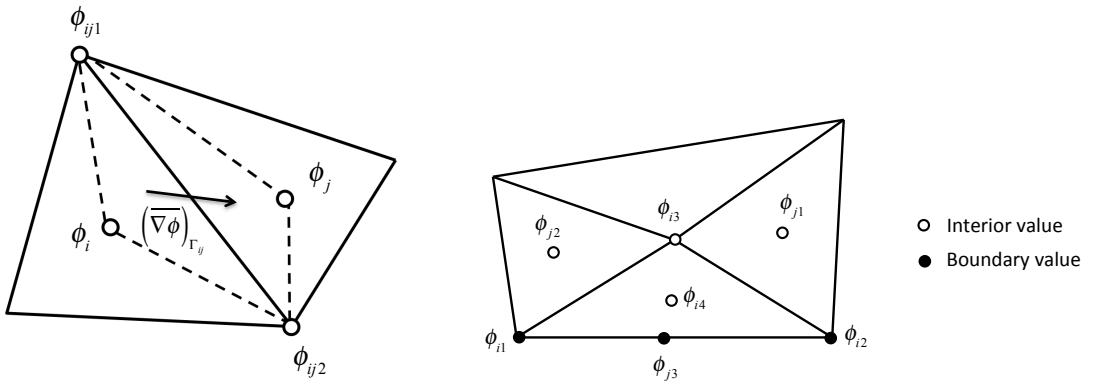


Figure 2.5: The moment for gradient reconstruction across two face adjacent cells (left) and reconstruction stencils for boundary cell(right).

For finite volume method on unstructured grids, how to accurately reconstruct the first order derivatives over boundary edge is not trivial task, especially when associates with heavily distorted elements. The traditional FVM approaches which use two neighbour VIAs adjacent to boundary edge are proven to be grossly inaccurate and considerably depend on mesh quality. In this study, we propose a monotonous, compact and robust reconstruction method by making full use of four topologically adjacent points $\phi_i, \phi_j, \phi_{ij1}, \phi_{ij2}$ closely surrounding the face Γ_{ij}. It's noted that ϕ_i, ϕ_j are PV at center of cell Ω_i and Ω_j which are not straightforward in VPM scheme thus approximated by the formulations as shown in Table 2.10. Although higher order reconstruction can also be made by employing extended stencil as mentioned in [73], for reconciling accuracy and complexity, the second order, linear piecewise reconstruction is adopted hereafter in the form of

$$\Psi(x, y) = a + bx + cy + O\left(\triangle h^2\right). \tag{2.41}$$

With simple substitution of both coordinate and corresponding PVs into (2.41), this linear equation system is then expressed in the matrix form as:

$$\begin{bmatrix} 1 & x_i & y_i \\ 1 & x_j & y_j \\ 1 & x_{ij1} & y_{ij1} \\ 1 & x_{ij2} & y_{ij2} \end{bmatrix} \begin{bmatrix} a \\ b \\ c \end{bmatrix} = \begin{bmatrix} \phi_i \\ \phi_j \\ \phi_{ij1} \\ \phi_{ij2} \end{bmatrix}.$$

We represent this equation by $\mathbf{M} \cdot \mathbf{A} = \mathbf{B}$ and unknown coefficients a, b, c of (2.41) can be determined by the least square method[144, 81] for minimizing $|\mathbf{B} - \mathbf{M} \cdot \mathbf{A}|^2$. The solution is yielded as $\mathbf{A} = \left(\mathbf{M}^T\mathbf{M}\right)^{-1}\mathbf{M}^T\mathbf{B}$, where $\left(\mathbf{M}^T\mathbf{M}\right)^{-1}\mathbf{M}^T$ can be regarded as shape function and directly computed by the singular value decomposition(SVD) method

with storage for reuse. If we express $\left(\mathbf{M}^T\mathbf{M}\right)^{-1}\mathbf{M}^T$ as 4×4 square matrix with each entry m_{ij} located at i row j column,

$$\left(\mathbf{M}^T\mathbf{M}\right)^{-1}\mathbf{M}^T = \begin{bmatrix} m_{11} & m_{12} & m_{13} & m_{14} \\ m_{21} & m_{22} & m_{23} & m_{24} \\ m_{31} & m_{32} & m_{33} & m_{34} \end{bmatrix},$$

then the gradient integral average on face Γ_{ij} can be computed by:

$$\left(\overline{\nabla\phi}\right)_{\Gamma_{ij}} = \frac{1}{|\Gamma_{ij}|}\int_{\Gamma_{ij}}\left(\frac{\partial\Psi(x,y)}{\partial x},\frac{\partial\Psi(x,y)}{\partial y}\right)d\Gamma = \left(\frac{\partial\phi}{\partial x},\frac{\partial\phi}{\partial y}\right)_{\Gamma_{ij}}, \tag{2.42}$$

where

$$\begin{aligned}\left(\frac{\partial\phi}{\partial x}\right)_{\Gamma_{ij}} &= m_{21}\phi_i + m_{22}\phi_j + m_{23}\phi_{ij1} + m_{24}\phi_{ij2},\\ \left(\frac{\partial\phi}{\partial y}\right)_{\Gamma_{ij}} &= m_{31}\phi_i + m_{32}\phi_j + m_{33}\phi_{ij1} + m_{34}\phi_{ij2}.\end{aligned}$$

The reconstruction function involving domain boundary can also be accurately enforced for Dirichlet, Neumann, Dirichlet-Neumann boundary condition by constraining the least square reconstruction. The enforcement is actually implemented by explicitly specifying the give values or gradients at cell boundary in the reconstruction function.

- Boundary Constraints for Dirichlet Boundary Conditions:

$$\phi = a + bx + cy + O\left(\triangle h^2\right)$$

- Boundary Constraints for Neumann Boundary Conditions:

$$\nabla\phi = n_x b + n_y c + O\left(\triangle h^2\right)$$

For example, a Dirichlet-Neumann boundary condition is shown as in Fig. 2.5(right), ϕ_{i2} and ϕ_{i3} are specified with Dirichlet boundary condition, (ϕ_{xi1},ϕ_{yji1}) are set as Neumann boundary condition and ϕ_{j4} is the computed interior value. Then linear reconstruction function is constructed in term of matrix form as follows:

$$\begin{bmatrix} 1 & x_{i4} & y_{i4} \\ 0 & n_{xij} & 0 \\ 0 & 0 & n_{yij} \\ 1 & x_{i2} & y_{i2} \\ 1 & x_{i3} & y_{i3} \end{bmatrix}\begin{bmatrix} a \\ b \\ c \end{bmatrix} = \begin{bmatrix} \phi_{i4} \\ \phi_{xi1} \\ \phi_{yi1} \\ \phi_{i2} \\ \phi_{i3} \end{bmatrix}.$$

The gradients (ϕ_{xij},ϕ_{yij}) for boundary edge then are formulated in the same manner as

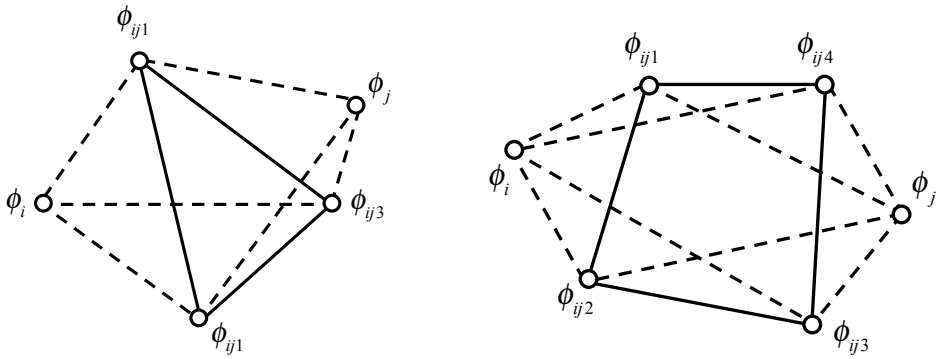


Figure 2.6: The moment for gradient reconstruction across two face adjacent cells of 3D arbitrary unstructured elements.

$$\left(\overline{\nabla\phi}\right)_{\Gamma_{ij}} = \left(\frac{\partial\phi}{\partial x}, \frac{\partial\phi}{\partial y}\right)_{\Gamma_{ij}} \tag{2.43}$$

where

$$\begin{aligned}
\left(\frac{\partial\phi}{\partial x}\right)_{\Gamma_{ij}} &= m_{21}\phi_{xi1} + m_{22}\phi_{yi1} + m_{23}\phi_{i2} + m_{24}\phi_{i3} + m_{25}\phi_{i4}, \\
\left(\frac{\partial\phi}{\partial y}\right)_{\Gamma_{ij}} &= m_{31}\phi_{xi1} + m_{32}\phi_{yi1} + m_{33}\phi_{i2} + m_{34}\phi_{i3} + m_{35}\phi_{i4}.
\end{aligned}$$

The more accurate boundary condition specified for curvilinear cell boundary can be prescribed by adding more DOFs at boundary edges and making reconstruction with higher order polynomials in the same procedure. For more detail, please refer to [45, 73].

In spite of numerous possibility of mixed-type elements, the moments for reconstruction of gradient at boundary surface are only associated with two situations, i.e. triangular face based reconstruction and quadrilateral face based reconstruction as shown in Fig. 2.6. The linear piecewise polynomial is constructed in the same form as

$$\Psi(x, y) = a + bx + cy + dz + O\left(\triangle h^2\right)$$

and corresponding linear equation systems are written as

$$\begin{bmatrix} 1 & x_i & y_i & z_i \\ 1 & x_j & y_j & z_j \\ 1 & x_{ij1} & y_{ij1} & z_{ij1} \\ \vdots & \vdots & \vdots & \vdots \\ 1 & x_{ijN} & y_{ijN} & z_{ijN} \end{bmatrix} \begin{bmatrix} a \\ b \\ c \\ d \end{bmatrix} = \begin{bmatrix} \phi_i \\ \phi_j \\ \phi_{ij1} \\ \vdots \\ \phi_{ijN} \end{bmatrix}$$

which can also be represented in matrix form as $\mathbf{M} \cdot \mathbf{A} = \mathbf{B}$. The N denotes total number of points on each surface. By the least-square approach, the unknown coefficients can be computed by $\mathbf{A} = \left(\mathbf{M}^T\mathbf{M}\right)^{-1}\mathbf{M}^T\mathbf{B}$ as in the same manner as described before.

2.6 Summary of chapter 2

Using multi-moments and multi-moment constraints on unstructured grids, volume integrated average and point value based multi-moment (VPM) method and multi-moment constrained finite volume (MCV) method based discretisation technique has been proposed. For VPM method, in addition to VIA which is the only computational variable of conventional FVM, PVs at cell vertices are defined as new DOFs in each grid cell. Using both VIA and PVs, higher order reconstruction function can be constructed within compact stencils which only associate with direct neighbouring cells adjacent to boundary surface. This reconstruction procedure can be equivalently expressed in the form of MCV method which approximates the VIA using PVs at both cell vertices and center. Despite of differences of formulation for each element type, the reconstruction function can be expressed in unified form of (2.7) and (2.25).

As the reconstruction function for each grid element is piecewisely constructed, first derivatives of reconstruction function and integrated average value at cell boundary are deduced straightforwardly. The first derivatives over cell boundary are also derived by making full use of DOFs adjacent to the surface and all the unknowns of linear reconstruction function can be determined by least-square method. Unlike k-exact least-square FVM method which utilizes wider reconstruction stencils for higher accuracy, present VPM/MCV scheme only involves DOFs adjacent to cell boundary and coefficients of reconstruction function can be computed beforehand on uniform local element. Different from local spectral high order scheme in representation of DG, SV and SD scheme, the PVs at cell vertices are continuous variables which share moments with surrounding elements. From multi-moment reconstruction procedure, we can recognize that both VPM and MCV possess advantage of accuracy and robustness against conventional FVM only with moderate increase in complexity and computational cost.

Chapter 3

Numerical models for Navier-stokes equations using VPM and MCV

3.1 Governing equation in conservation form

We consider the unsteady Navier-Stokes equations in conservation form denoted in [175] as the governing equations of Mach uniform solution

$$\frac{\partial \rho}{\partial t} + \nabla \cdot \mathbf{m} = 0, \tag{3.1}$$

$$\frac{\partial \mathbf{m}}{\partial t} + \nabla \cdot (\mathbf{m} \otimes \mathbf{u}) = -\nabla p + \nabla \cdot \tau, \tag{3.2}$$

$$\frac{\partial E}{\partial t} + \nabla \cdot (\mathbf{u}E) = -\nabla (p\mathbf{u}) + \nabla \cdot (\tau \otimes \mathbf{u}), \tag{3.3}$$

where ρ is density, $\mathbf{u} = (u_x, u_y, u_z) = (u, v, w)$ the velocity vector, $\mathbf{m} = (m_x, m_y, m_z) = (\rho u, \rho v, \rho w)$ the momentum vector, p the pressure and E the total energy. Considering perfect gas, the pressure can be obtained from the equation of state $p = (E - \rho \mathbf{u} \cdot \mathbf{u}/2)(\gamma - 1)$ where γ stands for ratio of specific heats. Under the assumption of Newtonian fluid, the components of viscous stress tensor τ are defined in the form like

$$\tau_{\alpha\beta} = \mu \left[\left(\frac{\partial u_\alpha}{\partial \beta} + \frac{\partial u_\beta}{\partial \alpha} \right) - \frac{2}{3} (\nabla \cdot \mathbf{u}) \hat{\delta} \right] \quad \alpha, \beta \in (x, y, z) \tag{3.4}$$

where μ is dynamic viscosity and $\hat{\delta}$ is Kronecker delta. For different research interests, some further assumptions are made for simplification.

In some applications where the viscosity is not much significant, we can ignore viscous term thus equations (3.1),(3.2),(3.3) become inviscid version of Navier-Stokes equaiton,

i.e. Euler equation. Euler equation is hyperbolic type of partial differential equation and many schemes have been developed as Riemann solvers to approximate hyperbolic flux in the past. Thus, the key to achieve the intended pressure based Mach uniform solver lies in the design of inviscid flux and velocity-pressure coupling solution. Hence, the governing equations for inviscid compressible flow turn out to be

$$\frac{\partial \rho}{\partial t} + \nabla \cdot \mathbf{m} = 0, \tag{3.5}$$

$$\frac{\partial \mathbf{m}}{\partial t} + \nabla \cdot (\mathbf{m} \otimes \mathbf{u}) = -\nabla p, \tag{3.6}$$

$$\frac{\partial E}{\partial t} + \nabla \cdot (\mathbf{u}E) = -\nabla (p\mathbf{u}), \tag{3.7}$$

On the other hand, for the low Mach number fluid $Ma \ll 1$, density variation is small enough that density can be treated as a constant variable, i.e. $\rho \cong$ const. . As the energy equation (3.3) is no longer required for enclosed numerical model, the governing equations for incompressible fluid dynamics are simplified as

$$\nabla \cdot \mathbf{u} = 0, \tag{3.8}$$

$$\frac{\partial \mathbf{u}}{\partial t} + \nabla \cdot (\mathbf{u} \otimes \mathbf{u}) = -\frac{1}{\rho}\nabla p + \nu \nabla^2 \mathbf{u}, \tag{3.9}$$

where ν the kinematic viscosity. The projection solution is carried out to solve (3.5), (3.6), (3.7) and (3.8), (3.9), which will be given in following section.

3.2 Mach uniform solution procedure based on projection method

In order to solve (3.5), (3.6), (3.7), as mentioned in [172, 175, 91], the flux term is separated into an advection part $F_1(\mathbf{u})$ and a non-advection part $F_2(\mathbf{u})$,

$$F_1(\mathbf{u}) = \begin{pmatrix} \mathbf{m} \\ \mathbf{m} \otimes \mathbf{u} \\ \mathbf{u}E \end{pmatrix} \quad F_2(\mathbf{u}) = \begin{pmatrix} 0 \\ p \\ \mathbf{u}p \end{pmatrix}$$

and the solution procedure is carried out based on projection method of Chorin [19] as follows.

1. Given the initial field ρ^n, $\mathbf{m}^n$ and E^n at time n as well as dependent variable $\mathbf{u^n} = \mathbf{m^n}/\rho^n$. The intermediate variables $\mathbf{m}^*$, E^* and density field at next time step ρ^{n+1}

are computed by using advection flux $F_1(\mathbf{u})$.

$$\begin{aligned}\frac{\partial \rho}{\partial t} &= -\nabla \cdot \mathbf{m}^n, \\ \frac{\partial \mathbf{m}}{\partial t} &= -\nabla \cdot \left(\mathbf{m}^n \otimes \mathbf{u}^n\right), \\ \frac{\partial E}{\partial t} &= -\nabla \cdot \left(\mathbf{u^n} E^n\right).\end{aligned} \tag{3.10}$$

2. The intermediate variables $\mathbf{m}^*$ and E^* must be projected to obey the equation of state and law of thermodynamics thus the pressure Poisson equation is formulated [91]

$$\left[1 + \rho^n \left(c^2\right)^n \triangle t^2 \nabla \left(\frac{1}{\rho^{n+1}} \nabla\right)\right] p^{n+1} = p^{\diamondsuit} + \rho^n \left(c^2\right)^n \triangle t \nabla \mathbf{u}^* \tag{3.11}$$

where $\mathbf{u}^* = \mathbf{m}^* / \rho^{n+1}$, $p^{\diamondsuit} = \left(E^* - \frac{1}{2}\rho^{n+1}\left(\mathbf{u}^*\right)^2\right)(\gamma - 1)$, and $c = \sqrt{\gamma p^{\diamondsuit} / \rho^{n+1}}$.

3. Correct the $\mathbf{m}^*$ and E^* by $F_2(\mathbf{u})$ with resulting pressure p^{n+1} at the projection step,

$$\frac{\mathbf{m}^{n+1} - \mathbf{m}^*}{\Delta t} = -\nabla p^{n+1}, \tag{3.12}$$

$$\frac{E^{n+1} - E^*}{\Delta t} = -\nabla \left(\mathbf{m}^{n+1} p^{n+1} / \rho^{n+1}\right). \tag{3.13}$$

Although the above method is also able to resolve incompressible flow, straightforward governing equations (3.8), (3.9) are adopted in this study. For brevity, we summarize the solution steps to update the velocity from time level n ($t = t^n$) to $n+1$ ($t = t^n + \Delta t$) as follows.

1. Given the velocity field $\mathbf{u}^n$ at step n, compute the intermediate velocity $\mathbf{u}^*$ from the momentum equation (3.9) without the pressure gradient term,

$$\frac{\partial \mathbf{u}}{\partial t} = -\nabla \cdot \left(\mathbf{u}^n \otimes \mathbf{u}^n\right) + \nu \nabla^2 \mathbf{u}^n. \tag{3.14}$$

2. The intermediate velocity $\mathbf{u}^*$ usually does not satisfy the continuity equation (3.8), and must be corrected by the projection procedure as shown in the next step. For this purpose, we solve the pressure field at step $n+1$ from the following Poisson equation,

$$\nabla \cdot \left(\frac{1}{\rho} \nabla p^{n+1}\right) = \frac{1}{\Delta t} \nabla \cdot \mathbf{u}^*. \tag{3.15}$$

3. Correct the velocity by the projection step,

$$\frac{\mathbf{u}^{n+1} - \mathbf{u}^*}{\Delta t} = -\frac{1}{\rho} \nabla p^{n+1}. \tag{3.16}$$

After the correction step stage, updated velocity $\mathbf{u}^{n+1}$ is enforced to satisfy continuity equation of $\nabla \cdot \mathbf{u}^{n+1} = 0$. Our major interest in this paper is to develop corresponding spatial discretization for the solution procedure as shown in next section.

3.3 Time integration method

The semi-discrete equations (3.10) and (3.14) are used to advance in sequential time steps. We summarize these equations into a form of ordinary differential equation,

$$\frac{d\phi}{dt} = \mathcal{L}(\phi) \tag{3.17}$$

where $\mathcal{L}(\phi)$ stands for the spatial approximations discussed afterwards. During one time step from t^n to t^{n+1}, two major classes of schemes are chosen to attain high accuracy.

The first kinds are multi-stage methods, best known for Runge-Kutta method which require a sequence of evaluation function in form of

$$\tfrac{d\phi}{dt} = \mathcal{L}(\phi^n, \phi^{n+\alpha_1}, \cdots, \phi^{n+\alpha_n}) \quad \alpha_1, \cdots, \alpha_n \in (0,1) \ .$$

Although arbitrary order can be achieved, due to its expensive computational cost, only second and third order Runge-Kutta schemes are used in this study. For instance, the third order TVD Runge-Kutta time integration method [140] is given as follows.

$$\begin{aligned}
\phi^{(1)} &= \phi^n + \Delta t \mathcal{L}(\phi^n) \\
\phi^{(2)} &= \frac{3}{4}\phi^n + \frac{1}{4}\phi^{(1)} + \frac{1}{4}\Delta t \mathcal{L}(\phi^{(1)}) \\
\phi^{*} &= \frac{1}{3}\phi^n + \frac{2}{3}\phi^{(2)} + \frac{2}{3}\Delta t \mathcal{L}(\phi^{(2)}),
\end{aligned} \tag{3.18}$$

where $\Delta t = t^{n+1} - t^n$ is the time integration interval. As the Runge-Kutta method only associates with quantities at previous time step ϕ^n as initial value, it shows superiority in stability and reliability particularly for compressible flow which usually involves solution discontinuities. For this matter, inviscid compressible numerical model in form of equations (3.5), (3.6), (3.7) are solved by Runge-Kutta scheme for time integration.

1. Given the initial density, momentum and total energy field ρ^n, $\mathbf{m}^n$,E^n at step n, we can compute provisional velocity field $\mathbf{u}^n = \mathbf{m}^n / \rho^n$, proceed for ρ^{n+1} and intermediate variables $\mathbf{m}^*$, E^* from the advection equation (3.10),

$$\mathcal{L}_\rho(\rho^n) = -\nabla \cdot (\rho^n \mathbf{u}^n), \tag{3.19}$$

$$\mathcal{L}_{\mathbf{m}}(\mathbf{m}^n) = -\nabla \cdot (\mathbf{m}^n \otimes \mathbf{u}^n), \tag{3.20}$$

$$\mathcal{L}_E(E^n) = -\nabla \cdot (\mathbf{u}^{\mathbf{n}} E^n). \tag{3.21}$$

$$\frac{\rho^{n+1}-\rho^n}{\triangle t} = \mathcal{L}_\rho(\rho^n, \rho^{(1)}, \rho^{(2)}), \tag{3.22}$$

$$\frac{\mathbf{m}^*-\mathbf{m}^n}{\triangle t} = \mathcal{L}_\mathbf{m}(\mathbf{m}^n, \mathbf{m}^{(1)}, \mathbf{m}^{(2)}), \tag{3.23}$$

$$\frac{E^*-E^n}{\triangle t} = \mathcal{L}_E(E^n, E^{(1)}, E^{(2)}). \tag{3.24}$$

2. Originated from momentum projection with relations of state equation and the first law of thermodynamics, the resulted ρ^{n+1}, $\mathbf{m}^*$, E^* can be used to formulate Poisson equation,

$$\left[1+\rho^n\left(c^2\right)^n \triangle t^2\nabla\left(\frac{1}{\rho^{n+1}}\nabla\right)\right]p^{n+1} = p^\diamondsuit + \rho^n\left(c^2\right)^n\triangle t\nabla\mathbf{u}^*. \tag{3.25}$$

3. Correct by pressure projection step, we can obtain final fields of momentum$\mathbf{m}^{n+1}$ and total energyE^{n+1} at time $n+1$.

$$\frac{\mathbf{m}^{n+1}-\mathbf{m}^*}{\Delta t} = -\nabla p^{n+1}, \tag{3.26}$$

$$\frac{E^{n+1}-E^*}{\Delta t} = -\nabla\left(\mathbf{m}^{n+1}p^{n+1}/\rho^{n+1}\right). \tag{3.27}$$

Alternative choice for time integration is the kind of multi-step methods which use available quantities from previous time steps

$$\tfrac{d\phi}{dt} = \mathcal{L}\left(\phi^n, \phi^{n-1}, \cdots, \phi^{n-k}\right) \quad k \in (0,n)\ .$$

Since multi-step methods can preserve high accuracy in a more efficient procedure, it is preferable for resolving incompressible Navier-Stokes equations. Referring to [154, 31], we use back-difference formula(BDF) to solve (3.8) and (3.9) by projection method as following.

1. Given the velocity field $\mathbf{u}^n$ at step n, compute the intermediate velocity $\mathbf{u}^*$ from the advection equation in (3.9),

$$\frac{\alpha_\mathbf{1}\mathbf{u}^* - \alpha_\mathbf{0}\mathbf{u^n} + \alpha_{-1}\mathbf{u}^{n-1}}{\triangle t} = -\nabla\cdot(\mathbf{u}^n\otimes\mathbf{u}^n). \tag{3.28}$$

2. Compute intermediate velocity $\mathbf{u}^{**}$ by solving the diffusion equation accounting for viscous term in (3.9) without the pressure gradient term,

$$\frac{\alpha_\mathbf{1}\left(\mathbf{u}^{**}-\mathbf{u}^*\right)}{\triangle t} = \nu\nabla^2\mathbf{u}^n. \tag{3.29}$$

3. The intermediate velocity $\mathbf{u}^{**}$ usually does not satisfy the mass conservation equation

(3.8), and must be corrected by the projection step. For this matter, we solve the pressure field at step $n+1$ from the following Poisson equation,

$$\nabla \cdot \left(\frac{1}{\rho} \nabla p^{n+1} \right) = \frac{\alpha_1}{\Delta t} \nabla \cdot \mathbf{u}^{**}. \tag{3.30}$$

4. Correct the velocity by the projection step,

$$\frac{\mathbf{u}^{n+1} - \mathbf{u}^{**}}{\Delta t} = -\frac{1}{\rho \alpha_1} \nabla p^{n+1}. \tag{3.31}$$

For first-order time accurate scheme(BDF1): $\alpha_1 = 1$, $\alpha_0 = -1$, $\alpha_{-1} = 0$ and for second-order time accurate scheme(BDF2)[154, 31] with variable step-size: $\alpha_1 = \frac{1+2\tau_n}{1+\tau_n}$, $\alpha_0 = -(1+\tau_n)$, $\alpha_{-1} = \frac{\tau_n^2}{1+\tau}$ where $\tau_n = \triangle t_n \, / \triangle t_{n-1}$. In this case, we use BDF1 for first-time step and BDF2 afterwards because BDF2 can not be self-starting. It is straightforward to show that the updated velocity satisfies $\nabla \cdot \mathbf{u}^{n+1} = 0$.

As our major interest of this study, spatial discretization will be described in detail subsequently. For simplicity, we illustrate the solution procedure by triangular element and extension for other type discrete elements can be carried out based on the same manner.

3.4 Time Evolution converting formulation

Given the time variation in VIA moments, the time variation in PV moments can be easily obtained via the Time-evolution converting (TEC) formula, which are in fact the spatial interpolation of time variation of a physical variable [172, 175]. The compatibility of TEC formula applicable for differential operator can be proved by using Gauss's theorem which converts volume integral into integral of surface average value over cell boundary,

$$\int_{\Omega_i} \nabla \star \phi \, d\Omega_i = \int_{\Gamma_{ij}} |\Gamma_{ij}| \, d\mathbf{n} \star \phi = \sum |\Gamma_{ij}| \, \mathbf{n}_{ij} \star \phi_{ij}$$

where star notation represents tensor product, i.e. inter, outer and cross. In order to illustrate TEC formula for PV ϕ_{ik} at vertex θ_{ik}, the surrounding VIAs $\overline{\phi}_l$ located at cell unions Ω_l sharing vertex θ_{ik} are provided as shown in Fig. 3.1 where l stands for ikl and $l = 1, 2, \cdots, L$. The faces bounding cell Ω_l are denoted as Γ_{lj}, $j = 1, 2, \cdots, J$ and outer boundary surfaces around union cells $\Lambda_{ik} = \cup \Omega_l$ are represented by $\Upsilon_{ik} = \cup \Gamma_l$, $l = 1, 2, \cdots, L$ as marked with red solid line in Fig. 3.1. There are various formulas for TEC scheme, we choose the simplest formulation as

$$\delta_t \phi_{ik} = \mathcal{TEC}(\delta_t \overline{\phi}_l) = \sum_{l=1}^{l=L} |\Omega_l| \, \delta_t \overline{\phi}_l \Big/ \sum |\Omega_l| \, .$$

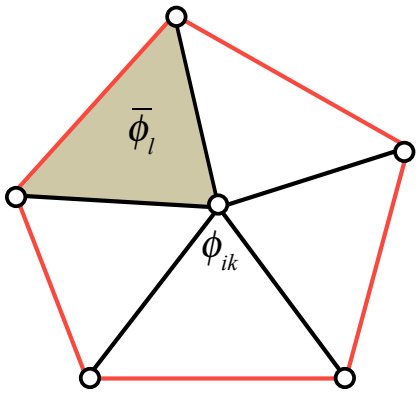


Figure 3.1: TEC formulation for mapping VIA to PV.

From Gauss's theorem, the TEC formulation for increment of PV $\delta_t\phi_{ik}$ evaluated by the time variation of VIA $\delta_t\overline{\phi}_i$ can be simplified as

$$\begin{aligned}\delta_t\phi_{ik} &= \sum \int_{\Omega_l} \nabla \star \phi \, d\Omega_l \, / \sum |\Omega_l| \\ &= \sum |\Upsilon_{ik}| \, \mathbf{n}_{ik} \star \phi_{ik} \, / \sum |\Omega_l| \, , \\ &= \tfrac{1}{|\Lambda_{ik}|} \int_{\Lambda} \nabla \star \phi \, d\Lambda_{ik}\end{aligned}$$

where $|\Lambda_{ik}|$ represents for area of union cells. As you can see, TEC formula converts the differential operator at vertex θ_{ik} to volume average moment of union cells Λ which is bounded to be second order accuracy.

For the purpose of higher accuracy, we make use of the least square minimization [154] technique described below. Provided the time variation of VIA $\delta_t\overline{\phi}_l$ where (x_l, y_l) is the centroid of cell l, the increment of not only PV at θ_{ik}, $\delta_t\phi_{ik}$, but also derivative values (DVs) $\delta_t\phi_{xik}$ and $\delta_t\phi_{yik}$ can be obtained from Appendix 1.

$$\begin{bmatrix} L & \sum_L x_l & \sum_L y_l \\ \sum_L x_l & \sum_L x_l^2 & \sum_L x_l y_l \\ \sum_L y_l & \sum_L x_l y_l & \sum_L y_l^2 \end{bmatrix} \begin{bmatrix} \delta_t\phi_{ik} \\ \delta_t\phi_{xik} \\ \delta_t\phi_{yik} \end{bmatrix} = \begin{bmatrix} \sum_L \delta_t\overline{\phi}_l \\ \sum_L \delta_t\overline{\phi}_l x_l \\ \sum_L \delta_t\overline{\phi}_l y_l \end{bmatrix} \tag{3.32}$$

The TEC formula is in fact an interpolation for an operator rather than a physical variable. It applies to any "forcing" term in the equations, thus it largely simplifies the computations. The TEC formula also allows the VPM model to easily make use of the existing modules in the finite volume framework. We denote a TEC formula that computes $\delta_t\phi_{ik}$ from $\delta_t\overline{\phi}_l$ by

$$\delta_t\phi_{ik} = \mathcal{TEC}(\delta_t\overline{\phi}_l). \tag{3.33}$$

For more details, please refer to Appendix 1.

3.5 Spatial discretization of advection term

The advection equation in 2D is written in conservative form as

$$\frac{\partial \phi}{\partial t} = -\nabla \cdot (\phi \mathbf{u}), \tag{3.34}$$

where ϕ is the physical quantity, which stands for either u or v in 2D Navies-Stokes equations. By default, all terms on the right hand side are known at each time level, we omit the superscript n hereafter unless it is needed. Both the PV of the physical field ϕ at cell vertices and VIA in VPM scheme or equivalent cell-central PV in MCV scheme, are treated as the prognostic variables and updated separately. The PV moments at cell vertices are updated by point-wise Riemann solver while flux form of finite volume method is computed to preserve exact conservativeness for VIA or cell-central PV moment. The advection equations for both VPM and MCV are summarized as following

$$\text{PV at cell vertices}: \quad \frac{d\phi_{ik}}{dt} = -\mathbf{u}_{ik} \cdot (\nabla \phi)_{ik},\ k = 1, 2, 3 \tag{3.35}$$

$$\text{VIA in VPM}: \quad \frac{d\overline{\phi}_i}{dt} = -\frac{1}{|\Omega_i|} \oint_{\Gamma_i} (\phi \mathbf{u} \cdot \mathbf{n})\, d\Gamma \tag{3.36}$$

$$\text{centeral PV in MCV}: \quad \frac{d\phi_{i4}}{dt} = \frac{4}{3}\left(-\frac{1}{|\Omega_i|} \oint_{\Gamma_i} (\phi \mathbf{u} \cdot \mathbf{n})\, d\Gamma\right) - \frac{1}{9}\left(\frac{d\phi_{i1}}{dt} + \frac{d\phi_{i2}}{dt} + \frac{d\phi_{i3}}{dt}\right) \tag{3.37}$$

Next, we describe the spatial discretization for the terms on the right hand sides of (3.37) and (3.35).

3.5.1 The piecewise reconstruction polynomial

We use piecewise reconstruction polynomial on triangular element for both VPM and MCV defined in the local coordinate system as:

$$\Phi_i(\xi, \eta) = c_{00} + c_{10}\xi + c_{01}\eta + c_{11}\xi\eta + c_{20}\xi^2 + c_{02}\eta^2. \tag{3.38}$$

With given DOFs in each cell, the unknown coefficients of reconstruction function (3.38) can be uniquely determined in single grid cell as shown in Section 2.3. Different from prognostic variables like VIA or PVs, DVs at the cell center, $\phi_{\xi i}$ and $\phi_{\eta i}$, are intermediate variables which play the critical role in determining numerical flux at cell boundary.

In order to accurately evaluate the gradient (ϕ_{xi}, ϕ_{yi}) at cell center, we make full use of DOFs based on Taylor approximation:

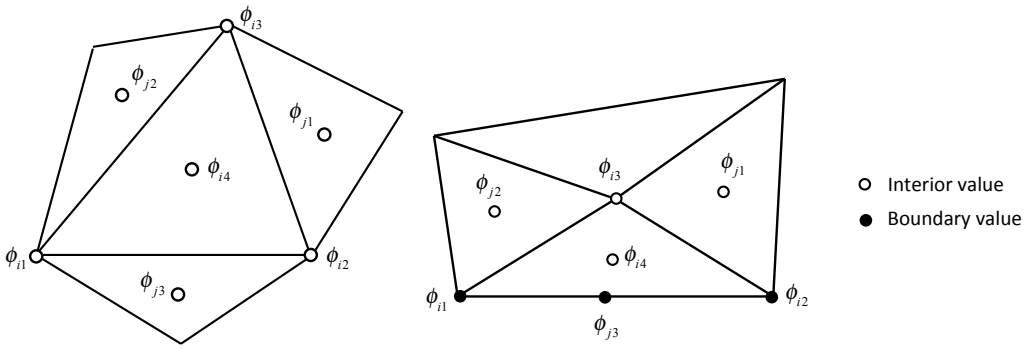


Figure 3.2: Reconstruction stencil for gradient approximation

$$\phi = \phi_0 + \left(\triangle x \frac{\partial \phi}{\partial x} + \triangle y \frac{\partial \phi}{\partial y} \right) + \frac{1}{2!} \left(\triangle x \frac{\partial \phi}{\partial x} + \triangle y \frac{\partial \phi}{\partial y} \right)^2 + O\left(\triangle h^3 \right) \tag{3.39}$$

where $\triangle x = x - x_{i4}$, $\triangle y = y - y_{i4}$. As demonstrated in Section 2.3, the PV at cell center is straightforward in MCV while needs to be reconstructed in VPM. Then, we use seven moments including three moment at the centroid of extended stencil cells to make over-determined equation system as:

$$\begin{bmatrix} \triangle x_{i1} & \triangle y_{i1} & \triangle x_{i1}^2 & \triangle x_{i1}\triangle y_{i1} & \triangle y_{i1}^2 \\ \triangle x_{i2} & \triangle y_{i2} & \triangle x_{i2}^2 & \triangle x_{i2}\triangle y_{i2} & \triangle y_{i2}^2 \\ \triangle x_{i3} & \triangle y_{i3} & \triangle x_{i3}^2 & \triangle x_{i3}\triangle y_{i3} & \triangle y_{i3}^2 \\ \triangle x_{j1} & \triangle y_{j1} & \triangle x_{j1}^2 & \triangle x_{j1}\triangle y_{j1} & \triangle y_{j1}^2 \\ \triangle x_{j2} & \triangle y_{j2} & \triangle x_{j2}^2 & \triangle x_{j2}\triangle y_{j2} & \triangle y_{j2}^2 \\ \triangle x_{j3} & \triangle y_{j3} & \triangle x_{j3}^2 & \triangle x_{j3}\triangle y_{j3} & \triangle y_{j3}^2 \end{bmatrix} \begin{bmatrix} \frac{\partial \phi}{\partial x} \\ \frac{\partial \phi}{\partial y} \\ \frac{1}{2}\frac{\partial^2 \phi}{\partial x^2} \\ \frac{\partial^2 \phi}{\partial x \partial y} \\ \frac{1}{2}\frac{\partial^2 \phi}{\partial y^2} \end{bmatrix} = \begin{bmatrix} \phi_{i1} - \phi_{i4} \\ \phi_{i2} - \phi_{i4} \\ \phi_{i3} - \phi_{i4} \\ \phi_{j1} - \phi_{i4} \\ \phi_{j2} - \phi_{i4} \\ \phi_{j3} - \phi_{i4} \end{bmatrix} \tag{3.40}$$

The (ϕ_{xi}, ϕ_{yi}) can be computed directly by solving $\mathbf{A} = \left(\mathbf{M}^T\mathbf{M}\right)^{-1}\mathbf{M}^T\mathbf{B}$ with SVD approach which permits the computation of a pseudo-inverse matrix and can be stored for reuse during the whole simulation. However, this method requires complicated matrix calculations and large amount of memory resources. Moreover, this computational cost will even further increase for three dimensional reconstruction polynomial. Although it is affordable for current modern computational architecture, in this paper, more practical and memory-saving methods are proposed and used instead. Among the remarkable possibilities for computing $(\phi_{\xi i}, \phi_{\eta i})$, two kind of formulations are chosen due to the success in preserving of accuracy and efficiency in practice. The first kind approach is to treat the derivatives at surface center as average of discontinuous moments from two straddling reconstruction stencils by the formulations denoted in the Section 2.5.1. The other approach is to view the surface derivatives as continuous, monotonic quantities and

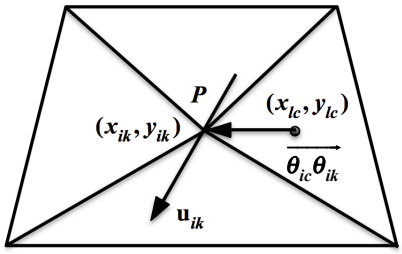


Figure 3.3: Point gradient operator in the advection term.

computed through the least square approximation as Section 2.5.3. After surface derivatives $\phi_{\vec{x}ij} = (\phi_{xij}, \phi_{yij})$ are determined on global coordinate, the derivatives at cell center (ϕ_{xi}, ϕ_{yi}) are computed by arithmetic average formula in term of $\frac{1}{J}\sum\left(\phi_{x_{ij}}, \phi_{y_{ij}}\right)$ and then $(\phi_{\xi i}, \phi_{\eta i})$ in local cell is obtained by global-to-local mapping denoted in Section 2.2. Hereafter, we refer approaches for evaluation of (ϕ_{xi}, ϕ_{yi}) by (3.39) and above two as "DIA-A", "DIA-B" and "DIA-C" respectively.

3.5.2 The advection flux in (3.37)

The advection flux for cell Ω_i is approximated by the summation of those across each boundary segment,

$$\oint_{\Gamma_{ij}} (\phi \mathbf{u} \cdot \mathbf{n})\, d\Gamma = \sum_{j=1}^{3} \left(|\Gamma_{ij}| \overline{\phi \mathbf{u}}_{\Gamma_{ij}} \cdot \mathbf{n}_{ij} \right) \approx \sum_{j=1}^{3} \left(|\Gamma_{ij}| \overline{\phi}_{\Gamma_{ij}} \overline{\mathbf{u}}_{\Gamma_{ij}} \cdot \mathbf{n}_{ij} \right), \tag{3.41}$$

where $|\Gamma_{ij}|$ represents the length of edge Γ_{ij}, $\overline{\phi}_{\Gamma_{ij}}$ the line-integrated average value of ϕ along Γ_{ij}, and $\overline{\mathbf{u}}_{\Gamma_{ij}} = (\overline{u}_{\Gamma_{ij}}, \overline{v}_{\Gamma_{ij}})$ the corrected divergence-free velocity over edge Γ_{ij}.

The line-integrated average $\overline{\phi}_{\Gamma_{ij}}$ is discontinuous across boundary edge and thus computed by piecewise reconstruction polynomial in upwind side cell.

$$\begin{cases} \overline{\phi}_{\Gamma_{i1}} = \int_0^1 \Phi_{iup}(\xi, 0) d\xi = \frac{1}{6}\phi_{i1} + \frac{1}{6}\phi_{i2} + \frac{1}{6}\phi_{i3} + \frac{1}{2}\phi_{i4} + \frac{1}{6}\phi_{\xi i} - \frac{1}{3}\phi_{\eta i}, \\ \overline{\phi}_{\Gamma_{i2}} = \int_0^1 \Phi_{iup}(0, \eta) d\eta = \frac{1}{6}\phi_{i1} + \frac{1}{6}\phi_{i2} + \frac{1}{6}\phi_{i3} + \frac{1}{2}\phi_{i4} - \frac{1}{3}\phi_{\xi i} + \frac{1}{6}\phi_{\eta i}, \\ \overline{\phi}_{\Gamma_{i3}} = \int_0^1 \Phi_{iup}(\xi, 1-\xi) d\xi = \frac{1}{6}\phi_{i2} + \frac{1}{6}\phi_{i1} + \frac{1}{6}\phi_{i3} + \frac{1}{2}\phi_{i4} + \frac{1}{6}\phi_{\xi i} + \frac{1}{6}\phi_{\eta i}. \end{cases} \tag{3.42}$$

where Φ_{iup} denotes the reconstruction function (3.38) over the unwinding cell, i.e.

$$iup = \begin{cases} = i, \text{ for } \mathbf{n}_{ij} \cdot \overline{\mathbf{u}}_{\Gamma_{ij}} > 0; \\ = ij, \text{ otherwise.} \end{cases} \tag{3.43}$$

3.5.3 The gradient operator in the advection term in (3.35)

The PV moment at the vertices (θ_{ik}) of the triangular mesh element Ω_i, ϕ_{ik} ($k = 1, 2, 3$) as shown in Fig. 3.3, is predicted from the differential form equation (3.35) where the gradients of the advection terms are computed from a weighted upwinding scheme,

$$\left(\frac{\partial \phi}{\partial x}\right)_{ik} = \sum_{l=1}^{L} \omega_l \Phi_{xl}\left(\theta_{ik}\right)$$

for derivative with respect to x and

$$\left(\frac{\partial \phi}{\partial y}\right)_{ik} = \sum_{l=1}^{L} \omega_l \Phi_{yl}\left(\theta_{ik}\right)$$

for derivative with respect to y where subscript $l\,(l = 1, 2 \ldots L)$ stands for union of cells Ω_{ikl} sharing vertex θ_{ik} . The weights ω_l is computed by

$$\omega_l = \frac{\max\left(0, \mathbf{u}_{ik} \cdot \overrightarrow{\theta_{lc}\theta_{ik}}\right)}{\sum_{l=1}^{L} \max\left(0, \mathbf{u}_{ik} \cdot \overrightarrow{\theta_{lc}\theta_{ik}}\right)} \tag{3.44}$$

where $\overrightarrow{\theta_{lc}\theta_{lk}}$ denotes the vector from the center of cell Ω_{ikl} to vertex θ_{ik}. It is clear from (3.44) that the gradient computed in the upwinding cell is used, which is effectively a point-wise Riemann solution.

3.6 Slope limiting projection

As well known, any convection schemes higher than first-order will generate numerical oscillation. Harten [52] introduced the notation of Total Variation Diminishing (TVD) which can create a difference schemes higher than first-order accuracy but without spurious oscillation. Afterwards, Sweby[52] further characterized this flux limiting procedure in a form of combination of selected higher-order differencing scheme ϕ^{HD} with first-order upwind differencing scheme ϕ^{UD} which is switched by a flux limiter function $\Psi\left(r\right)$ where r is indicator function chose to identify the smoothness. In this study, we select VPM/MCV method as high order scheme, thus the integrated average value on cell boundary Γ_{ij} with flux limiting procedure turned to be:

$$\phi_{ij} = \phi_{ij}^{\mathrm{UD}} + \Psi(r)\left(\phi_{ij}^{\mathrm{VPM/MCV}} - \phi_{ij}^{\mathrm{UD}}\right) \tag{3.45}$$

According to [26], the indicator function r for an arbitrary unstructured grid is formulated as $r = \frac{(2\nabla\phi_i \cdot (x_i - x_j, y_i - y_j))}{\phi_i - \phi_j} - 1$ where $\nabla\phi_i$ is gradient of upwind side cell and ϕ_i, ϕ_j are point values at two neighbour cell center adjacent to surface ij. $\nabla\phi_i$ is computed by

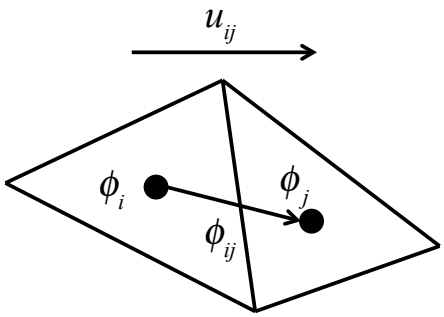


Figure 3.4: Schematic diagram of indicator function.

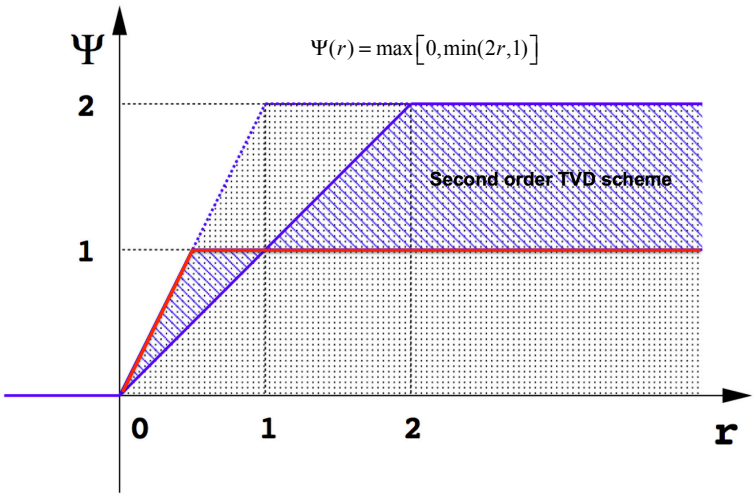


Figure 3.5: TVD monotonicity region of present limiter on Sweby‘s diagram.

the least square method as described in (3.39). The notation of indicator function r is plotted as a schematic diagram as Fig. 3.4.

Following Sweby [147], TVD limiters are characterized as monotonicity region on a $\Psi(r)$ diagram. As Sweby [147] pointed out, any flux limiter function, $\Psi(r)$, formulated to lie within the TVD monotonicity region (denoted as shadow region in Fig. 3.5) yields a TVD limiter. Besides, the flux limiter function formulated within the hatched region of Fig. 3.5 can guarantee second order accuracy. In the study, following Sweby's research and success in practice, we choose flux limiter function as $\Psi(r) = \max[0, \min(2r, 1)]$ which is plotted as red line in Fig. 3.5. With flux limiter function determined, the integrated average value $\overline{\phi}_{ij}$ on cell boundary Γ_{ij} can be reconstructed straightforwardly in the form of (3.45).

3.7 Spatial discretization of diffusion term

The diffusion equation in 2D can be write as

$$\frac{\partial \phi}{\partial t} = \nu \nabla^2 \phi, \tag{3.46}$$

In the same manner of advection scheme, the PVs at cell vertex ϕ_{ik} $(k = 1, 2, 3)$ are solved by finite difference approach while VIA in VPM or cell-central PV in MCV is updated by the conservative flux form.

$$\text{PV at cell vertices}: \quad \frac{d\phi_{ik}}{dt} = \nu(\nabla^2\phi)_{ik},\ k = 1, 2, 3 \tag{3.47}$$

$$\text{VIA in VPM}: \quad \frac{d\overline{\phi}_i}{dt} = \frac{\nu}{|\Omega_i|} \oint_{\Gamma_i} (\mathbf{n} \cdot \nabla\phi)\, d\Gamma \tag{3.48}$$

$$\text{centeral PV in MCV}: \quad \frac{d\phi_{i4}}{dt} = \frac{4}{3}\left(\frac{\nu}{|\Omega_i|} \oint_{\Gamma_i} (\mathbf{n} \cdot \nabla\phi)\, d\Gamma\right) - \frac{1}{9}\left(\frac{d\phi_{i1}}{dt} + \frac{d\phi_{i2}}{dt} + \frac{d\phi_{i3}}{dt}\right) \tag{3.49}$$

The total diffusion flux for cell Ω_i is approximated by the summation of the first-order derivative across each boundary edge.

$$\oint_{\Gamma_i} (\mathbf{n} \cdot \nabla\phi)\, d\Gamma = \sum_{j=1}^{3} \left(|\Gamma_{ij}| \left(\overline{\phi}_{x\Gamma_{ij}} n_{xij} + \overline{\phi}_{y\Gamma_{ij}} n_{yij}\right)\right), \tag{3.50}$$

where $\overline{\phi}_{x\Gamma_{ij}}$ and $\overline{\phi}_{y\Gamma_{ij}}$ represent the line-integrated average values of ϕ_x and ϕ_y along boundary edge Γ_{ij} computed from reconstruction function Ψ_{ij} in Section 2.5.3. According to reconstruction function computed from time level n or $n + 1$, the diffusion equation can be solved by explicit or implicit formulation.

3.7.1 The explicit scheme for diffusion equation

For many problems, the maximum time step size ensuring stable solutions of diffusion equation is much larger than that of stability restriction. For this matter, explicit scheme is preferred for efficiency. The $\left(\overline{\phi}_{x\Gamma_{ij}}, \overline{\phi}_{y\Gamma_{ij}}\right)$ required for diffusion flux in (3.50) are directly computed by (2.42) from given value, while the PVs at cell vertex can be explicitly computed by approximating $(\nabla^2\phi)_{ik}$ based on least-square approach.

As shown in Fig. 3.6, we denote $\Omega_{ikl}(l = 1, 2, \cdots, L)$ as the collection of points on both cell vertices and cell centers that connect with vertex (θ_{ik}) . It should be note that the PV moments at cell centers ϕ_{ikl} are not straightforward in VPM thus approximated

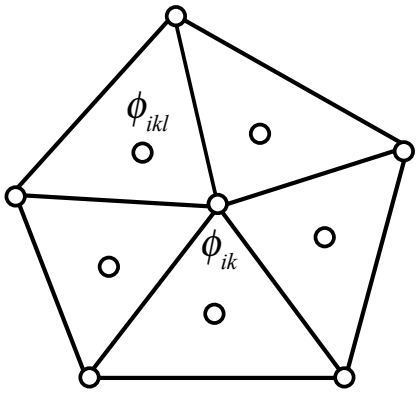


Figure 3.6: Point Laplace operator in the diffusion term.

by VIA as denoted in Table 2.10. The point-wise value of the diffusion term at θ_{ik} can be obtained by Taylor approximation as:

$$\phi = \phi_0 + \left(\triangle x \frac{\partial \phi}{\partial x} + \triangle y \frac{\partial \phi}{\partial y} \right) + \frac{1}{2!} \left(\triangle x \frac{\partial \phi}{\partial x} + \triangle y \frac{\partial \phi}{\partial y} \right)^2 + O\left(\triangle h^3 \right)$$

$$\begin{bmatrix} \triangle x_{ik1} & \triangle y_{ik1} & \triangle x_{ik1}^2 & \triangle x_{ik1} \triangle y_{ik1} & \triangle y_{ik1}^2 \\ \triangle x_{ik2} & \triangle y_{ik2} & \triangle x_{ik2}^2 & \triangle x_{ik2} \triangle y_{ik2} & \triangle y_{ik2}^2 \\ \triangle x_{ik3} & \triangle y_{ik3} & \triangle x_{ik3}^2 & \triangle x_{ik3} \triangle y_{ik3} & \triangle y_{ik3}^2 \\ \triangle x_{ik4} & \triangle y_{ik4} & \triangle x_{ik4}^2 & \triangle x_{ik4} \triangle y_{ik4} & \triangle y_{ik4}^2 \\ \vdots & \vdots & \vdots & \vdots & \vdots \\ \triangle x_{ikL} & \triangle y_{ikL} & \triangle x_{ikL}^2 & \triangle x_{ikL} \triangle y_{ikL} & \triangle y_{ikL}^2 \end{bmatrix} \begin{bmatrix} \frac{\partial \phi}{\partial x} \\ \frac{\partial \phi}{\partial y} \\ \frac{1}{2} \frac{\partial^2 \phi}{\partial x^2} \\ \frac{\partial^2 \phi}{\partial x \partial y} \\ \frac{1}{2} \frac{\partial^2 \phi}{\partial y^2} \end{bmatrix} = \begin{bmatrix} \phi_{ik1} - \phi_{ik} \\ \phi_{ik2} - \phi_{ik} \\ \phi_{ik3} - \phi_{ik} \\ \phi_{ik4} - \phi_{ik} \\ \vdots \\ \phi_{ikL} - \phi_{ik} \end{bmatrix}$$

The $\left(\frac{\partial^2 \phi}{\partial x^2}, \frac{\partial^2 \phi}{\partial y^2} \right)$ are obtained by solving above over-determined equation system based on least-square approach. Then we can compute the Laplacian operator for diffusion equation:

$$\nu (\nabla^2 \phi)_{ik} = \nu \left(\frac{\partial^2 \phi}{\partial x^2} + \frac{\partial^2 \phi}{\partial y^2} \right), \tag{3.51}$$

Although sophisticated updating method for PVs should be implement as described above, due to the computational expensive operation of matrix inversion, we use simplified method based on TEC formulation [177] in practice. As the first step in this procedure, variation of VIA $\delta \overline{\phi}_i$ against time increment δt, $\frac{d\overline{\phi}_i}{dt}$ is computed by finite volume formulation where $\overline{\phi}_i$ is straightforward moment in VPM scheme while provisional multi-moment

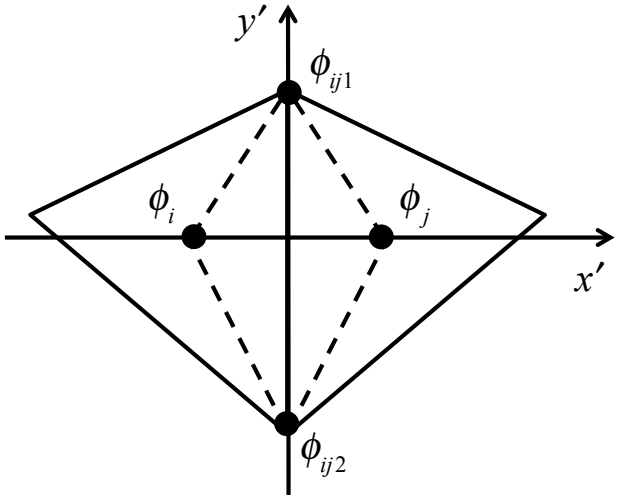


Figure 3.7: Gradient reconstruction for orthogonal the boundary edge.

constrained variable for MCV scheme denoted in Table 2.18.

$$\frac{d\overline{\phi}_i}{dt} = \sum_{j=1}^{3} \left(|\Gamma_{ij}| \left(\overline{\phi}_{x\Gamma_{ij}} n_{xij} + \overline{\phi}_{y\Gamma_{ij}} n_{yij} \right) \right), \tag{3.52}$$

$$\frac{d\phi_{ik}}{dt} = \mathcal{TEC}\left(\frac{d\overline{\phi}_{ikl}}{dt} \right), \; l = 1, \ldots, L, \tag{3.53}$$

$$\frac{d\phi_{i4}}{dt} = \frac{4}{3}\left(\frac{\nu}{|\Omega_i|} \oint_{\Gamma_i} (\mathbf{n} \cdot \nabla\phi)\, d\Gamma \right) - \frac{1}{9}\left(\frac{d\phi_{i1}}{dt} + \frac{d\phi_{i2}}{dt} + \frac{d\phi_{i3}}{dt} \right). \tag{3.54}$$

The implementation of (3.52), (3.53), (3.54) make diffusion equation much more efficient and can be extended to implicit scheme straightforwardly which will be introduced in the next section.

3.7.2 The implicit scheme for diffusion equation

The implicit scheme for diffusion term is required to eradicate restrictive time step of satiability involving very small discrete elements such as micro-fluid flow or turbulent flow. The straightforward implementation by computing (2.42) in term of time level $n+1$ is found to be unstable due to the fact that the resulting matrix can not guarantee diagonal dominance property.

- Remark 1: As shown in Fig. 2.5, if the vector $\theta_i\theta_j$ connecting two adjacent cell center θ_i and θ_j is equally divided and strictly orthogonal to the boundary edge $\theta_{ij1}\theta_{ij2}$, the gradient flux normal to edge $\theta_{ij1}\theta_{ij2}$ can be simplified as $\frac{\phi_j^{n+1} - \phi_i^{n+1}}{|\theta_j - \theta_i|} |\Gamma_{ij}|$.

To facilitate the discussion, as show in Fig. 3.7, the related four PVs$(\theta_i, \theta_j, \theta_{ij1}, \theta_{ij2})$ is mapped to a rotated reference coordinate $x' - y'$ where each coordinate is denoted as

$(\triangle x', 0), (-\triangle x', 0), \left(0, y'_{ij1}\right)$ and $\left(0, y'_{ij12}\right)$. In the same manner, linear piecewise reconstruction can be constructed in term of $\Psi'(x,y) = a + bx' + cy' + O\left(\triangle h^2\right)$. The matrix form is written as $\mathbf{M} \cdot \mathbf{A} = \mathbf{B}$ which stands for

$$\begin{bmatrix} 1 & \triangle x' & 0 \\ 1 & -\triangle x' & 0 \\ 1 & 0 & y'_{ij1} \\ 1 & 0 & y'_{ij2} \end{bmatrix} \begin{bmatrix} a \\ b \\ c \end{bmatrix} = \begin{bmatrix} \phi_i \\ \phi_j \\ \phi_{ij1} \\ \phi_{ij2} \end{bmatrix}.$$

Then the matrix $\mathbf{A}$ can be computed by

$$\begin{aligned} \mathbf{A} &= \left(\mathbf{M}^T\mathbf{M}\right)^{-1}\mathbf{M}^T\mathbf{B} \\ &= \begin{bmatrix} \frac{\left(y'_{ij1}\right)^2+\left(y'_{ij2}\right)^2}{J} & \frac{\left(y'_{ij1}\right)^2+\left(y'_{ij2}\right)^2}{J} & \frac{-y'_{ij2}\left(y'_{ij1}-y'_{ij2}\right)}{J} & \frac{y'_{ij1}\left(y'_{ij1}-y'_{ij2}\right)}{J} \\ \frac{1}{2\triangle x'} & \frac{-1}{2\triangle x'} & 0 & 0 \\ \frac{y'_{ij1}+y'_{ij2}}{J} & \frac{-\left(y'_{ij1}+y'_{ij2}\right)}{J} & \frac{3y'_{ij1}-y'_{ij2}}{J} & \frac{y'_{ij1}-3y'_{ij2}}{J} \end{bmatrix} \begin{bmatrix} \phi_i \\ \phi_j \\ \phi_{ij1} \\ \phi_{ij2} \end{bmatrix} \end{aligned}$$

where $J = 3\left(y'_{ij1}\right)^2 + 3\left(y'_{ij2}\right)^2 - 2y'_{ij1}y'_{ij2}$. The gradient flux normal to edge $(\theta_{ij1}\theta_{ij2})$ then is expressed by $\frac{\phi_j-\phi_i}{2\triangle x'}\left|\overline{\theta_{ij1}\theta_{ij2}}\right|$ which can also be written as $\frac{\phi_j^{n+1}-\phi_i^{n+1}}{|\theta_j-\theta_i|}|\Gamma_{ij}|$.

- Remark 2: As shown in Fig. 2.5, if the vector $\theta_i\theta_j$ connecting two adjacent cell center θ_i and θ_j is divided unequally or non-orthogonal to the boundary edge, according to [75, 79], the gradient flux can be computed by an explicit correction approach. In this study, we splitted the calculation into two parts: implicit orthogonal calculation $\frac{\phi_j^{n+1}-\phi_i^{n+1}}{|\theta_j-\theta_i|}|\Gamma_{ij}|$ and explicit non-orthogonal correction $\left(\left(\overline{\nabla\phi}\right)_{\Gamma_{ij}}^{n+L} - \frac{\phi_j^{n+L}-\phi_i^{n+L}}{|\theta_j-\theta_i|}\mathbf{n}_{ij}\right)\cdot \mathbf{n}_{ij}|\Gamma_{ij}|$. The variable with superscript of $n+L$ represents the intermediate value for sub-iteration where L is in the range of $(0,1)$. The $\left(\overline{\nabla\phi}\right)_{\Gamma_{ij}}^{n+L}$ is computed from (2.42) by using $\phi_i, \phi_j, \phi_{ij1}$ and ϕ_{ij2} at time level $n+L$.

The unified formula for the implicit gradient flux with non-orthogonal correction thus is written as:

$$|\Gamma_{ij}|(\overline{\phi}_{x\Gamma_{ij}}n_{xij} + \overline{\phi}_{y\Gamma_{ij}}n_{yij}) = \frac{\phi_j^{n+1}-\phi_i^{n+1}}{|\theta_j-\theta_i|}|\Gamma_{ij}| + \left(\left(\overline{\nabla\phi}\right)_{\Gamma_{ij}}^{n+L} - \frac{\phi_j^{n+L}-\phi_i^{n+L}}{|\theta_j-\theta_i|}\mathbf{n}_{ij}\right)\cdot\mathbf{n}_{ij}|\Gamma_{ij}| \tag{3.55}$$

Using the gradient flux (3.55), the approach for implicit diffusion term is formulated as (3.56),(3.57),(3.58). It's noteworthy that the $\overline{\phi}_i^n$ in MCV is provisional VIA and computed

by constrained condition denoted in Table 2.18.

$$\frac{\overline{\phi}_i^{n+1} - \overline{\phi}_i^n}{\triangle t} = \sum_{j=1}^{3} \left(|\Gamma_{ij}| \left(\overline{\phi}_{x\Gamma_{ij}} n_{xij} + \overline{\phi}_{y\Gamma_{ij}} n_{yij} \right) \right), \tag{3.56}$$

$$\frac{\phi_{ik}^{n+1} - \phi_{ik}^n}{\triangle t} = \mathcal{TEC} \left(\frac{d\overline{\phi}_{ikl}}{dt} \right), \; l = 1, \ldots, L, \tag{3.57}$$

$$\phi_{i4}^{n+1} = \frac{4}{3}\overline{\phi}_i^{n+1} - \frac{1}{9}\phi_{i1}^{n+1} - \frac{1}{9}\phi_{i2}^{n+1} + \frac{1}{9}\phi_{i3}^{n+1}. \tag{3.58}$$

The approach for boundary condition is ensured by computing (2.43) with interior value ϕ_{i4} at $n+1$ level and others at n level which enhance diagonal dominance of incorporated matrix. By this approach, the resulting matrix is proven to be exactly diagonal dominant with robustness enhancement by minimizing the discretized error owing to non-orthogonality.

3.8 Spatial discretization of Poisson equation for pressure field

In the present formulation, the Poisson equations of (3.15) and (3.11) are recast in an integral form.

$$\oint_{\Omega_i} p^{n+1} d\Omega + \rho^n \left(c^2\right)^n \triangle t^2 \cdot \oint_{\Gamma_i} \left(\frac{1}{\rho^{n+1}} \mathbf{n} \cdot \nabla p^{n+1} \right) d\Gamma = p^{\diamondsuit} + \rho^n \left(c^2\right)^n \triangle t \nabla \mathbf{u}^* \tag{3.59}$$

$$\oint_{\Gamma_i} \left(\frac{1}{\rho} \mathbf{n} \cdot \nabla p^{n+1} \right) d\Gamma = \frac{1}{\Delta t} \oint_{\Gamma_i} \left(\mathbf{n} \cdot \mathbf{u}^* \right) d\Gamma. \tag{3.60}$$

Discretizing (3.59) and (3.60) over cell Ω_i yields

$$\begin{aligned} & p^{n+1} |\Omega_i| + \rho^n \left(c^2\right)^n \triangle t^2 \cdot \textstyle\sum_{j=1}^{3} \left(\frac{|\Gamma_{ij}|}{\rho_{ij}^{n+1}} \left(\frac{\partial \overline{p}}{\partial r} \right)_{ij} \mathbf{e}_{ij} \cdot \mathbf{n}_{ij} \right) \\ = \quad & p^{\diamondsuit} |\Omega_i| + \rho^n \left(c^2\right)^n \triangle t \textstyle\sum_{j=1}^{3} \left(|\Gamma_{ij}| (\overline{u}^*_{\Gamma_{ij}} n_{xij} + \overline{v}^*_{\Gamma_{ij}} n_{yij}) \right) \end{aligned} \tag{3.61}$$

$$\sum_{j=1}^{3} \left(\frac{|\Gamma_{ij}|}{\rho_{ij}} \left(\frac{\partial \overline{p}}{\partial r} \right)_{ij} \mathbf{e}_{ij} \cdot \mathbf{n}_{ij} \right) = \frac{1}{\Delta t} \sum_{j=1}^{3} \left(|\Gamma_{ij}| (\overline{u}^*_{\Gamma_{ij}} n_{xij} + \overline{v}^*_{\Gamma_{ij}} n_{yij}) \right), \tag{3.62}$$

where $(\overline{u}^*_{\Gamma_{ij}}, \overline{v}^*_{\Gamma_{ij}})$ on the right hand side are obtained from reconstruction function in the same manner as described before. Among the various methods for evaluation of the pressure gradient at cell boundary, two approaches are adopted in this study. The first approach named by "PS-VIA" only defines VIA in each grid cell and gradient over cell boundary is approximated by a linear interpolation spanned over two neighboring cells sharing edge Γ_{ij}. We denote $(\frac{\partial \overline{p}}{\partial r})_{ij} \mathbf{e}_{ij}$ as the pressure gradient along line segment

$\mathbf{r}_{ij} = \mathbf{r}(\theta_{cij}) - \mathbf{r}(\theta_{ci})$ with $\mathbf{r}(\theta_{cij}) = (x_{cij}, y_{cij})$ and $\mathbf{r}(\theta_{ci}) = (x_{ci}, y_{ci})$ being the position vectors of the centroids of cells Ω_{ij} and Ω_i respectively, i.e.

$$x_{ci} = \frac{1}{3}\sum_{k=1}^{3} x_{ik},\ x_{cij} = \frac{1}{3}\sum_{k=1}^{3} x_{ijk},\ y_{ci} = \frac{1}{3}\sum_{k=1}^{3} y_{ik},\ y_{cij} = \frac{1}{3}\sum_{k=1}^{3} y_{ijk}.$$

The unit vector of $\mathbf{r}_{ij}$ is denoted by $\mathbf{e}_{ij} = (e_{xij}, e_{yij}) = \mathbf{r}_{ij}/|\mathbf{r}_{ij}|$.

The linear interpolation function over two neighboring cells Ω_i and Ω_{ij} is then written in the following form,

$$\mathcal{P}(x, y) = p_0 + \left(\frac{\partial \overline{p}}{\partial r}\right)_{ij} (e_{xij}x + e_{yij}y). \tag{3.63}$$

The unknowns p_0 and $(\frac{\partial \overline{p}}{\partial r})_{ij}$ in (3.63) are uniquely determined by requiring

$$\frac{1}{|\Omega_i|}\iint_{\Omega_i} \mathcal{P}(x, y)d\Omega = \overline{p}_i, \tag{3.64}$$

$$\frac{1}{|\Omega_{ij}|}\iint_{\Omega_{ij}} \mathcal{P}(x, y)d\Omega = \overline{p}_{ij}. \tag{3.65}$$

From (3.64) and (3.65), with some algebraic manipulation, we have

$$\left(\frac{\partial \overline{p}}{\partial r}\right)_{ij} = \frac{(\overline{p}_{ij} - \overline{p}_i)}{e_{xij}(x_{cij} - x_{ci}) + e_{yij}(y_{cij} - y_{ci})}. \tag{3.66}$$

Following [129, 79], we consider a correction to the non-orthogonality of the mesh. We decompose the normal vector of edge Γ_{ij} as follows,

$$\mathbf{n}_{ij} = \frac{\mathbf{e}_{ij}}{\mathbf{e}_{ij} \cdot \mathbf{n}_{ij}} + \mathbf{n}_{\parallel ij}, \tag{3.67}$$

where $\mathbf{n}_{\parallel ij}$ represents a vector co-linear with edge Γ_{ij}. The pressure gradient term in (3.62) is then split into two parts, i.e. the orthogonal part and the non-orthogonal correction part,

$$\left(\frac{\partial \overline{p}}{\partial r}\right)_{ij} \mathbf{e}_{ij} \cdot \mathbf{n}_{ij} = \frac{1}{\mathbf{e}_{ij} \cdot \mathbf{n}_{ij}} \left(\frac{\partial \overline{p}}{\partial r}\right)_{ij} + \left(\frac{\partial \overline{p}}{\partial r}\right)_{ij} \mathbf{e}_{ij} \cdot \mathbf{n}_{\parallel ij} \tag{3.68}$$

As adopted in [75], we calculate the orthogonal component implicitly using the values at level $n + 1$ and the non-orthogonal correction explicitly with the values at level n,

$$\left(\frac{\partial \overline{p}}{\partial r}\right)_{ij} \mathbf{e}_{ij}\cdot\mathbf{n}_{ij} \approx \frac{1}{\mathbf{e}_{ij}\cdot\mathbf{n}_{ij}}\left(\frac{\partial \overline{p}}{\partial r}\right)_{ij}^{n+1} + \left(\frac{\partial \overline{p}}{\partial r}\right)_{ij}^{n} \mathbf{e}_{ij}\cdot\mathbf{n}_{\|ij} \tag{3.69}$$

$$= \frac{1}{\mathbf{e}_{ij}\cdot\mathbf{n}_{ij}} \frac{(\overline{p}_{ij}^{n+1} - \overline{p}_{i}^{n+1})}{e_{xij}(x_{cij}-x_{ci}) + e_{yij}(y_{cij}-y_{ci})}$$

$$+ \frac{(\overline{p}_{ij}^{n} - \overline{p}_{i}^{n})}{e_{xij}(x_{cij}-x_{ci}) + e_{yij}(y_{cij}-y_{ci})} \mathbf{n}_{\|ij}\cdot\mathbf{e}_{ij}. \tag{3.70}$$

Thus, Poisson equation (3.61) and (3.62) for pressure are finally written as

$$p^{n+1}\left|\Omega_i\right| + \rho^n\left(c^2\right)^n \triangle t^2 \cdot \sum_{j=1}^{3} \alpha_{ij}(\overline{p}_{ij}^{n+1} - \overline{p}_{i}^{n+1}) = p^{\diamondsuit}\left|\Omega_i\right| + \rho^n\left(c^2\right)^n \triangle t\beta_i + \gamma_i \tag{3.71}$$

$$\sum_{j=1}^{3} \alpha_{ij}(\overline{p}_{ij}^{n+1} - \overline{p}_{i}^{n+1}) = \frac{1}{\Delta t}\beta_i + \gamma_i \tag{3.72}$$

where

$$\alpha_{ij} = \frac{1}{\mathbf{e}_{ij}\cdot\mathbf{n}_{ij}} \frac{\left|\Gamma_{ij}\right|}{\rho_{ij}\left(e_{xij}(x_{cij}-x_{ci}) + e_{yij}(y_{cij}-y_{cij})\right)},$$

$$\beta_i = \sum_{j=1}^{3}\left(\left|\Gamma_{ij}\right|\left(\overline{u}_{\Gamma_{ij}}^{*} n_{xij} + \overline{v}_{\Gamma_{ij}}^{*} n_{yij}\right)\right),$$

$$\gamma_i = \sum_{j=1}^{3} \frac{\left|\Gamma_{ij}\right|}{\rho_{ij}}\left(\frac{(\overline{p}_{ij}^{n} - \overline{p}_{i}^{n})}{e_{xij}(x_{cij}-x_{ci}) + e_{yij}(y_{cij}-y_{cij})} \mathbf{n}_{\|ij}\cdot\mathbf{e}_{ij}\right).$$

Equation (3.72) is a simultaneously linked linear algebraic equation for pressure $\overline{p}_i^{n+1}$ and can be solved by iterative solvers.

The PS-VIA method has advantages in simplicity, efficiency and adaptability for resolving discontinuities attributed to its compact stencil and straightforward procedure. For incompressible flow, alternative approach, which we call it as PS-MCV, is proposed to improve accuracy and robustness. On each grid element, in addition to prognostic PV at cell center, PVs at cell vertices are added which are approximated by surrounding PVs at cell center based on the least square method. Using implicit procedure in (3.55), the pressure gradient flux can be computed as:

$$\left(\frac{\partial \overline{p}}{\partial r}\right)_{ij} \mathbf{e}_{ij}\cdot\mathbf{n}_{ij} = \frac{\left|\Gamma_{ij}\right|}{\rho_{ij}} \frac{\left(p_j^{n+1} - p_i^{n+1}\right)}{e_{xij}(x_{cij}-x_{ci}) + e_{yij}(y_{cij}-y_{ci})}$$

$$+ \frac{\left|\Gamma_{ij}\right|}{\rho_{ij}}\left(\left(\overline{\nabla p}\right)_{\Gamma_{ij}}^{n+L} - \frac{p_j^{n+l} - p_i^{n+l}}{e_{xij}(x_{cij}-x_{ci}) + e_{yij}(y_{cij}-y_{ci})} \mathbf{n}_{ij}\right)\cdot\mathbf{n}_{ij} \tag{3.73}$$

The resulting Poisson equation is expressed in the form of

$$\sum_{j=1}^{3} \alpha_{ij}(\overline{p}_{ij}^{n+1} - \overline{p}_{i}^{n+1}) = \frac{1}{\Delta t}\beta_i + \delta_i \tag{3.74}$$

where

$$\begin{aligned}
\alpha_{ij} &= \frac{1}{\mathbf{e}_{ij}\cdot\mathbf{n}_{ij}} \frac{|\Gamma_{ij}|}{\rho_{ij}\left(e_{xij}(x_{cij}-x_{ci}) + e_{yij}(y_{cij}-y_{ci})\right)}, \\
\beta_i &= \sum_{j=1}^{3} \left(|\Gamma_{ij}| \left(\overline{u}^{*}_{\Gamma_{ij}} n_{xij} + \overline{v}^{*}_{\Gamma_{ij}} n_{yij} \right) \right), \\
\delta_i &= \sum_{j=1}^{3} \frac{|\Gamma_{ij}|}{\rho_{ij}} \left(\left(\overline{\nabla p}\right)^{n+l}_{\Gamma_{ij}} - \frac{p_j^{n+l} - p_i^{n+l}}{e_{xij}(x_{cij}-x_{ci}) + e_{yij}(y_{cij}-y_{ci})} \mathbf{n}_{ij} \right) \cdot \mathbf{n}_{ij} \left|\Gamma_{ij}\right|.
\end{aligned}$$

By this explicit correction method, the intermediate value p_i^{n+L} and p_j^{n+L} is directly obtained from the matrix iteration and approach to $n+1$ level until given residual satisfied.

3.8.1 Projection of the velocity field

As the final step in the solution procedure of incompressible flow, the velocity field must be projected onto a divergence-free subset. From the pressure field computed by (3.72) or (3.74), the intermediate velocity $(\overline{u}^{*}_{\Gamma_{ij}}, \overline{v}^{*}_{\Gamma_{ij}})$ is firstly corrected to satisfy divergence free condition and then the after-correction velocity will be used as advection velocity in the next time step. For the rigorous conservative property, the pressure gradient for correction must be ensured strictly consistent with pressure gradient formulation in Poisson equation which can be expressed in term of (3.69) or (3.73).

$$\overline{u}^{n+1}_{\Gamma_{ij}} = \overline{u}^{*}_{\Gamma_{ij}} - \frac{\Delta t}{\rho\omega} \left(|\Gamma_{ij}|\, e_{xij} n_{xij} (\frac{\partial \overline{p}}{\partial r})^{n+1}_{ij} \right), \tag{3.75}$$

$$\overline{v}^{n+1}_{\Gamma_{ij}} = \overline{v}^{*}_{\Gamma_{ij}} - \frac{\Delta t}{\rho\omega} \left(|\Gamma_{ij}|\, e_{yij} n_{yij} (\frac{\partial \overline{p}}{\partial r})^{n+1}_{ij} \right). \tag{3.76}$$

If Runge-Kutta mehtod is adopted for velocity prediction step, $\omega = 1$ while for multi-step BDF method, ω is specified with α_1. According to the study of [35, 60], the volume integrated average pressure gradient $\left(\overline{\nabla p}\right)_i$ should be calculated from surrounding face-based pressure gradient $\left(\overline{\nabla p}\right)_{\Gamma_{ij}}$ by face-area weighted least square approach by minimizing

$$\epsilon = \sum_{j=1}^{3} \left(\left(\overline{\nabla p}\right)_i \cdot \mathbf{n}_{ij} - \left(\overline{\nabla p}\right)_{\Gamma_{ij}} \cdot \mathbf{n}_{ij} \right)^2 |\Gamma_{ij}| \tag{3.77}$$

Here, $\mathbf{n}_{ij}$ is unit normal vector on surface Γ_{ij} . We assume $\left(\overline{\nabla p}\right)_i = \left(\frac{\partial \overline{p}}{\partial x}, \frac{\partial \overline{p}}{\partial y}\right)$ and $\mathbf{n}_{ij} = (n_{xij}, n_{yij})$, then we can construct linear equation system as:

$$\sum_{j=1}^{3}|\Gamma_{ij}|\begin{pmatrix} n_{xij}n_{xij} & n_{xij}n_{yij} \\ n_{xij}n_{yij} & n_{yij}n_{yij} \end{pmatrix}\cdot\begin{pmatrix} \frac{\partial\overline{p}}{\partial x} \\ \frac{\partial\overline{p}}{\partial y} \end{pmatrix}=\sum_{j=1}^{3}\begin{pmatrix} |\Gamma_{ij}|\,n_{xij}\left(\overline{\nabla p}\right)_{x\Gamma_{ij}}^{n+1} \\ |\Gamma_{ij}|\,n_{yij}\left(\overline{\nabla p}\right)_{y\Gamma_{ij}}^{n+1} \end{pmatrix}$$

We can readily compute $\left(\frac{\partial\overline{p}}{\partial x},\frac{\partial\overline{p}}{\partial y}\right)$ by inversing the matrix in the left hand side. Then the velocity of VIA in VPM scheme is updated as:

$$\overline{u}_i^{n+1}=\overline{u}_i^{*}-\frac{\Delta t}{\rho\omega}\frac{\partial\overline{p}}{\partial x}, \tag{3.78}$$

$$\overline{v}_i^{n+1}=\overline{v}_i^{*}-\frac{\Delta t}{\rho\omega}\frac{\partial\overline{p}}{\partial y},. \tag{3.79}$$

Given the time increments of VIA, we update the velocity at the cell vertices by the time-evolution converting (TEC) formula[177],

$$u_{ik}^{n+1}=u_{ik}^{*}+\mathcal{TEC}\left(\overline{u}_i^{n+1}-\overline{u}_i^{*}\right), \tag{3.80}$$

$$v_{ik}^{n+1}=v_{ik}^{*}+\mathcal{TEC}\left(\overline{v}_i^{n+1}-\overline{v}_i^{*}\right). \tag{3.81}$$

It is noted that for MCV scheme, provisional VIA as well as prognostic PV at cell center $\left(u_i^{n+1},v_i^{n+1}\right)$ can be converted bi-directionally by multi-moment constrained formulations in Table (2.18).

For compressible flow, pressure is resolved by equation of (3.71) and projected to both momentum and total energy equations. In the same way, the provisional velocity $(\overline{u}_{\Gamma_{ij}}^{*},\overline{v}_{\Gamma_{ij}}^{*})$ for advective flux is updated by (3.82) and (3.83) where pressure gradient is computed in form of (3.69).

$$\overline{u}_{\Gamma_{ij}}^{n+1}=\overline{u}_{\Gamma_{ij}}^{*}-\frac{\Delta t}{\rho}\left(|\Gamma_{ij}|\,e_{xij}n_{xij}(\frac{\partial\overline{p}}{\partial r})_{ij}^{n+1}\right), \tag{3.82}$$

$$\overline{v}_{\Gamma_{ij}}^{n+1}=\overline{v}_{\Gamma_{ij}}^{*}-\frac{\Delta t}{\rho}\left(|\Gamma_{ij}|\,e_{yij}n_{yij}(\frac{\partial\overline{p}}{\partial r})_{ij}^{n+1}\right). \tag{3.83}$$

The pressure at cell center $\left(\frac{\partial\overline{p}}{\partial x},\frac{\partial\overline{p}}{\partial y}\right)$ can be estimated by formulation of (3.77), then VIA of momentum at level $n+1$ is updated as:

$$\overline{m}_{x_i}^{\,n+1}=\overline{m}_{xi}^{*}-\frac{\partial\overline{p}}{\partial x}\triangle t, \tag{3.84}$$

$$\overline{m}_{y_i}^{\,n+1}=\overline{m}_{yi}^{*}-\frac{\partial\overline{p}}{\partial y}\Delta t. \tag{3.85}$$

With resolved pressure at level $n+1$, the total energy $\overline{E}$ is updated by

$$\overline{E}^{n+1} = \overline{E}^{*} - \nabla \cdot \left(\overline{\mathbf{u}}_{\Gamma_{ij}}^{n+1} p_{\Gamma_{ij}}^{n+1} \right) \triangle t. \tag{3.86}$$

Given the time increments of VIA, we update the PV of $\overline{\mathbf{m}}_{ik}^{n+1}$ as well as E_{ik}^{n+1} at the vertices by TEC formula in the same manner,

$$m_{x_{ik}}^{n+1} = m_{x_{ik}}^{*} + \mathcal{TEC} \left(\overline{m}_{x_i}^{n+1} - \overline{m}_{x_i}^{*} \right), \tag{3.87}$$

$$m_{y_{ik}}^{n+1} = m_{y_{ik}}^{*} + \mathcal{TEC} \left(\overline{m}_{y_i}^{n+1} - \overline{m}_{y_i}^{*} \right), \tag{3.88}$$

$$E_{ik}^{n+1} = E_{ik}^{*} + \mathcal{TEC} \left(\overline{E}_{i}^{n+1} - \overline{E}_{i}^{*} \right). \tag{3.89}$$

For MCV scheme, prognostic PV moments at cell center $\mathbf{m}_i$, E_i are constrained by formulation of Table 2.18. Although the numerical procedure is demonstrated on triangular element for 2D, the spatial discretization for other type grids can be derived straightforwardly based on the VPM/MCV reconstruction formulation denoted in chapter 2.

3.9 Summary of solution procedures

In order to facilitate the users to follow the algorithm of clarity, we give a summary for the entire solution procedure as the following steps.

1. Given initial velocity field at step n, reconstruction function for VPM/MCV is constructed with gradient at cell center $(\phi_{\xi i}, \phi_{\eta i})$ computed by approaches of DIA-A, DIA-B or DIA-C denoted in section 3.5.1.

2. DOFs of advection equation in VPM/MCV is updated by (3.35), (3.36) or (3.37).

3. The diffusion equation is computed by the formulation of (3.47), (3.48) or (3.49). Particularly, TEC formulation is used for simplicity in practice.

4. Compute the face integrated average for velocity field $(\overline{u}_{\Gamma_{ij}}^{*}, \overline{v}_{\Gamma_{ij}}^{*})$ by Table 2.21 or 2.22 and solve Poisson equation formulated as (3.61) or (3.62) to get pressure $\overline{p}_i^{n+1}$ at step $n+1$.

5. The intermediate velocity $(\overline{u}_{\Gamma_{ij}}^{*}, \overline{v}_{\Gamma_{ij}}^{*})$ is corrected by pressure $\overline{p}_i^{n+1}$ with formulation of (3.75), (3.76) for incompressible flow and (3.82), (3.83) for compressible flow. Prognostic VIAs are updated by projection formulation and PVs by TEC formulation referring to (3.78), (3.79),(3.80), (3.81) for incompressible solver and (3.84), (3.85),(3.86),(3.87), (3.88),(3.89) for compressible solver.

As can be seen from above, the solution procedure is very efficient. Inside each time step, the associated advection–diffusion-typed momentum equation and Poisson equation are solved only once with trivial cost which will be confirmed by subsequent numerical examples.

3.10 Verification tests

3.10.1 Advection of sine wave

To evaluate the convergence rate of the advection scheme presented in Section 3.37, we compute the advection transport of a sine function as in [59] with gradually refined grids. The advected profile is initially defined as

$$\phi_0(x, y) = \sin 2\pi(x + y) \tag{3.90}$$

over a $[0, 1] \times [0, 1]$ computational domain, the periodic boundary condition is imposed in both x and y directions. A constant and uniform advection velocity is specified as $u = v = 1.0$. Numerical experiments are conducted on gradually refined grids generated by Delaunay algorithm with doubly increased resolution. The time step of $\Delta t = 0.001$ is used throughout all computations.

The L_1 errors and the convergence rates of VPM/MCV with gradient moments evaluated by "DIA-B" approach and other standard schemes at $t = 1.0$ are firstly investigated and given in Table 3.1 for grids of different resolutions.

Table 3.1: Comparison of L_1 errors and convergence rates of different advection schemes.

Cell number	QUICK	Rate	SUPERBEE	Rate	MUSCL	Rate	VPM/MCV	Rate
226	1.916×10^{-1}	–	1.027×10^{-1}	–	2.409×10^{-1}	–	1.297×10^{-1}	–
894	4.821×10^{-2}	2.01	7.228×10^{-2}	0.51	6.548×10^{-2}	1.89	1.772×10^{-2}	2.90
3588	1.254×10^{-2}	1.94	3.327×10^{-2}	1.12	1.887×10^{-2}	1.79	2.188×10^{-3}	3.01
14412	3.605×10^{-3}	1.79	1.162×10^{-2}	1.51	5.618×10^{-3}	1.74	2.735×10^{-4}	2.99
57518	1.103×10^{-3}	1.71	3.458×10^{-3}	1.75	1.682×10^{-3}	1.74	3.522×10^{-5}	2.95

It is observed that the presented scheme is of 3th order accuracy. Because the multi-moment reconstruction is of second order, the VIA is theoretically expected to be of third order accuracy, which is justified by the numerical output. For comparison, we also include the numerical results from other standard advection schemes used in conventional FVM codes, such as the QUICK scheme [94], superbee-TVD scheme [128] and MUSCL scheme [159, 160], which are available in the OpenFOAM [166, 75] platform. These standard schemes are widely used for unstructured grids and show convergence rates less than 2nd order, among which the QUICK scheme is more accurate for this smooth-profile test problem. Moreover, a comparison between the errors of VPM and standard schemes shows a large improvement in numerical accuracy by VPM/MCV scheme. On the grid of 57518 elements, for example, the L_1 error of VPM is only 3% of the QUICK scheme.

In order to quantify the computational cost in comparison with the conventional FVM, we run this advection test with different grid resolutions for 1000 steps on a PC with a

single CPU (Intel(R) Xeon E5-2687W, 3.10GHZ). We give in Table 3.2 the DOFs for the memory requirement and elapsed time for CPU consumption. It is observed that for the triangular mesh the number of DOFs increases about 51%. Shown in Table 3.2, the elapsed time increase may reach 1.5 fold in comparison with the QUICK scheme. From Table 3.1, we see that the numerical error of VPM on a 5463-element grid is smaller than that of the QUICK scheme on a 14412-element grid. It shows that for a given error level the VPM/MCV-RK scheme is much more efficient in terms of both memory requirement and CPU consumption compared to the standard schemes due to its high accuracy and faster convergence.

Table 3.2: Computational cost estimation for advection calculation of VPM/MCV in comparison with the QUICK scheme.

Elements	QUICK			VPM/MCV		
	DOFs	Time(s)	L_1 error	DOFs	Time(s)	L_1 error
226	226	0.21	1.916×10^{-1}	360	0.22	1.297×10^{-1}
894	894	0.35	4.821×10^{-2}	1382	0.55	1.772×10^{-2}
3588	3588	0.84	1.254×10^{-2}	5463	1.67	2.188×10^{-3}
14412	14412	2.66	3.605×10^{-3}	21779	6.27	2.735×10^{-4}
57518	57518	9.95	1.103×10^{-3}	86598	25.95	3.522×10^{-5}

Next, we investigate accuracy and convergence rate of MCV/VPM scheme incorporated with gradient moments by approaches of "DIA-A", "DIA-B" and "DIA-C" under the same computational condition described before. As shown in the Table 3.3, compared with DIA-A approach, DIA-B and DIA-C approaches have attained same third order convergence rate but demonstrated a slightly lost in accuracy. Among the three approaches, DIA-C shows the closest accuracy to most exact DIA-A while without matrix inversion operation and massive memory usage. It is seen that DIA-C has achieved most balanced performance between accuracy and efficiency which is critical for engineering applications. Integrated TVD flux limiter function with DIA-A approach where gradient moments required at cell center are estimated in the same manner, the MCV/VPM scheme is tested and results are given in Table 3.3 and Fig. 3.8. Although relatively small degradation is observed, the results are still shown to converged with over second order which is superior than conventional FVM schemes. All the results reveal that "DIA-A", "DIA-B" as well as "DIA-C" approaches provide competitive performance and TVD limiter is able to resolve smooth region with higher order accuracy.

3.10.2 Solid rotation of 2D cone

It is well known that numerical solutions on unstructured grid depend on the quality of computational grid. In this test, we examine the robustness of the advection scheme to

Cell number	DIA-A	Rate	DIA-B	Rate	DIA-C	Rate	TVD limiter	Rate
226	9.157×10^{-2}	–	1.297×10^{-1}	–	9.302×10^{-2}	–	1.631×10^{-1}	–
894	1.254×10^{-2}	2.90	1.772×10^{-2}	2.90	1.264×10^{-2}	2.90	2.752×10^{-2}	2.58
3588	1.555×10^{-3}	3.00	2.188×10^{-3}	3.01	1.563×10^{-3}	3.01	5.236×10^{-3}	2.39
14412	1.954×10^{-4}	2.98	2.735×10^{-4}	2.99	1.949×10^{-4}	2.99	9.733×10^{-4}	2.42
57518	2.520×10^{-5}	2.90	3.522×10^{-5}	2.95	2.542×10^{-5}	2.94	1.756×10^{-4}	2.46

Table 3.3: Comparison of L_1 errors and convergence rates for different gradient moments as well as TVD limiter.

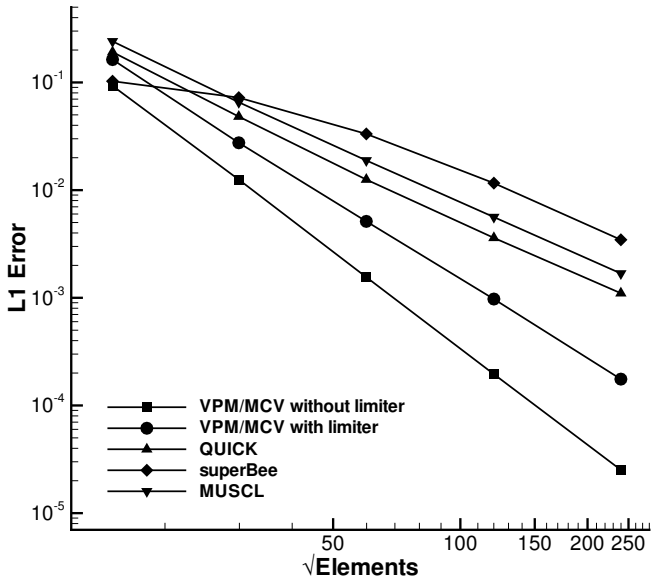


Figure 3.8: Numerical error for MCV/VPM scheme with and without flux limiter function and compared with conventional FVM scheme.

the quality of computational grid. A 2D cone of the initial distribution specified by

$$\phi_0(x, y) = \exp\left(\frac{(x-0.5)^2 + (y-0.75)^2}{0.015}\right) \tag{3.91}$$

over $[0, 1] \times [0, 1]$ is transported with a rotational velocity field defined by $u = -2\pi(y-0.5)$ and $v = 2\pi(x-0.5)$.

We use two unstructured grids with triangular elements. As shown in Fig. 3.9, grid A is generated by the Delaunay algorithm and has good quality, while grid B has a region where the mesh elements are distorted with large skewness and high aspect ratio. The numerical results of the VPM/MCV scheme after one revolution of rotation are shown in Fig. 3.10. It is found that the degradation in mesh quality doesn't significantly affect the numerical results.

Fig. 3.11, 3.12 and 3.13 display the corresponding outputs of other standard schemes on the two grids. Compared against Fig. 3.10, it is found that the VPM scheme is the

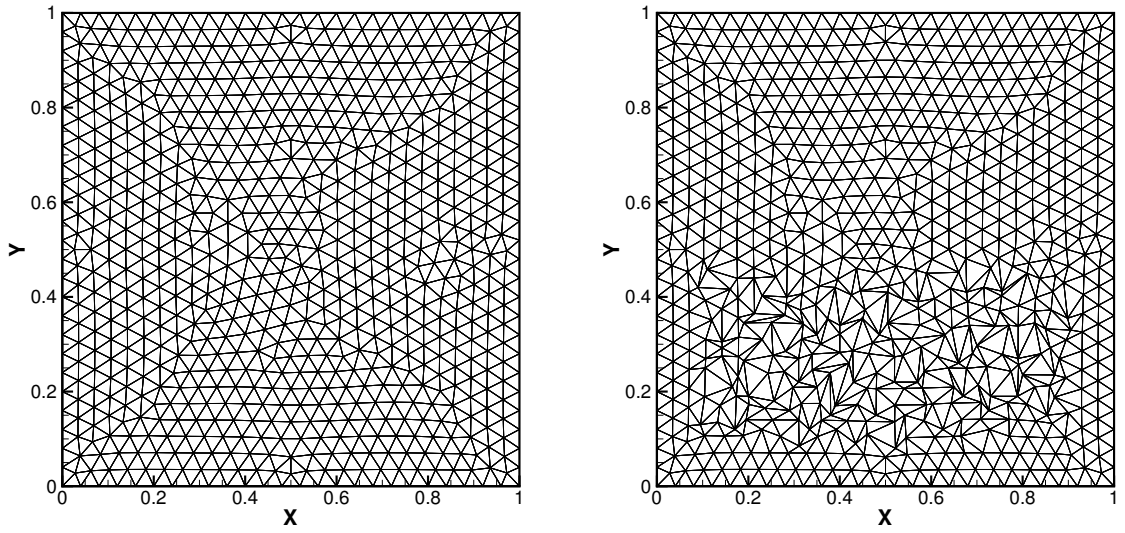


Figure 3.9: The computational meshes for advection test. Left (grid A): a mesh generated by Delaunay algorithm. Right (grid B): a mesh where a region has heavily distorted triangular elements of bad conditions in orthogonality, skewness and uniformity.

most accurate on both grids. More important, the conventional schemes are more sensitive to the mesh quality, whose numerical results look remarkably worse on grid B.

To quantify this observation, we give in Table 3.4 the L_1 errors on both A and B grids for VPM method and other standard finite volume schemes with the "degradation error" defined by L_1 errors on grid B subtract L_1 errors on grid A as

$$\text{Degradation error} = \frac{\left(\sum_{i=1}^{N_e}(|\phi_{ni}-\phi_{ei}||\Omega_i|)\right)_{\text{grid B}} - \left(\sum_{i=1}^{N_e}(|\phi_{ni}-\phi_{ei}||\Omega_i|)\right)_{\text{grid A}}}{\sum_{i=1}^{N_e}(|\phi_{ei}||\Omega_i|)}. \tag{3.92}$$

As an indicator of the robustness to the computational grid, a smaller value of the degradation error shows a better robustness in respect to the quality of mesh elements.

Table 3.4: Numerical errors on different grids and degradation rate.

Scheme	L_1 error on grid A	L_1 error on grid B	Degradation error
VPM/MCV	0.08442	0.11203	0.0276
QUICK	0.13231	0.27172	0.1394
Superbee	0.17124	0.27551	0.1043
MUSCL	0.11604	0.34715	0.2311

We can see that having the smallest degradation error, the present VPM/MCV scheme is the most robust one in regard to the computational grid, and thus retains the numerical accuracy even on a grid of worse quality. It is very sensible if we consider that in the present scheme both the cell average and vertex value are updated, which compensates

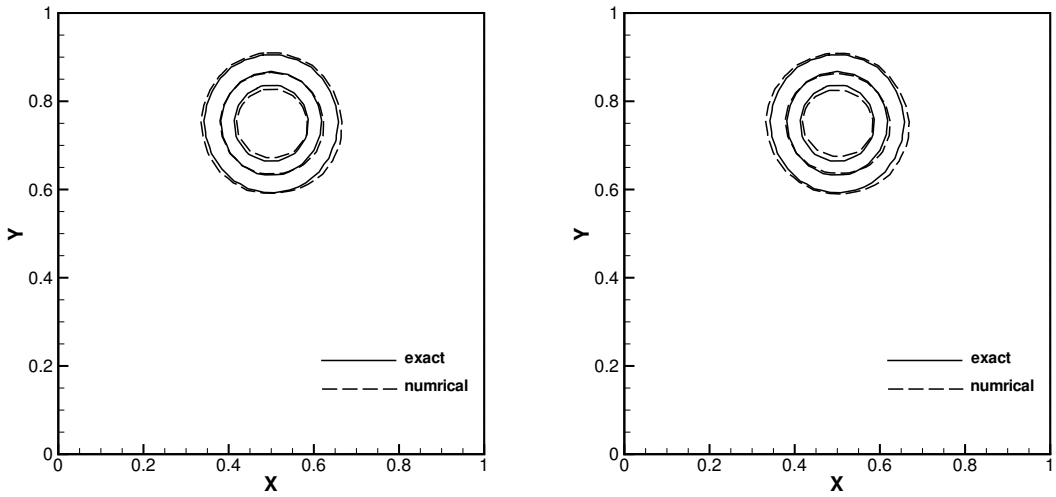


Figure 3.10: The numerical results of VPM/MCV scheme for the solid rotation advection tests on grid A (left) and grid B (right).

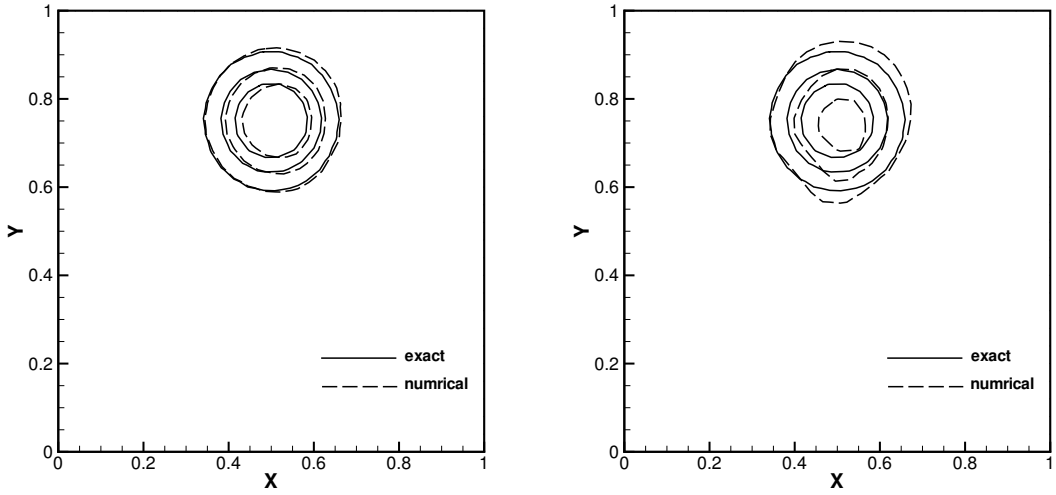


Figure 3.11: Same as Fig. 3.10 but by the QUICK scheme.

the loss of the information due to the worse nonorthogonality and skewness of the mesh.

3.10.3 Advection transport of discontinuities

The capability of present scheme to handle discontinuities is verified by a 2D advection test transporting a square pulse in a rotating velocity field [63]. The initial profile is defined by

$$\phi_0(x,y) = \begin{cases} 1.0 & \text{if } 0.2 \le x \le 0.4,\ 0.4 \le y \le 0.6, \\ 0 & \text{otherwise} \end{cases}$$

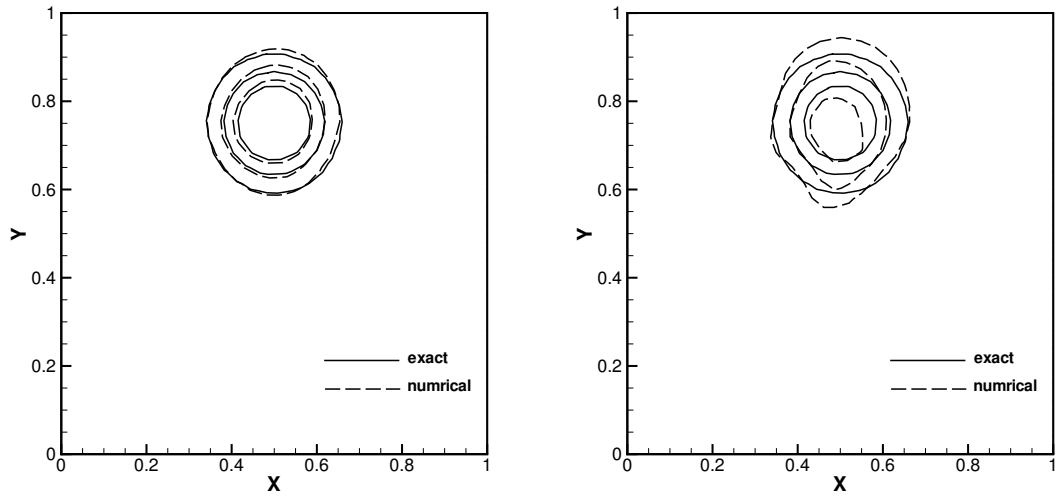


Figure 3.12: Same as Fig. 3.10 but by the superbee TVD scheme.

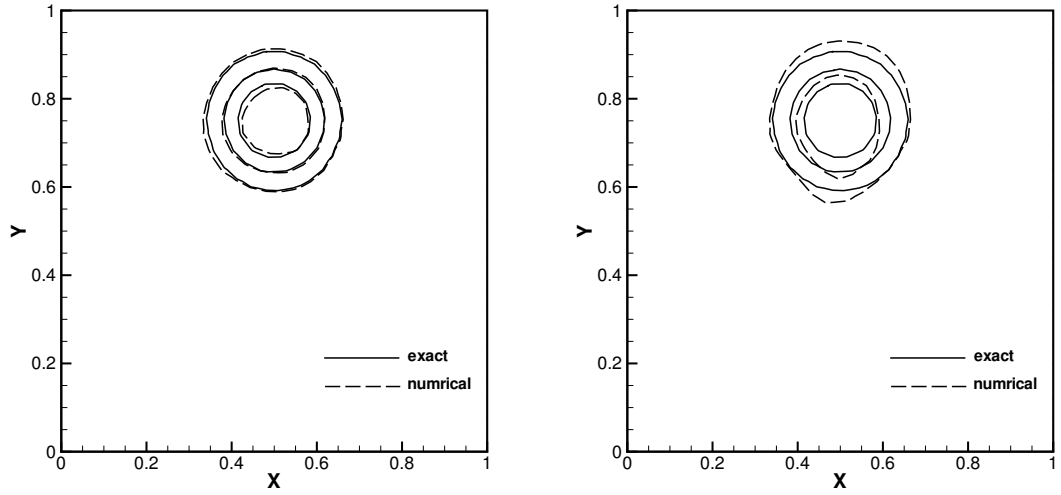


Figure 3.13: Same as Fig. 3.10 but by the MUSCL scheme.

The computational domain, $[0,1] \times [0,1]$, is spaced by 2937 unstructured quadrilateral cells. The velocity field is prescribed by $u = 2\pi\,(0.5 - y)$ and $v = 2\pi\,(x - 0.5)$.

Numerical results after one revolution are shown in Fig. 3.14 in comparison with the QUICK scheme. VPM/MCV scheme looks obviously superior. As expected, both schemes generate numerical oscillations near the solution discontinuities without any limiting projection. We show the numerical oscillation errors in Table 3.5. VPM/MCV scheme has less over-shots and under-shots compared to the QUICK scheme. It is noted that without any particular treatment, the present methods can keep sufficient stability due to upwind-biased flux formulation. In order to verify performance of TVD limiter to restrain spurious oscillation, we compute advection of Zalesak initial shape prescribed as

$$\Big((x-0.5)^2 + (y-0.75)^2\Big) \leq 0.15^2 \;\wedge\; |x-0.5| \geq 0.025 \;\vee\; y \geq 0.85$$

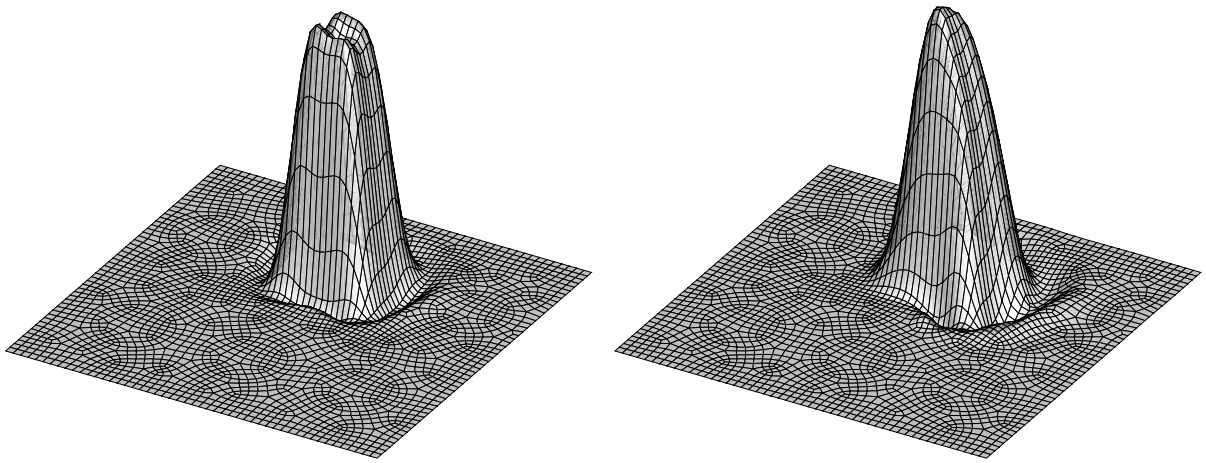


Figure 3.14: Bird's eye view of square pulse advected after one revolution by VPM/MCV (left) and QUICK(right) on unstructured quadrilateral grid.

Table 3.5: Maximum and minimum values in the numerical solutions.

Method	Max	Min
VPM/MCV	1.1147	-6.19×10^{-2}
QUICK	1.1883	-1.15×10^{-1}

for one round revolution. It should be note that unphysical oscillation is still observed in the initial several steps of the computation while rapidly removed with overshoot and undershoot lower than 10^{-3}. From Fig. 3.15 and 3.16, it clearly reveals that the devised TVD limiter effectively suppresses oscillation without introducing excessive diffusive dissipation.

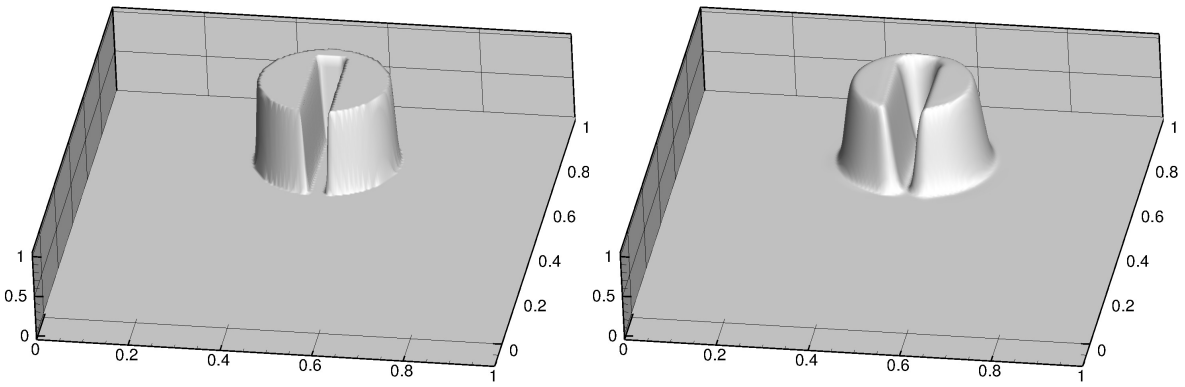


Figure 3.15: Bird's eye view of Zalesak profile advected after one revolution by VPM/MCV scheme equipped with TVD limiter. Left: initial profile, Right: profile after one revolution.

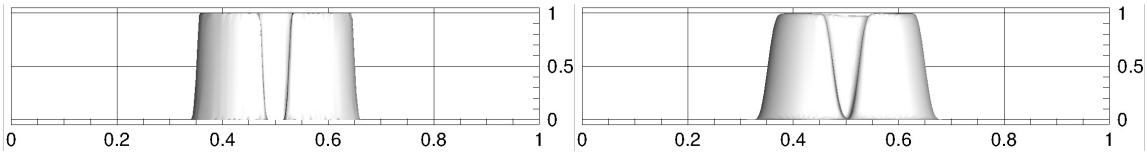


Figure 3.16: X-Z plane view of Zalesak profile advected after one revolution by VPM/MCV scheme equipped with TVD limiter. Left: initial profile, Right: profile after one revolution.

3.10.4 TEC formulation

To evaluate the convergence rate of the TEC scheme, we compute PV at cell vertices from VIA with TEC formulation and validate solution by exact value of sine function on gradually refined grids. The initial VIA is defined by formulation

$$\phi_0(x, y) = \sin 2\pi(x + y) \tag{3.93}$$

over a $[0, 1] \times [0, 1]$ computational domain, the periodic boundary condition is imposed in both x and y directions. The results are give in (3.6) and it is observed that TEC scheme is overall of 2th order accuracy in both L_1 and L_2 norms.

Table 3.6: Numerical errors and convergence orders of least square TEC scheme.

Cell number	L_1 error	L_1 order	L_2 error	L_2 order
226	8.274×10^{-2}	–	8.403×10^{-2}	–
894	2.131×10^{-2}	1.97	2.152×10^{-2}	1.98
3588	5.272×10^{-3}	2.01	5.301×10^{-3}	2.02
14412	1.319×10^{-3}	1.99	1.326×10^{-3}	1.99
57518	3.307×10^{-4}	2.00	3.329×10^{-4}	2.00

Table 3.7: Numerical errors of the least square TEC scheme.

Cell number	L_1 error	L_2 error	L_∞ order
Grid A	2.131×10^{-2}	2.152×10^{-2}	3.119×10^{-2}
Grid B	2.068×10^{-2}	2.111×10^{-2}	3.335×10^{-2}

In order to verify the robustness of this TEC scheme, we generate two type mesh as shown in Fig. 3.17 where distorted elements are generated to distribute on the major region of domain. Both L_1, L_2 and L_∞ are investigated and given in Table 3.7. As we can see, there is no significant accuracy lost observed due to bad quality of grid. It's seen that TEC scheme provides convenient and robust facility for adding any forcing term of PV with approximation from VIA in the governing equations.

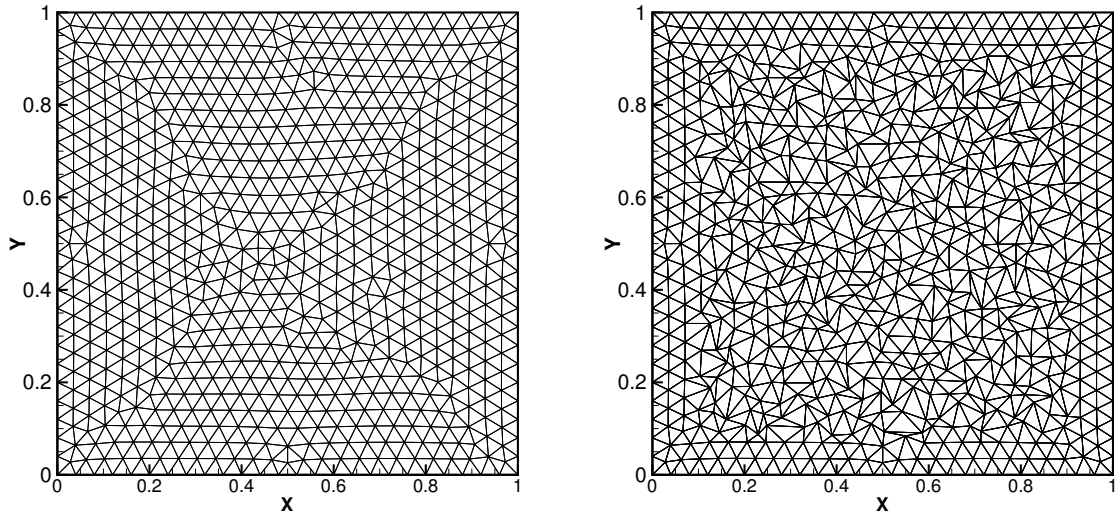


Figure 3.17: The computational meshes for Poisson equation test. Left (grid A): a mesh generated by Delaunay algorithm. Right (grid B): a mesh where a region has heavily distorted triangular elements with bad conditions in orthogonality, skewness and uniformity.

3.10.5 Elliptic equation for Poisson problem

The Poisson equation $\triangle\phi = \omega$ is solved in domain of $[0,1]^2$[35]. The exact solution for this problem with Dirichlet boundary condition is given by $\phi_{exact}(x,y) = \cos(\pi x)\cos(\pi y)$ and the forcing term is in the form of $\omega(x,y) = 2\pi^2\cos(\pi x)\cos(\pi y)$. We solve this equation by MCV, FVM and FEM respectively on different grid resolution and the L_1 error and convergence rate are given in the Table 3.8. We can find the present scheme has consistent 2-order convergence rate and the L_1 error is even 5 times smaller than FEM method which is usually thought to be more accurate and stable than finite volume type method for elliptic type equation.

Table 3.8: Numerical errors and convergence orders of Poisson equation.

Cell number	L_1 error of MCV	Rate	L_1 error of VPM	Rate	L_1 error of FEM	Rate
226	3.491×10^{-3}	–	1.421×10^{-2}	–	1.746×10^{-2}	–
894	7.616×10^{-4}	2.20	5.206×10^{-3}	1.46	4.335×10^{-3}	2.03
3588	1.864×10^{-4}	2.03	2.183×10^{-3}	1.25	1.075×10^{-3}	2.01
14412	4.330×10^{-5}	2.10	1.056×10^{-3}	1.04	2.670×10^{-4}	2.00
57518	1.027×10^{-5}	2.08	5.415×10^{-4}	0.97	6.726×10^{-5}	2.00

In order to evaluate the robustness of this method, we generate grid A and grid B as shown in Fig. 3.17. Grid A is generated by the Delaunay algorithm and has good quality, while grid B has a region filled with heavily distorted elements with large skewness and high aspect ratio. Furthermore, we compute FVM, MCV and FEM methods on both

Method	L_1 error for grid A	L_1 error for grid B	Degradation error
MCV	4.898×10^{-4}	1.219×10^{-3}	7.292×10^{-4}
FVM	3.873×10^{-3}	8.996×10^{-3}	5.123×10^{-3}
FEM	2.755×10^{-3}	3.678×10^{-3}	9.230×10^{-4}

Table 3.9: Degradation error for Poisson equation computed by MCV, FVM and FEM methods.

grids and calculate the L_1 error as well as degradation error defined by (3.92) for each case. From Table 3.9, we can find, no matter on grid A and grid B, both L_1 error and degradation error of MCV method are only about 1/7 of FVM method. Moreover, the L_1 error of MCV scheme computed on grid B is only 1/3 of FVM's result on grid A. We also can note L_1 error of MCV method is less than 1/3 of FEM method and degradation error is only 80% compared with FEM method. This indicates that using PVs located at cell center and cell vertices and evaluating with the least-square approximation, MCV scheme can substantially improve the accuracy and minimize the error due to non-orthogonality of grid, thus possesses powerful capability to ensure reliability and stability for the problems involving complex geometry.

3.10.6 Taylor vortex problem

To evaluate the accuracy of the whole incompressible fluid solver, we compute the Taylor vortex problem [136, 35]. An analytical solution for this problem is available as

$$u(x,y,t) = -\cos(\pi x)\sin(\pi y)\exp\left(-\frac{2\pi^2 t}{Re}\right), \tag{3.94}$$

$$v(x,y,t) = \sin(\pi x)\cos(\pi y)\exp\left(-\frac{2\pi^2 t}{Re}\right), \tag{3.95}$$

$$p(x,y,t) = -\frac{1}{4}(\cos(2\pi x)+\sin(2\pi y))\exp\left(-\frac{4\pi^2 t}{Re}\right), \tag{3.96}$$

where Re is the Reynolds number. Differing in Runge-Kutta method or BDF method for time integration and corresponding PS-MCV or PS-MCV method for Poisson formulation as described in section 3.3, we develop VPM/MCV-RK and VPM/MCV-BDF separately for comparison.

We compute this test problem over $[-1,1]\times[-1,1]$ domain with the periodical boundary condition, using grids of different resolutions generated by Delaunay algorithm. We use $Re = 100$ in this example. Our interest here is to evaluate the numerical accuracy in spatial discretization, and a relatively small time stepping increment ($\Delta t = 10^{-4}$) is used. We firstly verify the performance of VPM/MCV-RK model and the numerical errors and convergence rates for both velocity and pressure fields at $t = 0.1$ are shown in Table 3.10

Table 3.10: Numerical errors and convergence rates of VPM and conventional FVM models for Taylor vortex problem.

Method	Cell number	L_2 error of $\|\mathbf{u}\|$	Order in $\|\mathbf{u}\|$	L_2 error of p	Order in p
VPM/MCV (RK)	902	7.842×10^{-3}	–	2.361×10^{-2}	–
	3604	1.409×10^{-3}	2.48	5.523×10^{-3}	2.10
	14362	2.183×10^{-4}	2.70	1.173×10^{-3}	2.24
	57670	3.598×10^{-5}	2.59	3.015×10^{-4}	1.95
FVM (QUICK)	902	3.744×10^{-2}	–	3.284×10^{-1}	–
	3604	1.443×10^{-2}	1.38	1.423×10^{-1}	1.21
	14362	6.987×10^{-3}	1.05	6.710×10^{-2}	1.09
	57670	3.029×10^{-3}	1.20	4.147×10^{-2}	0.69
FVM (Superbee)	902	4.322×10^{-2}	–	3.581×10^{-1}	–
	3604	1.704×10^{-2}	1.34	1.469×10^{-1}	1.29
	14362	7.188×10^{-3}	1.25	6.756×10^{-2}	1.12
	57670	3.027×10^{-3}	1.24	4.113×10^{-2}	0.71
FVM (MUSCL)	902	3.778×10^{-2}	–	3.619×10^{-1}	–
	3604	1.569×10^{-2}	1.27	1.469×10^{-1}	1.30
	14362	7.283×10^{-3}	1.11	6.609×10^{-2}	1.16
	57670	3.087×10^{-3}	1.23	4.083×10^{-2}	0.69

and Fig. 3.18. We also include the results of the conventional finite volume method with the QUICK, superbee-TVD and MUSCL schemes as the advection solvers. It should be noted that the conventional FVM model was generated by merging the templates provided by the OpenFOAM source code into the projection solution procedure shown in 3.8.1.

It is observed that the VPM/MCV-RK method is more accurate than the conventional FVM models regarding both numerical errors and convergence rate. Numerical solution in velocity of VPM/MCV-RK shows a convergence rate (order) higher than 2.5. In the results on the refined mesh (57670 cells), due to the high convergence rate the numerical errors of VPM/MCV-RK model in both velocity and pressure are reduced down to only 1% of those in the conventional FVM models. It is also found that the errors in velocity are approximately one-tenth of those in pressure in all results.

Using both VIA and PV as the computational variables causes an increase in memory requirement. For a single physical field, we need to keep the PVs at the element vertices as the new degrees of freedom (DOFs) in addition to the VIAs used in the conventional FVM. It also leads to an increase in CPU consumption. As described before, the spatial discretization can be computed efficiently. Being the computational variables, the PVs at cell vertices are always ready for use in the calculation of the numerical fluxes, which largely simplify the operations and save CPU time.

The computational cost of the full fluid solver is also evaluated using Taylor vortex test

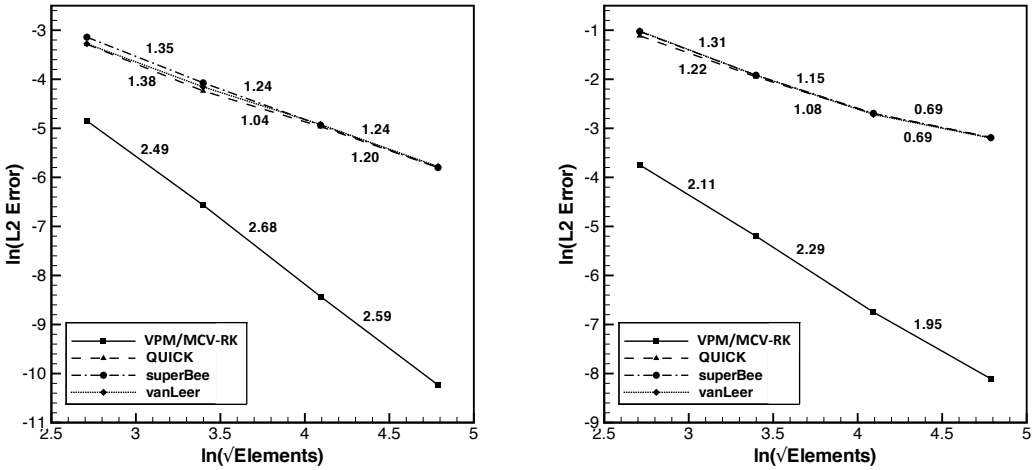


Figure 3.18: The numerical errors and convergence rates for velocity (left) and pressure (right).

shown above. The elapse time is measured by integrating the incompressible fluid model for 1000 steps with a small time step interval. In order to compare the VPM/MCV-RK model with the QUICK conventional FVM model in terms of both numerical accuracy and computational cost, we also include the numerical errors obtained in the previous test. Shown in Table 3.11, about 34% increase is seen in the memory requirement due to the fact that we only use the VIA for pressure field. The increase in elapse time varies with grid resolution, which is smaller for a coarse grid and becomes larger toward a saturation value of 42% when the number of grid cells is larger than 10^4. The increase in CPU consumption of the whole fluid solver is less significant than that of the pure advection computation. This result is consistent with the common understanding that the pressure Poisson equation consumes a large portion of the CPU time. It is observed that the numerical errors of VPM/MCV-RK can be smaller than the conventional FVM by two orders of magnitude. Similar to the advection case, we can conclude that the VPM/MCV-RK model is much superior in computational efficiency and requires much less hardware resource to reach a given error level in comparison with conventional FVM model. This justifies the practical utility of the VPM/MCV-RK method.

Table 3.11: Computation cost and numerical accuracy for incompressible fluid solvers.

	QUICK				VPM/MCV-RK			
Elements	DOFs	Time(s)	L_2 error of $\|\mathbf{u}\|$	L_2 error of p	DOFs	Time(s)	L_2 error of $\|\mathbf{u}\|$	L_2 error of p
902	2706	4.24	3.74×10^{-2}	3.28×10^{-1}	3690	5.03	7.84×10^{-3}	2.36×10^{-2}
3604	10812	12.43	1.44×10^{-2}	1.42×10^{-1}	14578	16.27	1.40×10^{-3}	5.52×10^{-3}
14362	43086	47.78	6.99×10^{-3}	6.71×10^{-2}	57770	68.25	2.18×10^{-4}	1.17×10^{-3}
57670	173010	226.32	3.03×10^{-3}	4.15×10^{-2}	231322	317.60	3.60×10^{-5}	3.01×10^{-4}

With the same computational condition, we reproduce this test by the other numerical

model of VPM/MCV-BDF. The L_2 error and convergence rate for both velocity and pressure are shown in Fig. 3.12. Compared with results of FVM-QUICK and VPM/MCV-RK[177], the present scheme possesses relative higher accuracy and superior convergence rate than VPM/MCV-RK scheme with only half extra cost in CPU time. The same with VPM/MCV-RK scheme, it shows absolute superiority compared with FVM-QUICK for both velocity and pressure in accuracy and convergence rate.

Table 3.12: L_2 error and convergence rate for incompressible solvers and compared with FVM(QUICK) and VPM method.

Elements		902	3604	14362	57670
FVM-QUICK	L_2 error of $\|\mathbf{u}\|$	5.379×10^{-2}	2.219×10^{-2}	6.920×10^{-3}	1.642×10^{-3}
	Rate	–	1.28	1.69	2.07
	L_2 error of p	5.781×10^{-1}	2.436×10^{-1}	6.743×10^{-2}	2.582×10^{-2}
	Rate	–	1.25	1.86	1.38
	Time(s)	4.24	12.43	47.78	226.32
VPM/MCV-RK	L_2 error of $\|\mathbf{u}\|$	7.851×10^{-3}	1.410×10^{-3}	2.183×10^{-4}	4.121×10^{-5}
	Rate	–	2.48	2.70	2.40
	L_2 error of p	2.819×10^{-2}	6.603×10^{-3}	1.194×10^{-3}	3.779×10^{-4}
	Rate	–	2.10	2.47	1.66
	Time(s)	5.03	16.27	68.25	317.60
VPM/MCV-BDF	L_2 error of $\|\mathbf{u}\|$	5.645×10^{-3}	8.837×10^{-4}	1.265×10^{-4}	1.780×10^{-5}
	Rate	–	2.68	2.81	2.82
	L_2 error of p	3.131×10^{-2}	5.941×10^{-3}	1.075×10^{-3}	2.623×10^{-4}
	Rate	–	2.40	2.47	2.03
	Time(s)	4.08	13.04	57.22	281.25

To evaluate the robustness, we compute this problem on both grid A and grid B which scaled to $[-1, 1]^2$. The time steps is automatically adjusted by CFL number 0.1. We computed L_1 error and degradation error on time 1 and compare with the results of FVM-QUICK, VPM/MCV-RK method. The L_1 error of VPM/MCV-BDF on grid B is significantly reduced compared with VPM/MCV-RK and only a little higher than L_1 error of VPM/MCV-RK on grid A. For velocity, we can find both L_1 error and degradation error is about 1/4 of VPM/MCV-RK and only 1/7 of FVM-QUICK. The L_1 error of pressure is also found smaller for both grids. More visually, we plot the pressure contour profile on grid B for FVM-QUICK, VPM/MCV-RK and VPM/MCV-BDF as shown in Fig. 3.19. We can realize the result of VPM/MCV-BDF scheme is most accurate among three type methods and its profile is visually indistinguishable from that of exact solution. Compared with profile of FVM-QUICK and VPM/MCV-RK scheme, we almost cannot observe evident degradation caused by heavily distorted elements. This demonstrates the adopted least square approximation can effectively improve the robustness of the scheme

Method	L_1 error of $\|\mathbf{u}\|$			L_1 error of p		
	Grid A	Grid B	Degradation error	Grid A	Grid B	Degradation error
FVM-QUICK	2.416×10^{-2}	6.876×10^{-2}	4.460×10^{-2}	1.434×10^{-1}	2.502×10^{-1}	1.068×10^{-1}
VPM/MCV-RK	9.562×10^{-3}	3.348×10^{-2}	2.392×10^{-2}	4.267×10^{-2}	7.598×10^{-2}	3.331×10^{-2}
VPM/MCV-BDF	3.592×10^{-3}	1.071×10^{-2}	7.118×10^{-3}	1.002×10^{-2}	3.547×10^{-2}	2.545×10^{-2}

Table 3.13: Degradation error for shear vortex problem computed by FVM(QUICK), VPM/MCV-RK and VPM/MCV-BDF method.

Elements	Initial kinetic	VPM/MCV-RK		VPM/MCV-BDF	
		Final kinetic	Dissipation rate	Final kinetic	Dissipation rate
902	0.247876	0.244266	1.456×10^{-2}	0.245400	9.989×10^{-3}
3604	0.249466	0.247922	6.189×10^{-3}	0.249110	1.427×10^{-3}
14362	0.249867	0.248611	5.027×10^{-3}	0.249812	2.201×10^{-4}
57670	0.249967	0.248749	4.873×10^{-3}	0.249962	2.000×10^{-5}

Table 3.14: Kinetic variation and related dissipation rate.

as it evaluates the surrounding information in more exact way.

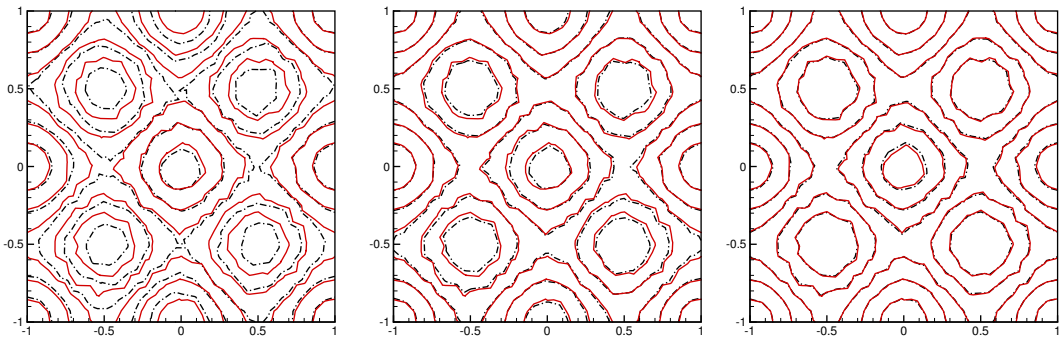


Figure 3.19: Pressure contour profile computed on Grid B by QUICK, VPM/MCV-RK, VPM/MCV-BDF method respectively(left to right). The red solid line is for exact solution and black dot line is for present results.

For turbulent flow simulation, the dissipative scale is a crutial issue which often overwhelms the effect of subgrid model and molecular viscosity of large-eddy simulation (LES). In order to investigate the numerical dissipation, kinetic energy is introduced by integrating over the whole periodic domain $K_{\text{taylor}} = \frac{1}{4}\int_{-1}^{1}\int_{-1}^{1}\frac{u^2+v^2}{2}dxdy$ where u, v are velocity component for x, y direction. Therefore, exact and numerical kinetic energy is obtained as

$$K_{\text{exact}} = \tfrac{1}{4}e^{-\frac{4\pi^2 t}{Re}},$$
$$K_{\text{numerical}} = \frac{1}{\sum|\Omega_i|}\sum\left(\frac{u_i^2+v_i^2}{2}\,|\Omega_i|\right),$$

where the subscript stands for the quantity of ith cell. The simulation of Taylor vortex

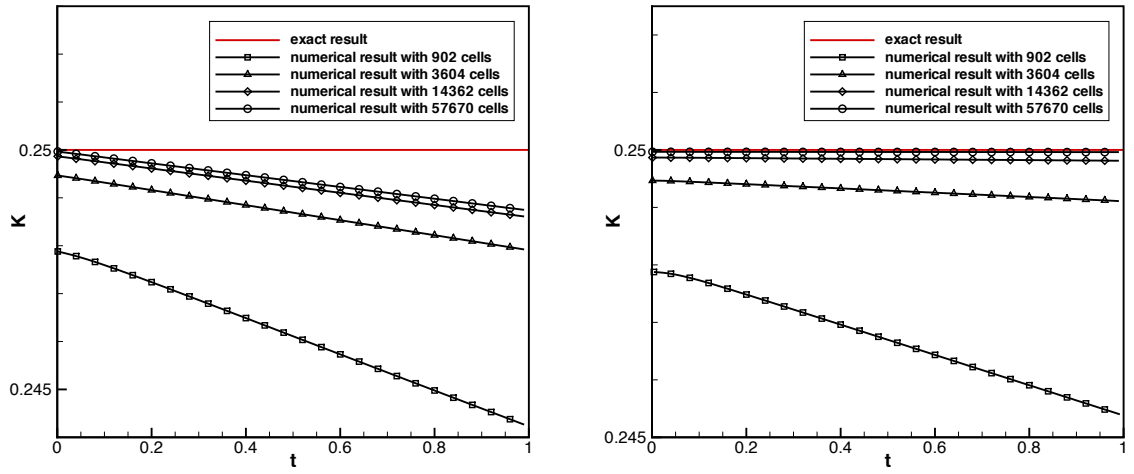


Figure 3.20: The kinetic energy for inviscid simulation of Taylor vortex problem with time step 0.001. Left: results of VPM/MCV-RK computed on different grid resolution. Right: results of VPM/MCV-BDF computed on different grid resolution.

problem in the limit of infinite Reynolds number should result in a steady solution of non-decaying vortex with constant kinetic energy, $K = 1/4$. The numerical experiment is performed with periodic boundary condition, time step as 0.001 on the different grid resolution and ends at time with 1. As shown in Fig. 3.20, the numerical dissipation of VPM/MCV-BDF scheme is significantly reduced compared with VPM/MCV-RK scheme and we can observe rapid convergence behavior by mesh refinement. In order to quantitatively verify the numerical dissipation, we define dissipation rate as

$$\text{dissipation rate} = \frac{K_{\text{initial}} - K_{\text{final}}}{K_{\text{initial}}}, \tag{3.97}$$

where K_{initial} and K_{final} represent initial and final numerical dissipation as shown in Table 3.14. Given in Table 3.14, numerical dissipation as well as dissipation rate of VPM/MCV-BDF scheme is much smaller than results of VPM/MCV-RK and converges as fast as nearly three order as shown as in Fig. 3.21. On the finest mesh with 57670 elements, the numerical dissipation generated by VPM/MCV-BDF scheme is negligible which can also be confirmed from Fig. 3.20. This improvement comes from both sophisticated spatial discretization procedure and BDF2 scheme for higher order of temporal accuracy which effectively suppressed the numerical dissipation and dispersion. This indicates VPM/MCV-BDF scheme is a quite desirable platform to be further developed to solve turbulent flow problem.

3.10.7 Lid driven square cavity problem

This is the most widely used benchmark test for numerical codes designed to solve viscous incompressible flows[41]. Incompressible flow is enclosed in a square $[0, 1] \times [0, 1]$ domain.

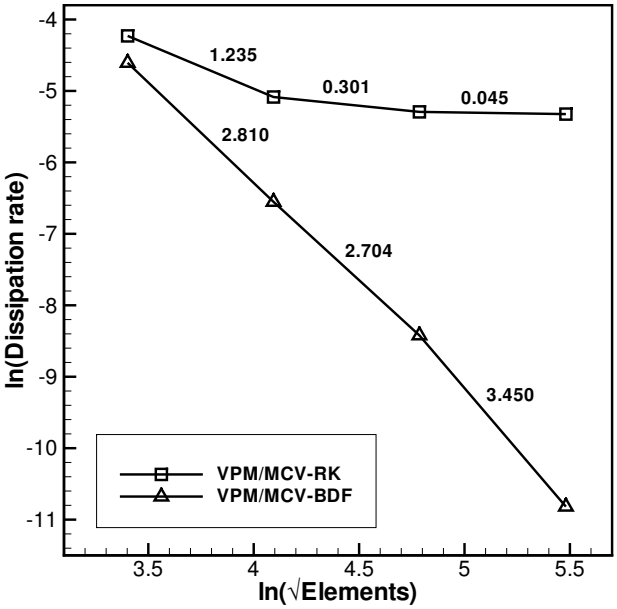


Figure 3.21: Convergence rate of dissipation rate.

Nonslip boundary conditions are imposed on the 4 walls. The upper wall $y = 1$ is moving at a constant speed ($u = 1,\ v = 0$). Numerical tests are carried out with triangular unstructured grids (upper-left panel of Fig. 3.22) of different resolutions. It is known that a steady solution is reached with this Reynolds number, which is identified by the criterion of $\max |p_i^{n+1} - p_i^n| < 10^{-9}$. We plot the numerical results of different grid resolutions in Fig. 3.22. It is observed that the numerical solution of present model converges to the reference solution with a modest mesh resolution. We also show the results of the conventional FVM with different advection schemes in Fig. 3.23 for comparison. It is obvious that the present model is more accurate than the conventional FVM.

At meanwhile, numerical tests are carried out on quadrilateral unstructured grid shown in the top-left panel of Fig. 3.24 with different resolutions. We plot the numerical results also in Fig. 3.24. The stream line (top-right panel) of the steady solution on the grid of 4523 cells visually verifies the numerical solution where the primary and secondary vortices are well resolved. The velocity component profiles across both horizontal and vertical central lines are displayed in the bottom panels of Fig. 3.24. We use different grid resolutions to see how fast the numerical solution approaches the reference solution. It is observed that the numerical solution of present model converges to the reference solution with a modest mesh resolution.

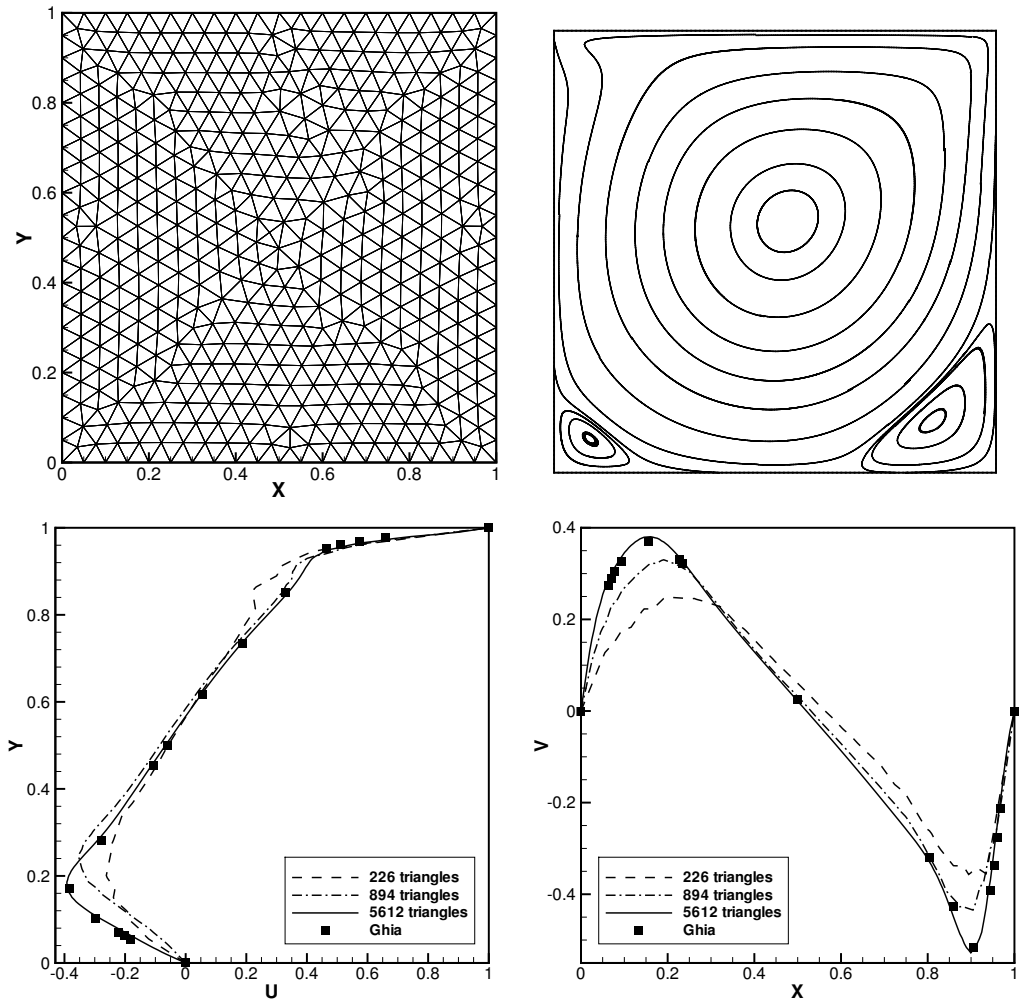


Figure 3.22: Numerical results of square cavity flow problem. Displayed are stream line on a 5612-cell mesh (left), u profiles along $x = 0.5$ line (middle) and v profiles along $y = 0.5$ line (right) on grids of different resolutions.

3.10.8 Lid driven forward-step cavity problem

A cavity with a forward-step shown in the upper-left panel of Fig. 3.25 is used in [117] to evaluate numerical solvers developed in general coordinates. Compared to the square cavity in Fig. 3.22, the lower-left corner of the flow path is blocked which will generate separations, significant secondary vortices and other complexity in flow patterns [28]. Numerical results are given in Fig. 3.25 with the reference velocity profiles provided in [117] which are computed on a 512×512 curvilinear grids. Shown in Fig. 3.25 (middle and right panels), the present model is able to reproduce adequate solutions even with much coarser mesh resolutions. The solutions on meshes of more than 2704 cells agree well with the reference solution.

The forward-step cavity generated with quadrilateral elements shown in the top-left panel of Fig. 3.26 is also used for verification. The streamline is plotted in the top-

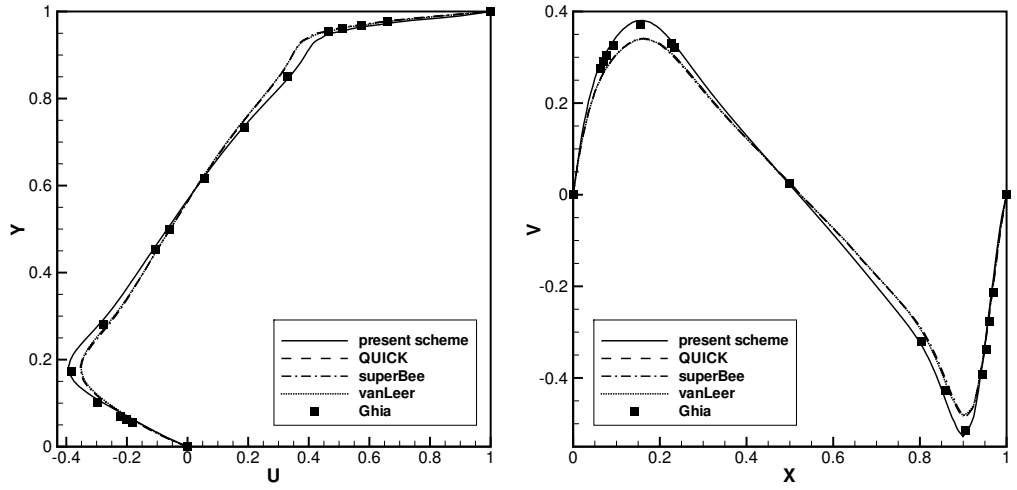


Figure 3.23: Numerical results of square cavity flow problem on a 5612-cell mesh. Displayed are the u profile along $x = 0.5$ line (left) and v profile along $y = 0.5$ line (right).

right panel of Fig. 3.26 which looks quite similar to the reference solution in [117]. To quantitatively evaluate the numerical output, we show profiles of the velocity components in both x and y directions in Fig. 3.26 in comparison with the reference solutions from a high resolution simulation provided in [117] which were computed on a 512×512 curvilinear grids. As we can see in the bottom panels in Fig. 3.26, the present model is able to reproduce adequate solutions even with much coarser mesh resolutions. The solutions on meshes of more than 1942 quadrilateral cells agree well with the reference solution.

3.10.9 Lid driven skew cavity problem

Numerical examples of viscous flow in skew cavities with inclined angles of 30° and 45° are found in [27] and [117]. Our numerical results are shown in Fig. 3.27 and Fig. 3.28. The reference solution in [27] is computed on 320×320 structured grids. In the case of 30°, the numerical solution converges to the reference solution with a much coarser grid compared to the case of 45°, which is common to other existing works in the literature. Even though the 45° cavity flow requires a relatively higher resolution mesh for converged solution, it is still much less in comparison with other conventional FVM schemes.

3.10.10 Lid driven semi-circular cavity problem

We compute the lid-driven viscous incompressible flow in a semi-circular cavity (top left panel of Fig. 3.29) which has been extensively investigated in [43]. We use the results in [43] for comparison which are computed on a triangular mesh with a representative size of 1/128. Shown in Fig. 3.29, our results converge to the reference results even with a relatively low mesh resolution.

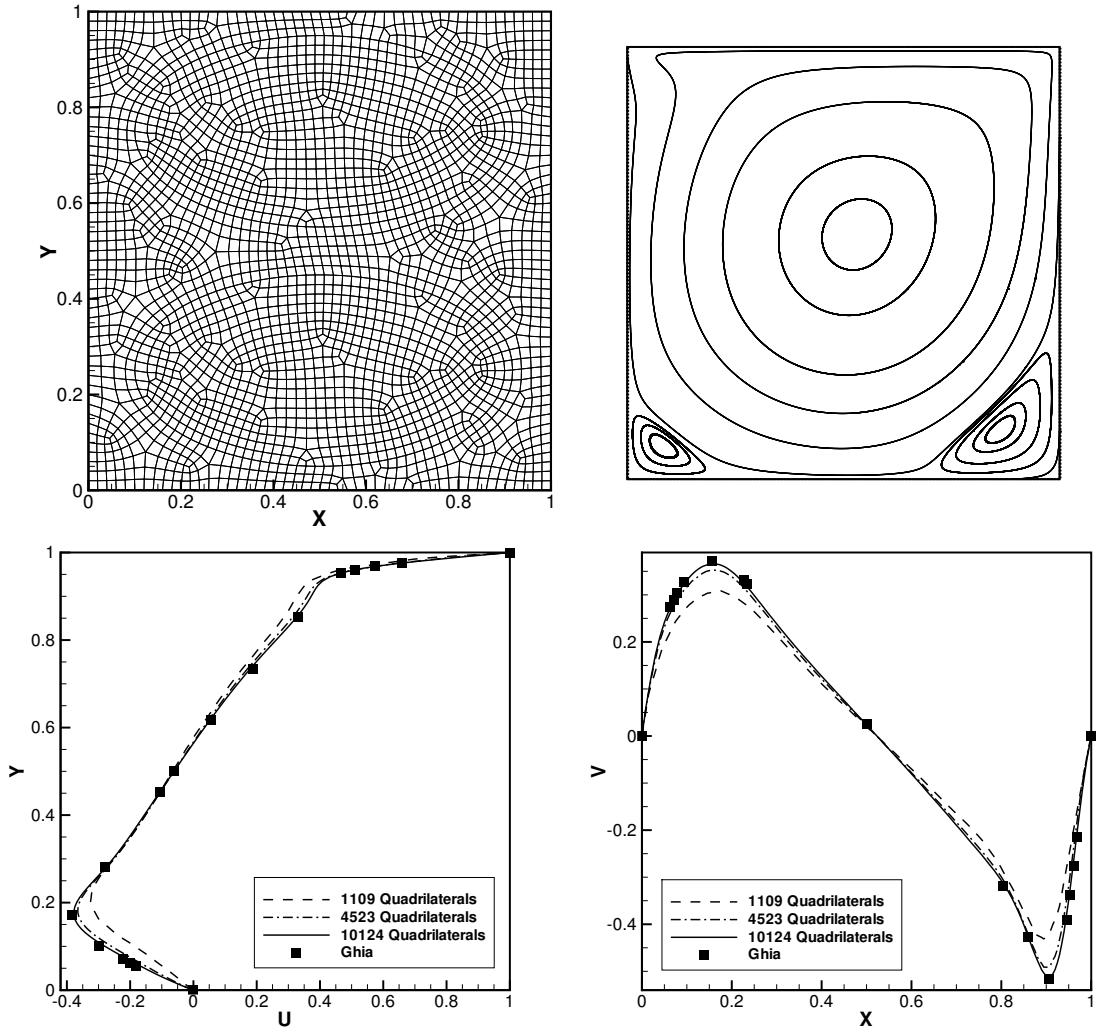


Figure 3.24: Numerical results of square cavity flow problem. Displayed are computational grid (top-left), stream line on a 4523-cell mesh (top-right), u profiles along $x = 0.5$ line (bottom-left) and v profiles along $y = 0.5$ line (bottom-right) on grids of different resolutions.

Again the semi-circular cavity generated with quadrilateral mesh with a representative size of 1/125 is investigated for comparison. Shown in Fig. 3.30, the present model accurately reproduces the numerical results given in the literature. The numerical solution quickly converges to the reference solution when the computational grid is refined. It is seen that our results converge to the reference results even with a relatively low mesh resolution.

3.10.11 3D lid driven cubic cavity problem

We verify the 3D model by simulating a 3D lid driven flow in a unit cube $[-0.5, 0.5] \times [-0.5, 0.5] \times [-0.5, 0.5]$. Following [5], a constant velocity ($v(-0.5, y, z) = 1$) is imposed on surface $x = -0.5$. We compute this test using both regular Cartesian grid (Fig. 3.31(left))

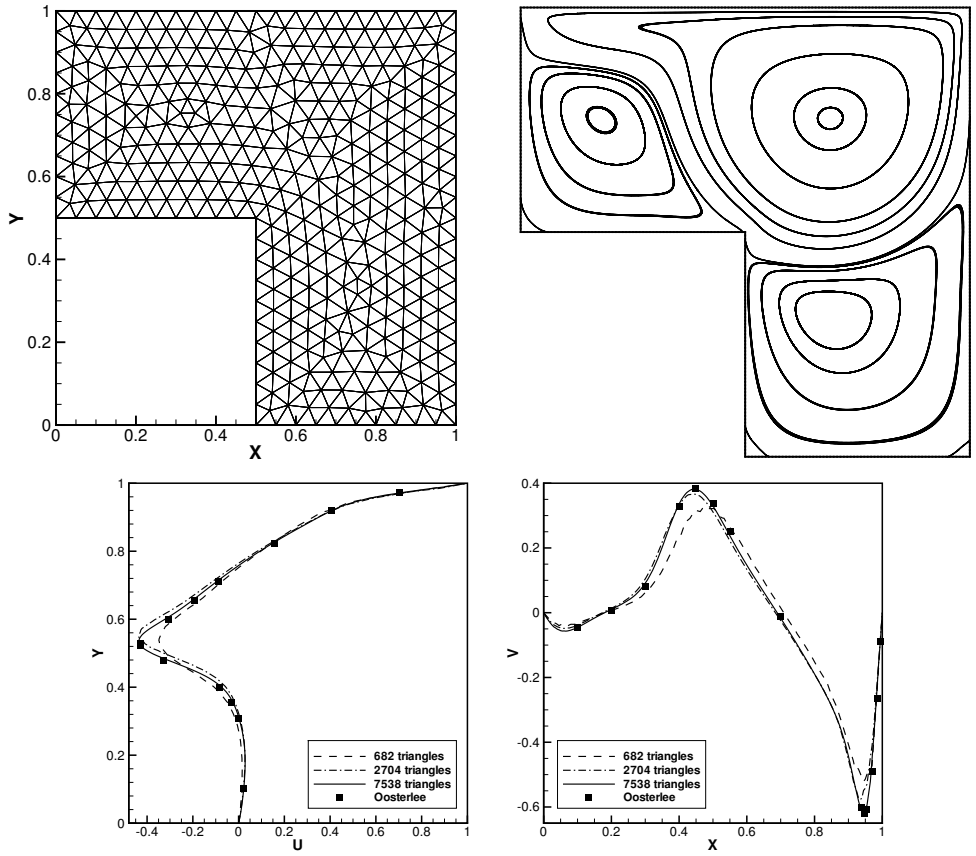


Figure 3.25: Numerical results of forward-step cavity flow problem. Displayed are stream line on a 7538-cell mesh (left), u profile along $x = 0.75$ line (middle) and v profile along $y = 0.75$ line (right).

and irregular hexahedral grid (Fig. 3.31(right)) of different resolutions.

The velocity component in y direction (v) along centerline $(x, 0, 0)$ and that in x direction (u) along centerline $(0, y, 0)$ are plotted in Fig. 3.32 and 3.33 on both Cartesian grid and the irregular hexahedral grid respectively. It is observed that the difference in the results of the Cartesian grids and the irregular hexahedral grids is not significant through all resolutions, which manifests again the robustness of the numerical model. For comparison, we also include the numerical results in [5] as a reference solution which are solved by a Chebyshev-collocation method with $96 \times 96 \times 64$ Gauss-Lobatto points. It is seen that the present model converges quickly to the reference solution on both regular and irregular grids.

The pressure and flow fields on different cross sections are displayed in Fig. 3.34, 3.35 and 3.36. The consistent flow structures developed under the boundary driving and the 3D geometrical constraint. The similar flow patterns are also reported in [184, 48, 139].

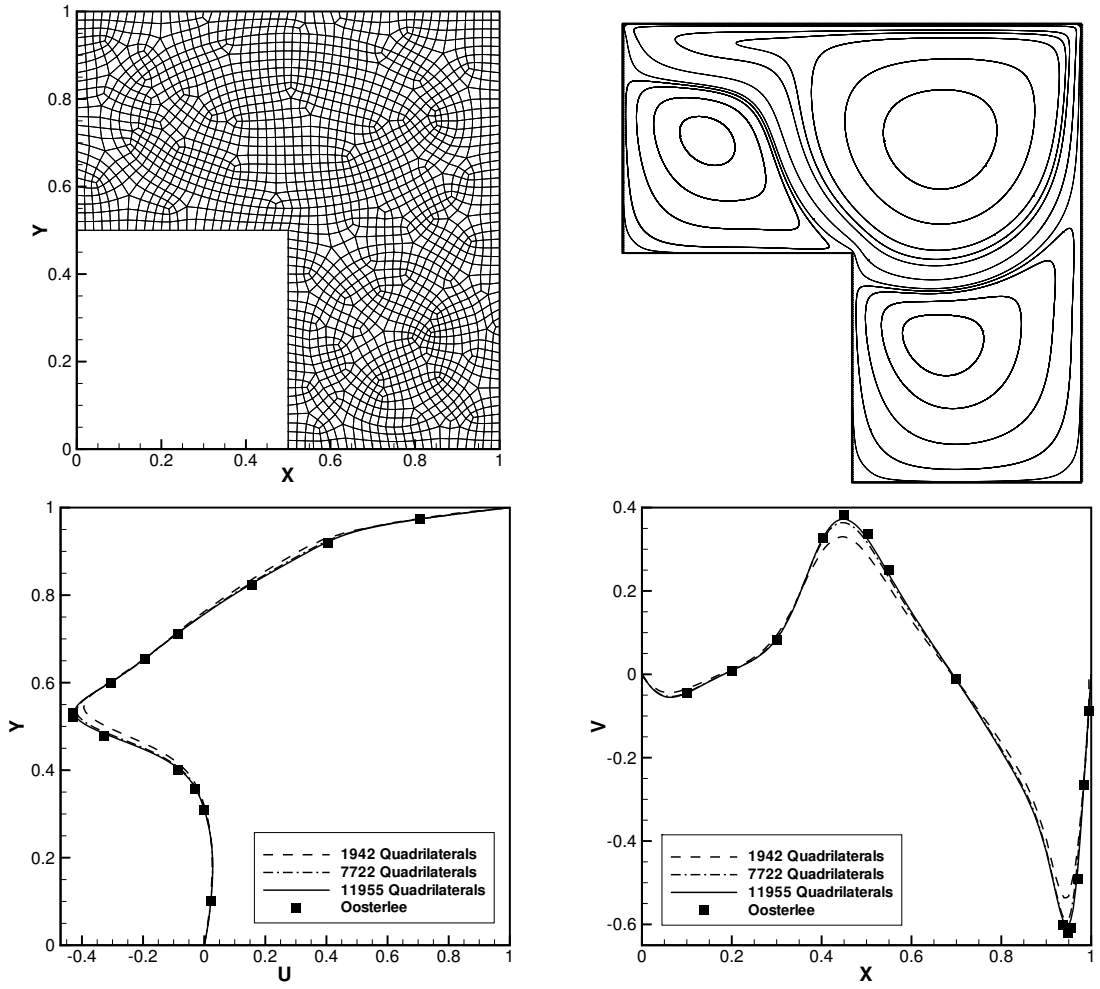


Figure 3.26: Numerical results of forward-step cavity flow problem. Displayed are computational grid (top-left), stream line on a 7722-cell mesh (top-right), u profiles along $x = 0.75$ line (bottom-left) and v profiles along $y = 0.75$ line (bottom-right) on grids of different resolutions.

3.10.12 2D circular explosion shock tests

The symmetric two-dimensional explosion which reported in [150] is chosen to verify the performance of suppressing oscillation for present VPM/MCV scheme integrated TVD limiter. On the computation domain of $[-1, 1] \times [-1, 1]$, the following initial condition is generated:

$$(\rho, m_x, m_y, p) = \begin{cases} (1, 0, 0, 1) & \text{for } r \leq 0.4, \\ (0.125, 0, 0, 0.1) & \text{for } r > 0.4. \end{cases} \tag{3.98}$$

where $r = \sqrt{x^2 + y^2}$ is the radius. The numerical results are resolved by 230498 triangular elements as shown in Fig. 3.37 in the bird's views of the density and pressure at time of 0.25. From results, we can clearly observe axis-symmetric configuration that contains cir-

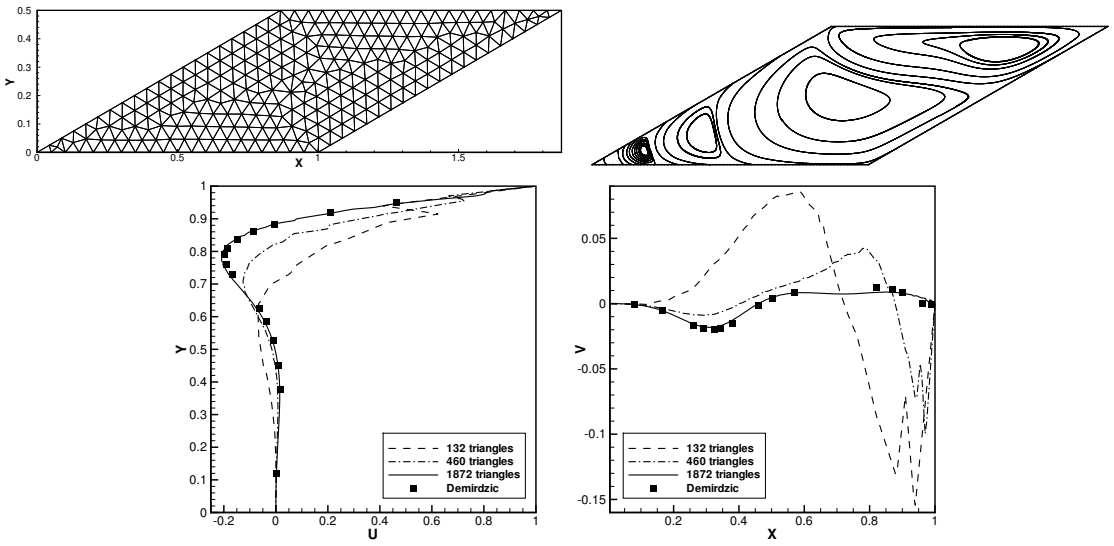


Figure 3.27: Numerical results of a 30° inclined skew cavity flow problem. Displayed are stream line on a 1872-cell mesh (left), u profile along $y = \tan(30^o)(x - 0.5)$ line (middle) and v profile along $y = \tan(30^o)/2$ line (right).

Table 3.15: Computation cost for advection of QUICK and VPM schemes.

Cell No.	QUICK			VPM		
	DOFs	Time(s)	Accuracy	DOFs	Time(s)	Accuracy
121	121	0.37	4.365×10^{-1}	263	0.39	1.334×10^{-1}
484	484	0.53	9.966×10^{-2}	1009	0.91	1.854×10^{-2}
1936	1936	1.15	2.942×10^{-2}	3954	2.91	2.272×10^{-3}
7744	7744	3.51	8.224×10^{-3}	15649	10.86	3.539×10^{-4}
30844	30844	12.54	2.285×10^{-3}	62009	63.77	4.705×10^{-5}

cular out-going shock wave, contact discontinuity and rarefaction wave expanding inward which indicate shock wave, contact discontinuity and rarefaction fan are well resolved.

The capability of present method for resolving low Mach flow is verified by another initial condition reported in [175] as following:

$$(\rho, m_x, m_y, p) = \begin{cases} \left(10^{-3}, 0, 0, 10^4\right) & \text{for } r \leq 0.4, \\ \left(10^{-3}, 0, 0, 0.1\right) & \text{for } r > 0.4. \end{cases} \tag{3.99}$$

The maximum Mach number in this case is as low as 0.01. From result of Fig. 3.38, we can find axis-symmetrical configuration along with very large jumps across the shock and the contact discontinuity are adequately reproduced. Unlike the result in [175], neither overshoot/undershoot of pressure across discontinuity, nor diffusion of density in expansion region is observed in present simulation which indicates present VPM/MCV scheme integrated with TVD limiter can resolve compressible flow in wide range of Mach number with remarkable resolution.

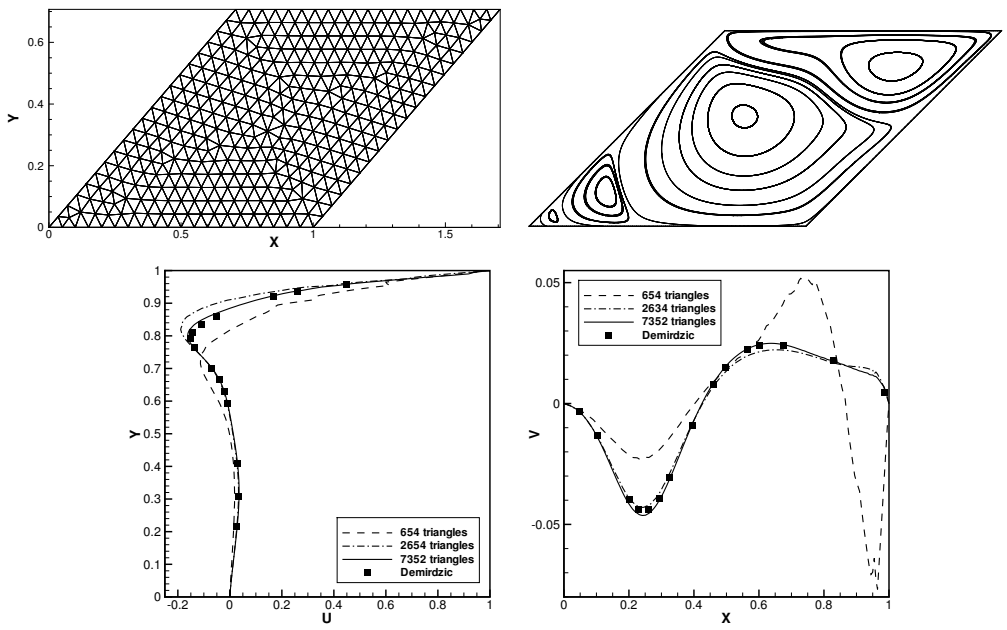


Figure 3.28: Numerical results of a 45° inclined skew cavity flow problem. Displayed are stream line on a 7352-cell mesh (left), u profile along $y = \tan(45^o)(x - 0.5)$ line (middle) and v profile along $y = \tan(45^o)/2$ line (right).

3.10.13 Mach 3 wind tunnel with a step

Mach 3 wind tunnel with a step is proposed by Woodward and Colella [167] as a standard benchmark problem for the 2D Euler equations. The computation is set up by a Mach 3 inflow attacking a step of the wind tunnel which will generate bow and reflected shock waves. The test domain is described as 3 units long and 1 unit wide, with a 0.2 unit high step located at 0.6 units from the left hand side of the tunnel. We set initial condition as $\rho = 1.4$, $p = 1$ and ideal gas with property of $\gamma = 0.14$ everywhere in the domain. The inflow and outflow boundary condition are prescribed on left and right side of domain respectively. A reflection solid wall boundary condition is imposed for top and bottom side of the domain. The numerical results at time of 4s are shown in Fig. 3.39. We can find the numerical solution looks very competitive such that shock waves are adequately resolved as well as jointed point of the three shocks.

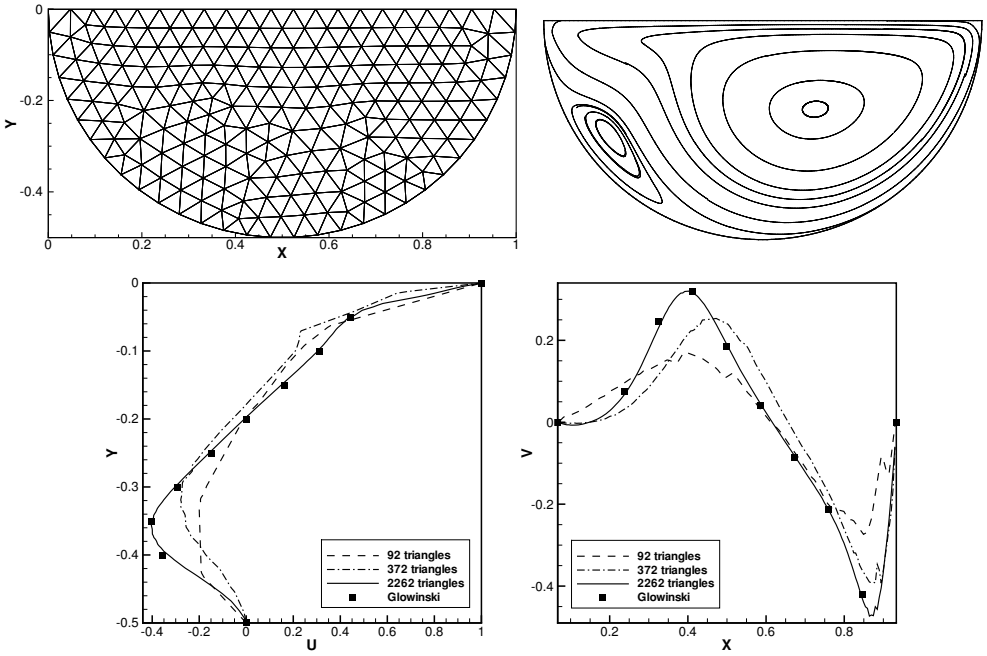


Figure 3.29: Numerical results of semi-circular cavity flow problem. Displayed are stream line on a 2266-cell mesh (left), u profile along $x = 0.5$ line (middle) and v profile along $y = -0.25$ line (right).

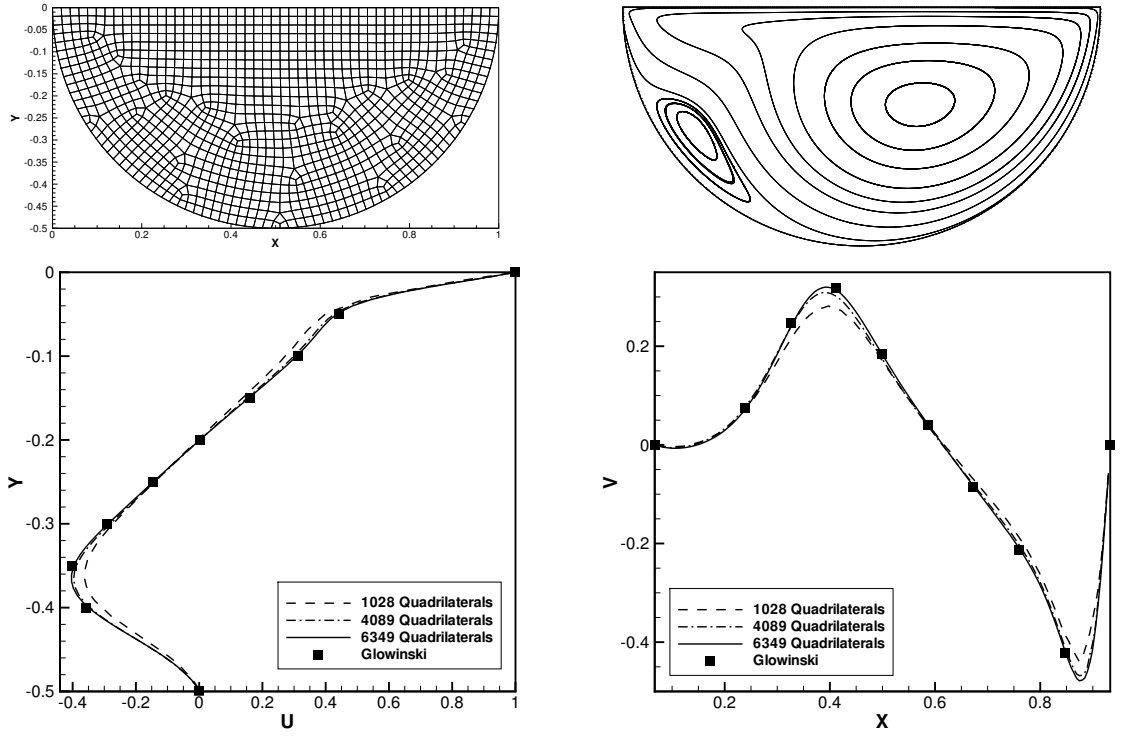


Figure 3.30: Numerical results of semi-circular cavity flow problem. Displayed are computational grid (top-left), stream line on a 4089-cell mesh (top-right), u profiles along $x = 0.5$ line (bottom-left) and v profiles along $y = -0.25$ line (bottom-right) on grids of different resolutions.

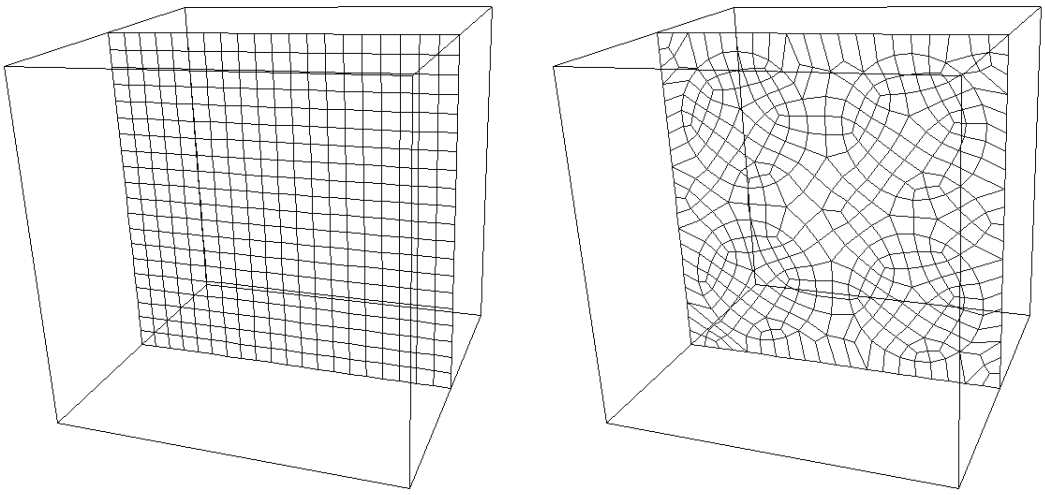


Figure 3.31: Grids used for the 3D lid driven cubic cavity flows. Left: regular Cartesian grid; Right: irregular hexahedral grid.

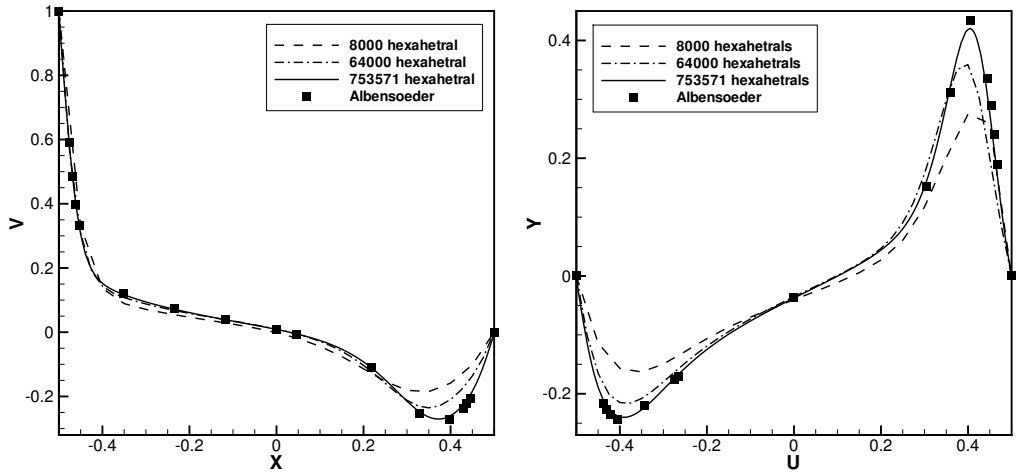


Figure 3.32: Numerical results on Cartesian grid for the 3D lid driven cavity flow. Displayed are v profile along centerline $(x, 0, 0)$ (left) and u profile along centerline $(0, y, 0)$ (right). The reference results of [5] was computed by a Chebyshev-collocation method with $96 \times 96 \times 64$ Gauss-Lobatto points.

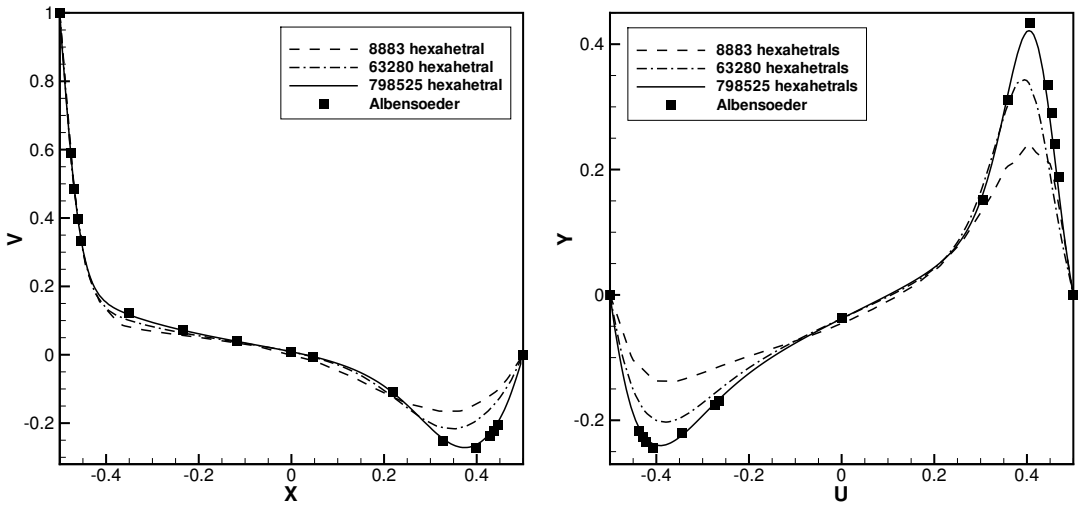


Figure 3.33: Same as Fig. 3.32 but using the irregular hexahedral grid.

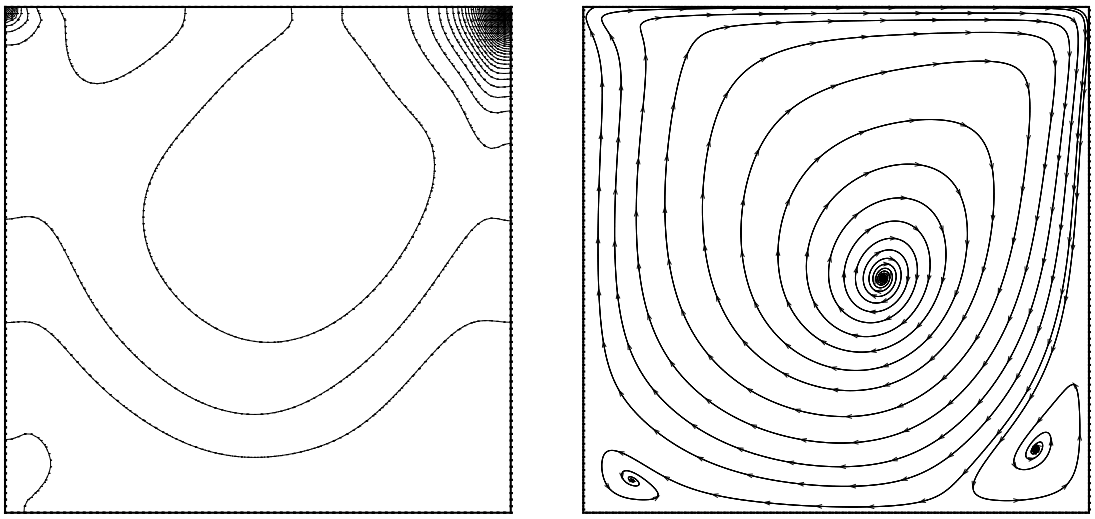


Figure 3.34: Pressure contours (left) and stream lines (right) on $z = 0$ cross-section of the 3D lid-driven cavity flow.

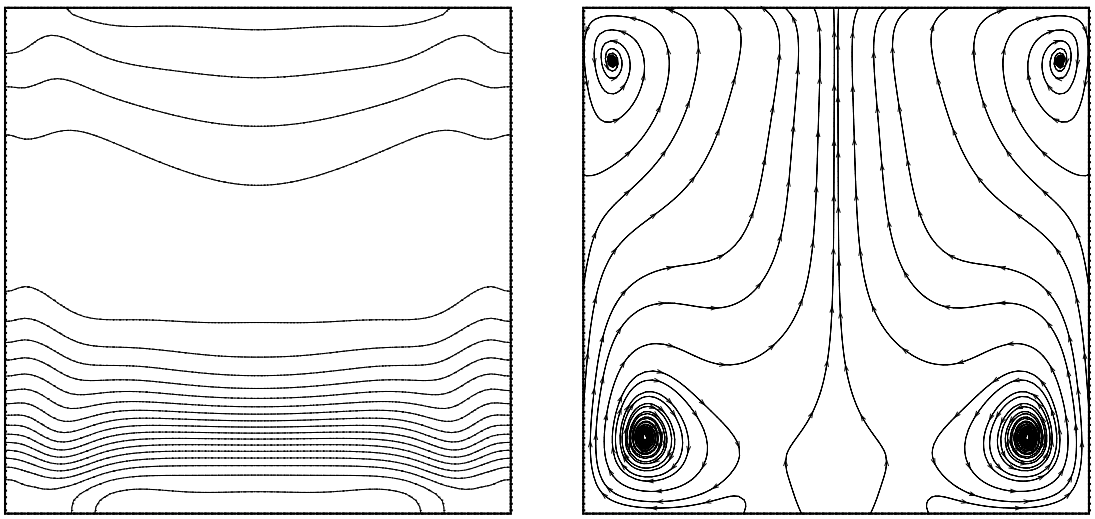


Figure 3.35: Same as Fig. 3.34 but on $y = 0$ cross-section.

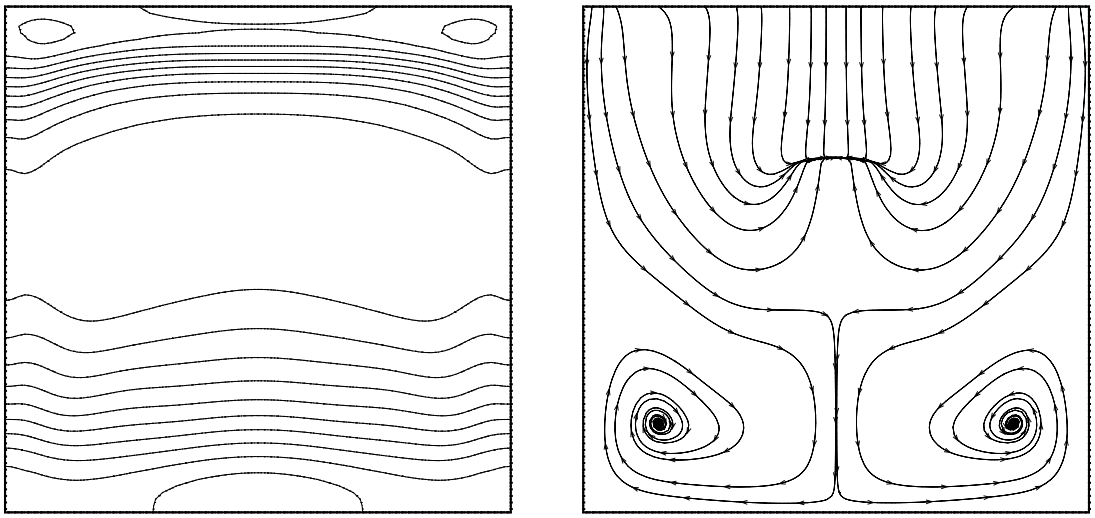


Figure 3.36: Same as Fig. 3.34 but on $x = 0$ cross-section.

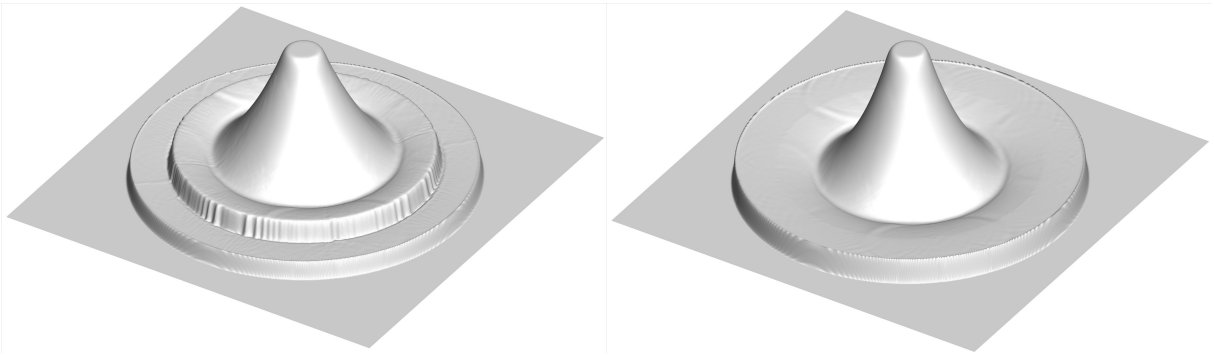


Figure 3.37: Bird's eye views of the density (left) and pressure (right) of the circular explosion test with condition of (3.98) at time of 0.25.

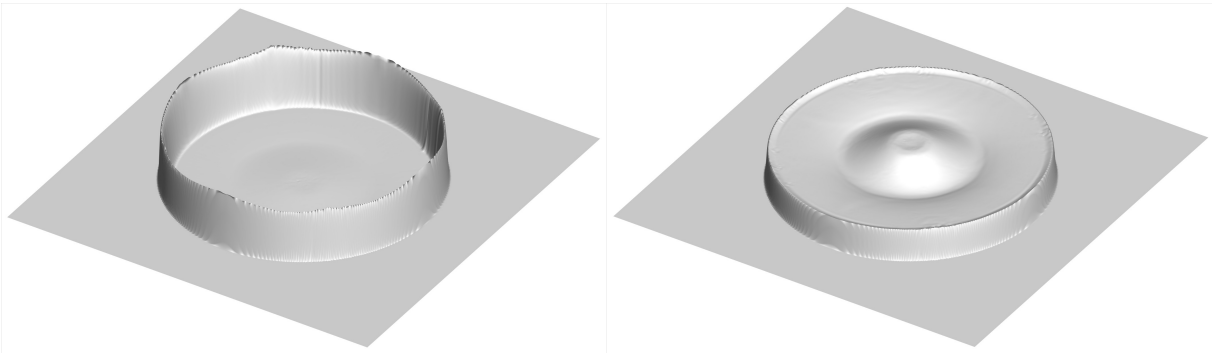


Figure 3.38: Bird's eye views of the density (left) and pressure (right) of the circular explosion test with condition of (3.99) at time of 0.00012.

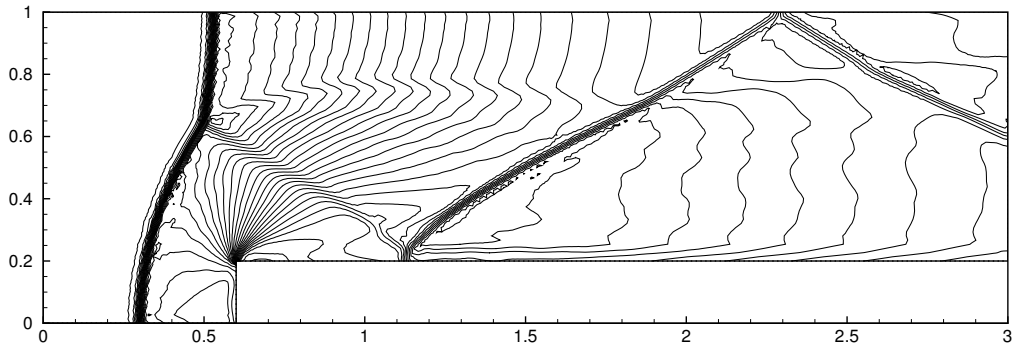


Figure 3.39: Numerical results showing the contour plots of density for the flow past a step test.

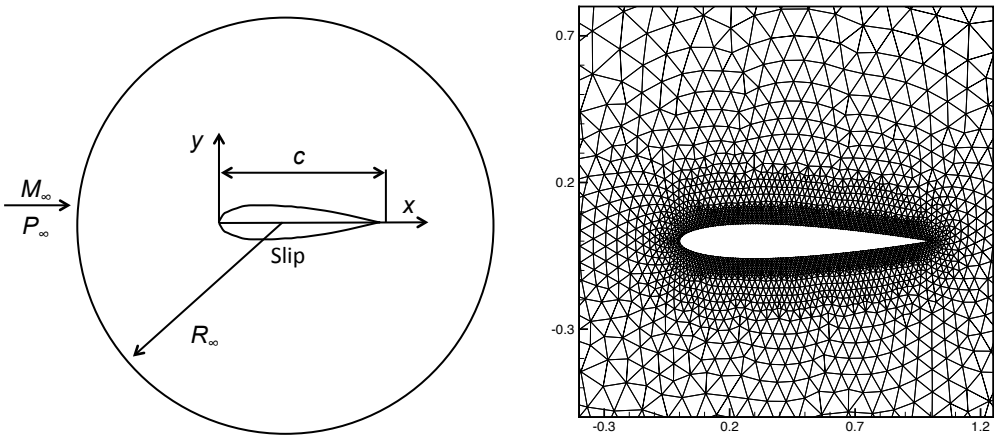


Figure 3.40: Computational structure and grids used in NACA 0012 airfoil test case.

3.10.14 NACA 0012 airfoil

Unlike previous verification tests, we seek to validate the compressible model by conducting simulation on NACA 0012 airfoil[149] and compare results with experiment data. The exact formula of NACA 0012 airfoil is given as

$$y = \pm 0.6 * [0.2969\sqrt{x} - 0.1260x - 0.3516x^2 + 0.2843x^3 - 0.1015x^4]$$

which creates an airfoil with chord $c = 1.0$m using x between 0 and 1.0m. The airfoil is surrounded by an external circular computational domain with radius $R_\infty = 25$m as shown in Fig. 3.40. The inflow attack the inlet with angle of 4 degree by ideal gas of specific heat ratio $\gamma = 1.4$. The thermodynamic pressure is set as $P_\infty = 85419$Pa and Mach number of inlet is specified as $M_\infty = 0.75$. The slip boundary conditions and Riemann boundary conditions are imposed on internal subdomain and external subdomain respectively. The space is discretized with 6620 triangle cells and 6864 nodes as in Fig. 3.40. The pressure coefficient C_p along boundary of airfoil is plotted as Fig. 3.41. We can find present result is in satisfied agreement with experiment data and obviously superior than the results computed by professional aerodynamic source code AeroFoam.

3.10.15 Square cavity flow with wide range of Reynolds number

For high Reynolds number flow, the square lid-driven cavity flow is chosen as first example due to its simplicity in geometry and boundary condition which has been investigated for decades from both theoretical/numerical and experimental point of view[138, 33, 16]. However, it is still a great challenge to realize stable, accurate and efficient approach without any special technique, as mentioned in [86]. The present VPM/MCV-BDF scheme sheds some light to this fundamental issue owing to its property of low diffusion effects. As for Reynolds number higher than 5000, it is still lack of agreement for whether it can

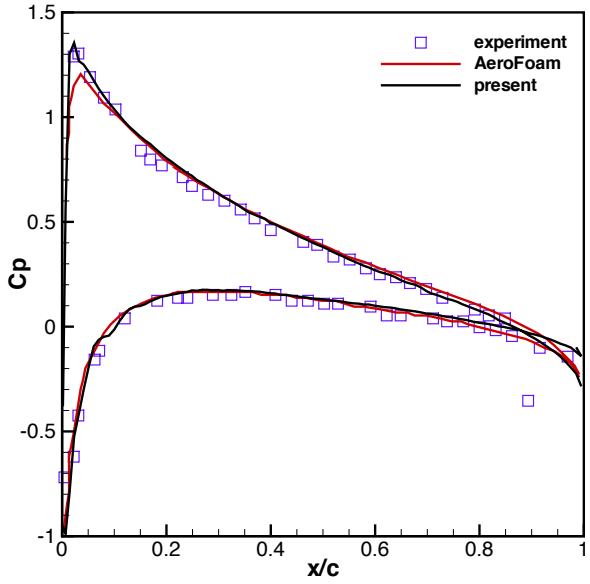


Figure 3.41: Pressure coefficient C_p distribution along boundary of NACA 0012 airfoil.

reach steady solution, which is beyond the scope of present study. For this matter, we verify the benchmark results with relative coarse grid for Reynolds number ranging from 100 to 5000.

As shown in Fig. 3.42(left), the computational domain $[0,1] \times [0,1]$ is divided into non-overlapped hybrid triangular and quadrilateral elements. The boundary condition and schematics of vortices are shown in Fig. 3.42(right). The abbreviation BR, BL and TL represent bottom right, bottom left and top left corner of cavity respectively. The number behind the abbreviation is labeled according to the size of corresponding vortices appearing in the flow.

Fig. 3.43 shows streamline of three Reynolds number from left to right. Initially, the center of primary eddy(where its value is minimum) appeares some right and closed to the lid. With Reynolds number increasing, it is evident that the centre of primary eddy moves lower and towards to the geometric center of cavity. At the meanwhile, both second eddies of BL1 and BR1 grow in size, and BR1's growth is greater which can also be observed from its streamfunction value as shown afterwards. On the Reynolds number of 5000, the emergence of the upstream eddy TL is observed to attach to a plane wall which agrees well with literatures. In Fig. 3.44, the vorticity defined as $\omega = (\partial v/\partial x) - (\partial u/\partial y)$ is draw for a range of $-10 \leq \omega \leq 3$. As the Reynolds number increases, the vorticity in primary eddy becomes nearly constant due to the quasi-linear property of velocity profile, while vorticity changes more dramatically near the boundary.

The Fig. 3.45 presents the $u-$velocity profile along a vertical line and the $v-$velocity along a horizontal line passing through the geometric center of the cavity respectively. These profiles are in good agreement with that of Ghia et al.[41] marked with square

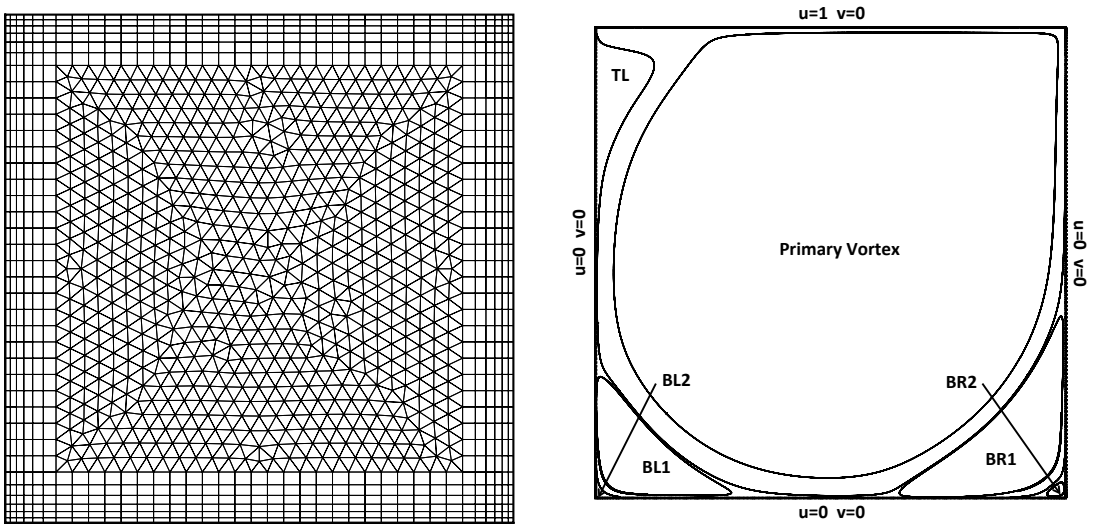


Figure 3.42: Computational grid and nomenclature of vortices for square lid driven cavity flow.

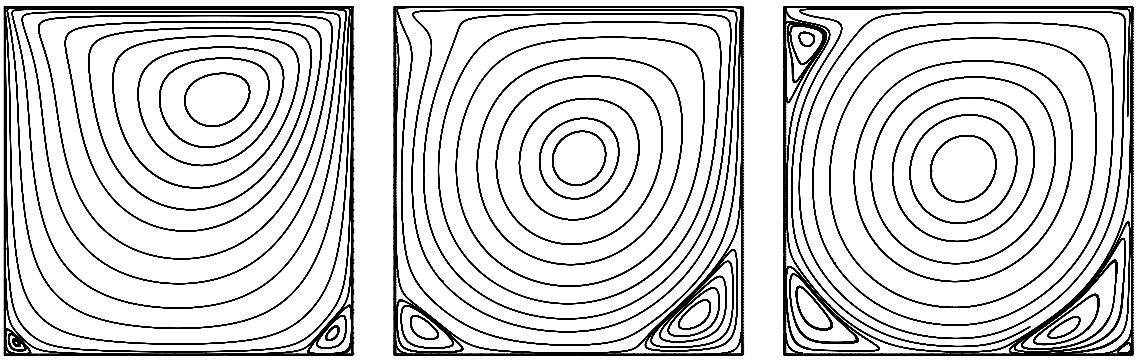


Figure 3.43: Streamline of square cavity flow for Reynolds number of 100, 1000, 5000 (left to right).

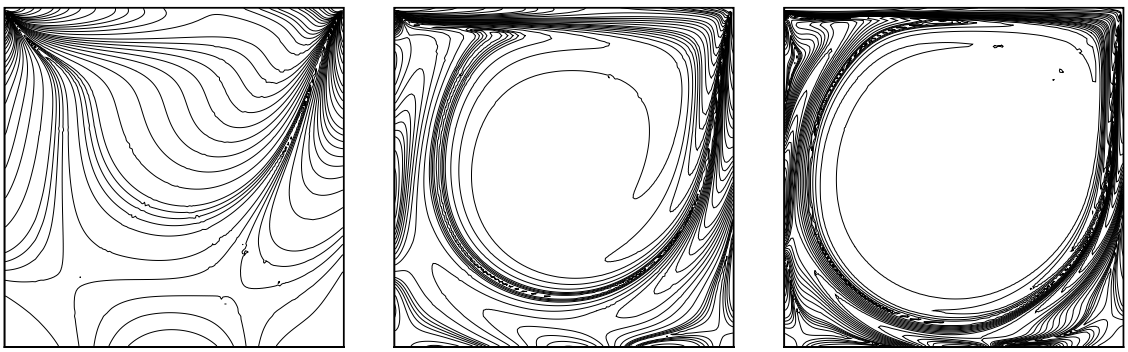


Figure 3.44: Vorticity contours of square cavity flow for Reynolds number of 100, 1000, 5000 (left to right).

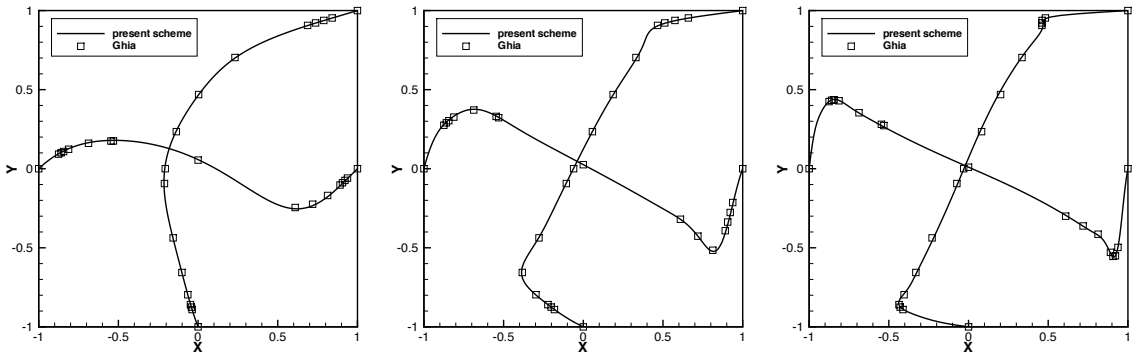


Figure 3.45: Vertical and horizontal velocity profiles along centre lines of square cavity for Reynolds number of 100, 1000, 5000 (left to right).

Reference	No.	ψ	ω	x	y
Present		0.118682	2.06492	0.5308	0.5653
E. Erturk et.al	Reference[33]	0.118942	2.067213	0.5300	0.5650
Barragy and Carey	Reference[9]	0.118930	–	–	–
Botella and Peyret	Reference[14]	0.1189366	2.067753	0.5308	0.5652
Schreiber and Keller	Reference[135]	0.11894	2.0677	0.52857	0.56429
Wright and Gaskell	Reference[168]	0.118821	2.06337	0.5308	0.5659
Nishida and Satofuka	Reference[113]	0.119004	2.068546	0.5313	0.5625
Benjamin and Denny	Reference[12]	0.1193	2.078	–	–
Li et al.	Reference[96]	0.118448	2.05876	0.5313	0.5625
Ghia et al.	Reference[41]	0.117929	2.04968	0.5313	0.5625
Vanka	Reference[161]	0.1173	–	0.5438	0.5625
Hou et al.	Reference[62]	0.1178	2.0760	0.5333	0.5647
Liao and Zhu	Reference[98]	0.1160	2.0234	0.5313	0.5625

Table 3.16: Comparison of maximum streamfunction value, the vorticity value and location of primary vortex, for Reynolds number of 1000.

symbols.

As stated in [47, 33], for the numerical solution of driven flow, the value of streamfunction at primary eddy center appears to be a reliable indicator of accuracy and the value of vorticity at the vortex center is sensitive to the accuracy of wall boundary conditions. In order to quantitatively estimate the performance of present scheme, the streamfunction(ψ) of primary eddy center with its location (x, y) and vorticity(ω) at the center are presented in Table 3.16 and compared with available data. The present results show rather satisfied agreement with existed researches.

For the Reynolds number of 5000, the location (x, y) of primary and secondary eddy as well as the value of streanfunction(ψ) and vorticity(ω) at these locations are compared with results of Ghia et al[41] and Erturk[33] as shown in Table 3.17. It is seen that all the

Number	Property	Present	Ghia[41]	Erturk[33]
Primary	$\psi_{\min}$	-0.12060	-0.118966	-0.121289
	$\omega_{x,y}$	-1.90899	-1.86016	-1.926601
	(x, y)	$(0.5149, 0.5356)$	$(0.5117, 0.5352)$	$(0.5150, 0.5350)$
TL	$\psi_{\min}$	1.46524×10^{-3}	1.45641×10^{-3}	1.4416×10^{-3}
	$\omega_{x,y}$	2.06342	2.08843	2.062775
	(x, y)	$(0.0642, 0.9091)$	$(0.0625, 0.9102)$	$(0.0633, 0.9100)$
BL1	$\psi_{\min}$	1.3386×10^{-3}	1.36119×10^{-3}	1.3639×10^{-3}
	$\omega_{x,y}$	1.46302	1.53055	1.502628
	(x, y)	$(0.0732, 0.1351)$	$(0.0703, 0.1367)$	$(0.0733, 0.1367)$
BR1	$\psi_{\min}$	3.12800×10^{-3}	3.08358×10^{-3}	3.0604×10^{-3}
	$\omega_{x,y}$	2.72227	2.66354	2.724481
	(x, y)	$(0.8013, 0.0732)$	$(0.8086, 0.0742)$	$(0.8050, 0.0733)$
BL2	$\psi_{\min}$	-7.3723×10^{-8}	-7.0886×10^{-8}	-7.2080×10^{-8}
	$\omega_{x,y}$	-1.960×10^{-2}	-1.88395×10^{-2}	-1.2252×10^{-2}
	(x, y)	$(0.0125, 0.0068)$	$(0.0117, 0.0078)$	$(0.0083, 0.0083)$
BR2	$\psi_{\min}$	-1.6246×10^{-6}	-1.43226×10^{-6}	-1.4010×10^{-6}
	$\omega_{x,y}$	-3.036×10^{-2}	-3.19311×10^{-2}	-3.4108×10^{-2}
	(x, y)	$(0.9782, 0.0183)$	$(0.9805, 0.0195)$	$(0.9783, 0.0183)$

Table 3.17: Property of primary and secondary vortices for Reynolds number of 5000; streamfunction ψ and vorticity value ω, locations (x, y).

quantities are in good agreement with reference solution.

3.10.16 Isosceles triangular lid driven cavity flow

Another fluid flow example, flow in triangular cavity is considered since it has been drawn more and more attention in recent ten years due to inherent difficulties in approaches based on regular grid system. For isosceles triangular cavity problem, Erturk [34] Jagannathan [74] considered the Navier-Stokes equations in streamfunction and vorticity formulation which is not available for three dimensional problem. Kohno [86] computed more general Navier-Stokes equations in primitive variables by using specific flow-condition-based interpolations approach. In this test, without any special treatment, We compute the isosceles triangular flow of Reynolds number from 100 to 1000 by hybrid grid with triangular and quadrilateral elements. The comprehensive evaluation is performed by comparing with both numerical results in literature and experimental phenomenon.

Fig. 3.46 shows geometry of isosceles triangular cavity, boundary condition and hybrid grid generated by dominated triangular elements and quadrilateral elements for thin boundary layer. For simplicity of comparison with literature, the coordinate is mapped into regularized reference coordinate system (ξ, η). As suggested in [33, 34], fine grid mesh

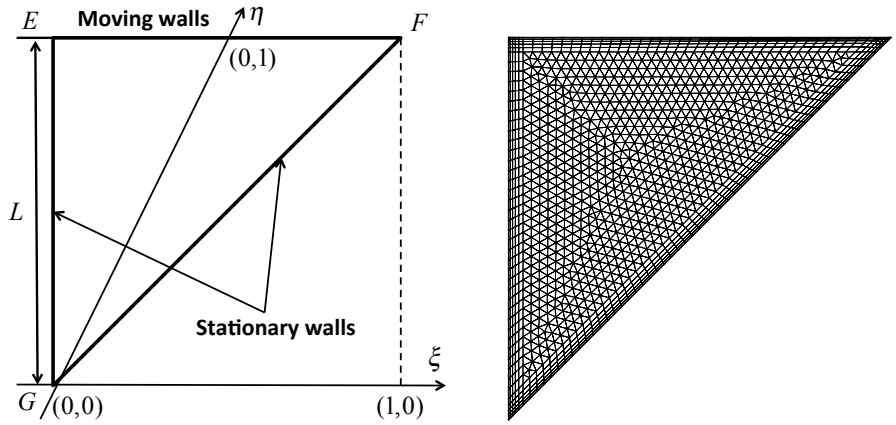


Figure 3.46: Geometry and computational grid of isosceles triangular lid driven cavity flow.

is necessary to obtain accurate solution especially for high Reynolds number. It is worth noting that this hybrid grid approach can effectively reduce the number of elements and thus we can accurately resolve this fluid flow in quite an efficient way.

Our results are firstly compared with experiment photographs of [44] which were visualized by adding small amounts of aluminum flakes to the fluid. As shown in Fig. 3.47 the first two cases are for two subcritical Reynolds number where lid motion moves away from the rectangular corner. The other two cases are for Reynolds number of 100 and 500 where lid motion moves towards the rectangular corner. We can find both primary and secondary eddy are visually agree well with experimental streakline. Due to refinement grids for boundary layer, the tertiary eddy is clearly resolved and more evident than the numerical results of [44] .

In order to comprehensively evaluate the performance of present scheme, we compute with Reynolds number of 100, 500 and 1000, and plot streamline and vorticity as shown in Fig. 3.48 and 3.49. Compared with results in [74], the fluid near boundary is well resolved and tertiary eddy is observed more clearly than ever before. With Reynolds number increasing, the centroid of primary eddy moves towards right corner and secondary and tertiary eddies grow in size and strength. The similar with square cavity, the vorticity becomes smooth near primary eddy while changes intensively near the boundary corner. The accuracy is further verified by compared with reference solution in [74] which is computed with high order spectral method. As shown in Fig. 3.50, 3.51 and 3.52, The quantity in term of horizontal velocity(u), vertical velocity(v) and vorticity(ω) are all in good agreement with published results of Jagannathan on three Reynolds number. More quantitatively, we tabulate location (x, y) of primary eddy and corresponding the value of streanfunction(ψ) and vorticity(ω) as shown in Table 3.18. Our results are proven to be comparable to the most accurate reference solution for these Reynolds numbers.

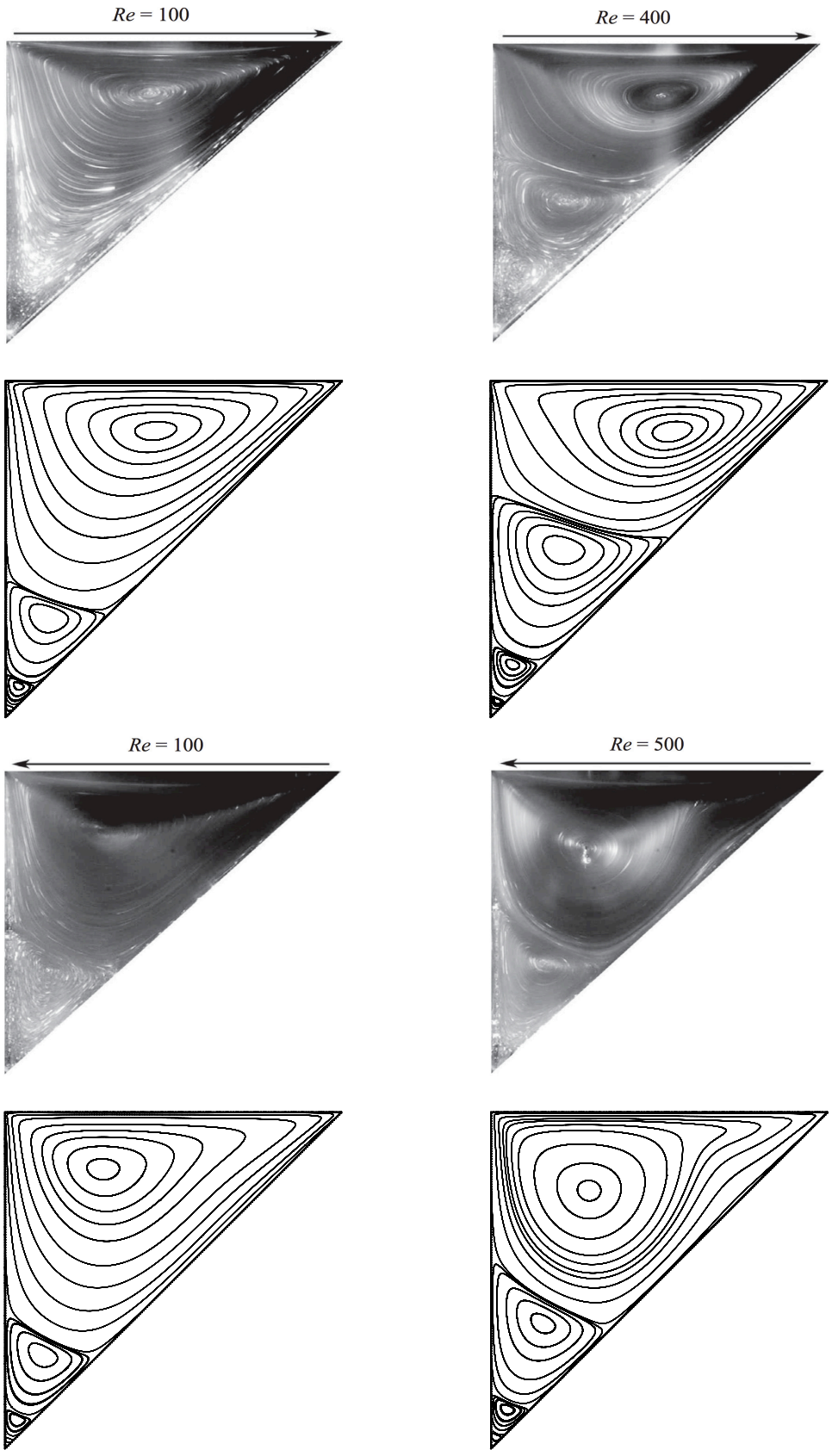


Figure 3.47: Experiment photographs[44] and numerical simulation for isosceles triangular cavity flow.

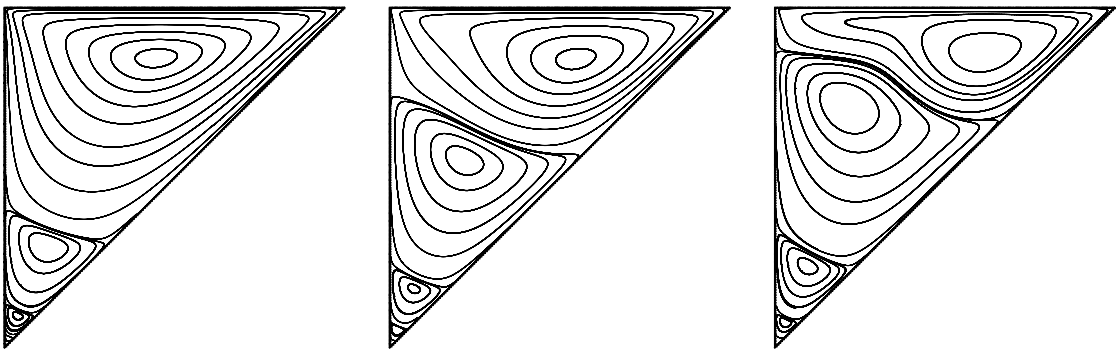


Figure 3.48: Streamline contours of isosceles triangular cavity flow for Reynolds number of 100, 500, 1000 (left to right).

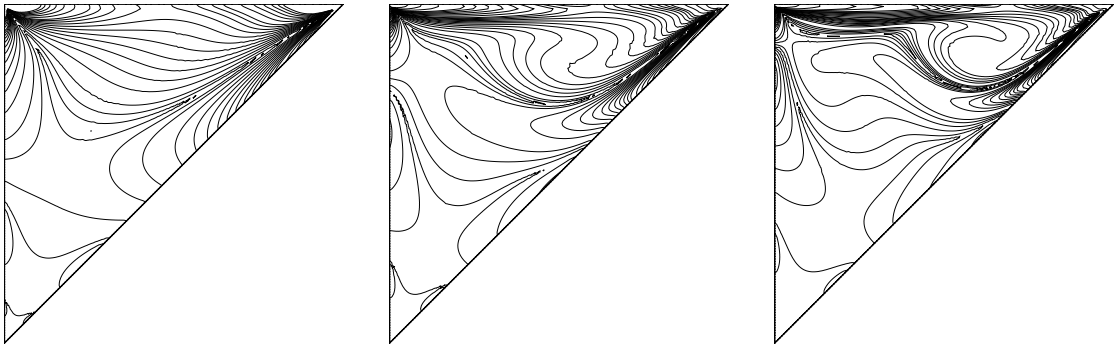


Figure 3.49: Vorticity contours of isosceles triangular cavity flow for Reynolds number of 100, 500, 1000 (left to right).

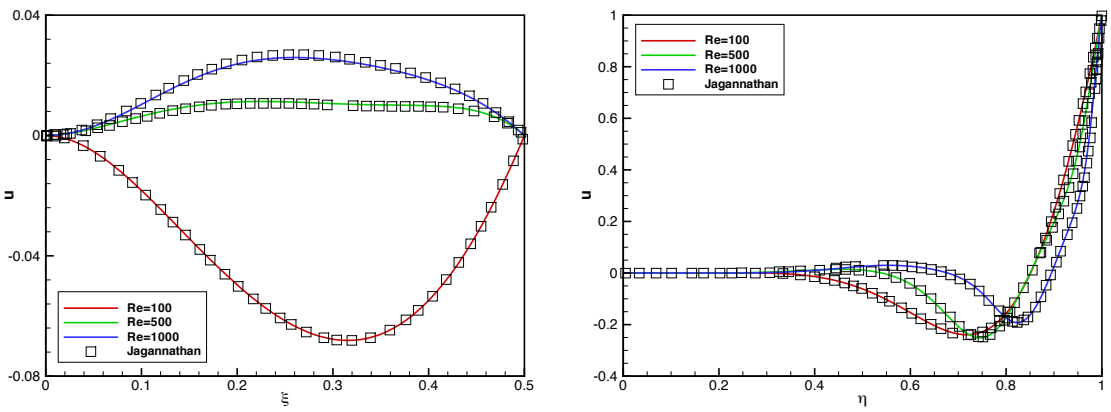


Figure 3.50: Horizontal velocity(u) along the line joining the center of EG and FG(left) and the line from G to the center of EF(right).

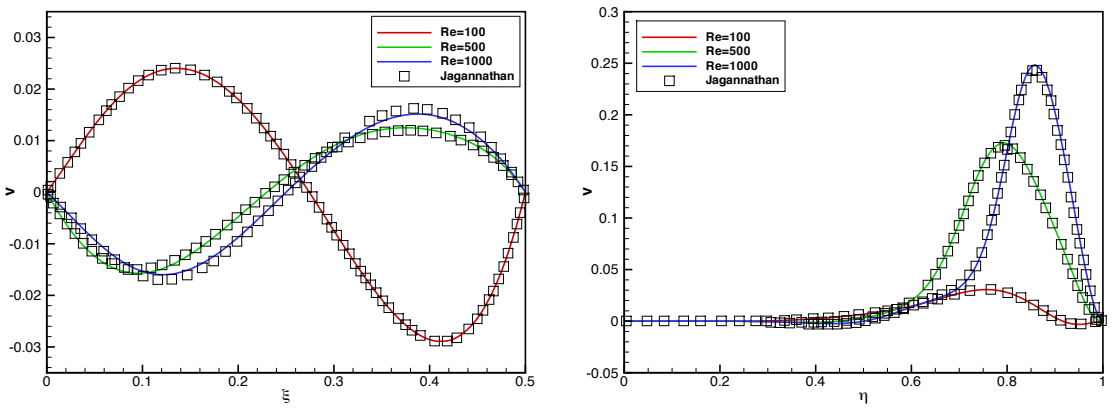


Figure 3.51: Vertical velocity(v) along the line joining the center of EG and FG(left) and the line from G to the center of EF(right).

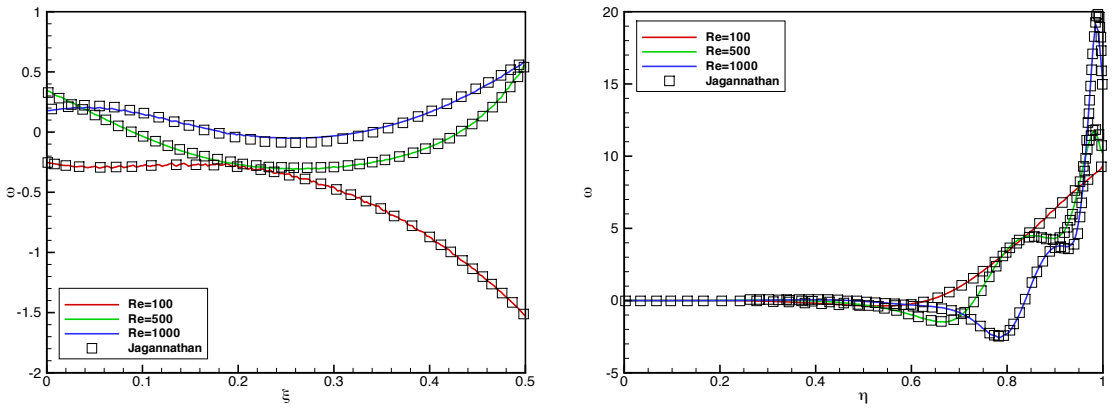


Figure 3.52: Vorticity(ω) along the line joining the center of EG and FG(left) and the line from G to the center of EF(right).

Re	$\psi_p \quad \omega_p$ (ξ_p, η_p)			
	present	Jagannathan[74]	Ahmed[2]	Erturk[34]
100	0.06462 5.03724 (0.5534, −0.1479)	0.06454 5.02899 (0.5535, −0.1479)	0.06452 5.02972 (0.5528, −0.1480)	0.06451 5.01902 (0.5527, −0.1484)
500	0.06078 5.7168 (0.4538, −0.1515)	0.06062 5.75363 (0.4518, −0.1507)	0.06072 5.75854 (0.4514, −0.1518)	0.06065 5.73737 (0.4531, −0.1504)
1000	0.05335 6.936 (0.3902, −0.1316)	0.05320 7.0092 (0.3905, −0.1319)	0.05325 6.99701 (0.3906, −0.1309)	0.05306 7.002235 (0.3906, −0.1309)

Table 3.18: Comparison characteristics of the primary vortex for different Reynolds numbers; streamfunction ψ_p and vorticity value ω_p, locations (ξ_p, η_p).

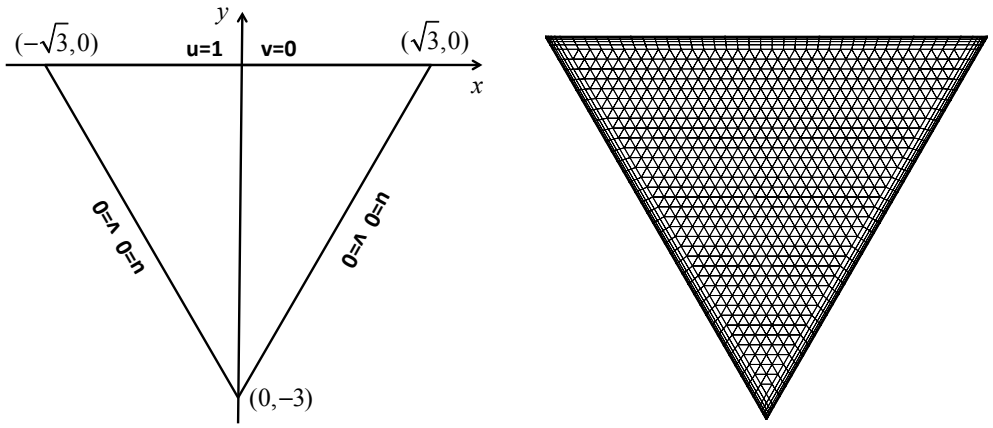


Figure 3.53: Geometry and computational grid of equilateral triangular lid driven cavity flow.

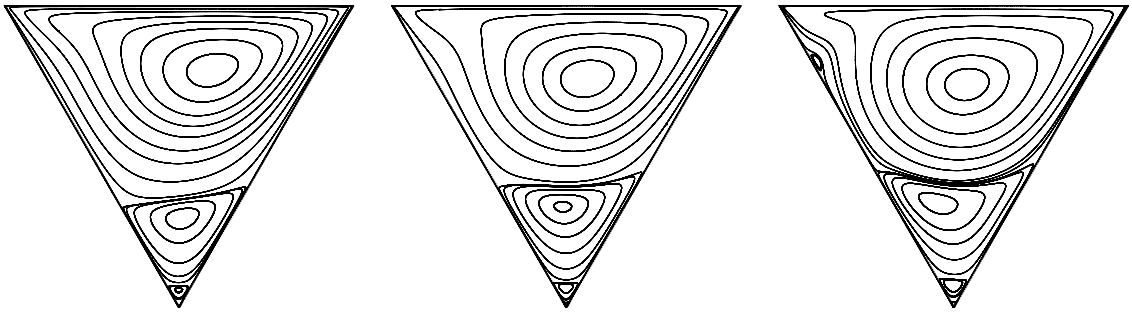


Figure 3.54: Streamline contours of equilateral triangular cavity flow for Reynolds number of 100, 200, 500 (left to right).

3.10.17 Equilateral triangular lid driven cavity flow

The equilateral triangular cavity is also found in literature[86, 34, 39, 108, 125, 74]. The no-slip conditions are imposed on the left and right boundaries, while an unit velocity is prescribed on the top boundary wall. As shown in Fig. 3.53, hybrid grid is used again to accurately resolve the flow near the boundary. The Reynolds number is defined as Ua/ν, where U is top wall velocity, a is characteristic length, and ν is viscosity. We compute for Reynolds number for 100, 200 and 500 which a is specified as 1 in all cases. As mentioned in [34], if the length scale is considered as $2\sqrt{3}$, the Reynolds number would be $2\sqrt{3}$ fold such that maximum Reynolds number would correspond to 1732. Qualitatively, Fig. 3.54 and 3.55 show the streamline and viscosity contour of flow for three Reynolds number respectively. Fig. 3.56 shows the velocity profile in x direction along the center line and y direction along horizontal line at $y = -1$. The results are compared with tabulated data in reference [86] which shows desirable agreement. In term of quantitative analysis, Table 3.19 tabulated the center of primary eddy and its streamfunction and vorticity values. We can find the present results are among the most accurate solution for this benchmark tests which can be used as future references.

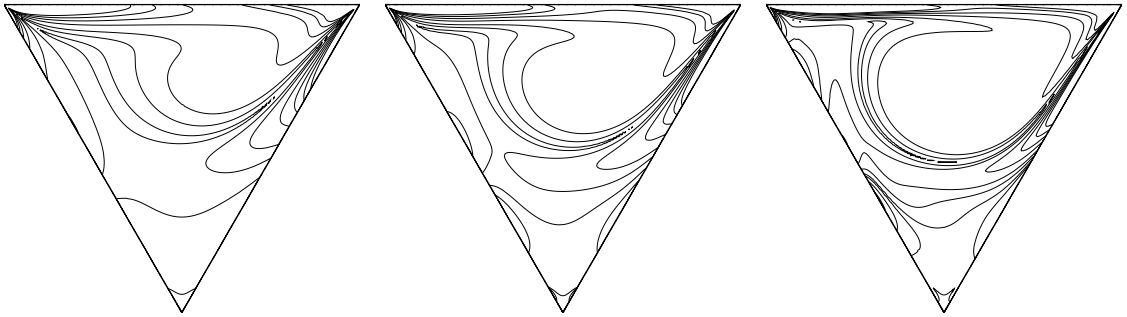


Figure 3.55: Vorticity contours of equilateral triangular cavity flow for Reynolds number of 100, 200, 500 (left to right).

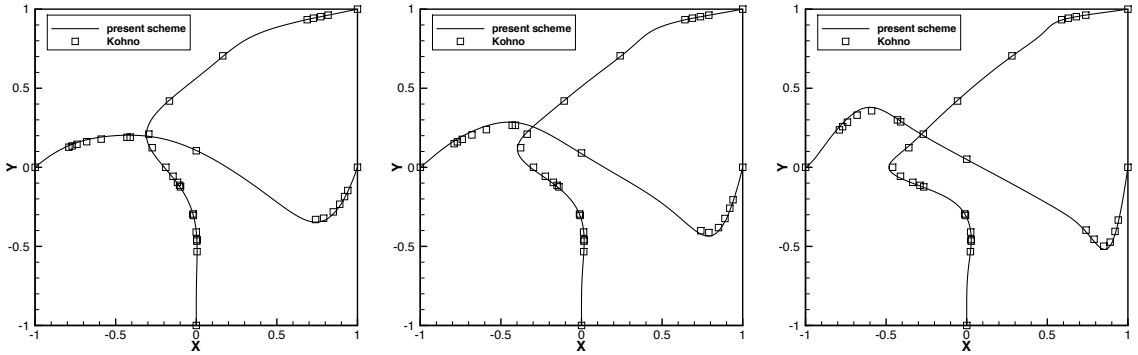


Figure 3.56: Vertical and horizontal velocity profiles along centre lines of equilateral triangular cavity for Reynolds number of 100, 200, 500 (left to right).

3.10.18 2D viscous flow around a circular cylinder

In order to validate the capability of present model to solve time-dependent problem, we simulate the viscous flow with $Re = 100$ passing a circular cylinder as proposed in [155, 154]. For this Reynolds number, the flow is time dependent and characterized by periodical vortex shedding in the downstream region of the cylinder. It provides a good test bed of transient flow to evaluate numerical models.

The computational condition is the same as in [154] (see case III therein for details). We use an unstructured grid with 81394 triangle elements locally refined near the cylinder. Fig. 3.58 shows the contours of velocity norm, pressure and vorticity fields at the instant when the lift force reaches the maximum. We can clearly observe the Karman vortex street behind the cylinder. All the fields recover the major features observed in [154]. The time histories of drag and lift coefficients are plotted in Fig. 3.59 which look in agreement with other standard solutions. An enlarged view of drag and lift coefficients are plotted in Fig. 3.60. The periodical oscillations are accurately reproduced, and the amplitudes remain perfectly constant.

Re	$\psi_p \quad \omega_p$ (ξ_p, η_p)		
	100	200	500
present	−0.2483 1.3643 (0.3340, −0.6428)	0.2625 1.2495 (0.2022, −0.7254)	0.2776 1.1760 (0.1325, −0.7824)
Kohno[86]	−− (0.3467, −0.6416)	−− (0.2133, −0.7265)	−− (0.1319, −0.7864)
Erturk[34]	−0.2482 1.3669 (0.3315, −0.6445)	0.2624 1.2518 (0.2030, −0.7266)	0.2774 1.1791 (0.1319, −0.7793)
Gaskell[39]	−0.249 1.365 (0.333, −0.644)	0.263 1.252 (0.208, −0.727)	0.281 1.187 (0.128, −0.783)
McQuain[108] Ribbens[125]	−0.247 1.373 (0.329, −0.645)	0.260 1.272 (0.208, −0.720)	0.269 1.1250 (0.173, −0.735)
Li and Tanng[74]	−0.244 1.264 (0.368, −0.635)	0.262 1.156 (0.173, −0.750)	0.278 1.124 (0.108, −0.787)

Table 3.19: Comparison characteristics of the primary vortex for different Reynolds numbers; streamfunction ψ_p and vorticity value ω_p, locations (ξ_p, η_p).

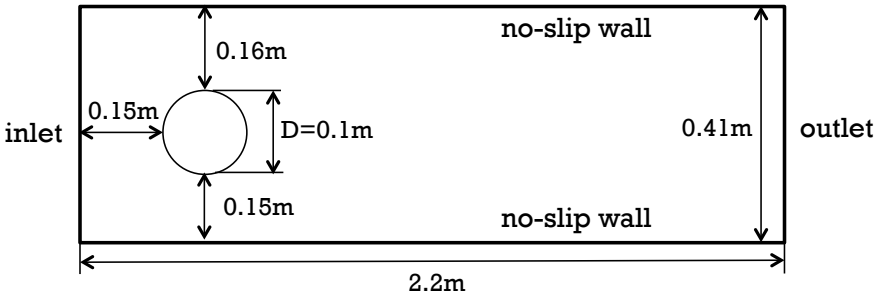


Figure 3.57: Geometry and boundary conditions for case of circular cylinder.

To quantitatively verify the numerical solutions, we compute the maximum drag coefficient $(C_d)_{max}$, the maximum lift coefficient $(C_L)_{max}$ and the Strouhal number which are summarized in Table 3.20 with the reference data from [155] and [154]. It is seen that the present results are among the most accurate solutions of the benchmark tests.

3.10.19 Viscous flow in a channel with a backward-facing step

We compute the viscous channel flow in presence of a backward-facing step [38], which is a well-suited test for a mesh with quadrilateral elements of large aspect ratio. The computational domain is $[0, 30] \times [-0.5, 0.5]$ for x and y directions respectively with the inlet of 0.5 height on the left boundary. The inlet velocity is specified for the x-component of a parabolic profile, $u = 24y(0.5 - y)$ for $0 \leq y \leq 0.5$. No-slip solid-surface condition is specified for the span-wise boundaries, while the outflow condition is set at the right

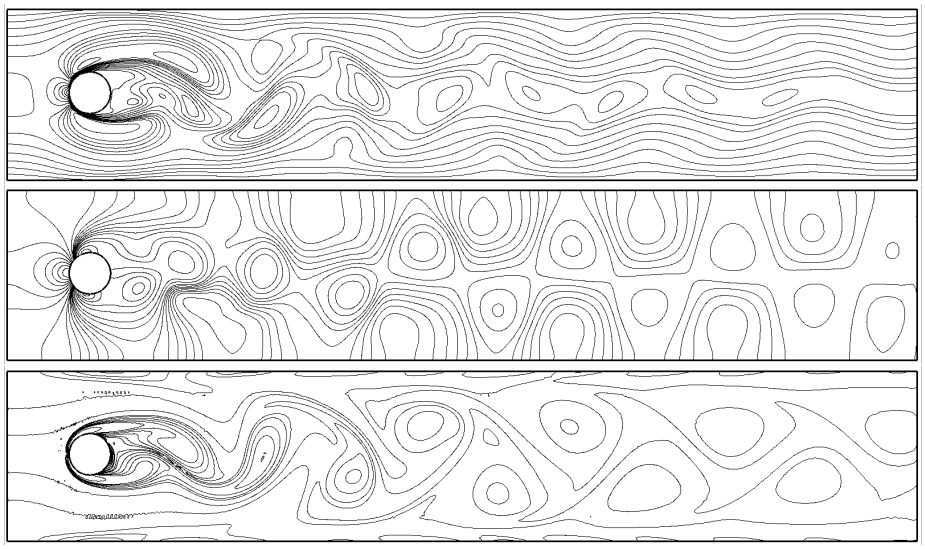


Figure 3.58: The physical fields at the instant when the lift force becomes largest. Displayed are velocity norm (top), pressure (middle) and vorticity (bottom) fields.

		$(C_d)_{max}$	$(C_L)_{max}$	St
present scheme		3.23	1.01	0.298
Shuangzhang[154]		3.215	1.0374	0.2959
Turek and Shahrouz[155]	Lower bound	3.22	0.99	0.295
	Upper bound	3.24	1.01	0.305

Table 3.20: Comparison between the present solution and the reference solutions.

exit. The Reynolds number is $Re = u_{avg}H/\nu = 800$ with u_{avg}, H and ν representing the average inlet velocity, channel height and kinematic viscosity. The grid used here follows [38] where the computational domain is divided into a uniformly spaced region and a gradually stretched region which is characterized by large aspect ratio. The numerical results on a 800×40 grid are plotted in Fig. 3.62, which agree well with those in [38]. The velocity profiles at $x = 7$ and $x = 15$ cross sections are shown in Fig. 3.63 against the solution in [38]. We further quantitatively examine the numerical solutions on grids of different resolutions in Table 3.21 to compare with the results in [83, 38]. Our numerical results show a good convergence to the reference solutions.

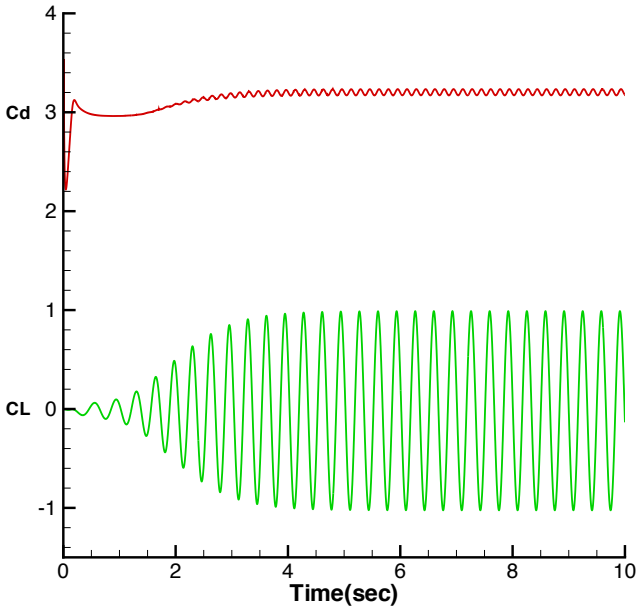


Figure 3.59: Time history of drag and lift coefficient.

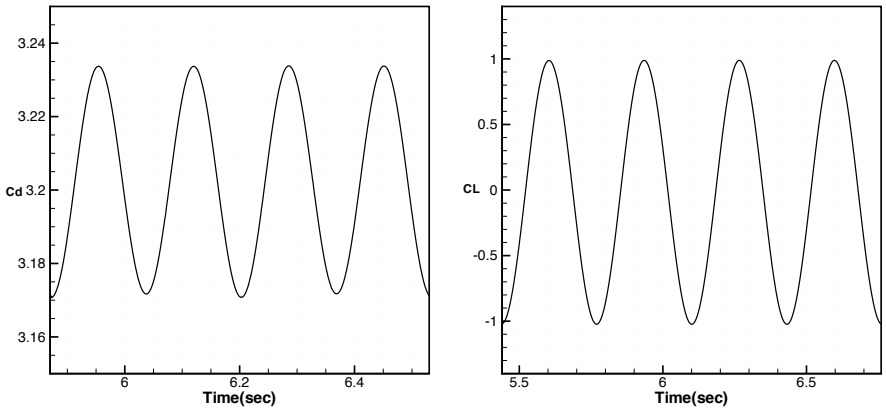


Figure 3.60: Zoomed view of time history of drag (left) and lift (right) coefficient.

3.10.20 Viscous flows passing a sphere with different Reynolds numbers

We further verify the present model by simulating viscous flows passing a sphere with different Reynolds numbers, which is widely used to evaluate numerical codes for incompressible viscous flows [78, 84]. As shown in Fig. 3.64, the computational domain is set as $15 \times 10 \times 10$ in streamwise (x), spanwise (y) and vertical(z) directions respectively. A unit sphere is located at $(5, 5, 5)$. The computational grid is composed of 661780 tetrahedral elements. We set the inlet flow velocity u_∞ to be unit, The Reynolds number is adjusted by altering the viscosity. The time step is variable to maintain a constant CFL number of 0.5. For small Reynolds numbers (Re= 50,100,150 and 200), we reach a steady axisymmetric flow which is realized when the variation in pressure is less than 10^{-9} in our numerical tests. Streamlines on (x, z)-plane cutting through the sphere center are shown

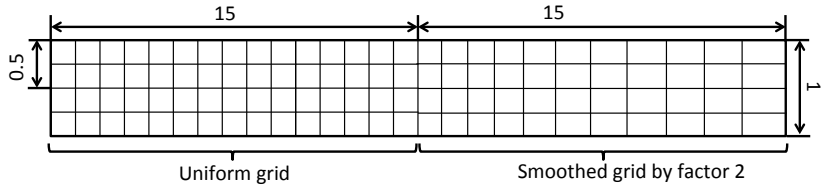


Figure 3.61: Geometry and computational grid for case of backward-facing step.

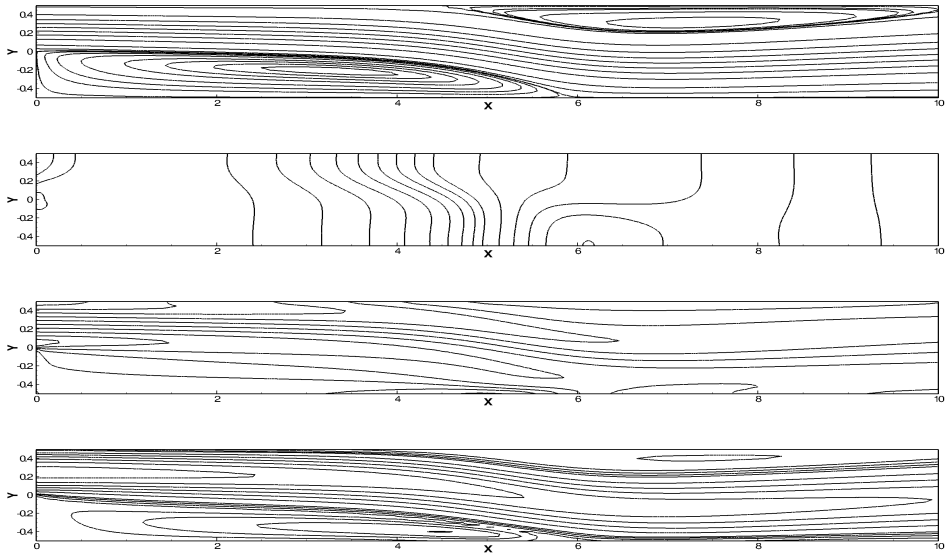


Figure 3.62: Numerical results of the back-facing step channel flow test on the 800×40 grid. Displayed are stream line, pressure contour, vorticity contour and velocity magnitude respectively from top to bottom.

in Fig. 3.65 for Reynolds numbers of 50,100,150 and 200, which visually agree well with those in [78].

The quantitative comparison has been also conducted with the available data in [78]. Shown in Fig. 3.66, we plot the polar separation angle, separation length, vortex position and drag coefficient against the Reynolds numbers up to 200 and compare our results with the existing numerical and experimental results summarized in [78]. It reveals that the present method is in good agreement with the well-accepted results for these steady viscous flows.

It is known that with the Reynolds number increasing, flow turns into a steady non-axisymmetric flow regime ($210 \leq \text{Re} \leq 270$), and then an unsteady flow regime ($\text{Re} \geq 280$). We compute two cases with the Reynolds number of 250 and 300 to reproduce these two flow regimes. The numerical results are given in Table 3.22. The drag and lift coefficients for both cases are in excellent agreement with the existing researches [78, 25, 84]. As expected a steady flow is reproduced in the case of $Re = 250$. A periodical flow is observed in the case of $Re = 300$. The Strouhal number at $\text{Re} = 300$ agrees well with the reported results aforementioned. Four snapshots of the instant vertical-component

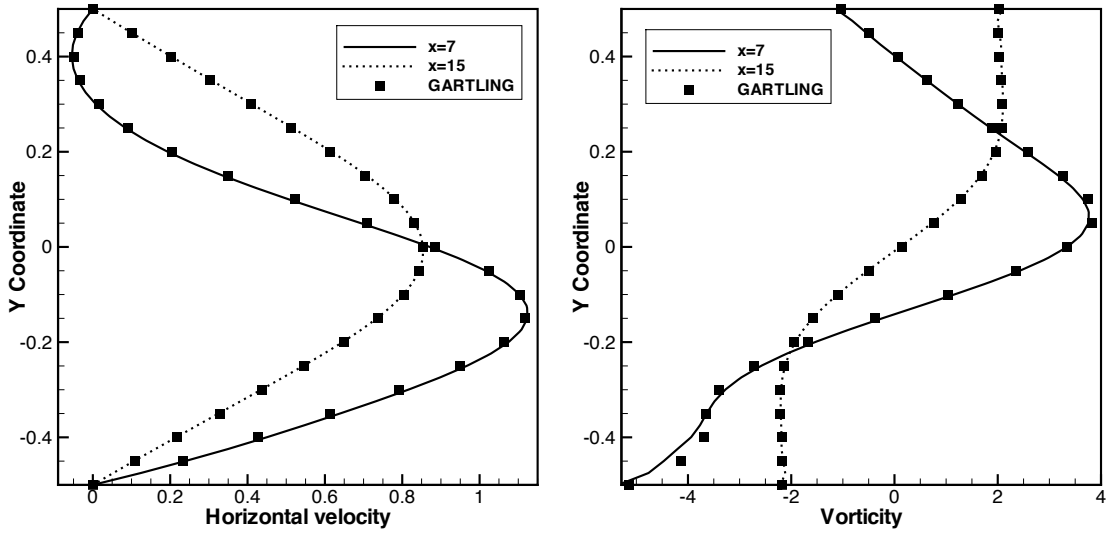


Figure 3.63: Magnitude of velocity and vorticity profile across the channel $x = 7$ and $x = 15$ for finest grid.

Table 3.21: Numerical results of backward-facing step channel flow and comparison with existing studies.

Grid	Length of lower wall eddy	Length of upper wall eddy
200×10	3.49	4.89
400×20	5.10	5.63
600×30	5.87	5.70
800×40	6.01	5.73
Reference results		
Kim and Moin[83]	6.0	5.75
Gartling[38]	6.10	5.63

vorticity field on the $x - y$ cross section cutting through the sphere center are plotted in Fig. 3.67. We set the start point $\phi = 0$ to the instant when the lift force reaches the minimum value. It is found that the vorticity structure evolves in time and looks quite similar to those reported in the existing researches [78].

3.10.21 Flow over a circular cylinder with Reynolds number of 3900

The flow over a circular cylinder is chosen as final example for validation of three-dimensional flow. Despite simplicity of circular shape, it is still a challenge for both experiment and numerical study to predict turbulence statistics behind the cylinder especially for higher Reynolds number. In this case, we simulate the circular cylinder with Reynolds number of 3900 which belongs to subcritical regime. As Prasad suggested [121], in this flow regime, the separating shear layers become very sensitive to various experimental factors by far, thus it is a desirable case to verify the capability of present model to use direct

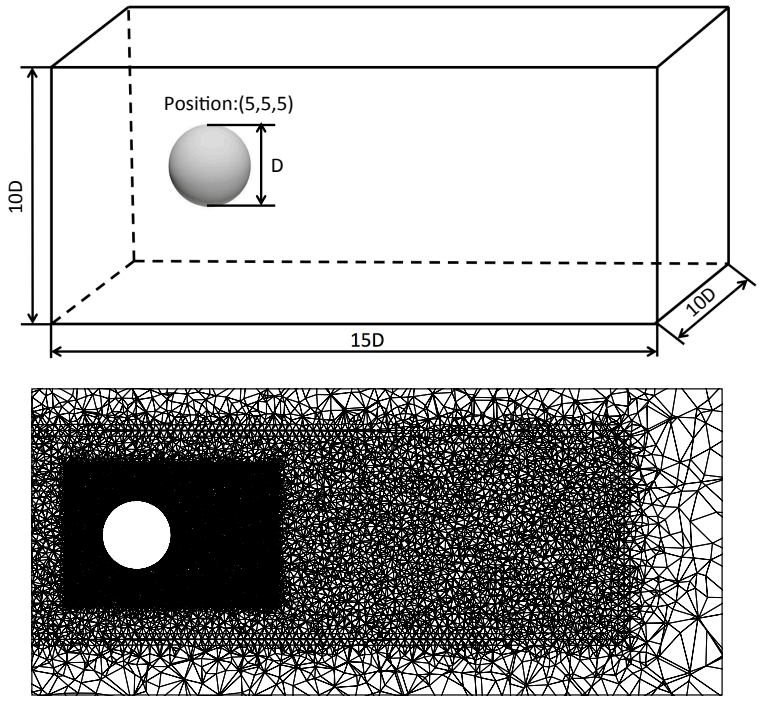


Figure 3.64: Geometry and computational grid for viscous flows passing a sphere.

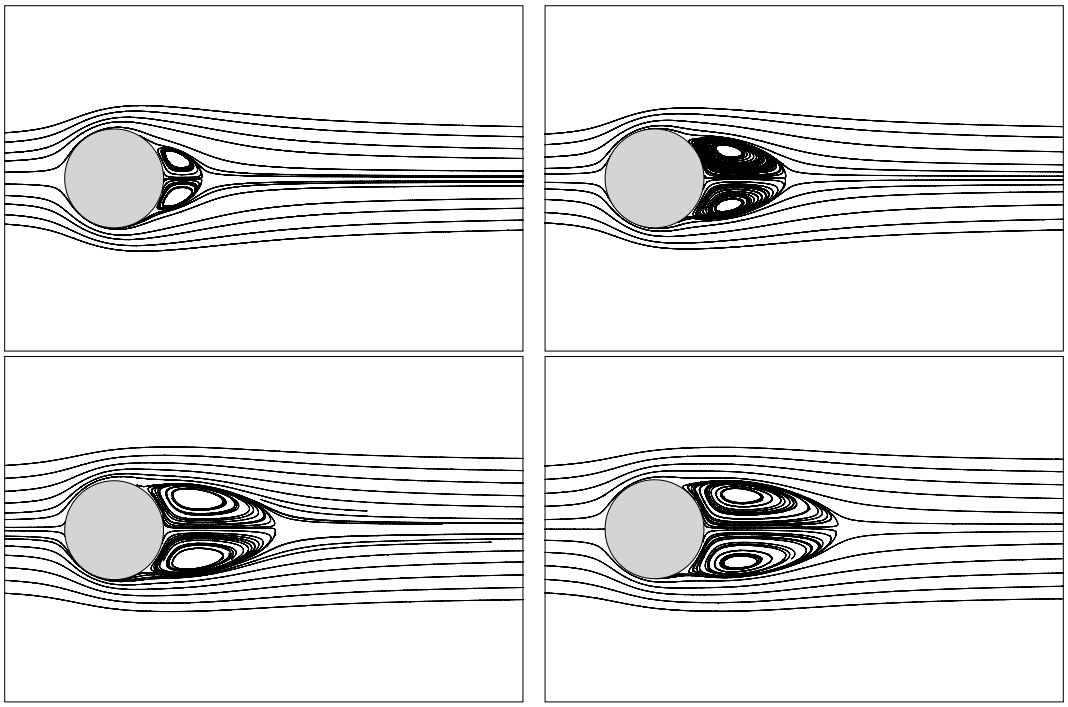


Figure 3.65: Streamlines on the central cross section of flows passing a sphere. Displayed are the steady cases with Reynolds numbers of 50 (top-left), 100 (top-right), 150 (bottom-left) and 200 (bottom-right).

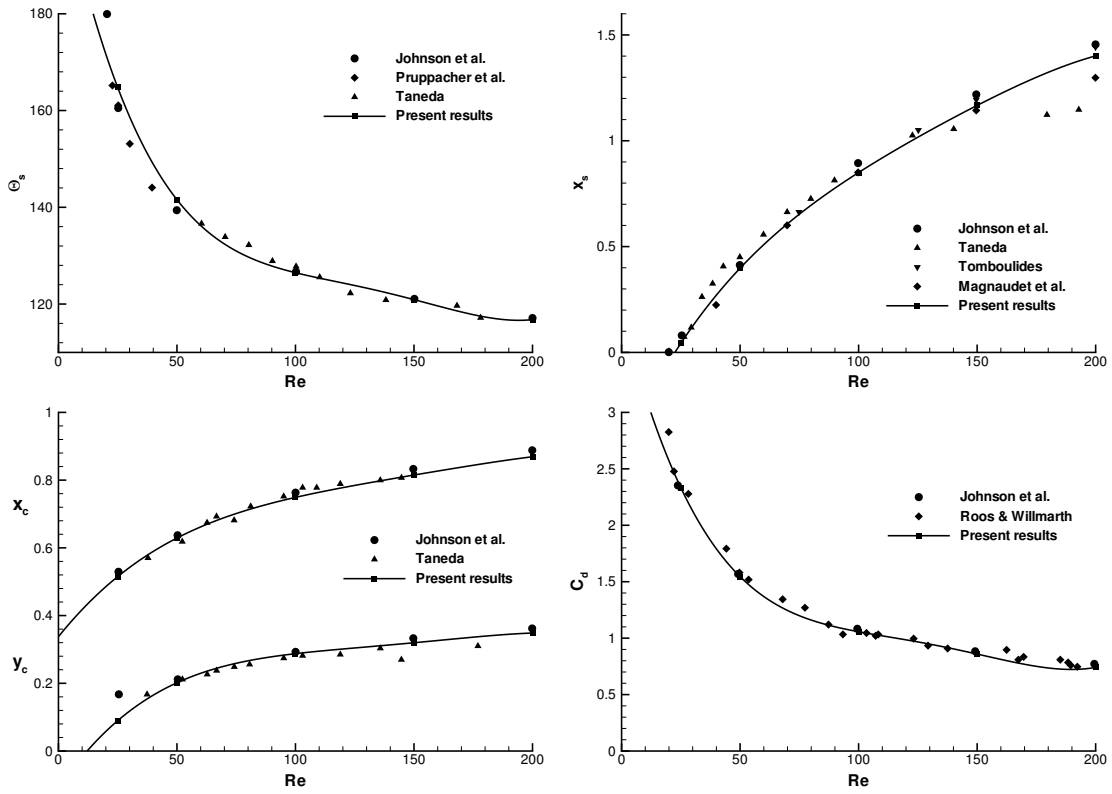


Figure 3.66: Flow geometry as a function of the Reynolds number. Displayed are the polar separation angle Θ_s (top-left), the separation length x_s (top-right), the vortex position (x_c, y_c) (bottom-left) and the drag coefficient C_d(bottom-right). See Fig. 4 and 5 in [78] as well as the references therein for the reproduced data.

numerical simulation(DNS) for high Reynolds number flow. The computation is performed on a domain whose inlet is $30D$ upstream and outlet is $35D$ behind the cylinder (D denotes the cylinder diameter). We use the domain of $50D$ in hight and πD in span direction. The nested grid is generated as shown in Fig. 3.68 with boundary layer refinement by hexahedral elements with the smallest immediately adjacent to the cylinder. The same as [106], the simulation is computed for a total time of $230D\,/\mathrm{U}_\infty$ where 80 time units are used to make initial condition out of domain and statistics are collected by subsequent 150 time units. The averaging operator for mean quantities is computed by $\langle\phi\rangle = \frac{1}{150D/\mathrm{U}_\infty}\int_{150D/\mathrm{U}_\infty}^{230D/\mathrm{U}_\infty}\phi(t)dt$.

We plot mean streamwise velocity($\langle u\rangle\,/U_c$) on the center line in Fig. 3.69 and our results agree well with available numerical and experiment data. The mean streamwise and cross-flow velocity at three locations downstream of cylinder are plotted in 3.70 and compared with LES result of [120] and experiment data in [89]. We can clearly see that the identification of U-shape profile in the very near wake is reproduced, which is confirmed by Parnaudeau et al. numerically and experimentally. Our results are in satisfactory agreement with LES numerical solution but deviate evidently from the experiment measures.

	Re	C_D	C_L	St
present scheme	250	0.71	0.062	
	300	0.659	0.069	0.135
Jumgwoo and Dongjoo[84]	250	0.701	0.059	
	300	0.657	0.067	0.134
Johnson and Patel [78]	250	0.70	0.062	
	300	0.656	0.069	0.137
Constantinescu and Squires[25]	250	0.70	0.062	
	300	0.655	0.065	0.136

Table 3.22: Numerical results of viscous flows over a sphere.

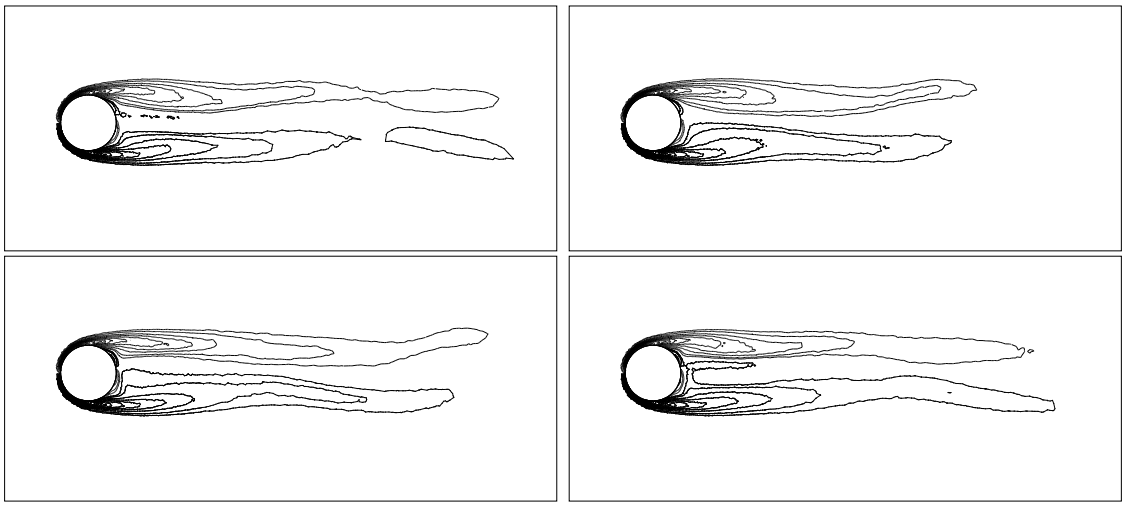


Figure 3.67: The contours of ω_z at Re=300 for a quarter period on xy-plane at $\phi = 0$ (top-left), $\phi = \pi/2$ (top-right), $\phi = \pi$ (bottom-left) and $\phi = 3\pi/2$ (bottom-right). Contours are drawn at 0.5 increment with the solid and dot lines for positive and negative values respectively.

As suggested in [89, 120], this may be caused by some external disturbances happened in experiment measurements.

In order to further confirm the performance of present model, we plot 2D maps of first order and second order statistics in the left column as shown in Fig. 3.71∼3.75 and compared with PIV results reported in [120]. The first two figures from top to bottom are mean velocity, i.e. $\langle u \rangle$, $\langle v \rangle$ normalized with U_c and subsequent three figures are variance of velocity fluctuations $\langle u'u' \rangle$, $\langle v'v' \rangle$,$\langle u'v' \rangle$ normalized with U_c^2 . We can see, the major characteristic of this Reynolds number is well reproduced and present results are shown to be in mutual agreement with PIV datas as well as LES results in reference of [120]. The global varaiables such as Strouhat number, minimum mean streamwise velocity, separation angle and length of recirculation region are tabulated in Table 3.23 and agree well with experiments and past computations.

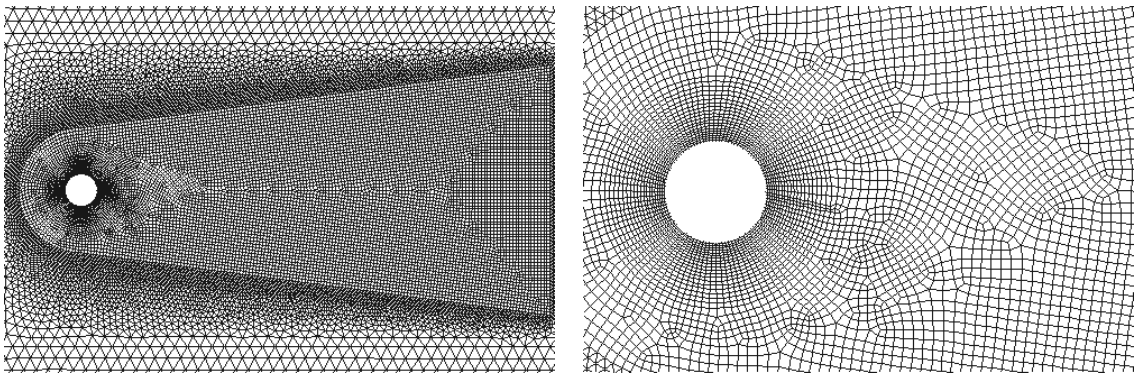


Figure 3.68: Cross-section of grids used in the circular cylinder simulation.

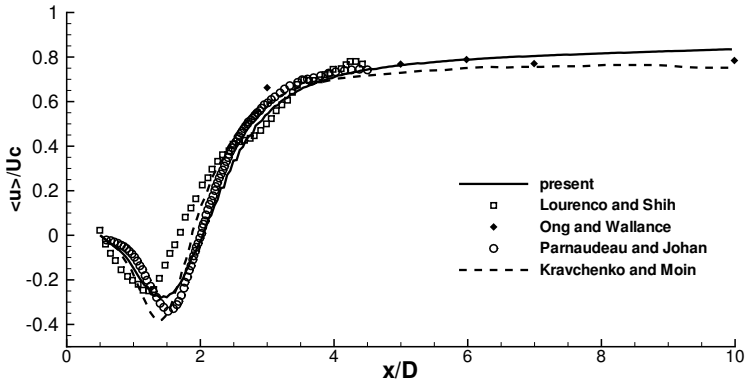


Figure 3.69: Streamwise velocity on the center line in the wake of a circular cylinder.

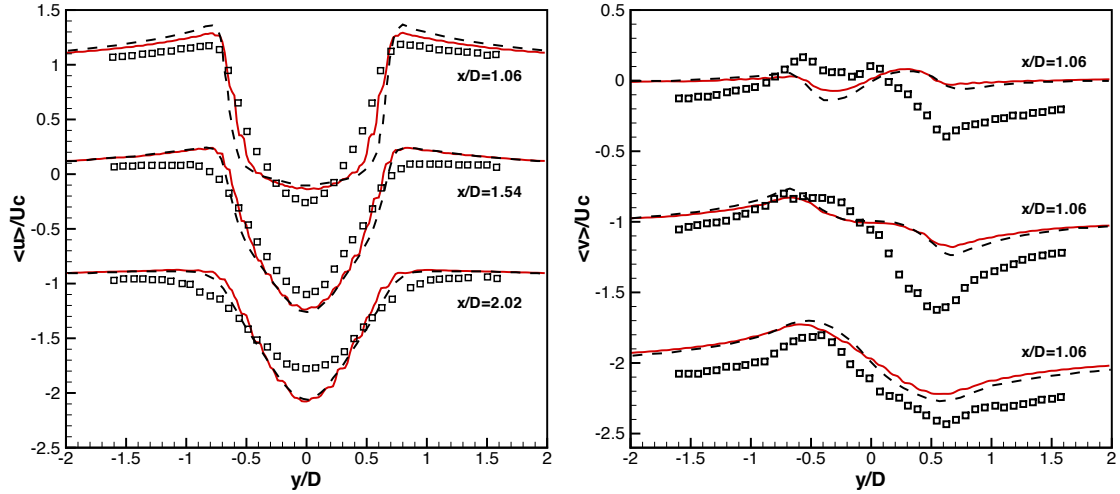


Figure 3.70: Streamwise velocity and cross-flow velocity at three locations in the wake of a circular cylinder.

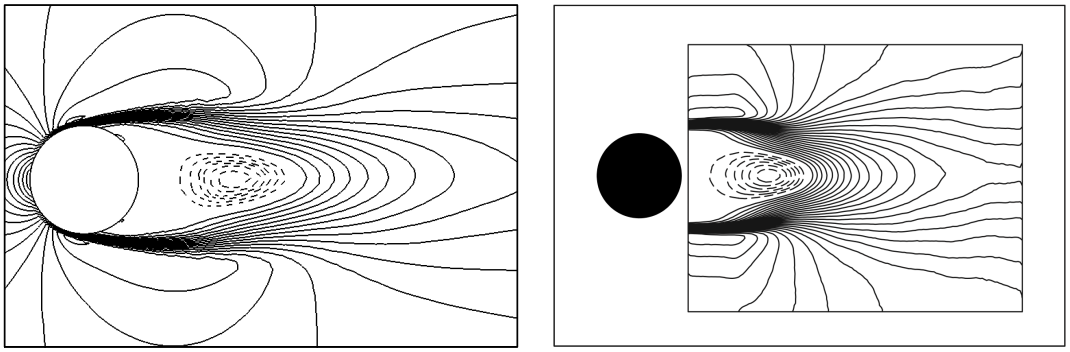


Figure 3.71: Isocontour maps of the mean streamwise velocity $\langle u \rangle$ normalized with U_c(left column, present result; right column, PIV in [120]).

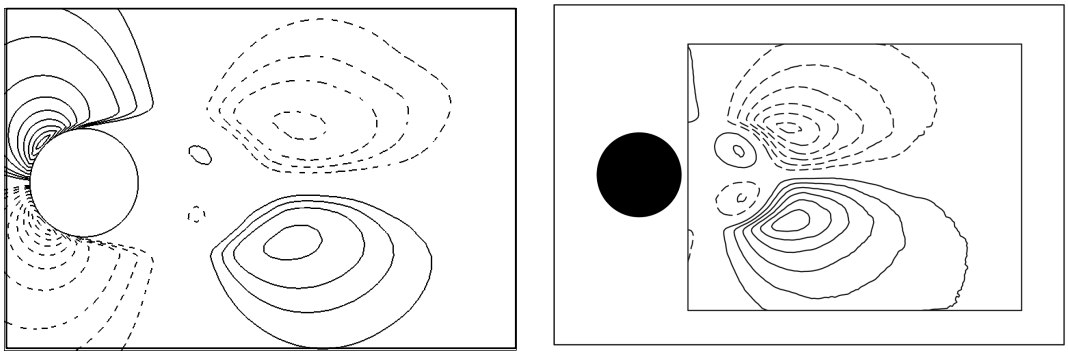


Figure 3.72: Isocontour maps of the mean cross-flow velocity $\langle v \rangle$ normalized with U_c(left column, present result; right column, PIV in [120]).

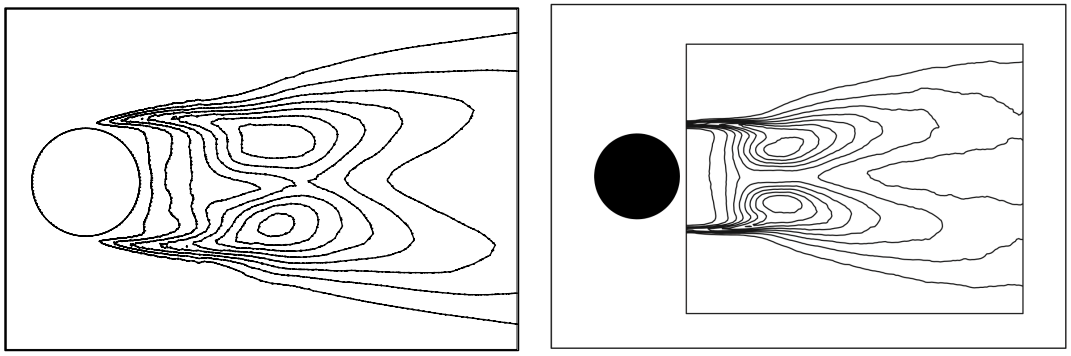


Figure 3.73: Isocontour maps of the variance of streamwise velocity fluctuations $\left\langle u^{'}u^{'} \right\rangle$ normalized with U_c^2(left column, present result; right column, PIV in [120]).

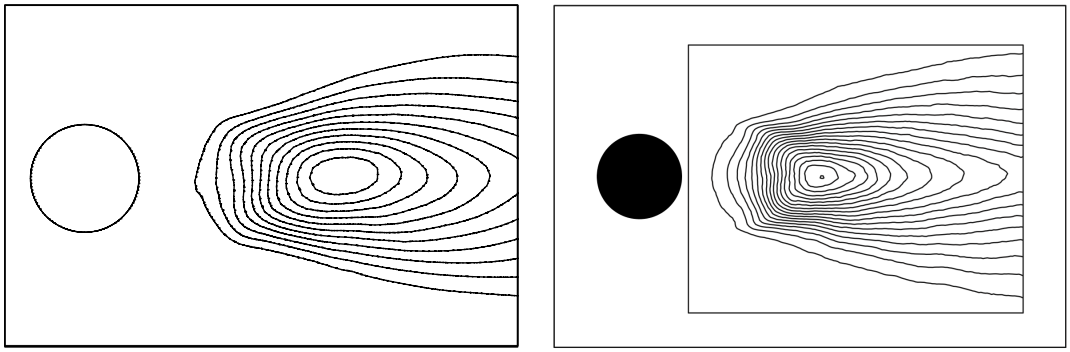


Figure 3.74: Isocontour maps of the variance of cross-flow velocity fluctuations $\left\langle v'v' \right\rangle$ normalized with U_c^2(left column, present result; right column, PIV in [120]).

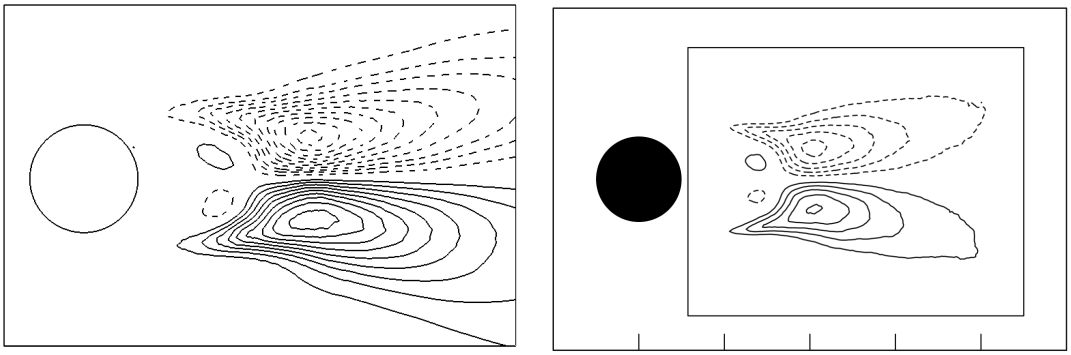


Figure 3.75: Isocontour maps of the covariance of the velocity fluctuations $\left\langle u'v' \right\rangle$ normalized with U_c^2(left column, present result; right column, PIV in [120]).

	St	U_{min}	θ_{sep} (°)	L_{rec}/D
Parnaudeau and Johan[120]	–	-0.34	–	1.51
Lourenco and Shih[104]	0.215	-0.24	86.0	1.40
Mittal and Moin[111]	0.207	-0.35	86.9	1.40
Kravchenko and Moin[89]	0.210	-0.37	88.0	1.35
Mahesh and Moin[106]	0.218	-0.31	87.6	1.35
Dong et al.[29]	0.203	-0.252	–	1.36
present	0.216	-0.28	87.6	1.50

Table 3.23: Comparison of statistics around circular cylinder at Reynolds number of 3900. St, U_{min}, θ_{sep}, L_{rec} denotes Strouhat number, minimum mean streamwise velocity, separation angle and length of recirculation region, respectively.

3.11 Summary of chapter 3

Using multi-moment reconstruction formulation, spatial discretization of unsteady Navier-stokes equations for Mach uniform compressible solver are described in detail particular for invscid compressible as well as viscous incompressible flow. VPM and MCV schemes are applied with projection solution procedure by a sequence of decomposed operators. Both Runge-Kutta scheme and BDF scheme are considered for time integration. For spatial discretization in first advection and diffusion step, VIA/PV moment in in VPM/MCV is updated based on finite volume formulation of flux form that ensures exact conservation, while the PV moments at cell vertices are point-wisely updated by a differential form that can be computed very efficiently in unstructured grids. Additional to prognostic DOFs in piecewise reconstruction, gradient moment at cell center is computed with surrounding cells and three different approaches are provided. TEC formulation as well as implicit procedure are proposed for diffusion equation to enhance practicality. In order to remove unphysical oscillation raised in high speed flow, TVD flux limiter suitable for VPM/MCV scheme is also devised. With intermediate variables at cell boundary determined, Poisson equation is formulated by enforcing momentum equation to satisfy closed-form conditions, i.e. continuity equation for incompressible flow and state equation as well as law of thermodynamics for compressible flow. Two approaches for spatial discretization of Poisson equation are proposed of which one kind is based on conventional FVM method with explicit non-orthogonal correction while another is constructed with help of PV at cell vertices to improve accuracy and robustness based on least square approximation.

In pressure projection step, dissipation minimized method is introduced which shows particular advantage in kinetic energy conserving for high Reynolds flow. The capability of present method is verified by numerous fundamental benchmark tests where analytical and experimental results are available. Compared with convectional FVM, present method show significant enhancement in accuracy and robustness particularly for distorted grid with only 30%˜40% extra computational cost. TVD limiter is proven to be effective to suppress the unphysical oscillation for high speed flow. The total kinetic energy is confirmed with excellent preservation and converges as high as three order. Above all, the present methods show remarkable performance to resolve a variety of problems including incompressible flow, high speed flow and high Reynolds number flow.

Chapter 4

Algebraic interface capturing scheme on unstructured grid

4.1 Algebraic numerical approaches for moving interface in multiphase flow

The volume of fluid (VOF) method is one of the most popular approaches for capturing/tracking moving interfaces in multi-fluid simulations particularly because of its rigorous numerical conservation. In a VOF method, volume fraction of a specific fluid is defined for all mesh cells of the computational domain. So, the interface that separates different fluids can be identified by examining the volume fraction values in the mesh cells.

The VOF schemes with algebraic reconstruction has drawn more and more attention owing to its efficiency and simplicity. Generally, the numerical flux is constructed by Eulerian advection schemes and combined with an anti-diffusion or artificial steepening treatment, which can be realized by either a built-in compressive mechanism or a post-processing step. Some representatives of this kind work can be found in [130, 158, 118, 69, 171, 116, 68, 142, 132]. Without the use of geometric calculations, we do not suffer substantial difficulty in extending an algebraic VOF to unstructured grid, which can be conducted more straightforwardly. However, a well-known observation is that the solution quality of an algebraic VOF is usually inferior to the PLIC VOF schemes.

Another algebraic VOF method, so-called tangent of THINC method [174], was proposed by using a hyperbolic tangent function to retrieve the jump distribution in the volume fraction function. The numerical flux is directly computed from the THINC reconstruction function, and the interface capturing calculation is simplified to a pure advection routine. The numerical diffusion that smears out the steepness in the volume fraction field can be completely removed by controlling the thickness of the jump transition. Following [30], some variants have been so far developed [186, 176, 187] to improve

the multi-dimensional solutions with the 1D solver as a building block. Without losing the simplicity, these schemes are able to produce high-quality numerical solutions comparable to the conventional PLIC VOF methods.

Fully multi-dimensional THINC schemes can be devised in a straightforward way by using multi-dimensional hyperbolic tangent function. In [66], we have proposed a Cartesian-grid version, so-called multidimensional THINC (MTHINC) method. In this study, an unstructured version, unstructured MTHINC (UMTHINC), for arbitrary unstructured grids is proposed for improvement in flexibility and generality. Particularly, higher-order interface approximation, like the quadratic surface, can also be formulated for interface reconstruction in quadrilateral and hexahedral elements.

4.2 Governing equation for volume fraction function

We consider multiple kinds of fluids filling in computational domain $\Omega \subset \mathbf{R}^3$. In order to distinguish one fluid, say fluid 1 out from others, it is natural to define a field function $H(\mathbf{x}, t)$ to indicate if a given point $\mathbf{x}$ falls in fluid 1 or not by,

$$H(\mathbf{x}, t) = \begin{cases} 1, & \text{if } \mathbf{x} \text{ is in fluid 1,} \\ 0, & \text{otherwise.} \end{cases} \tag{4.1}$$

Given the velocity of the fluid particle $\mathbf{u}$, the indicator function follows the Lagrangian invariant relation for advection,

$$\frac{d}{dt}\left(H(\mathbf{x}, t)\right) = 0, \tag{4.2}$$

where $d/dt = \partial/\partial t + \mathbf{u} \cdot \nabla$ denotes the material derivative in respect to time, and ∇ the gradient operator. The time evolution of the indicator function of Eulerian representation can be cast in the following advection equation,

$$\frac{\partial H}{\partial t} + \nabla \cdot (\mathbf{u}H) = H \nabla \cdot \mathbf{u}. \tag{4.3}$$

Provided that the computational domain Ω is divided into non-overlapped mesh elements $\Omega_i,\ i = 1, 2, \cdots, N$, the volume fraction of fluid 1 in cell Ω_i is then defined by,

$$\phi_i(t) \equiv \frac{1}{|\Omega_i|} \int_{\Omega_i(\mathbf{x})} H(\mathbf{x}, t) d\mathbf{x}, \tag{4.4}$$

where $|\Omega_i|$ is the volume of cell i. The interface separates fluid 1 from others in the cells where the volume fraction values between 0 and 1, i.e. $0 < \phi_i(t) < 1$, which are referred to as the interface cells.

From (4.3), the volume fraction of fluid 1 in cell Ω_i can be updated by a finite volume

formulation as,

$$\frac{\partial \phi_i(t)}{\partial t} + \frac{1}{|\Omega_i|}\sum_{j=1}^{J}\left(v_{n_{ij}}\int_{\Gamma_{ij}} H(\mathbf{x},t)_{iup}d\Gamma\right) = \frac{\phi_i(t)}{|\Omega_i|}\sum_{j=1}^{J}\left(v_{n_{ij}}\left|\Gamma_{ij}\right|\right), \tag{4.5}$$

where subscript ij denotes the index of the jth surface Γ_{ij} of cell Ω_i, J the number of the cell surfaces as shown in Fig. 2.1 and 2.2, $v_{n_{ij}} = \mathbf{v}_{ij}\cdot\mathbf{n}_{ij}$ the surface normal velocity on surface Γ_{ij} and $\mathbf{n}_{ij}$ the unit outward normal vector of Γ_{ij}. The index iup is determined by

$$iup = \begin{cases} = i, \text{ for } v_{n_{ij}} > 0; \\ = ij, \text{ otherwise.} \end{cases} \tag{4.6}$$

where ij denotes the index of neighboring cell that shares surface Γ_{ij} with cell Ω_i. The surface-average value is computed in the local coordinate system by Gauss quadrature formula as

$$\int_{\Gamma_{ij}} H(\mathbf{x},t)_{iup}d\Gamma = \sum_{q=1}^{m}\omega_q H(\xi_q,\eta_q,\gamma_q)_{iup}.$$

With all spatial discretization completed, we obtain a semi-discrete (ordinary differential) equation (4.5) for volume fraction evolving in time t. We apply the three-stage TVD Runge–Kutta method [140] to solve (4.5) and update the volume fraction values.

4.3 Multi-dimensional THINC scheme on unstructured grid

4.3.1 Reconstruction polynomial of multi-dimensional THINC formulation

In order to solve (4.5), we need to calculate the numerical flux, $v_{n_{ij}}\int_{\Gamma_{ij}} H(\mathbf{x},t)d\Gamma$, from the discrete VOF values ϕ_i, $i = 1, 2, \cdots, N$. In the THINC method, indicator function $H(\mathbf{x})$ is piecewisely approximated by a hyperbolic tangent function $H_i(\mathbf{x})$ on cell Ω_i,

$$H_i(\mathbf{x}) = \frac{1}{2}\left(1 + \tanh\left(\beta\left(\mathcal{P}_i(x,y,z) + \hat{d}_i\right)\right)\right), \tag{4.7}$$

where β is a parameter to control the sharpness of the transition jump in function $H_i(\mathbf{x})$, and $\mathcal{P}_i(x,y,z) + \hat{d}_i = 0$ is the equation of the interface with $\mathcal{P}_i(x,y,z)$ being a linear or quadratic polynomial.

We map physical coordinate $\mathbf{x} = (x,y,z)$ to local coordinate system $\boldsymbol{\xi} = (\xi,\eta,\zeta)$ by the basis functions, N_j which has been introduced in section 2.2. So the global coordinate

can be expressed in term of local coordinate system,

$$\mathbf{x} = \sum_{j=1}^{J} (\mathbf{x}_j N_j), \quad \mathbf{x} \in \Omega_i. \tag{4.8}$$

The hyperbolic tangent function in the local coordinate (ξ, η, ζ) is then written as,

$$H_i(\xi, \eta, \zeta) = \frac{1}{2} \left(1 + \tanh\left(\beta \left(\mathcal{P}_i(\xi, \eta, \zeta) + d_i\right)\right)\right), \tag{4.9}$$

and $\mathcal{P}_i(\xi, \eta, \zeta) + d_i = 0$ is the equation of the interface surface in the standard element in local coordinate. The polynomial for unstructured grid can be described as:

$$\begin{aligned} \mathcal{P}_i(\xi, \eta, \zeta) \quad = \quad & c^{(\xi)} a_{200} \xi^2 + c^{(\eta)} a_{020} \eta^2 + c^{(\zeta)} a_{002} \zeta^2 \\ & + c^{(\xi)} c^{(\eta)} a_{110} \xi\eta + c^{(\eta)} c^{(\zeta)} a_{011} \eta\zeta + c^{(\xi)} c^{(\zeta)} a_{101} \xi\zeta \\ & + a_{100} \xi + a_{010} \eta + a_{001} \zeta, \end{aligned} \tag{4.10}$$

where coefficients a_{srt} $(s, r, t = 0, 1, 2$ and $s + r + t \leq 2)$ are calculated from the interface normal and curvature tensor which are obtained from the given volume fraction values ϕ_i on cell Ω_i and its neighbors. For two dimensional case, the third dimension ζ in coordinates is ignored. The parameters $c^{(p)}$ $(p = \xi, \eta, \zeta)$ are set to either 0 or 1 according to different type elements which summarized as shown in Table 4.1.

The only unknown d in (4.9) indicates the location of the interface and is determined by integrating the function $H_i(\xi, \eta, \zeta)$ over cell Ω_i in the local coordinate system $\boldsymbol{\xi}$,

$$\int_{\Omega_i} H_i(\xi, \eta, \zeta) d\xi d\eta d\zeta = \phi_i. \tag{4.11}$$

Unfortunately, there is no general analytical expression for multi-dimensional integral of functions $H_i(\xi, \eta, \zeta)$. In practice, as mentioned in [66], a combined approach is introduced by employing 1D analytical integration of the hyperbolic tangent function and the Gaussian quadrature for the multi-dimensional integral calculation. Here, we define 1D analytical and numerical integration operators for function of $q(r) = \left(1 + \tanh\left(\beta \left(a_0 r + d\right)\right)\right)/2$ as $I_A^{(r)}$: and $I_N^{(r)}$: , respectively, where r belong to axis $[0, 1]$. The expression of $I_A^{(r)}$: and $I_N^{(r)}$: are given as

$$\begin{cases} I_A^{(r)} : \; q(r) = \frac{1}{2} \left(1 + \frac{1}{\beta a_0} \left(\frac{\cosh(\beta(a_0 + d))}{\cosh(\beta d)}\right)\right), & \text{for analytical,} \\ I_N^{(r)} : \; q(r) = \frac{1}{2} \left(q\left(r_p^-\right) + q\left(r_p^+\right)\right), & \text{for numerical,} \end{cases}$$

where the numerical integration is applied with two-point Gaussian quadrature as $r_p^{\pm} = \left(1 \pm 1/\sqrt{3}\right)/2$.

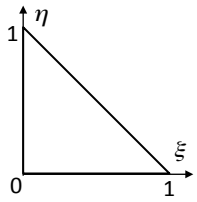
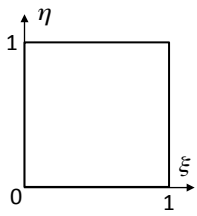
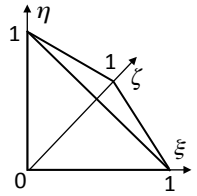
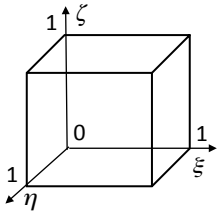
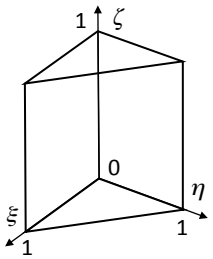
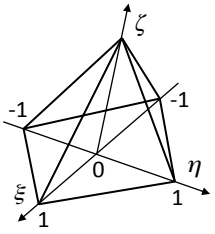
Element	Cell shape	$\left(c^{(\xi)}, c^{(\eta)}, c^{(\zeta)}\right)$
Triangular		$c^{(\xi)} = 0$ $c^{(\eta)} = 0$
Quadrilateral		$case\,1: \quad n_\xi = max(n_\xi, n_\eta)$ $c^{(\xi)} = 0$ $c^{(\eta)} = 1$ $case\,2: \quad n_\xi = max(n_\xi, n_\eta)$ $c^{(\xi)} = 1$ $c^{(\eta)} = 0$
Tetrahedral		$c^{(\xi)} = 0$ $c^{(\eta)} = 0$ $c^{(\zeta)} = 0$
Hexahedral		$\alpha, \beta \in (\xi, \eta, \zeta)$ $n_\alpha = max(n_\xi, n_\eta, n_\zeta)$ $c^{(\beta)} = 0$ for $\beta \equiv \alpha$ $c^{(\beta)} = 1$ for $\beta \neq \alpha$
Prismatic		$c^{(\xi)} = 0$ $c^{(\eta)} = 0$ $c^{(\zeta)} = 0$
Pyramidal		$c^{(\xi)} = 0$ $c^{(\eta)} = 0$ $c^{(\zeta)} = 0$

Table 4.1: Coefficients of multi-dimensional THINC reconstruction formulation for different type elements.

Once the reconstruction function $H_i(\xi, \eta, \zeta)$ is determined, the numerical fluxes can be computed by Gauss quadrature formula. And the volume fraction values ϕ_i can be updated by the finite volume formulation (4.5).

Next, we describe the algorithmic details to construct the THINC function on different type of grid elements. It is noted that we only make the reconstructions for the interface cells which are identified within $\epsilon \leq \phi_i \leq 1 - \epsilon$, where ϵ is a small value set to 10^{-8} in this paper.

4.3.2 The normal vector and curvature of the interface

Given the VOF values around an interface cell Ω_i, we first calculate the gradient $\nabla\phi_{ik} = (\phi_{xik}, \phi_{yik}, \phi_{zik})$ at the each vertex points (x_{ik}, y_{ik}, z_{ik}), $(k = 1, 2, \cdots, K)$ by the least-square method with the volume fraction values ϕ_{ikl} at the centroids $(x_{ikl}, y_{ikl}, z_{ikl})$ $(l = 1, 2, \cdots, L)$ among surrounding cells. We consider a linear polynomial at (x_{ik}, y_{ik}, z_{ik}),

$$\tilde{\Phi}(x, y, z) = \phi_{ij} + \phi_{xij}x + \phi_{yij}y + \phi_{zij}z, \tag{4.12}$$

and find ϕ_{ik}, ϕ_{xik}, ϕ_{yik} and ϕ_{zik} to minimize the following function,

$$\mathcal{I}_{ik} = \sum_{l=1}^{L} \left(\tilde{\Phi}(x_{ikl}, y_{ikl}, z_{ikl}) - \phi_{ikl} \right)^2, \tag{4.13}$$

which yields a set of four simultaneously linked linear algebraic equations to uniquely determine ϕ_{ik}, ϕ_{xik}, ϕ_{yik} and ϕ_{zik}. It is straightforward to get the formula to transform the first-order derivatives between the global coordinate system (x, y, z) and the local coordinate (ξ, η, ζ) according to Table 2.1 and 2.2,

$$\begin{aligned}
\phi_{\xi ik}(x, y, z) &= x_{\xi ik}\phi_{xi} + y_{\xi ik}\phi_{yik} + z_{\xi ik}\phi_{zik}, \\
\phi_{\eta ik}(x, y, z) &= x_{\eta ik}\phi_{xi} + y_{\eta ik}\phi_{yik} + z_{\eta ik}\phi_{zik}, \\
\phi_{\zeta ik}(x, y, z) &= x_{\zeta ik}\phi_{xi} + y_{\zeta ik}\phi_{yik} + z_{\zeta ik}\phi_{zik},
\end{aligned} \tag{4.14}$$

where the metric terms are directly obtained from (4.8). For two dimensional case, the quantities in third dimension ζ are ignored.

Given the gradients at vertex points (x_{ik}, y_{ik}, z_{ik}), $(k = 1, 2, \cdots, K)$, the normalized components are directly computed by

$$\begin{cases}
\psi_{\xi ik} = \phi_{\xi ik}/|\hat{\nabla}\phi_{ik}|, \\
\psi_{\eta ik} = \phi_{\eta ik}/|\hat{\nabla}\phi_{ik}|, \quad \text{for } k = 1, 2, \cdots K. \\
\psi_{\zeta ik} = \phi_{\zeta ik}/|\hat{\nabla}\phi_{ik}|,
\end{cases} \tag{4.15}$$

Dimensionality	Element	Unit normal vector
Two dimension	Trianglar Quadrilateral	$\psi_{\xi i} = \frac{1}{J}\sum_{j=1}^{J}\phi_{\xi ij}/\lvert\hat{\nabla}\phi_i\rvert,$ $\psi_{\eta i} = \frac{1}{J}\sum_{j=1}^{J}\phi_{\eta ij}/\lvert\hat{\nabla}\phi_i\rvert,$
Three dimension	Tetrahedral Hexahedral Prismatic	$\psi_{\xi i} = \frac{1}{J}\sum_{j=1}^{J}\phi_{\xi ij}/\lvert\hat{\nabla}\phi_i\rvert,$ $\psi_{\eta i} = \frac{1}{J}\sum_{j=1}^{J}\phi_{\eta ij}/\lvert\hat{\nabla}\phi_i\rvert,$ $\psi_{\zeta i} = \frac{1}{J}\sum_{j=1}^{J}\phi_{\zeta ij}/\lvert\hat{\nabla}\phi_i\rvert,$
	Pyramidal	$\psi_{\xi i} = \frac{1}{16}\left(3\left(\phi_{\xi i1}+\phi_{\xi i2}+\phi_{\xi i3}+\phi_{\xi i4}\right)+4\phi_{\xi i5}\right)/\lvert\hat{\nabla}\phi_i\rvert,$ $\psi_{\eta i} = \frac{1}{16}\left(3\left(\phi_{\eta i1}+\phi_{\eta i2}+\phi_{\eta i3}+\phi_{\eta i4}\right)+4\phi_{\eta i5}\right)/\lvert\hat{\nabla}\phi_i\rvert,$ $\psi_{\zeta i} = \frac{1}{16}\left(3\left(\phi_{\zeta i1}+\phi_{\zeta i2}+\phi_{\zeta i3}+\phi_{\zeta i4}\right)+4\phi_{\zeta i5}\right)/\lvert\hat{\nabla}\phi_i\rvert.$

Table 4.2: Unit normal vector at cell center for each element type.

Element	
Quadrilateral	$\psi_{\xi^2 i} = \frac{1}{2}(\psi_{\xi i2}+\psi_{\xi i3}-\psi_{\xi i1}-\psi_{\xi i4}),$ $\psi_{\eta^2 i} = \frac{1}{2}(\psi_{\eta i3}+\psi_{\eta i4}-\psi_{\eta i1}-\psi_{\eta i2}).$
Hexahedral	$\psi_{\xi^2 i} = \frac{1}{4}(\psi_{\xi i2}+\psi_{\xi i3}+\psi_{\xi i6}+\psi_{\xi i7}-\psi_{\xi i1}-\psi_{\xi i4}-\psi_{\xi i5}-\psi_{\xi i8}),$ $\psi_{\eta^2 i} = \frac{1}{4}(\psi_{\eta i3}+\psi_{\eta i4}+\psi_{\eta i7}+\psi_{\eta i8}-\psi_{\eta i1}-\psi_{\eta i2}-\psi_{\eta i5}-\psi_{\eta i6}),$ $\psi_{\zeta^2 i} = \frac{1}{4}(\psi_{\zeta i5}+\psi_{\zeta i6}+\psi_{\zeta i7}+\psi_{\zeta i8}-\psi_{\zeta i1}-\psi_{\zeta i2}-\psi_{\zeta i3}-\psi_{\zeta i4}),$ $\psi_{\xi\eta i} = \frac{1}{4}(\psi_{\xi i3}+\psi_{\xi i4}+\psi_{\xi i7}+\psi_{\xi i8}-\psi_{\xi i1}-\psi_{\xi i2}-\psi_{\xi i5}-\psi_{\xi i6}),$ $\psi_{\eta\xi i} = \frac{1}{4}(\psi_{\eta i2}+\psi_{\eta i3}+\psi_{\eta i6}+\psi_{\eta i7}-\psi_{\eta i1}-\psi_{\eta i4}-\psi_{\eta i5}-\psi_{\eta i8}),$ $\psi_{\eta\zeta i} = \frac{1}{4}(\psi_{\eta i5}+\psi_{\eta i6}+\psi_{\eta i7}+\psi_{\eta i8}-\psi_{\eta i1}-\psi_{\eta i2}-\psi_{\eta i3}-\psi_{\eta i4}),$ $\psi_{\zeta\eta i} = \frac{1}{4}(\psi_{\tau i3}+\psi_{\zeta i4}+\psi_{\tau i7}+\psi_{\zeta i8}-\psi_{\zeta i1}-\psi_{\zeta i2}-\psi_{\zeta i5}-\psi_{\zeta i6}),$ $\psi_{\xi\zeta i} = \frac{1}{4}(\psi_{\xi i5}+\psi_{\xi i6}+\psi_{\xi i7}+\psi_{\xi i8}-\psi_{\xi i1}-\psi_{\xi i2}-\psi_{\xi i3}-\psi_{\xi i4}),$ $\psi_{\zeta\xi i} = \frac{1}{4}(\psi_{\tau i2}+\psi_{\zeta i3}+\psi_{\tau i6}+\psi_{\zeta i7}-\psi_{\zeta i1}-\psi_{\zeta i4}-\psi_{\zeta i5}-\psi_{\zeta i8}).$

Table 4.3: Curvature tensor at the cell center for each element type.

where $\hat{\nabla}\phi_{ik} = (\phi_{\xi ik}, \phi_{\eta ik}, \phi_{\zeta ik})$.

The unit normal vector at the cell center is computed from local vectors on cell vertices based on reconstruction function in finite element method. We summarized the formulations as shown in Table 4.2, where $\hat{\nabla}\phi_i = (\frac{1}{K}\sum_{k=1}^{K}\phi_{\xi ik}, \frac{1}{K}\sum_{k=1}^{K}\phi_{\eta ik}, \frac{1}{K}\sum_{k=1}^{K}\phi_{\zeta ik})$ denoting a average at the cell center.

The second order derivatives at the cell center which are required to determine the curvature of the surface for quadrilateral and hexahedral element, are computed by a central differencing formula as denoted in Table 4.3.

For brevity, the unit normal vector (n_ξ, n_η, n_ζ) and the curvature tensor l_{pq}, $(p, q =$

$\xi, \eta, \zeta)$ of the interface are summarized as (4.16),

$$\begin{cases} n_\xi = \psi_{\xi i}, \\ n_\eta = \psi_{\eta i}, \\ n_\zeta = \psi_{\zeta i}, \\ l_{\xi\xi} = \psi_{\xi^2 i}, \\ l_{\eta\eta} = \psi_{\eta^2 i}, \\ l_{\zeta\zeta} = \psi_{\zeta^2 i}, \\ l_{\xi\eta} = \frac{1}{2}\left(\psi_{\xi\eta i} + \psi_{\eta\xi i}\right), \\ l_{\eta\zeta} = \frac{1}{2}\left(\psi_{\eta\zeta i} + \psi_{\zeta\eta i}\right), \\ l_{\zeta\xi} = \frac{1}{2}\left(\psi_{\xi\zeta i} + \psi_{\zeta\xi i}\right). \end{cases} \tag{4.16}$$

4.3.3 The THINC reconstruction function

- For triangular element

Based on geometric information of the interface, the linear polynomial (4.10) is determined by constraint conditions as (4.17),

$$\begin{cases} \left.\frac{\partial \mathcal{P}_i}{\partial \xi}\right|_{(\frac{1}{3},\frac{1}{3})} = n_\xi, \\ \left.\frac{\partial \mathcal{P}_i}{\partial \eta}\right|_{(\frac{1}{3},\frac{1}{3})} = n_\eta. \end{cases} \tag{4.17}$$

Some algebraic manipulation [66] gives explicitly the coefficients in (4.10) as

$$\begin{cases} a_{100} = n_\xi, \\ a_{010} = n_\eta. \end{cases} \tag{4.18}$$

After the polynomial $\mathcal{P}_i(\xi, \eta)$ is founded with the geometrical information retrieved from the VOF field, the unknown d in (4.9) is determined by integrating the function $H_i(\xi, \eta)$ over cell Ω_i in the local coordinate system through (4.11). In practice, the spatial integral is carried out alternatively by a combination of 1D rigorous integration of the hyperbolic tangent function and numerical quadratures in other dimensions. Here, we summarize the procedure to integrate (4.11) and find d as below.

Case 1: $|n_\xi| = \max(|n_\xi|, |n_\eta|)$

- Set $c^{(\xi)} = c^{(\eta)} = 0$ in $\mathcal{P}_i(\xi, \eta)$, $\mathcal{P}_i(\xi, \eta) = a_{100}\xi + a_{010}\eta$,

- Calculate the exact integral in ξ direction,

$$\begin{aligned} \overline{H}_i^{\xi}(\eta) &= \tfrac{1}{1-\eta} \int_0^{1-\eta} H_i(\xi,\eta)d\xi \\ &= \frac{1}{2\,(1-\eta)}\left(1-\eta+\frac{1}{\beta a_{100}}\ln\left(\frac{\cosh(\beta(\mathcal{P}_i(1-\eta,\eta)+d_i)}{\cosh(\beta(\mathcal{P}_i(0,\eta)+d_i)}\right)\right), \end{aligned} \tag{4.19}$$

- Use Gauss numerical quadrature to evaluate the integral with respect to η,

$$\overline{\overline{H}^{\xi}}_i^{\eta} = \int_0^1 \overline{H}_i^{\xi}(\eta)d\eta = \overline{H}_i^{\xi}(1\,/3), \tag{4.20}$$

- Solve

$$\overline{H}_i^{\xi}(1\,/3) = \phi_i \tag{4.21}$$

$$\begin{aligned} &\overline{H}_i^{\xi}(1\,/3) \\ =\ &\tfrac{1}{2}+\tfrac{3}{2\beta a_{100}}\ln\left(\frac{\cosh\left(\beta\left(\frac{2}{3}a_{100}+\frac{1}{3}a_{010}+d\right)\right)}{\cosh\left(\beta\left(\frac{1}{3}a_{010}+d\right)\right)}\right)=\phi_i \end{aligned}$$

Case 2: $|n_\eta| = \max(|n_\xi|, |n_\eta|)$

- Set $c^{(\xi)} = c^{(\eta)} = 0$ in $\mathcal{P}_i(\xi,\eta)$, $\mathcal{P}_i(\xi,\eta) = a_{100}\xi + a_{010}\eta$,
- Calculate the exact integral in η direction,

$$\begin{aligned} \overline{H}_i^{\eta}(\xi) &= \frac{1}{1-\xi}\int_0^{1-\xi} H_i(\xi,\eta)d\eta \\ &= \frac{1}{2\,(1-\xi)}\left(1-\xi+\frac{1}{\beta a_{010}}\ln\left(\frac{\cosh(\beta(\mathcal{P}_i(\xi,1-\xi)+d_i)}{\cosh(\beta(\mathcal{P}_i(\xi,0)+d_i)}\right)\right), \end{aligned} \tag{4.22}$$

- Use Gauss numerical quadrature to evaluate the integral with respect to ξ,

$$\overline{\overline{H}^{\eta}}_i^{\xi} = \int_0^1 \overline{H}_i^{\eta}(\xi)d\xi = \overline{H}_i^{\eta}(1\,/3), \tag{4.23}$$

- Solve

$$\overline{H}_i^{\eta}(1\,/3) = \phi_i \tag{4.24}$$

$$\begin{aligned} &\overline{H}_i^{\eta}(1\,/3) \\ =\ &\tfrac{1}{2}+\tfrac{3}{2\beta a_{010}}\ln\left(\frac{\cosh\left(\beta\left(\frac{1}{3}a_{100}+\frac{2}{3}a_{010}+d\right)\right)}{\cosh\left(\beta\left(\frac{1}{3}a_{100}+d\right)\right)}\right)=\phi_i \end{aligned}$$

The d is determined as

$$d = \frac{1}{2\beta}\ln\left(\frac{1-AQ}{AB(Q-A)}\right)$$

- Case 1:

$$\begin{cases} A &= \exp\left(\frac{2}{3}\beta a_{100}\right) \\ B &= \exp\left(\frac{2}{3}\beta a_{010}\right) \\ Q &= \exp\left(\frac{2}{3}\beta a_{100}\left(2\phi-1\right)\right) \end{cases}$$

- Case 2:

$$\begin{cases} A &= \exp\left(\frac{2}{3}\beta a_{010}\right) \\ B &= \exp\left(\frac{2}{3}\beta a_{100}\right) \\ Q &= \exp\left(\frac{2}{3}\beta a_{010}\left(2\phi-1\right)\right) \end{cases}$$

- For quadrilateral element

Based on geometric information of the interface, the quadratic polynomial (4.10) is determined by constraint conditions as (4.25),

$$\begin{cases} \left.\frac{\partial \mathcal{P}_i}{\partial \xi}\right|_{(\frac{1}{2},\frac{1}{2})} = n_\xi, \\ \left.\frac{\partial \mathcal{P}_i}{\partial \eta}\right|_{(\frac{1}{2},\frac{1}{2})} = n_\eta, \\ \left.\frac{\partial^2 \mathcal{P}_i}{\partial \xi^2}\right|_{(\frac{1}{2},\frac{1}{2})} = l_{\xi\xi}, \\ \left.\frac{\partial^2 \mathcal{P}_i}{\partial \eta^2}\right|_{(\frac{1}{2},\frac{1}{2})} = l_{\eta\eta}. \end{cases} \tag{4.25}$$

Some algebraic manipulation [66] gives explicitly the coefficients in (4.10) as

$$\begin{cases} a_{100} = n_\xi - \frac{1}{2}c^{(\xi)}l_{\xi\xi}, \\ a_{010} = n_\eta - \frac{1}{2}c^{(\eta)}l_{\eta\eta}, \\ a_{200} = \frac{1}{2}c^{(\xi)}l_{\xi\xi},\ a_{020} = \frac{1}{2}c^{(\eta)}l_{\eta\eta}. \end{cases} \tag{4.26}$$

After the polynomial $\mathcal{P}_i(\xi,\eta)$ is founded with coefficients denoted in (4.26), the unknown d in (4.9) can be determined in the same manner. Here, we summarize the procedure to integrate (4.11) and find d as below.

Case 1: $|n_\xi| = \max(|n_\xi|, |n_\eta|)$

- Set $c^{(\xi)} = 0$ in $\mathcal{P}_i(\xi,\eta)$, $\mathcal{P}_i(\xi,\eta) = a_{020}\eta^2 + a_{100}\xi + a_{010}\eta$,

- Calculate the exact integral in ξ direction,

$$\begin{aligned}\overline{H}_i^{\xi}(\eta) &= \int_0^1 H_i(\xi,\eta)d\xi \\ &= \frac{1}{2}\left(1+\frac{1}{\beta a_{100}}\ln\left(\frac{\cosh(\beta(\mathcal{P}_i(1,\eta)+d_i)}{\cosh(\beta(\mathcal{P}_i(0,\eta)+d_i)}\right)\right),\end{aligned} \tag{4.27}$$

- Use Gauss numerical quadrature to evaluate the integral with respect to η,

$$\overline{\overline{H}^{\xi}}_i^{\eta} = \int_0^1 \overline{H}_i^{\xi}(\eta)d\eta = \sum_{p=1}^{m}\omega_p\overline{H}_i^{\xi}(\eta_p), \tag{4.28}$$

  where (η_p) and ω_p are Gauss quadrature points and corresponding weights respectively. For quadrilateral element, a two-point 1D formula ($m = 2$) is used.

- Solve

$$\sum_{p=1}^{m}\omega_p\overline{H}_i^{\xi}(\eta_p) = \phi_i \tag{4.29}$$

$$\begin{aligned}& I_N^{(\eta)} : \left(I_A^{(\xi)} : H_i(\xi,\eta)\right) \\ =\ & I_N^{(\eta)} : \overline{H}_i^{\xi}(\eta) \\ =\ & \tfrac{1}{4}\left(1+\tfrac{1}{\beta a_{100}}\ln\left(\tfrac{\cosh(\beta(\mathcal{P}_i(1,r_p^-)+d_i)}{\cosh(\beta(\mathcal{P}_i(0,r_p^-)+d_i)}\right)\right)+\tfrac{1}{4}\left(1+\tfrac{1}{\beta a_{100}}\ln\left(\tfrac{\cosh(\beta(\mathcal{P}_i(1,r_p^+)+d_i)}{\cosh(\beta(\mathcal{P}_i(0,r_p^+)+d_i)}\right)\right) \\ =\ & \tfrac{1}{2}+\tfrac{1}{8\beta a_{100}}\ln\left(\tfrac{(AB^-D+1)(AB^+D+1)}{A(B^-D+1)(B^+D+1)}\right)=\phi_i\end{aligned}$$

Case 2: $|n_\eta| = \max(|n_\xi|, |n_\eta|)$

- Set $c^{(\eta)} = 0$ in $\mathcal{P}_i(\xi,\eta)$, $\mathcal{P}_i(\xi,\eta) = a_{200}\xi^2 + a_{100}\xi + a_{010}\eta$,
- Calculate the exact integral in η direction,

$$\begin{aligned}\overline{H}_i^{\eta}(\xi) &= \int_0^1 H_i(\xi,\eta)d\eta \\ &= \frac{1}{2}\left(1+\frac{1}{\beta a_{010}}\ln\left(\frac{\cosh(\beta(\mathcal{P}_i(\xi,1)+d_i)}{\cosh(\beta(\mathcal{P}_i(\xi,0)+d_i)}\right)\right),\end{aligned} \tag{4.30}$$

- Use Gauss numerical quadrature to evaluate the integral with respect to ξ,

$$\overline{\overline{H}^{\eta}}_i^{\xi} = \int_0^1 \overline{H}_i^{\eta}(\xi)d\xi = \sum_{p=1}^{m}\omega_p\overline{H}_i^{\eta}(\xi_p), \tag{4.31}$$

- Solve

$$\sum_{p=1}^{m}\omega_p\overline{H}_i^{\eta}(\xi_p) = \phi_i \tag{4.32}$$

$$
\begin{aligned}
& I_N^{(\xi)} : \left(I_A^{(\eta)} : H_i(\xi,\eta) \right) \\
= \;& I_N^{(\xi)} : \overline{H}_i^{\eta}(\eta) \\
= \;& \tfrac{1}{4}\left(1+\tfrac{1}{\beta a_{010}}\ln\left(\tfrac{\cosh(\beta(\mathcal{P}_i(r_p^-,1)+d_i)}{\cosh(\beta(\mathcal{P}_i(r_p^-,0)+d_i)}\right)\right)+\tfrac{1}{4}\left(1+\tfrac{1}{\beta a_{010}}\ln\left(\tfrac{\cosh(\beta(\mathcal{P}_i(r_p^+,1)+d_i)}{\cosh(\beta(\mathcal{P}_i(r_p^+,0)+d_i)}\right)\right) \\
= \;& \tfrac{1}{2}+\tfrac{1}{4\beta a_{010}}\ln\left(\tfrac{\left(AB^-D+1\right)\left(AB^+D+1\right)}{A(B^-D+1)(B^+D+1)}\right)=\phi_i
\end{aligned}
$$

A quadratic equation for $D=\exp(2\beta d)$ is

$$
AB^-\left(A-Q\right)D^2+A\left(B^-+B^+\right)\left(1-Q\right)D+1-AQ=0
$$

- Case 1:

$$
\begin{cases}
A &= \exp\left(2\beta a_{100}\right) \\
B^{\pm} &= \exp\left(2\beta\left(a_{020}\left(r_p^{\pm}\right)^2+a_{010}r_p^{\pm}\right)\right) \\
Q &= \exp\left(2\beta a_{100}\left(2\phi-1\right)\right)
\end{cases}
$$

- Case 2:

$$
\begin{cases}
A &= \exp\left(2\beta a_{010}\right) \\
B^{\pm} &= \exp\left(2\beta\left(a_{200}\left(r_p^{\pm}\right)^2+a_{002}\left(r_p^{-}\right)^2+a_{100}r_p^{\pm}\right)\right) \\
Q &= \exp\left(2\beta a_{010}\left(2\phi-1\right)\right)
\end{cases}
$$

- For tetrahedral element

Based on geometric information of the interface, the linear polynomial (4.10) is determined by constraint conditions as (4.33),

$$
\begin{cases}
\left.\frac{\partial\mathcal{P}_i}{\partial\xi}\right|_{(\frac{1}{4},\frac{1}{4},\frac{1}{4})} = n_\xi, \\
\left.\frac{\partial\mathcal{P}_i}{\partial\eta}\right|_{(\frac{1}{4},\frac{1}{4},\frac{1}{4})} = n_\eta, \\
\left.\frac{\partial\mathcal{P}_i}{\partial\zeta}\right|_{(\frac{1}{4},\frac{1}{4},\frac{1}{4})} = n_\zeta.
\end{cases}
\tag{4.33}
$$

Some algebraic manipulation [66] gives explicitly the coefficients in (4.10) as

$$
\begin{cases}
a_{100} = n_\xi, \\
a_{010} = n_\eta, \\
a_{001} = n_\zeta.
\end{cases}
\tag{4.34}
$$

After the polynomial $\mathcal{P}_i(\xi,\eta,\zeta)$ is founded with coefficients of a_{100}, a_{010} and a_{001}, the unknown d in (4.9) is determined as following.

Case 1: $|n_\xi| = \max(|n_\xi|, |n_\eta|, |n_\zeta|)$

- Set $c^{(\xi)} = c^{(\eta)} = c^{(\zeta)} = 0$ in $\mathcal{P}_i(\xi,\eta,\zeta)$, $\mathcal{P}_i(\xi,\eta,\zeta) = a_{100}\xi + a_{010}\eta + a_{001}\zeta$,
- Calculate the exact integral in ξ direction,

$$\begin{aligned}\overline{H}_i^{\xi}(\eta,\zeta) &= \frac{1}{1-\eta-\zeta}\int_0^{1-\eta-\zeta} H_i(\xi,\eta,\zeta)d\xi \qquad (4.35)\\ &= \frac{1}{2\,(1-\eta-\zeta)}\left(1+\frac{1}{\beta a_{100}}\ln\left(\frac{\cosh(\beta(\mathcal{P}_i(1-\eta-\zeta,\eta,\zeta)+d_i)}{\cosh(\beta(\mathcal{P}_i(0,\eta,\zeta)+d_i)}\right)\right),\end{aligned}$$

- Use Gauss numerical quadrature to evaluate the integral with respect to η and ζ,

$$\overline{\overline{H}^{\xi}}_i^{\eta\zeta} = \int_0^1\int_0^1 \overline{H}_i^{\xi}(\eta,\zeta)d\eta d\zeta = \overline{H}_i^{\xi}(1\,/4\,,1\,/4), \qquad (4.36)$$

- Solve

$$\overline{H}_i^{\xi}(1\,/4\,,1\,/4) = \phi_i \qquad (4.37)$$

$$\begin{aligned}&\overline{H}_i^{\xi}(1\,/4\,,1\,/4)\\ =\;& \tfrac{1}{2}+\tfrac{2}{\beta a_{100}}\ln\left(\frac{\cosh\left(\beta\left(\frac{1}{2}a_{100}+\frac{1}{4}a_{010}+\frac{1}{4}a_{001}+d\right)\right)}{\cosh\left(\beta\left(\frac{1}{4}a_{010}+\frac{1}{4}a_{001}+d\right)\right)}\right)=\phi_i\end{aligned}$$

Case 2: $|n_\eta| = \max(|n_\xi|, |n_\eta|, |n_\zeta|)$

- Set $c^{(\xi)} = c^{(\eta)} = c^{(\zeta)} = 0$ in $\mathcal{P}_i(\xi,\eta,\zeta)$, $\mathcal{P}_i(\xi,\eta,\zeta) = a_{100}\xi + a_{010}\eta + a_{001}\zeta$,
- Calculate the exact integral in η direction,

$$\begin{aligned}\overline{H}_i^{\eta}(\xi,\zeta) &= \frac{1}{1-\xi-\zeta}\int_0^{1-\xi-\zeta} H_i(\xi,\eta,\zeta)d\eta \qquad (4.38)\\ &= \frac{1}{2\,(1-\xi-\zeta)}\left(1+\frac{1}{\beta a_{010}}\ln\left(\frac{\cosh(\beta(\mathcal{P}_i(\xi,1-\xi-\zeta,\zeta)+d_i)}{\cosh(\beta(\mathcal{P}_i(\xi,0,\zeta)+d_i)}\right)\right),\end{aligned}$$

- Use Gauss numerical quadrature to evaluate the integral with respect to ξ and ζ,

$$\overline{\overline{H}^{\eta}}_i^{\xi\zeta} = \int_0^1\int_0^1 \overline{H}_i^{\eta}(\xi,\zeta)d\xi d\zeta = \overline{H}_i^{\eta}(1\,/4\,,1\,/4), \qquad (4.39)$$

- Solve

$$\overline{H}_i^{\eta}(1\,/4\,,1\,/4) = \phi_i \qquad (4.40)$$

$$\begin{aligned}&\overline{H}_i^{\eta}(1\,/4\,,1\,/4)\\ =\;& \tfrac{1}{2}+\tfrac{2}{\beta a_{010}}\ln\left(\frac{\cosh\left(\beta\left(\frac{1}{4}a_{100}+\frac{1}{2}a_{010}+\frac{1}{4}a_{001}+d\right)\right)}{\cosh\left(\beta\left(\frac{1}{4}a_{100}+\frac{1}{4}a_{001}+d\right)\right)}\right)=\phi_i\end{aligned}$$

Case 3: $|n_\zeta| = \max(|n_\xi|, |n_\eta|, |n_\zeta|)$

- Set $c^{(\xi)} = c^{(\eta)} = c^{(\zeta)} = 0$ in $\mathcal{P}_i(\xi, \eta, \zeta)$, $\mathcal{P}_i(\xi, \eta, \zeta) = a_{100}\xi + a_{010}\eta + a_{001}\zeta$,
- Calculate the exact integral in ζ direction,

$$\begin{aligned} \overline{H}_i^{\zeta}(\xi, \eta) &= \frac{1}{1-\xi-\eta} \int_0^{1-\xi-\eta} H_i(\xi, \eta, \zeta) d\zeta \qquad (4.41) \\ &= \frac{1}{2\,(1-\xi-\eta)} \left(1 + \frac{1}{\beta a_{001}} \ln\left(\frac{\cosh(\beta(\mathcal{P}_i(\xi, \eta, 1-\xi-\eta) + d_i)}{\cosh(\beta(\mathcal{P}_i(\xi, \eta, 0) + d_i)}\right)\right), \end{aligned}$$

- Use Gauss numerical quadrature to evaluate the integral with respect to ξ and η,

$$\overline{\overline{H}^{\zeta}}_i^{\xi\eta} = \int_0^1 \int_0^1 \overline{H}_i^{\zeta}(\xi, \eta) d\xi d\eta = \overline{H}_i^{\zeta}(1/4\,, 1/4), \qquad (4.42)$$

- Solve

$$\overline{H}_i^{\zeta}(1/4\,, 1/4) = \phi_i \qquad (4.43)$$

$$\begin{aligned} &\overline{H}_i^{\zeta}(1/4\,, 1/4) \\ = \;& \tfrac{1}{2} + \tfrac{2}{\beta a_{001}} \ln\left(\frac{\cosh\left(\beta\left(\frac{1}{4}a_{100} + \frac{1}{4}a_{010} + \frac{1}{2}a_{001} + d\right)\right)}{\cosh\left(\beta\left(\frac{1}{4}a_{100} + \frac{1}{4}a_{010} + d\right)\right)}\right) = \phi_i \end{aligned}$$

The d is determined as

$$d = \frac{1}{2\beta} \ln\left(\frac{1 - AQ}{AB(Q - A)}\right)$$

- Case 1:

$$\begin{cases} A &= \exp\left(\frac{1}{2}\beta a_{100}\right) \\ B &= \exp\left(\frac{1}{2}\beta\left(a_{010} + a_{001}\right)\right) \\ Q &= \exp\left(\frac{1}{2}\beta a_{100}\left(2\phi - 1\right)\right) \end{cases}$$

- Case 2:

$$\begin{cases} A &= \exp\left(\frac{1}{2}\beta a_{010}\right) \\ B &= \exp\left(\frac{1}{2}\beta\left(a_{100} + a_{001}\right)\right) \\ Q &= \exp\left(\frac{1}{2}\beta a_{010}\left(2\phi - 1\right)\right) \end{cases}$$

- Case 3:

$$\begin{cases} A &= \exp\left(\frac{1}{2}\beta a_{001}\right) \\ B &= \exp\left(\frac{1}{2}\beta\left(a_{100} + a_{010}\right)\right) \\ Q &= \exp\left(\frac{1}{2}\beta a_{001}\left(2\phi - 1\right)\right) \end{cases}$$

- For hexahedral element

Based on geometric information of the interface, the quadratic polynomial (4.10) is determined by constraint conditions as (4.44),

$$\begin{cases} \left.\frac{\partial \mathcal{P}_i}{\partial \xi}\right|_{(\frac{1}{2},\frac{1}{2},\frac{1}{2})} = n_\xi, \\ \left.\frac{\partial \mathcal{P}_i}{\partial \eta}\right|_{(\frac{1}{2},\frac{1}{2},\frac{1}{2})} = n_\eta, \\ \left.\frac{\partial \mathcal{P}_i}{\partial \zeta}\right|_{(\frac{1}{2},\frac{1}{2},\frac{1}{2})} = n_\zeta, \\ \left.\frac{\partial^2 \mathcal{P}_i}{\partial \xi^2}\right|_{(\frac{1}{2},\frac{1}{2},\frac{1}{2})} = l_{\xi\xi}, \\ \left.\frac{\partial^2 \mathcal{P}_i}{\partial \eta^2}\right|_{(\frac{1}{2},\frac{1}{2},\frac{1}{2})} = l_{\eta\eta}, \\ \left.\frac{\partial^2 \mathcal{P}_i}{\partial \zeta^2}\right|_{(\frac{1}{2},\frac{1}{2},\frac{1}{2})} = l_{\zeta\zeta}, \\ \left.\frac{\partial^2 \mathcal{P}_i}{\partial \xi \partial \eta}\right|_{(\frac{1}{2},\frac{1}{2},\frac{1}{2})} = l_{\xi\eta}, \\ \left.\frac{\partial^2 \mathcal{P}_i}{\partial \eta \partial \zeta}\right|_{(\frac{1}{2},\frac{1}{2},\frac{1}{2})} = l_{\eta\zeta}, \\ \left.\frac{\partial^2 \mathcal{P}_i}{\partial \xi \partial \zeta}\right|_{(\frac{1}{2},\frac{1}{2},\frac{1}{2})} = l_{\xi\zeta}. \end{cases} \tag{4.44}$$

Some algebraic manipulation [66] gives explicitly the coefficients in (4.10) as

$$\begin{cases} a_{100} = n_\xi - \frac{1}{2}\left(c^{(\xi)} l_{\xi\xi} + c^{(\xi)} c^{(\eta)} l_{\xi\eta} + c^{(\xi)} c^{(\zeta)} l_{\xi\zeta}\right), \\ a_{010} = n_\eta - \frac{1}{2}\left(c^{(\eta)} l_{\eta\eta} + c^{(\xi)} c^{(\eta)} l_{\xi\eta} + c^{(\eta)} c^{(\zeta)} l_{\eta\zeta}\right), \\ a_{001} = n_\zeta - \frac{1}{2}\left(c^{(\zeta)} l_{\zeta\zeta} + c^{(\xi)} c^{(\zeta)} l_{\xi\zeta} + c^{(\eta)} c^{(\zeta)} l_{\eta\zeta}\right), \\ a_{110} = c^{(\xi)} c^{(\eta)} l_{\xi\eta},\ a_{011} = c^{(\eta)} c^{(\zeta)} l_{\eta\zeta},\ a_{101} = c^{(\xi)} c^{(\zeta)} l_{\xi\zeta}, \\ a_{200} = \frac{1}{2} c^{(\xi)} l_{\xi\xi},\ a_{020} = \frac{1}{2} c^{(\eta)} l_{\eta\eta},\ a_{002} = \frac{1}{2} c^{(\zeta)} l_{\zeta\zeta}. \end{cases} \tag{4.45}$$

After the polynomial $\mathcal{P}_i(\xi, \eta, \zeta)$ is founded with coefficients of (4.45), the unknown d in (4.9) is determined by the same way as shown below.

Case 1: $|n_\xi| = \max(|n_\xi|, |n_\eta|, |n_\zeta|)$

- Set $c^{(\xi)} = 0$ in $\mathcal{P}_i(\xi, \eta, \zeta)$, $\mathcal{P}_i(\xi, \eta, \zeta) = a_{020}\eta^2 + a_{002}\zeta^2 + a_{011}\eta\zeta + a_{100}\xi + a_{010}\eta + a_{001}\zeta$,
- Calculate the exact integral in ξ direction,

$$\begin{aligned} \overline{H}_i^{\xi}(\eta, \zeta) &= \int_0^1 H_i(\xi, \eta, \zeta) d\xi \\ &= \frac{1}{2}\left(1 + \frac{1}{\beta a_{100}} \ln\left(\frac{\cosh(\beta(\mathcal{P}_i(1, \eta, \zeta) + d_i)}{\cosh(\beta(\mathcal{P}_i(0, \eta, \zeta) + d_i)}\right)\right), \end{aligned} \tag{4.46}$$

- Use Gauss numerical quadrature to evaluate the integral with respect to η and ζ,

$$\overline{\overline{H}^{\xi}}_i^{\eta\zeta} = \int_0^1 \int_0^1 \overline{H}_i^{\xi}(\eta,\zeta)d\eta d\zeta = \sum_{p,q=1}^{m} \omega_{pq}\overline{H}_i^{\xi}(\eta_p,\zeta_q), \tag{4.47}$$

  where (η_p,ζ_q) and ω_{pq} are Gauss quadrature points and corresponding weights respectively. A four-point 2D formula ($m=2$) is used.

- Solve

$$\sum_{p,q=1}^{m} \omega_{pq}\overline{H}_i^{\xi}(\eta_p,\zeta_q) = \phi_i \tag{4.48}$$

$$\begin{aligned}
& I_N^{(\zeta)} : \left(I_N^{(\eta)} : \left(I_A^{(\xi)} : H_i(\xi,\eta,\zeta)\right)\right) \\
= \;& I_N^{(\zeta)} : \left(I_N^{(\eta)} : \overline{H}_i^{\xi}(\eta,\zeta)\right) \\
= \;& \tfrac{1}{8}\left(1+\tfrac{1}{\beta a_{100}}\ln\left(\tfrac{\cosh(\beta(\mathcal{P}_i(1,r_p^-,r_p^-)+d_i)}{\cosh(\beta(\mathcal{P}_i(0,r_p^-,r_p^-)+d_i)}\right)\right)+\tfrac{1}{8}\left(1+\tfrac{1}{\beta a_{100}}\ln\left(\tfrac{\cosh(\beta(\mathcal{P}_i(1,r_p^+,r_p^-)+d_i)}{\cosh(\beta(\mathcal{P}_i(0,r_p^+,r_p^-)+d_i)}\right)\right) \\
+ \;& \tfrac{1}{8}\left(1+\tfrac{1}{\beta a_{100}}\ln\left(\tfrac{\cosh(\beta(\mathcal{P}_i(1,r_p^-,r_p^+)+d_i)}{\cosh(\beta(\mathcal{P}_i(0,r_p^-,r_p^+)+d_i)}\right)\right)+\tfrac{1}{8}\left(1+\tfrac{1}{\beta a_{100}}\ln\left(\tfrac{\cosh(\beta(\mathcal{P}_i(1,r_p^+,r_p^+)+d_i)}{\cosh(\beta(\mathcal{P}_i(0,r_p^+,r_p^+)+d_i)}\right)\right) \\
= \;& \tfrac{1}{2}+\tfrac{1}{8\beta a_{100}}\ln\left(\tfrac{\left(AB^-D+1\right)\left(AB^+D+1\right)\left(AC^-D+1\right)\left(AC^+D+1\right)}{A^2(B^-D+1)(B^+D+1)(C^-D+1)(C^+D+1)}\right) = \phi_i
\end{aligned}$$

Case 2: $|n_\eta| = \max(|n_\xi|,|n_\eta|,|n_\zeta|)$

- Set $c^{(\eta)}=0$ in $\mathcal{P}_i(\xi,\eta,\zeta)$, $\mathcal{P}_i(\xi,\eta,\zeta) = a_{200}\xi^2+a_{002}\zeta^2+a_{101}\xi\zeta+a_{100}\xi+a_{010}\eta+a_{001}\zeta$,

- Calculate the exact integral in η direction,

$$\begin{aligned}
\overline{H}_i^{\eta}(\xi,\zeta) &= \int_0^1 H_i(\xi,\eta,\zeta)d\eta \\
&= \frac{1}{2}\left(1+\frac{1}{\beta a_{010}}\ln\left(\frac{\cosh(\beta(\mathcal{P}_i(\xi,1,\zeta)+d_i)}{\cosh(\beta(\mathcal{P}_i(\xi,0,\zeta)+d_i)}\right)\right),
\end{aligned} \tag{4.49}$$

- Use Gauss numerical quadrature to evaluate the integral with respect to ξ and ζ,

$$\overline{\overline{H}^{\eta}}_i^{\xi\zeta} = \int_0^1 \int_0^1 \overline{H}_i^{\eta}(\xi,\zeta)d\xi d\zeta = \sum_{p,q=1}^{m} \omega_{pq}\overline{H}_i^{\eta}(\xi_p,\zeta_q), \tag{4.50}$$

- Solve

$$\sum_{p,q=1}^{m} \omega_{pq}\overline{H}_i^{\eta}(\xi_p,\zeta_q) = \phi_i \tag{4.51}$$

$$
\begin{aligned}
& I_N^{(\zeta)} : \Big(I_N^{(\xi)} : \Big(I_A^{(\eta)} : H_i(\xi,\eta,\zeta) \Big) \Big) \\
= \;& I_N^{(\zeta)} : \Big(I_N^{(\xi)} : \overline{H}_i^{\eta}(\eta,\zeta) \Big) \\
= \;& \tfrac{1}{8}\left(1+\tfrac{1}{\beta a_{010}}\ln\left(\tfrac{\cosh(\beta(\mathcal{P}_i(r_p^-,1,r_p^-)+d_i)}{\cosh(\beta(\mathcal{P}_i(r_p^-,0,r_p^-)+d_i)}\right)\right)+\tfrac{1}{8}\left(1+\tfrac{1}{\beta a_{010}}\ln\left(\tfrac{\cosh(\beta(\mathcal{P}_i(r_p^+,1,r_p^-)+d_i)}{\cosh(\beta(\mathcal{P}_i(r_p^+,0,r_p^-)+d_i)}\right)\right) \\
+ \;& \tfrac{1}{8}\left(1+\tfrac{1}{\beta a_{010}}\ln\left(\tfrac{\cosh(\beta(\mathcal{P}_i(1,r_p^-,r_p^+)+d_i)}{\cosh(\beta(\mathcal{P}_i(0,r_p^-,r_p^+)+d_i)}\right)\right)+\tfrac{1}{8}\left(1+\tfrac{1}{\beta a_{010}}\ln\left(\tfrac{\cosh(\beta(\mathcal{P}_i(r_p^+,1,r_p^+)+d_i)}{\cosh(\beta(\mathcal{P}_i(r_p^+,0,r_p^+)+d_i)}\right)\right) \\
= \;& \tfrac{1}{2}+\tfrac{1}{8\beta a_{010}}\ln\left(\tfrac{\big(AB^-D+1\big)\big(AB^+D+1\big)\big(AC^-D+1\big)\big(AC^+D+1\big)}{A^2(B^-D+1)(B^+D+1)(C^-D+1)(C^+D+1)}\right)=\phi_i
\end{aligned}
$$

Case 3: $|n_\zeta| = \max(|n_\xi|, |n_\eta|, |n_\zeta|)$

- Set $c^{(\zeta)} = 0$ in $\mathcal{P}_i(\xi,\eta,\zeta)$, $\mathcal{P}_i(\xi,\eta,\zeta) = a_{200}\xi^2 + a_{020}\eta^2 + a_{110}\xi\eta + a_{100}\xi + a_{010}\eta + a_{001}\zeta$,
- Calculate the exact integral in ζ direction,

$$
\begin{aligned}
\overline{H}_i^{\zeta}(\xi,\eta) &= \int_0^1 H_i(\xi,\eta,\zeta)d\zeta \qquad (4.52)\\
&= \frac{1}{2}\left(1+\frac{1}{\beta a_{001}}\ln\left(\frac{\cosh(\beta(\mathcal{P}_i(\xi,\eta,1)+d_i)}{\cosh(\beta(\mathcal{P}_i(\xi,\eta,0)+d_i)}\right)\right),
\end{aligned}
$$

- Use Gauss numerical quadrature to evaluate the integral with respect to ξ and η,

$$
\overline{\overline{H}^{\zeta}}_i^{\xi\eta} = \int_0^1\int_0^1 \overline{H}_i^{\zeta}(\xi,\eta)d\xi d\eta = \sum_{p,q=1}^{m}\omega_{pq}\overline{H}_i^{\zeta}(\xi_p,\eta_q), \qquad (4.53)
$$

- Solve

$$
\sum_{p,q=1}^{m}\omega_{pq}\overline{H}_i^{\zeta}(\xi_p,\eta_q) = \phi_i \qquad (4.54)
$$

$$
\begin{aligned}
& I_N^{(\eta)} : \Big(I_N^{(\xi)} : \Big(I_A^{(\zeta)} : H_i(\xi,\eta,\zeta) \Big) \Big) \\
= \;& I_N^{(\eta)} : \Big(I_N^{(\xi)} : \overline{H}_i^{\zeta}(\eta,\zeta) \Big) \\
= \;& \tfrac{1}{8}\left(1+\tfrac{1}{\beta a_{001}}\ln\left(\tfrac{\cosh(\beta(\mathcal{P}_i(r_p^-,r_p^-,1)+d_i)}{\cosh(\beta(\mathcal{P}_i(r_p^-,r_p^-,0)+d_i)}\right)\right)+\tfrac{1}{8}\left(1+\tfrac{1}{\beta a_{001}}\ln\left(\tfrac{\cosh(\beta(\mathcal{P}_i(r_p^+,r_p^-,1)+d_i)}{\cosh(\beta(\mathcal{P}_i(r_p^+,r_p^-,0)+d_i)}\right)\right) \\
+ \;& \tfrac{1}{8}\left(1+\tfrac{1}{\beta a_{001}}\ln\left(\tfrac{\cosh(\beta(\mathcal{P}_i(1,r_p^-,r_p^+)+d_i)}{\cosh(\beta(\mathcal{P}_i(0,r_p^-,r_p^+)+d_i)}\right)\right)+\tfrac{1}{8}\left(1+\tfrac{1}{\beta a_{001}}\ln\left(\tfrac{\cosh(\beta(\mathcal{P}_i(r_p^+,r_p^+,1)+d_i)}{\cosh(\beta(\mathcal{P}_i(r_p^+,r_p^+,0)+d_i)}\right)\right) \\
= \;& \tfrac{1}{2}+\tfrac{1}{8\beta a_{001}}\ln\left(\tfrac{\big(AB^-D+1\big)\big(AB^+D+1\big)\big(AC^-D+1\big)\big(AC^+D+1\big)}{A^2(B^-D+1)(B^+D+1)(C^-D+1)(C^+D+1)}\right)=\phi_i
\end{aligned}
$$

A quartic equation for $D = \exp(2\beta d)$ is

$$
\begin{aligned}
& A^2B^-B^+C^-C^+\left(A^2-Q\right)D^4 + A^2\left(B^-B^+\left(C^-+C^+\right)+\left(B^-+B^+\right)C^-C^+\right)\left(A-Q\right)D^3 \\
+ \quad & A^2\left(\left(B^-+B^+\right)\left(C^-+C^+\right)+B^-B^+ + C^-C^+\right)\left(1-Q\right)D^2 + A\left(B^-+B^++C^-+C^+\right)\left(1-AQ\right)D \\
+ \quad & 1-A^2Q = 0
\end{aligned}
$$

- Case 1:

$$
\begin{cases}
A &= \exp\left(2\beta a_{100}\right) \\
B^{\pm} &= \exp\left(2\beta\left(a_{020}\left(r_p^{\pm}\right)^2 + a_{002}\left(r_p^{-}\right)^2 + a_{011}r_p^{\pm}r_p^{-} + a_{010}r_p^{\pm} + a_{001}r_p^{-}\right)\right) \\
C^{\pm} &= \exp\left(2\beta\left(a_{020}\left(r_p^{-}\right)^2 + a_{002}\left(r_p^{\pm}\right)^2 + a_{011}r_p^{\pm}r_p^{-} + a_{010}r_p^{-} + a_{001}r_p^{\pm}\right)\right) \\
Q &= \exp\left(4\beta a_{100}\left(2\phi-1\right)\right)
\end{cases}
$$

- Case 2:

$$
\begin{cases}
A &= \exp\left(2\beta a_{010}\right) \\
B^{\pm} &= \exp\left(2\beta\left(a_{200}\left(r_p^{\pm}\right)^2 + a_{002}\left(r_p^{-}\right)^2 + a_{101}r_p^{\pm}r_p^{-} + a_{100}r_p^{\pm} + a_{001}r_p^{-}\right)\right) \\
C^{\pm} &= \exp\left(2\beta\left(a_{200}\left(r_p^{-}\right)^2 + a_{002}\left(r_p^{\pm}\right)^2 + a_{101}r_p^{\pm}r_p^{-} + a_{100}r_p^{-} + a_{001}r_p^{\pm}\right)\right) \\
Q &= \exp\left(4\beta a_{010}\left(2\phi-1\right)\right)
\end{cases}
$$

- Case 3:

$$
\begin{cases}
A &= \exp\left(2\beta a_{001}\right) \\
B^{\pm} &= \exp\left(2\beta\left(a_{200}\left(r_p^{\pm}\right)^2 + a_{020}\left(r_p^{-}\right)^2 + a_{110}r_p^{\pm}r_p^{-} + a_{100}r_p^{\pm} + a_{010}r_p^{-}\right)\right) \\
C^{\pm} &= \exp\left(2\beta\left(a_{200}\left(r_p^{-}\right)^2 + a_{020}\left(r_p^{\pm}\right)^2 + a_{110}r_p^{\pm}r_p^{-} + a_{100}r_p^{-} + a_{010}r_p^{\pm}\right)\right) \\
Q &= \exp\left(4\beta a_{001}\left(2\phi-1\right)\right)
\end{cases}
$$

- For prismatic element

Based on geometric information of the interface, the linear polynomial (4.10) is determined

by constraint conditions as (4.55),

$$\begin{cases} \left.\frac{\partial \mathcal{P}_i}{\partial \xi}\right|_{(\frac{1}{3},\frac{1}{3},\frac{1}{2})} = n_\xi, \\ \left.\frac{\partial \mathcal{P}_i}{\partial \eta}\right|_{(\frac{1}{3},\frac{1}{3},\frac{1}{2})} = n_\eta, \\ \left.\frac{\partial \mathcal{P}_i}{\partial \zeta}\right|_{(\frac{1}{3},\frac{1}{3},\frac{1}{2})} = n_\zeta. \end{cases} \tag{4.55}$$

Some algebraic manipulation [66] gives explicitly the coefficients in (4.10) as

$$\begin{cases} a_{100} = n_\xi, \\ a_{010} = n_\eta, \\ a_{001} = n_\zeta. \end{cases} \tag{4.56}$$

After the polynomial $\mathcal{P}_i(\xi,\eta,\zeta)$ is founded with coefficients of (4.45), the unknown d in (4.9) is determined by integration procedure as below.

Case 1: $|n_\xi| = \max(|n_\xi|, |n_\eta|, |n_\zeta|)$

- Set $c^{(\xi)} = c^{(\eta)} = c^{(\zeta)} = 0$ in $\mathcal{P}_i(\xi,\eta,\zeta)$, $\mathcal{P}_i(\xi,\eta,\zeta) = a_{100}\xi + a_{010}\eta + a_{001}\zeta$,
- Calculate the exact integral in ξ direction,

$$\begin{aligned} \overline{H}_i^{\xi}(\eta,\zeta) &= \frac{1}{1-\eta}\int_0^{1-\eta} H_i(\xi,\eta,\zeta)d\xi \\ &= \frac{1}{2\,(1-\eta)}\left(1 + \frac{1}{\beta a_{100}}\ln\left(\frac{\cosh(\beta(\mathcal{P}_i(1-\eta,\eta,\zeta)+d_i)}{\cosh(\beta(\mathcal{P}_i(0,\eta,\zeta)+d_i)}\right)\right), \end{aligned} \tag{4.57}$$

- Use Gauss numerical quadrature to evaluate the integral with respect to η and ζ,

$$\overline{\overline{H}^{\xi}}_i^{\eta\zeta} = \int_0^1\int_0^1 \overline{H}_i^{\xi}(\eta,\zeta)d\eta d\zeta = \frac{1}{2}\left(\overline{H}_i^{\xi}(1/3\,, r_p^+) + \overline{H}_i^{\xi}(1/3\,, r_p^-)\right), \tag{4.58}$$

- Solve

$$\frac{1}{2}\left(\overline{H}_i^{\xi}(1/3\,, r_p^+) + \overline{H}_i^{\xi}(1/3\,, r_p^-)\right) = \phi_i \tag{4.59}$$

$$\begin{aligned} & \tfrac{1}{2}\left(\overline{H}_i^{\xi}(1/3\,, r_p^+) + \overline{H}_i^{\xi}(1/3\,, r_p^-)\right) \\ = \;& \tfrac{1}{2} + \tfrac{3}{8\beta a_{100}}\ln\left(\frac{\cosh\left(\beta\left(\frac{2}{3}a_{100}+\frac{1}{3}a_{010}+r_p^+ a_{001}+d\right)\right)}{\cosh\left(\beta\left(\frac{1}{3}a_{010}+r_p^- a_{001}+d\right)\right)}\right) \\ + \;& \tfrac{3}{8\beta a_{100}}\ln\left(\frac{\cosh\left(\beta\left(\frac{2}{3}a_{100}+\frac{1}{3}a_{010}+r_p^+ a_{001}+d\right)\right)}{\cosh\left(\beta\left(\frac{1}{3}a_{010}+r_p^- a_{001}+d\right)\right)}\right) \\ = \;& \phi_i \end{aligned}$$

Case 2: $|n_\eta| = \max(|n_\xi|, |n_\eta|, |n_\zeta|)$

- Set $c^{(\xi)} = c^{(\eta)} = c^{(\zeta)} = 0$ in $\mathcal{P}_i(\xi,\eta,\zeta)$, $\mathcal{P}_i(\xi,\eta,\zeta) = a_{100}\xi + a_{010}\eta + a_{001}\zeta$,
- Calculate the exact integral in η direction,

$$\begin{aligned} \overline{H}_i^{\eta}(\xi,\zeta) &= \frac{1}{1-\xi}\int_0^{1-\xi} H_i(\xi,\eta,\zeta)d\eta \\ &= \frac{1}{2\,(1-\xi)}\left(1+\frac{1}{\beta a_{010}}\ln\left(\frac{\cosh(\beta(\mathcal{P}_i(\xi,1-\xi,\zeta)+d_i)}{\cosh(\beta(\mathcal{P}_i(\xi,0,\zeta)+d_i)}\right)\right), \end{aligned} \tag{4.60}$$

- Use Gauss numerical quadrature to evaluate the integral with respect to ξ and ζ,

$$\overline{\overline{H}^{\eta}}_i^{\xi\zeta} = \int_0^1\int_0^1 \overline{H}_i^{\eta}(\xi,\zeta)d\xi d\zeta = \frac{1}{2}\left(\overline{H}_i^{\eta}(1/3\,,r_p^+) + \overline{H}_i^{\eta}(1/3\,,r_p^-)\right), \tag{4.61}$$

- Solve

$$\frac{1}{2}\left(\overline{H}_i^{\eta}(1/3\,,r_p^+) + \overline{H}_i^{\eta}(1/3\,,r_p^-)\right) = \phi_i \tag{4.62}$$

$$\begin{aligned} & \tfrac{1}{2}\left(\overline{H}_i^{\eta}(1/3\,,r_p^+) + \overline{H}_i^{\eta}(1/3\,,r_p^-)\right) \\ = \;& \tfrac{1}{2} + \tfrac{3}{8\beta a_{010}}\ln\left(\frac{\cosh\left(\beta\left(\frac{2}{3}a_{100}+\frac{1}{3}a_{010}+r_p^+a_{001}+d\right)\right)}{\cosh\left(\beta\left(\frac{1}{3}a_{100}+r_p^+a_{001}+d\right)\right)}\right) \\ + \;& \tfrac{3}{8\beta a_{010}}\ln\left(\frac{\cosh\left(\beta\left(\frac{2}{3}a_{100}+\frac{1}{3}a_{010}+r_p^-a_{001}+d\right)\right)}{\cosh\left(\beta\left(\frac{1}{3}a_{100}+r_p^-a_{001}+d\right)\right)}\right) \\ = \;& \phi_i \end{aligned}$$

Case 3: $|n_\zeta| = \max(|n_\xi|, |n_\eta|, |n_\zeta|)$

- Set $c^{(\xi)} = c^{(\eta)} = c^{(\zeta)} = 0$ in $\mathcal{P}_i(\xi,\eta,\zeta)$, $\mathcal{P}_i(\xi,\eta,\zeta) = a_{100}\xi + a_{010}\eta + a_{001}\zeta$,
- Calculate the exact integral in ζ direction,

$$\begin{aligned} \overline{H}_i^{\zeta}(\xi,\eta) &= \int_0^1 H_i(\xi,\eta,\zeta)d\zeta \\ &= \frac{1}{2}\left(1+\frac{1}{\beta a_{001}}\ln\left(\frac{\cosh(\beta(\mathcal{P}_i(\xi,\eta,1)+d_i)}{\cosh(\beta(\mathcal{P}_i(\xi,\eta,0)+d_i)}\right)\right), \end{aligned} \tag{4.63}$$

- Use Gauss numerical quadrature to evaluate the integral with respect to ξ and η,

$$\overline{\overline{H}^{\zeta}}_i^{\xi\eta} = \int_0^1\int_0^{1-\eta} \overline{H}_i^{\zeta}(\xi,\eta)d\xi d\eta = \frac{1}{3}\left(\overline{H}_i^{\zeta}(1/6\,,1/6) + \overline{H}_i^{\zeta}(2/3\,,1/6) + \overline{H}_i^{\zeta}(1/6\,,2/3)\right), \tag{4.64}$$

- Solve

$$\frac{1}{3}\left(\overline{H}_i^{\zeta}(1/6\,,1/6) + \overline{H}_i^{\zeta}(2/3\,,1/6) + \overline{H}_i^{\zeta}(1/6\,,2/3)\right) = \phi_i \tag{4.65}$$

$$
\begin{aligned}
& \tfrac{1}{3}\left(\overline{H}_i^{\zeta}(1/6\,,1/6)+\overline{H}_i^{\zeta}(2/3\,,1/6)+\overline{H}_i^{\zeta}(1/6\,,2/3)\right)\\
= \;& \tfrac{1}{2}+\tfrac{1}{6\beta a_{001}}\ln\left(\frac{\cosh\left(\beta\left(\frac{1}{6}a_{100}+\frac{1}{6}a_{010}+a_{001}+d\right)\right)}{\cosh\left(\beta\left(\frac{1}{6}a_{100}+\frac{1}{6}a_{010}+d\right)\right)}\right)\\
+ \;& \tfrac{1}{6\beta a_{001}}\ln\left(\frac{\cosh\left(\beta\left(\frac{2}{3}a_{100}+\frac{1}{6}a_{010}+a_{001}+d\right)\right)}{\cosh\left(\beta\left(\frac{2}{3}a_{100}+\frac{1}{6}a_{010}+d\right)\right)}\right)\\
+ \;& \tfrac{1}{6\beta a_{001}}\ln\left(\frac{\cosh\left(\beta\left(\frac{1}{6}a_{100}+\frac{2}{3}a_{010}+a_{001}+d\right)\right)}{\cosh\left(\beta\left(\frac{1}{6}a_{100}+\frac{2}{3}a_{010}+d\right)\right)}\right)\\
= \;& \phi_i
\end{aligned}
$$

The d is determined from $d=\ln(D)/(2\beta)$

- Case 1:

$$B^{+}B^{-}\left(A^{2}-Q\right)D^{2}+\left(B^{+}+B^{-}\right)(1-Q)\,D+\left(A^{-2}-Q\right)=0$$

$$
\begin{cases}
A & = & \exp\left(\frac{2}{3}\beta a_{100}\right)\\
B^{\pm} & = & \exp\left(2\beta\left(\frac{1}{3}a_{010}+r_p^{\pm}a_{001}\right)\right)\\
Q & = & \exp\left(2\beta a_{100}\left(\frac{4}{3}\phi-\frac{2}{3}\right)\right)
\end{cases}
$$

- Case 2:

$$B^{+}B^{-}\left(A^{2}-Q\right)D^{2}+\left(B^{+}+B^{-}\right)(1-Q)\,D+\left(A^{-2}-Q\right)=0$$

$$
\begin{cases}
A & = & \exp\left(\frac{2}{3}\beta a_{010}\right)\\
B^{\pm} & = & \exp\left(2\beta\left(\frac{1}{3}a_{100}+r_p^{\pm}a_{001}\right)\right)\\
Q & = & \exp\left(2\beta a_{010}\left(\frac{4}{3}\phi-\frac{2}{3}\right)\right)
\end{cases}
$$

- Case 3:

$$
\begin{aligned}
& B_1B_2B_3\left(A^{3}-Q\right)D^{3}+(A-Q)\left(B_1B_2+B_1B_3+B_2B_3\right)D^{2}\\
+ \;& \left(B_1+B_2+B_3\right)\left(A^{-1}-Q\right)D+\left(A^{-3}-Q\right)=0
\end{aligned}
$$

$$
\begin{cases}
A & = & \exp\left(\beta a_{001}\right)\\
B_1 & = & \exp\left(2\beta\left(\frac{1}{6}a_{100}+\frac{1}{6}a_{010}\right)\right)\\
B_2 & = & \exp\left(2\beta\left(\frac{2}{3}a_{100}+\frac{1}{6}a_{010}\right)\right)\\
B_3 & = & \exp\left(2\beta\left(\frac{1}{6}a_{100}+\frac{2}{3}a_{010}\right)\right)\\
Q & = & \exp\left(3\beta a_{001}\left(2\phi-1\right)\right)
\end{cases}
$$

- For pyramidal element

Based geometric information of the interface, the quadratic polynomial (4.10) is determined by constraint conditions as (4.66),

$$\begin{cases} \left.\frac{\partial \mathcal{P}_i}{\partial \xi}\right|_{(0,0,\frac{1}{2})} = n_\xi, \\ \left.\frac{\partial \mathcal{P}_i}{\partial \eta}\right|_{(0,0,\frac{1}{2})} = n_\eta, \\ \left.\frac{\partial \mathcal{P}_i}{\partial \zeta}\right|_{(0,0,\frac{1}{2})} = n_\zeta. \end{cases} \tag{4.66}$$

Some algebraic manipulation [66] gives explicitly the coefficients in (4.10) as

$$\begin{cases} a_{100} = n_\xi, \\ a_{010} = n_\eta, \\ a_{001} = n_\zeta. \end{cases} \tag{4.67}$$

After the polynomial $\mathcal{P}_i(\xi,\eta,\zeta)$ is founded with coefficients of (4.45), the unknown d in (4.9) is determined as below.

Case 1: $|n_\xi| = \max(|n_\xi|, |n_\eta|, |n_\zeta|)$

- Set $c^{(\xi)} = c^{(\eta)} = c^{(\zeta)} = 0$ in $\mathcal{P}_i(\xi,\eta,\zeta)$, $\mathcal{P}_i(\xi,\eta,\zeta) = a_{100}\xi + a_{010}\eta + a_{001}\zeta$,
- Calculate the exact integral in ξ direction,

$$\begin{aligned}
\overline{H}^{\xi}_{i1}(\eta,\zeta) &= \frac{1}{1-\eta-\zeta}\int_0^{1-\eta-\zeta} H_i(\xi,\eta,\zeta)d\xi \qquad (4.68)\\
&= \frac{1}{2\,(1-\eta-\zeta)}\left(1+\frac{1}{\beta a_{100}}\ln\left(\frac{\cosh(\beta(\mathcal{P}_i(1-\eta-\zeta,\eta,\zeta)+d_i)}{\cosh(\beta(\mathcal{P}_i(0,\eta,\zeta)+d_i)}\right)\right),\\
\overline{H}^{\xi}_{i2}(\eta,\zeta) &= \frac{1}{1-\eta-\zeta}\int_{\eta+\zeta-1}^{0} H_i(\xi,\eta,\zeta)d\xi\\
&= \frac{1}{2\,(1-\eta-\zeta)}\left(1+\frac{1}{\beta a_{100}}\ln\left(\frac{\cosh(\beta(\mathcal{P}_i(0,\eta,\zeta)+d_i)}{\cosh(\beta(\mathcal{P}_i(\eta+\zeta-1,\eta,\zeta)+d_i)}\right)\right),\\
\overline{H}^{\xi}_{i3}(\eta,\zeta) &= \frac{1}{1+\eta-\zeta}\int_{\zeta-\eta-1}^{0} H_i(\xi,\eta,\zeta)d\xi\\
&= \frac{1}{2\,(1+\eta-\zeta)}\left(1+\frac{1}{\beta a_{100}}\ln\left(\frac{\cosh(\beta(\mathcal{P}_i(0,\eta,\zeta)+d_i)}{\cosh(\beta(\mathcal{P}_i(\zeta-\eta-1,\eta,\zeta)+d_i)}\right)\right),\\
\overline{H}^{\xi}_{i4}(\eta,\zeta) &= \frac{1}{1+\eta-\zeta}\int_0^{1+\eta-\zeta} H_i(\xi,\eta,\zeta)d\xi\\
&= \frac{1}{2\,(1+\eta-\zeta)}\left(1+\frac{1}{\beta a_{100}}\ln\left(\frac{\cosh(\beta(\mathcal{P}_i(1+\eta-\zeta,\eta,\zeta)+d_i)}{\cosh(\beta(\mathcal{P}_i(0,\eta,\zeta)+d_i)}\right)\right),
\end{aligned}$$

- Use Gauss numerical quadrature to evaluate the integral with respect to η and

ζ,

$$\overline{\overline{H}^{\xi}}_{i}^{\eta\zeta} = \frac{1}{4}\left(\overline{H}^{\xi}_{i1}(1/4\,,1/4) + \overline{H}^{\xi}_{i2}(1/4\,,1/4) + \overline{H}^{\xi}_{i3}(-1/4\,,1/4) + \overline{H}^{\xi}_{i4}(-1/4\,,1/4)\right), \tag{4.69}$$

- Solve

$$\frac{1}{4}\left(\overline{H}^{\xi}_{i1}(1/4\,,1/4) + \overline{H}^{\xi}_{i2}(1/4\,,1/4) + \overline{H}^{\xi}_{i3}(-1/4\,,1/4) + \overline{H}^{\xi}_{i4}(-1/4\,,1/4)\right) = \phi_i \tag{4.70}$$

$$\begin{aligned}
& \tfrac{1}{4}\left(\overline{H}^{\xi}_{i1}(1/4\,,1/4) + \overline{H}^{\xi}_{i2}(1/4\,,1/4) + \overline{H}^{\xi}_{i3}(-1/4\,,1/4) + \overline{H}^{\xi}_{i4}(-1/4\,,1/4)\right) \\
= \;& \tfrac{1}{2} + \tfrac{1}{2\beta a_{100}} \ln\left(\frac{\cosh\left(\beta\left(\frac{1}{2}a_{100}+\frac{1}{4}a_{010}+\frac{1}{4}a_{001}+d\right)\right)}{\cosh\left(\beta\left(\frac{1}{4}a_{010}+\frac{1}{4}a_{001}+d\right)\right)}\right) \\
+ \;& \tfrac{1}{2\beta a_{100}} \ln\left(\frac{\cosh\left(\beta\left(\frac{1}{4}a_{010}+\frac{1}{4}a_{001}+d\right)\right)}{\cosh\left(\beta\left(-\frac{1}{2}a_{100}+\frac{1}{4}a_{010}+\frac{1}{4}a_{001}+d\right)\right)}\right) \\
+ \;& \tfrac{1}{2\beta a_{100}} \ln\left(\frac{\cosh\left(\beta\left(-\frac{1}{4}a_{010}+\frac{1}{4}a_{001}+d\right)\right)}{\cosh\left(\beta\left(-\frac{1}{2}a_{100}-\frac{1}{4}a_{010}+\frac{1}{4}a_{001}+d\right)\right)}\right) \\
+ \;& \tfrac{1}{2\beta a_{100}} \ln\left(\frac{\cosh\left(\beta\left(\frac{1}{2}a_{100}-\frac{1}{4}a_{010}+\frac{1}{4}a_{001}+d\right)\right)}{\cosh\left(\beta\left(-\frac{1}{4}a_{010}+\frac{1}{4}a_{001}+d\right)\right)}\right) \\
= \;& \phi_i
\end{aligned}$$

Case 2: $|n_\eta| = \max(|n_\xi|, |n_\eta|, |n_\zeta|)$

- Set $c^{(\xi)} = c^{(\eta)} = c^{(\zeta)} = 0$ in $\mathcal{P}_i(\xi,\eta,\zeta)$, $\mathcal{P}_i(\xi,\eta,\zeta) = a_{100}\xi + a_{010}\eta + a_{001}\zeta$,
- Calculate the exact integral in η direction,

$$\begin{aligned}
\overline{H}^{\eta}_{i1}(\xi,\zeta) &= \frac{1}{1-\xi-\zeta}\int_0^{1-\xi-\zeta} H_i(\xi,\eta,\zeta)d\eta \qquad (4.71)\\
&= \frac{1}{2\,(1-\xi-\zeta)}\left(1 + \frac{1}{\beta a_{010}}\ln\left(\frac{\cosh(\beta(\mathcal{P}_i(\xi,1-\xi-\zeta,\zeta)+d_i)}{\cosh(\beta(\mathcal{P}_i(\xi,0,\zeta)+d_i)}\right)\right),\\
\overline{H}^{\eta}_{i2}(\xi,\zeta) &= \frac{1}{1+\xi-\zeta}\int_0^{1+\xi-\zeta} H_i(\xi,\eta,\zeta)d\eta\\
&= \frac{1}{2\,(1+\xi-\zeta)}\left(1 + \frac{1}{\beta a_{010}}\ln\left(\frac{\cosh(\beta(\mathcal{P}_i(\xi,1+\xi-\zeta,\zeta)+d_i)}{\cosh(\beta(\mathcal{P}_i(\xi,0,\zeta)+d_i)}\right)\right),\\
\overline{H}^{\eta}_{i3}(\xi,\zeta) &= \frac{1}{1+\xi-\zeta}\int_{\zeta-\xi-1}^{0} H_i(\xi,\eta,\zeta)d\eta\\
&= \frac{1}{2\,(1+\xi-\zeta)}\left(1 + \frac{1}{\beta a_{010}}\ln\left(\frac{\cosh(\beta(\mathcal{P}_i(\xi,0,\zeta)+d_i)}{\cosh(\beta(\mathcal{P}_i(\xi,\zeta-\xi-1,\zeta)+d_i)}\right)\right),\\
\overline{H}^{\eta}_{i4}(\xi,\zeta) &= \frac{1}{1-\xi-\zeta}\int_{\zeta+\xi-1}^{0} H_i(\xi,\eta,\zeta)d\eta\\
&= \frac{1}{2\,(1-\xi-\zeta)}\left(1 + \frac{1}{\beta a_{010}}\ln\left(\frac{\cosh(\beta(\mathcal{P}_i(\xi,0,\zeta)+d_i)}{\cosh(\beta(\mathcal{P}_i(\xi,\zeta+\xi-1,\zeta)+d_i)}\right)\right),
\end{aligned}$$

- Use Gauss numerical quadrature to evaluate the integral with respect to ξ and ζ,

$$\overline{\overline{H}^{\eta}}_{i}^{\xi\zeta} = \frac{1}{4}\left(\overline{H}^{\eta}_{i1}(1/4\,,1/4) + \overline{H}^{\eta}_{i2}(-1/4\,,1/4) + \overline{H}^{\eta}_{i3}(-1/4\,,1/4) + \overline{H}^{\eta}_{i4}(1/4\,,1/4)\right), \tag{4.72}$$

- Solve

$$\overline{H}^{\eta}_{i}(1/4\,,1/4) = \phi_i \tag{4.73}$$

$$\begin{aligned}
& \tfrac{1}{4}\left(\overline{H}^{\eta}_{i1}(1/4\,,1/4) + \overline{H}^{\eta}_{i2}(-1/4\,,1/4) + \overline{H}^{\eta}_{i3}(-1/4\,,1/4) + \overline{H}^{\eta}_{i4}(1/4\,,1/4)\right) \\
= \;& \tfrac{1}{2} + \tfrac{1}{2\beta a_{010}} \ln\left(\frac{\cosh\left(\beta\left(\frac{1}{4}a_{100}+\frac{1}{2}a_{010}+\frac{1}{4}a_{001}+d\right)\right)}{\cosh\left(\beta\left(\frac{1}{4}a_{100}+\frac{1}{4}a_{001}+d\right)\right)}\right) \\
+ \;& \tfrac{1}{2\beta a_{010}} \ln\left(\frac{\cosh\left(\beta\left(-\frac{1}{4}a_{100}+\frac{1}{2}a_{010}+\frac{1}{4}a_{001}+d\right)\right)}{\cosh\left(\beta\left(-\frac{1}{4}a_{100}+\frac{1}{4}a_{001}+d\right)\right)}\right) \\
+ \;& \tfrac{1}{2\beta a_{010}} \ln\left(\frac{\cosh\left(\beta\left(-\frac{1}{4}a_{100}+\frac{1}{4}a_{001}+d\right)\right)}{\cosh\left(\beta\left(-\frac{1}{4}a_{100}-\frac{1}{2}a_{010}+\frac{1}{4}a_{001}+d\right)\right)}\right) \\
+ \;& \tfrac{1}{2\beta a_{010}} \ln\left(\frac{\cosh\left(\beta\left(\frac{1}{4}a_{100}+\frac{1}{4}a_{001}+d\right)\right)}{\cosh\left(\beta\left(\frac{1}{4}a_{100}-\frac{1}{2}a_{010}+\frac{1}{4}a_{001}+d\right)\right)}\right) \\
= \;& \phi_i
\end{aligned}$$

Case 3: $|n_\zeta| = \max(|n_\xi|, |n_\eta|, |n_\zeta|)$

- Set $c^{(\xi)} = c^{(\eta)} = c^{(\zeta)} = 0$ in $\mathcal{P}_i(\xi,\eta,\zeta)$, $\mathcal{P}_i(\xi,\eta,\zeta) = a_{100}\xi + a_{010}\eta + a_{001}\zeta$,
- Calculate the exact integral in ζ direction,

$$\begin{aligned}
\overline{H}^{\zeta}_{i1}(\xi,\eta) &= \frac{1}{1-\xi-\eta}\int_0^{1-\xi-\eta} H_i(\xi,\eta,\zeta)d\zeta \qquad (4.74)\\
&= \frac{1}{2\,(1-\xi-\eta)}\left(1 + \frac{1}{\beta a_{001}}\ln\left(\frac{\cosh(\beta(\mathcal{P}_i(\xi,\eta,1-\xi-\eta)+d_i)}{\cosh(\beta(\mathcal{P}_i(\xi,\eta,0)+d_i)}\right)\right), \\
\overline{H}^{\zeta}_{i2}(\xi,\eta) &= \frac{1}{1+\xi-\eta}\int_0^{1+\xi-\eta} H_i(\xi,\eta,\zeta)d\zeta \\
&= \frac{1}{2\,(1+\xi-\eta)}\left(1 + \frac{1}{\beta a_{001}}\ln\left(\frac{\cosh(\beta(\mathcal{P}_i(\xi,\eta,1+\xi-\eta)+d_i)}{\cosh(\beta(\mathcal{P}_i(\xi,\eta,0)+d_i)}\right)\right), \\
\overline{H}^{\zeta}_{i3}(\xi,\eta) &= \frac{1}{1+\xi+\eta}\int_0^{1+\xi+\eta} H_i(\xi,\eta,\zeta)d\zeta \\
&= \frac{1}{2\,(1+\xi+\eta)}\left(1 + \frac{1}{\beta a_{001}}\ln\left(\frac{\cosh(\beta(\mathcal{P}_i(\xi,\eta,1+\xi+\eta)+d_i)}{\cosh(\beta(\mathcal{P}_i(\xi,\eta,0)+d_i)}\right)\right), \\
\overline{H}^{\zeta}_{i4}(\xi,\eta) &= \frac{1}{1-\xi-\eta}\int_0^{1-\xi+\eta} H_i(\xi,\eta,\zeta)d\zeta \\
&= \frac{1}{2\,(1-\xi+\eta)}\left(1 + \frac{1}{\beta a_{001}}\ln\left(\frac{\cosh(\beta(\mathcal{P}_i(\xi,\eta,1-\xi+\eta)+d_i)}{\cosh(\beta(\mathcal{P}_i(\xi,\eta,0)+d_i)}\right)\right),
\end{aligned}$$

- Use Gauss numerical quadrature to evaluate the integral with respect to ξ and

η,

$$\overline{\overline{H}^{\zeta}}_{i}^{\xi\eta} = \frac{1}{4}\left(\overline{H}_{i1}^{\zeta}(1/4\,,1/4) + \overline{H}_{i2}^{\zeta}(-1/4\,,1/4) + \overline{H}_{i3}^{\zeta}(-1/4\,,-1/4) + \overline{H}_{i4}^{\zeta}(1/4\,,-1/4)\right), \tag{4.75}$$

- Solve

$$\frac{1}{4}\left(\overline{H}_{i1}^{\zeta}(1/4\,,1/4) + \overline{H}_{i2}^{\zeta}(-1/4\,,1/4) + \overline{H}_{i3}^{\zeta}(-1/4\,,-1/4) + \overline{H}_{i4}^{\zeta}(1/4\,,-1/4)\right) = \phi_i \tag{4.76}$$

$$\begin{aligned}
& \tfrac{1}{4}\left(\overline{H}_{i1}^{\zeta}(1/4\,,1/4) + \overline{H}_{i2}^{\zeta}(-1/4\,,1/4) + \overline{H}_{i3}^{\zeta}(-1/4\,,-1/4) + \overline{H}_{i4}^{\zeta}(1/4\,,-1/4)\right) \\
= \;& \tfrac{1}{2} + \tfrac{1}{2\beta a_{001}} \ln\left(\frac{\cosh\left(\beta\left(\frac{1}{4}a_{100}+\frac{1}{4}a_{010}+\frac{1}{2}a_{001}+d\right)\right)}{\cosh\left(\beta\left(\frac{1}{4}a_{100}+\frac{1}{4}a_{010}+d\right)\right)}\right) \\
+ \;& \tfrac{1}{2\beta a_{001}} \ln\left(\frac{\cosh\left(\beta\left(-\frac{1}{4}a_{100}+\frac{1}{4}a_{010}+\frac{1}{2}a_{001}+d\right)\right)}{\cosh\left(\beta\left(-\frac{1}{4}a_{100}+\frac{1}{4}a_{010}+d\right)\right)}\right) \\
+ \;& \tfrac{1}{2\beta a_{001}} \ln\left(\frac{\cosh\left(\beta\left(-\frac{1}{4}a_{100}-\frac{1}{4}a_{010}+\frac{1}{2}a_{001}+d\right)\right)}{\cosh\left(\beta\left(-\frac{1}{4}a_{100}-\frac{1}{4}a_{010}+d\right)\right)}\right) \\
+ \;& \tfrac{1}{2\beta a_{001}} \ln\left(\frac{\cosh\left(\beta\left(\frac{1}{4}a_{100}+\frac{1}{4}a_{010}-\frac{1}{2}a_{001}+d\right)\right)}{\cosh\left(\beta\left(\frac{1}{4}a_{100}-\frac{1}{4}a_{010}+d\right)\right)}\right) \\
= \;& \phi_i
\end{aligned}$$

The d is determined from $d = \ln(D)/(2\beta)$

- Case 1:

$$\begin{aligned}
& B_1^2 B_2^2\left(A_1^2 - A_2^2 Q\right) D^4 + B_1 B_2\left(B_1 + B_2\right)\left(1 + A_1^2 - Q - Q A_2^2\right) D^3 \\
+ \;& \left(\left(B_1 + B_2\right)^2(1-Q) + B_1 B_2\left(A_1^2 + A_1^{-2} - A_2^2 Q - Q A_2^{-2}\right)\right) D^2 \\
+ \;& \left(\left(A_1^2+1\right)\left(B_1+B_2\right) A_1^{-2} - \left(A_2^2+1\right)\left(B_1+B_2\right) Q A_2^{-2}\right) D \\
+ \;& A_1^{-2} - Q A_2^{-2} = \phi_i
\end{aligned}$$

$$\begin{cases}
A_1 &= \exp\left(\frac{1}{2}\beta a_{001}\right) \\
A_2 &= \exp\left(-\frac{1}{2}\beta a_{001}\right) \\
B_1 &= \exp\left(\frac{1}{2}\beta\left(a_{010} + a_{001}\right)\right) \\
B_1 &= \exp\left(\frac{1}{2}\beta\left(-a_{010} + a_{001}\right)\right) \\
Q &= \exp\left(4\beta a_{001}\left(\phi - \frac{1}{2}\right)\right)
\end{cases}$$

- Case 2:

$$
\begin{aligned}
& B_1^2 B_2^2 \left(A_1^2 - A_2^2 Q\right) D^4 + B_1 B_2 \left(B_1 + B_2\right) \left(1 + A_1^2 - Q - Q A_2^2\right) D^3 \\
+ & \left(\left(B_1 + B_2\right)^2 (1 - Q) + B_1 B_2 \left(A_1^2 + A_1^{-2} - A_2^2 Q - Q A_2^{-2}\right)\right) D^2 \\
+ & \left(\left(A_1^2 + 1\right) \left(B_1 + B_2\right) A_1^{-2} - \left(A_2^2 + 1\right) \left(B_1 + B_2\right) Q A_2^{-2}\right) D \\
+ & A_1^{-2} - Q A_2^{-2} = \phi_i
\end{aligned}
$$

$$
\begin{cases}
A_1 &= \exp\left(\frac{1}{2}\beta a_{001}\right) \\
A_2 &= \exp\left(-\frac{1}{2}\beta a_{001}\right) \\
B_1 &= \exp\left(\frac{1}{2}\beta \left(a_{100} + a_{001}\right)\right) \\
B_1 &= \exp\left(\frac{1}{2}\beta \left(-a_{100} + a_{001}\right)\right) \\
Q &= \exp\left(4\beta a_{001} \left(\phi - \frac{1}{2}\right)\right)
\end{cases}
$$

- Case 3:

$$
\begin{aligned}
& B_1 B_2 B_3 B_4 \left(A^4 - Q\right) D^4 + \left(B_1 B_3 B_4 + B_2 B_3 B_4 + B_1 B_2 B_4 + B_1 B_2 B_3\right) \left(A^2 - Q\right) D^3 \\
+ & \left(B_1 B_4 + B_2 B_4 + B_3 B_4 + B_1 B_2 + B_1 B_3 + B_2 B_3\right) (1 - Q) D^2 \\
+ & \left(B_1 + B_2 + B_3 + B_4\right) \left(A^{-2} - Q\right) D + \left(A^{-4} - Q\right) \\
= & \phi_i
\end{aligned}
$$

$$
\begin{cases}
A &= \exp\left(\frac{1}{2}\beta a_{001}\right) \\
B_1 &= \exp\left(\frac{1}{2}\beta \left(a_{100} + a_{010}\right)\right) \\
B_2 &= \exp\left(\frac{1}{2}\beta \left(-a_{100} + a_{010}\right)\right) \\
B_3 &= \exp\left(\frac{1}{2}\beta \left(-a_{100} - a_{010}\right)\right) \\
B_4 &= \exp\left(\frac{1}{2}\beta \left(a_{100} - a_{010}\right)\right) \\
Q &= \exp\left(4\beta a_{001} \left(\phi - \frac{1}{2}\right)\right)
\end{cases}
$$

4.4 Verification tests

In the remaining section, I will mainly show verification of quadratic interface reconstruction on quadrilateral and hexahedral elements. For more results on triangular and tetrahedral elements, please refer to our published paper [67].

4.4.1 Interface reconstructions for a circular shape

In order to evaluate the capability of the scheme to reconstruct a curved surface, we retrieve a 2D circular interface from volume fraction values on a Cartesian grid and a quadrilateral unstructured grid as shown in Fig. 4.1. A circle with the radius of R = 0.4

is centered on a $[0,1] \times [0,1]$ square, and the indication function is calculated by

$$H(\mathbf{x}) = \begin{cases} 1, & \text{if } \sqrt{(\mathrm{x}-0.5)^2 + (\mathrm{y}-0.5)^2} \leq \mathrm{R}. \\ 0, & \text{otherwise.} \end{cases} \tag{4.77}$$

We divide the computational domain into a 4×4 mesh, and obtain the volume fraction values by (4.4). The volume integral on each cell is numerically approximated by sampling $H(\mathbf{x})$ at 100×100 points evenly spaced within the cell.

By the numerical procedure described above, we find the cell-wise THINC reconstruction functions on both Cartesian and unstructured quadrilateral grids. We show the retrieved interface in Fig. 4.1, i.e. the 0.5 contour of reconstruction function (4.9) where $\mathcal{P}_i(\xi, \eta) + d_i = 0$ holds. β is set to be 2 in this example. It is seen that from the given volume fraction field the curved interface can be recovered with adequate accuracy. It is noted that given the normal and curvature information as well as the volume fraction we are able to identify the jump transition by finding the THINC reconstruction function through the procedures described above. There is not any geometrical computation involved.

$$\text{Error} = \frac{\sum_{i=1}^{N} (|\phi_{ni} - \phi_{ei}|)}{N} \tag{4.78}$$

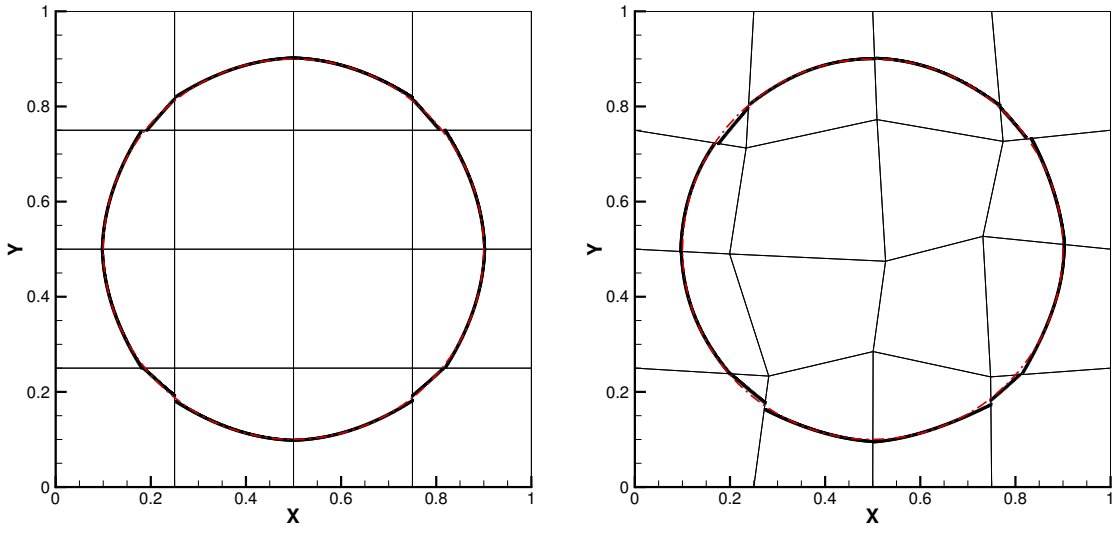


Figure 4.1: Interface reconstructions for a circular shape with exact unit normal vector. Left (grid A): a structured quadrilateral mesh. Right (grid B): a unstructured quadrilateral mesh.

From the Fig. 4.1, we can find the the present scheme can accurately capture the interface on both structured and unstructured quadrilateral mesh by the exact unit normal vector. The results of Table 4.4 suggests the present numerical method for unit normal

Table 4.4: Numerical error for interface reconstruction with exact and numerical unit normal vector.

Revolution	structured	unstructured
exact	3.146×10^{-3}	2.876×10^{-3}
numerical	3.248×10^{-3}	2.925×10^{-3}

vector can get sufficient accuracy.

4.4.2 Zalesak body rotation on quadrilateral mesh

The well-known Zalesak's solid rotation problem [191] is tested on quadrilateral mesh. Initially, a slotted disk in the computational domain $[0,1] \times [0,1]$ is defined by specifying the indication function as,

$$H(\mathbf{x}) = \begin{cases} 1, & \text{if } \left\{\sqrt{(x-0.5)^2 + (y-0.75)^2} \leq 0.15\right\} \setminus \{|x-0.5| \leq 0.025 \text{ and } y \leq 0.85\}. \\ 0, & \text{otherwise.} \end{cases} \tag{4.79}$$

The velocity field is given as $(u, v) = (y - 0.5, 0.5 - x)$ and time increment $\triangle t$ is set so as to let the maximum CFL number be 0.25. The initial volume fraction values ϕ_i are obtained from sampling $H(\mathbf{x})$ at 100×100 points in each cell.

We compute this test problem on both a Cartesian grid and an unstructured quadrilateral grid as shown in Fig. 4.4 (a) and (b). In order to have the same initial profile for both grids, we make the region containing the initial disk in the unstructured grid identical to that in the Cartesian grid. The enlarged views of the numerical solutions with $\beta = 2.3$ after one revolution of rotation are plotted in Fig. 4.4 from (c) to (f) for the both grids. It is observed that the present scheme reproduces the interface, which is identified by the 0.5 contour lines, with accuracy comparable to other PLIC VOF schemes in [7, 123, 126, 8] on both grids. There is no significant difference in the numerical solutions on Cartesian grid and unstructured grid with distorted elements. In order to see the thickness of the jump transition in the volume fraction field, we also plot the contours of 0.05 and 0.95. It is shown that the jumps maintain a compact thickness within 2 to 3 cells across the interface.

It is noted that the jump thickness can be effectively controlled by parameter β. We have tested the value of β up to 8 for the present UMTHINC/QHQ scheme, and observed that a sharp interface can be obtained if β is larger than 4. Even for a small β, such as $\beta = 0.5$ or 1, the transition layer covers more grid cells but still keeps constant during the computation without being continuously smeared out, which is substantially different from the conventional Eulerian advection schemes.

The first two figures are computational mesh for both structured and unstructured

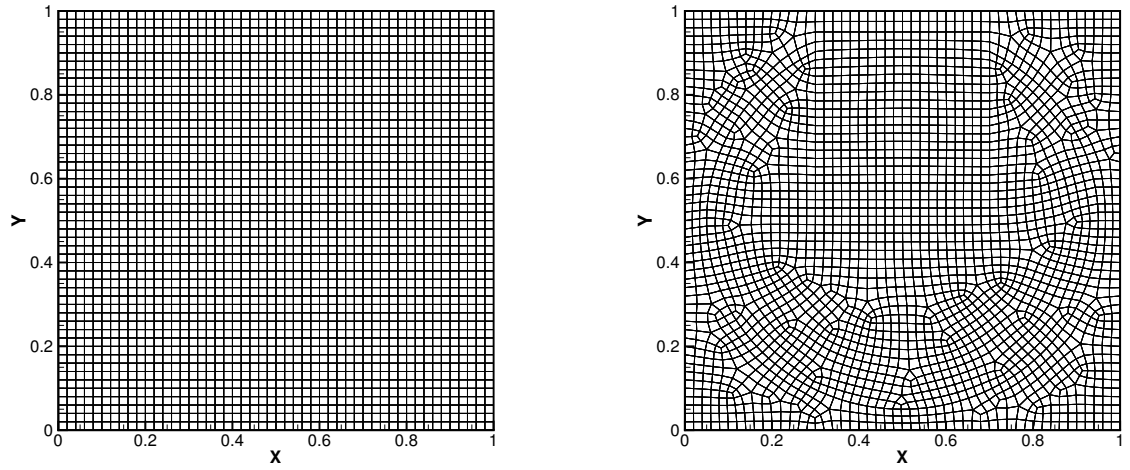


Figure 4.2: The computational meshes for advection test. Left (grid A): a structured quadrilateral mesh. Right (grid B): a unstructured quadrilateral mesh.

Table 4.5: Numerical errors of modified Zalesak slotted cylinder test.

Algorithms	Error
UMTHINC/QHQ (grid A)($\beta = 8$)	1.172×10^{-2}
UMTHINC/QHQ(grid B)($\beta = 8$)	1.184×10^{-2}
FCT-VOF[130]	3.29×10^{-2}
DDR/Youngs[55]	1.56×10^{-2}
DDR/Puckett[55]	1.50×10^{-2}
Youngs[130]	1.09×10^{-2}
ELVIR[8]	1.00×10^{-2}
GPCA[17]	9.79×10^{-3}
THINC[174]	3.52×10^{-2}
THINC/WLIC[186]	1.96×10^{-2}
THINC/SW[176]	1.34×10^{-2}

quadrilateral mesh. In order to compute at the same initial condition and easy to compare, we generate the two type grid with same structured part mesh near the Zalesak's body. The Fig. 4.4 compare the numerical results after one round solid rotation with the exact solution by the contour 0.5 interface. We can find the present scheme show the results without any oscillation or diffusion, which are comparable to most other schemes. The Fig. 4.3 scheme suggests the jump thickness, indicated by the contour 0.05 and 0.95, maintains compact within 2 to 3 cells along the interface. A quantitative comparison is conducted by Table [4.7,4.6,4.5] and we can see the present scheme keep the high accuracy on both structured and unstructured mesh. The interface of Zalesak test with different mesh resolution is summarized in Table 4.6. We can find results on both grids give sufficient accuracy and converge to exact solution rapidly.

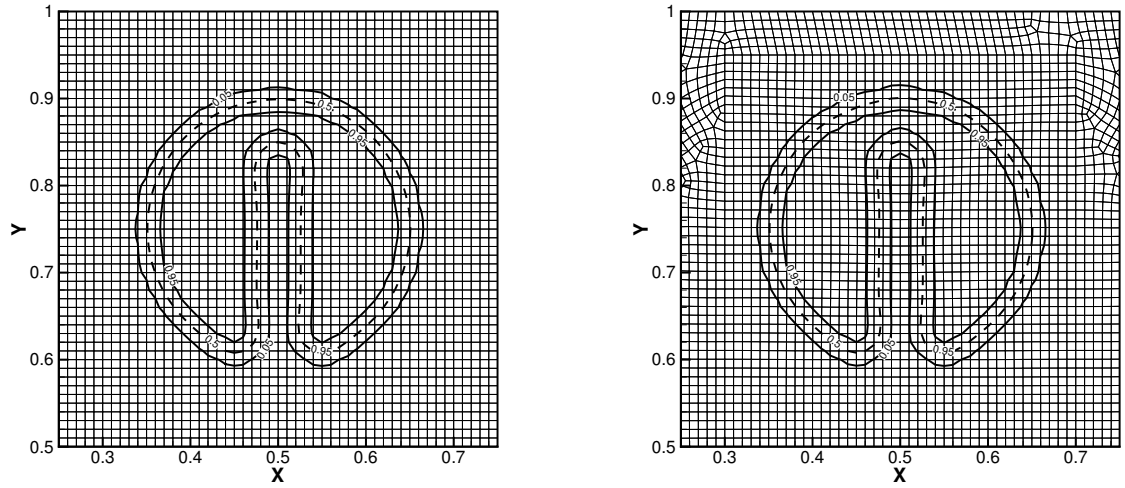


Figure 4.3: Numerical results of Zalesak slotted-cylinder test problems. Left (grid A): enlarged view of 0.05,0.5,0.95 contour on 10000 structured quadrilateral grids. Right (grid B): enlarged view of 0.05,0.5,0.95 contour on 10056 unstructured quadrilateral grids.

We have quantitatively compared our numerical results with other VOF schemes. In order to quantify the numerical errors, we define error as follows,

$$\mathrm{E}_R = \frac{\sum_{i=1}^{N_e}(|\phi_{ni} - \phi_{ei}||\Omega_i|)}{\sum_{i=1}^{N_e}(|\phi_{ei}||\Omega_i|)} \tag{4.80}$$

where ϕ_{ni} and ϕ_{ei} denote numerical and exact solutions respectively and $|\Omega_i|$ represents surface area of cell i.

Given the errors of several VOF schemes for Rudman-Zalesak slotted disk rotation test in [130, 17], we compute this test with the present method on both Cartesian grid (grid A) and unstructured quadrilateral grid (grid B) (Fig. 4.4 (a) and (b)), and show the numerical error E_R in Table 4.5 with other schemes. It is observed that the UMTHINC/QHQ has numerical accuracy comparable to the PLIC schemes that use geometrical reconstructions.

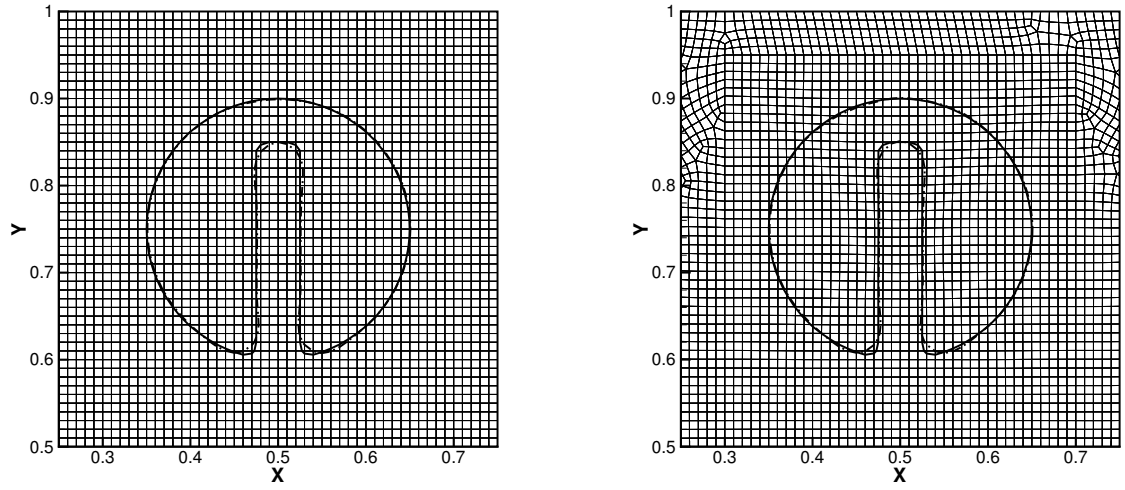


Figure 4.4: Numerical results of Zalesak slotted-cylinder test problems. Left (grid A): interface(contour 0.5) on 10000 structured quadrilateral grids. Right (grid B): interface(contour 0.5) on 10056 unstructured quadrilateral grids.

4.4.3 Shearing flow on quadrilateral mesh

In order to verify the ability of present scheme to deal with the heavily deformed and stretched interface, we compute the shearing flow benchmark test introduced in [126]. The computational meshes are the same as in the previous solid rotation test, denoted respectively by grid A for the Cartesian grid and grid B for the quadrilateral unstructured grid.

An initial circle with radius 0.15 is located at (0.5,0.75). The circle is transported by a time-dependent velocity field defined on a unit square by the stream function as,

$$\psi(x,y,t) = \frac{1}{\pi}\sin^2(\pi x)\sin^2(\pi y)\cos\left(\frac{\pi t}{T}\right), \quad x,y \in [0,1]\,. \tag{4.81}$$

The initial volume fraction profile is deformed by the velocity field up to the half period $T/2$, and then returned back to its initial state until $t = T$ by a reversed velocity. The maximum CFL number is 0.15 in this test.

The numerical results of UMTHINC/QHQ with $\beta = 8$ for $T = 2$ are plotted in Fig. 4.5. For this mildly deformed interface, UMTHINC/QHQ scheme perfectly resolves and transports the volume fraction field. The restored interfaces on both Cartesian and unstructured grids look identical to the exact solution. For a long time deformation ($T = 8$), the interface is heavily deformed so that the tail becomes too thin to be resolvable by the computational grid of finite resolution. Like other geometrical VOF schemes, the unresolvable thin tail breaks into small droplets as shown in Fig. 4.6. Some distortions are commonly seen when a heavily deformed interface is transported back to the initial position. The solutions shown in Fig. 4.6 reveal that the UMTHINC/QHQ scheme can

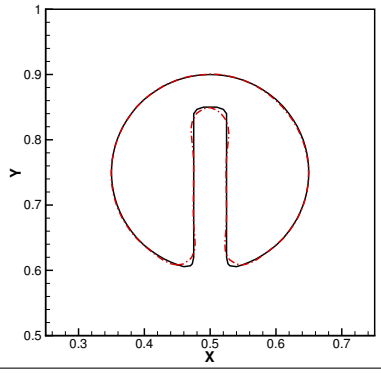
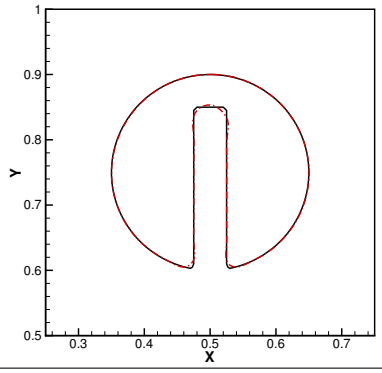
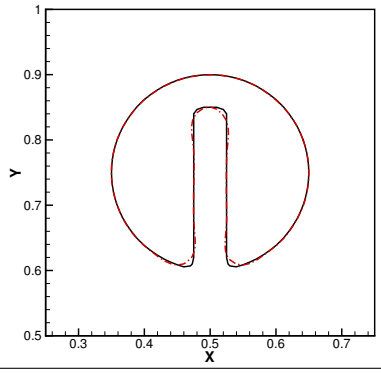
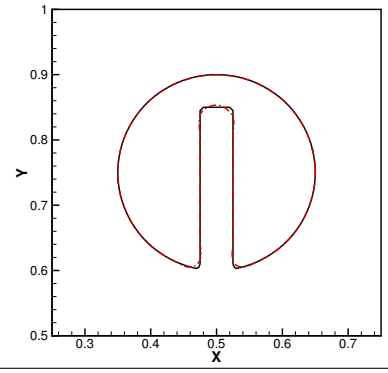
Mesh size	1 /100	1 /200
Structured grid		
Unstructured grid		

Table 4.6: Numerical results of Zalesak slotted-cylinder test problems on grid A and grid B with resolution of 1 /100 and 1 /200.

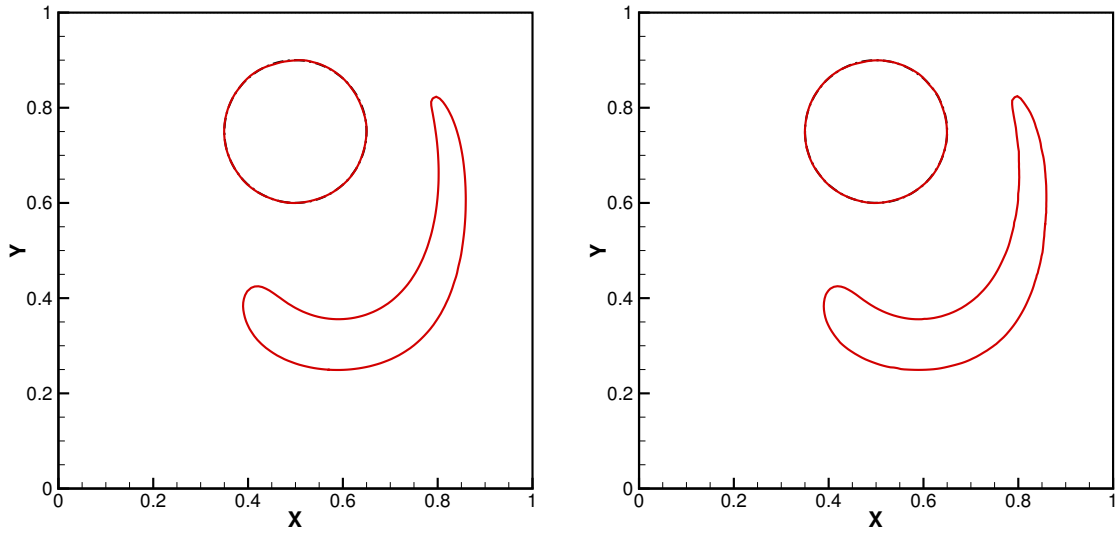


Figure 4.5: Numerical results for T=2 of time-dependent single vortex flow test problem on a Cartesian grid of 128×128 cells (left) and an unstructured quadrilateral grid of 16395 cells (right). The red lines indicate the numerical solutions at $T/2$ and T. The black dot line represents the initial profile (exact solution).

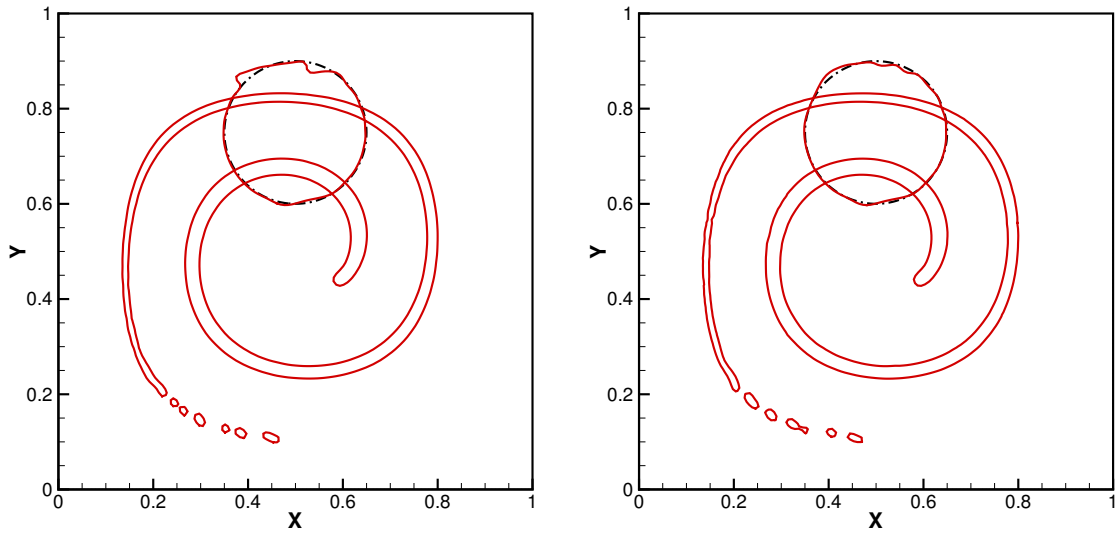


Figure 4.6: Same as Fig. 4.5, but for $T = 8$.

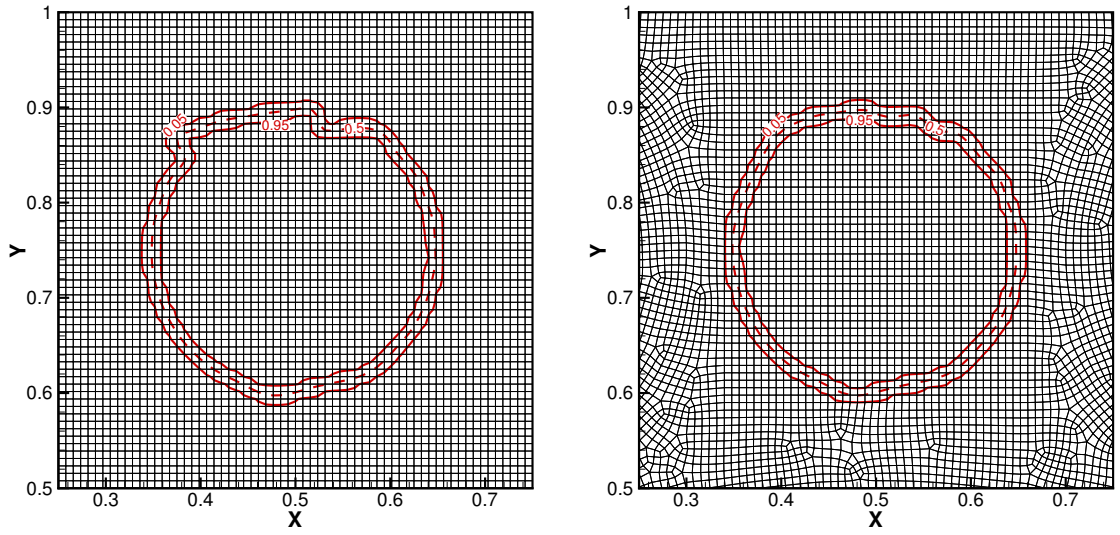


Figure 4.7: Contours of 0.05, 0.5, 0.95 of the volume fraction fields at $T = 8$.

Table 4.7: Numerical errors and convergence orders of Zalesak solid rotation on grid A and grid B comparison with THINC type schemes.

Revolution	1 /50	Order	1 /100	Order	1 /200
UMTHINC/QHQ (grid A)	8.31×10^{-2}	1.57	2.79×10^{-2}	0.90	1.49×10^{-2}
UMTHINC/QHQ(grid B)	7.49×10^{-2}	1.65	2.33×10^{-2}	0.82	1.32×10^{-2}
THINC/WLIC[186]	1.22×10^{-1}	1.27	5.05×10^{-2}	1.04	2.46×10^{-2}
VOF/WLIC[186]	1.29×10^{-1}	1.26	5.40×10^{-2}	0.75	2.38×10^{-2}
Original THINC[174]	1.32×10^{-1}	0.60	8.73×10^{-2}	0.60	4.79×10^{-2}

produce high-quality solution comparable to other existing PLIC/VOF schemes. See, for example, the results in [54] as well as others available in the literature. To show the capability of UMTHINC/QHQ to keep the compactness of the interface thickness, we plot the contours of $\phi = 0.05$, 0.5 and 0.95 for the thin tail and the restored cylinder in Fig. 4.7. It is observed that the thickness of transition region of ϕ from 0 to 1 remains compact during the computation even for the heavily distorted interface.

To qualitatively comparing UMTHINC/QHQ with other PLIC/VOF schemes, we define another error measure by,

$$\text{Error} = \sum_{i=1}^{N_e} (|\phi_{ni} - \phi_{ei}||\Omega_i|). \tag{4.82}$$

Table 4.8: Numerical errors and convergence rates of UMTHINC/QHQ schemes on comparison with other existing PLIC VOF schemes for the time-dependent single vortex test[126] at $T = 2$. We use the numerical results as well as the names of different PLIC schemes reported in [126, 54] and [134].

Grid resolution	32×32	Order	64×64	Order	128×128
Rider-Kothe/Puckett [126]	2.36×10^{-3}	2.01	5.85×10^{-4}	2.16	1.31×10^{-4}
Stream/Puckett [54]	2.37×10^{-3}	2.07	5.65×10^{-4}	2.10	1.32×10^{-4}
Stream/Youngs [54]	2.49×10^{-3}	1.82	7.06×10^{-4}	1.66	2.23×10^{-4}
ELVIRA/EL-LE [134]	2.52×10^{-3}	1.95	6.46×10^{-4}	2.15	1.45×10^{-5}
Linear fit/EL-LE [134]	1.75×10^{-3}	1.91	4.66×10^{-4}	2.19	1.02×10^{-4}
Quadratic fit/EL-LE [134]	1.88×10^{-3}	2.08	4.42×10^{-4}	2.24	9.36×10^{-5}
UMTHINC/QHQ (grid A)	3.34×10^{-3}	1.60	1.11×10^{-3}	1.31	4.45×10^{-4}
UMTHINC/QHQ (grid B)	3.99×10^{-3}	1.75	1.20×10^{-3}	1.68	3.64×10^{-4}

Table 4.8 shows the result of numerical errors and convergence rates for $T = 2$. We use the error data of the geometrical VOF schemes available in [126, 54, 134] for comparison. It is found that the numerical errors of UMTHINC/QHQ is overall larger than the referenced PLIC/VOF schemes, but still of the same order on all grid resolutions. The results of UMTHINC/QHQ on unstructured grid (grid B) are as accurate as those on the Cartesian

Table 4.9: Same as Table 4.8, but for $T = 8$.

Grid resolution	32×32	Order	64×64	Order	128×128
Rider-Kothe/Puckett [126]	4.78×10^{-2}	2.78	6.96×10^{-3}	2.27	1.44×10^{-3}
Stream/Puckett [54]	3.72×10^{-2}	2.45	6.79×10^{-3}	2.53	1.18×10^{-3}
Stream/Youngs [54]	3.61×10^{-2}	1.85	1.00×10^{-2}	2.22	2.16×10^{-3}
UMTHINC/QHQ (grid A)	6.41×10^{-2}	1.98	1.11×10^{-2}	2.33	3.23×10^{-3}
UMTHINC/QHQ (grid B)	6.46×10^{-2}	2.12	1.51×10^{-2}	2.65	2.29×10^{-3}

grid (grid A). Table 4.9 gives the results for the heavily deformed interface. We can see that the UMTHINC/QHQ scheme performs reasonably well for this more challenging problem as observed already in Fig. 4.7. It shows a convergence rate higher than 2nd order with the numerical errors comparable to the standard geometrical VOF schemes.

4.4.4 Zalesak solid rotation on hexahedral mesh

The three dimensional scheme for hexahedral mesh was firstly tested by solving the solid rotation of a notched sphere [66]. The initial profile of the volume fraction is specified as,

$$H(\mathbf{x}) = \begin{cases} 1, & \text{if } (x-0.5)^2 + (y-0.75)^2 + (z-0.5)^2 \leq 0.15^2 \wedge (|x-0.5| \geq 0.025 \vee y > 0.725); \\ 0, & \text{otherwise.} \end{cases} \tag{4.83}$$

The 3D computational mesh is shown in Fig. 4.8. We set the rotational velocity as $\mathbf{U} = (y - 0.5, 0.5 - x, 0)$, and the maximum CFL number as 0.5.

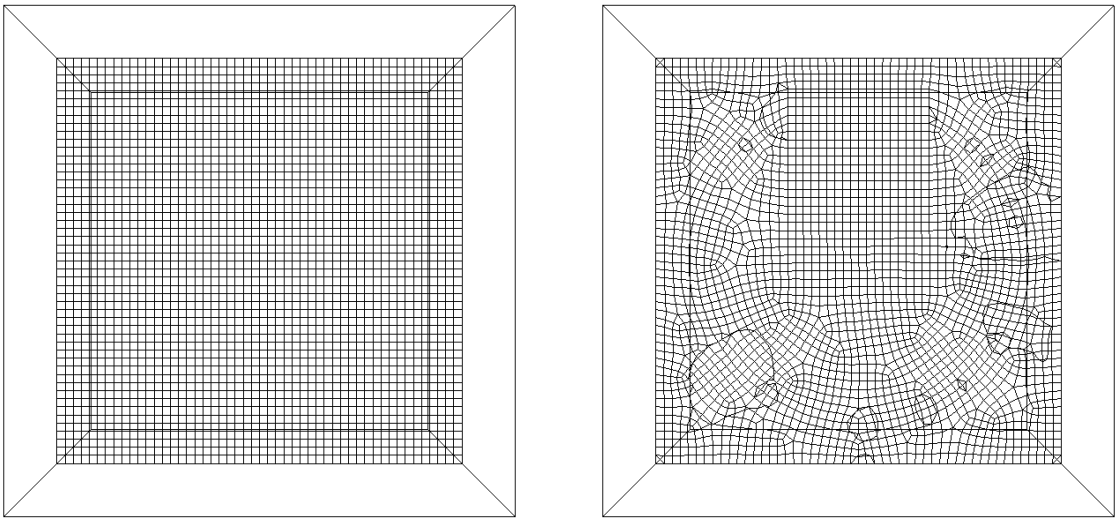


Figure 4.8: The computational meshes for Zalesak 3D rotation test. Left (grid A): a structured hexahedral mesh. Right (grid B): a unstructured hexahedral mesh.

From the Table 4.10, we can find the present scheme gets similar accuracy with

Table 4.10: Numerical errors and convergence orders of UMTHINC/QHQ in the Zalesak 3D solid rotational flow on grid A and grid B.

Revolution	1 /50	Order	1 /100	Order	1 /200
UMTHINC/QHQ (grid A)	1.10×10^{-3}	1.32	4.38×10^{-4}	0.98	2.22×10^{-4}
UMTHINC/QHQ (grid B)	1.21×10^{-3}	1.34	4.78×10^{-4}	0.92	2.51×10^{-4}
MTHINC[66]	1.19×10^{-3}	1.09	5.60×10^{-4}	0.91	3.56×10^{-4}

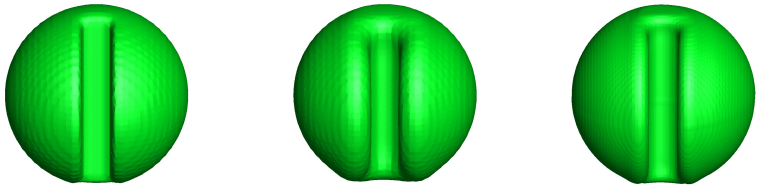


Figure 4.9: Numerical results for Zalesak 3D rotation test problems on structured hexahedral grids at $t = 2\pi$ with exact (Left), 100^3 (Middle), 200^3 (Right).

MTHINC scheme and converges with a first-order accuracy in space. The numerical error as well as convergence rate on unstructured grid is maintained at the same level that the difference with results of structured grid is negligible. Fig. 4.9 and 4.10 are the profile of contour 0.5 interface after one round solid rotation and we can observe geometrically faithful solutions which are competitive to other VOF type schemes.

4.4.5 Shearing flow on hexahedral mesh

A sphere with radius of 0.15 initially centered at (0.35,0.35,0.35) is transported by a deformational reverse velocity field used in [95],

$$\begin{cases} u(x,y,z) = 2\sin^2(\pi x)\sin(2\pi y)\sin(2\pi z)\cos(\pi t/T) \\ v(x,y,z) = -\sin(2\pi x)\sin^2(\pi y)\sin(2\pi z)\cos(\pi t/T) \\ w(x,y,z) = -\sin(2\pi x)\sin(2\pi y)\sin^2(\pi z)\cos(\pi t/T) \end{cases} \quad x,y,z \in [0,1].$$

The interface is distorted up to $T/2$ and returned back to its initial location after one period T. The period T is set to 3 in this test, and the maximum CFL number is set to 0.25. Shown in Fig. 4.11, a Cartesian grid (grid A) and an unstructured hexahedral grid (grid B) are used.

The numerical results on Cartesian and unstructured grids are plotted in Fig. 4.12 and Fig. 4.13. As we have seen before, the thickness of the transition layer spans over two to three grid cells. Without geometrical reconstruction, an arbitrariness is left in determining where the true interface locates. Taking the 0.5-contour surface as the interface, we observe that the interface has been resolved and transported with adequate accuracy.

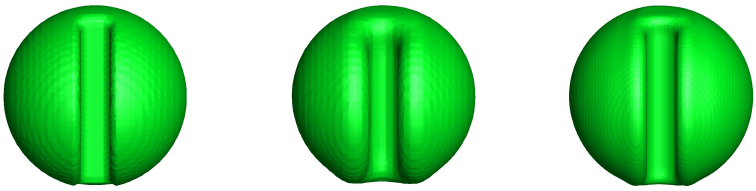
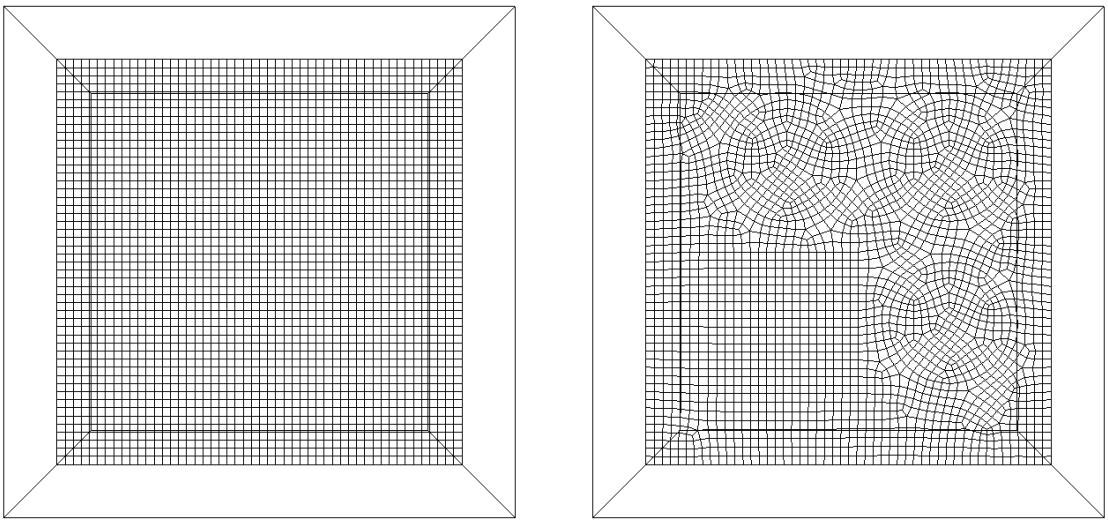


Figure 4.10: Numerical results for Zalesak 3D rotation test problems on unstructured hexahedral grids at $t = 2\pi$ with exact (Left), 995200(Middle), 8068200 (Right).



(a) Grid A (b) Grid B

Figure 4.11: The computational meshes for shear 3D test. Left (grid A): a Cartesian grid. Right (grid B): an unstructured hexahedral grid.

The numerical error and corresponding convergence rate are given in Table 4.11. We can find the present scheme has almost same accuracy compared with original MTHINC scheme on structured grid. By compared with numerical results of the RK-3D(the 3D version of Rider and Kothe PLIC scheme [126]), FMFPA-3D(face-matched flux polyhedron advection [56]) and splitted type multi-dimensional THINC/SW scheme, we can realize although the numerical error of present scheme are slightly larger than PLIC type schemes, however still competitive to most existed method. The result on unstructured mesh shows little higher accuracy. From the Fig. 4.12 and 4.13, we can observe that although the thin structure at the most heavily deformed state is not resolvable as other existing VOF schemes on coarser meshes, significant improvement can be found with the mesh refinement. The result on unstructured mesh show sufficient enough interface reconstruction and comparable with the result on the structured grid.

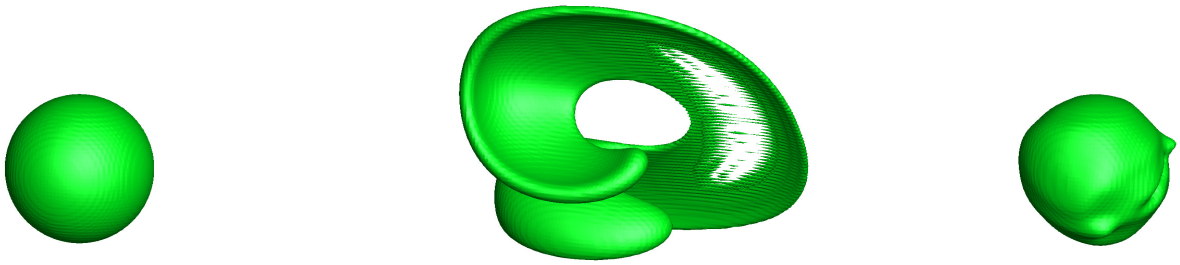


Figure 4.12: Numerical results for time-dependent 3D vortical deformation flow test on 128^3 Cartesian grid. Displayed are the iso-surface of contour 0.5 of the instantaneous solutions at time $t = 0,\ \frac{T}{2},\ T$ with $T = 3$.

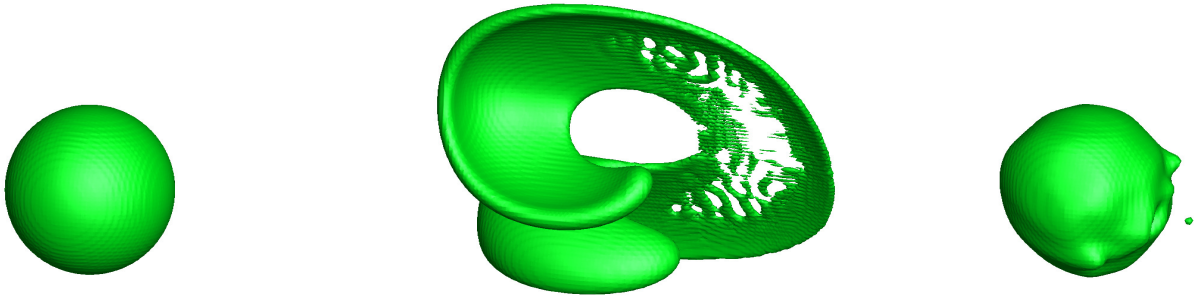


Figure 4.13: Same as Fig. 4.12, but on a unstructured hexahedral grid of 2166400 cells.

Table 4.11: Numerical errors and convergence orders for the time-dependent 3D vortical deformation flow test.

Revolution	32^3	Order	64^3	Order	128^3
RK-3D (Cartesian) [56]	7.85×10^{-3}	1.51	2.75×10^{-3}	1.89	7.41×10^{-4}
FMFPA-3D (Cartesian) [56]	7.44×10^{-3}	1.42	2.79×10^{-3}	1.97	7.14×10^{-4}
Youngs (Cartesian) [77]	7.47×10^{-3}	1.43	2.77×10^{-3}	1.77	8.14×10^{-4}
Youngs (Unstructured) [77]	1.02×10^{-2}	1.20	4.45×10^{-3}	2.24	9.43×10^{-4}
LVIRA (Cartesian) [77]	6.92×10^{-3}	1.51	2.43×10^{-3}	1.93	6.37×10^{-4}
LVIRA (Unstructured) [77]	1.02×10^{-2}	1.53	3.54×10^{-3}	2.30	7.20×10^{-4}
UMTHINC/QHQ (grid A)	7.76×10^{-3}	1.46	2.82×10^{-3}	1.68	8.77×10^{-4}
UMTHINC/QHQ (grid B)	8.72×10^{-3}	1.63	2.76×10^{-3}	1.94	7.04×10^{-4}

4.5 Summary of chapter 4

We have proposed a novel algebraic interface capturing method, UMTHINC, for arbitrary unstructured grids. Being the unstructured grid extension of the THINC methods which have been so far limited to the Cartesian grid and multi-dimensional splitting approach, UMTHINC method uses the multidimensional THINC formulation to reconstruct interface straightforwardly according to VOF value defined in each grid cell. With interface thickness specified by built-in parameter β, location of interface can be determined by VOF value. In order to make the computation efficient, we make the exact integration of the hyperbolic tangent function in the principal direction and compute the integration in other two directions by numerical quadrature. The principal direction is determined from the major component of normal direction of the interface. Without geometric reconstruction, complexity in PLIC type VOF scheme is completely avoided. As reconstruction function is built, the numerical flux at cell boundary is integrated by Gauss quadrature and VOF then is solved by advection equation based on finite volume formulation. In addition to linear reconstruction limited in majority of unstructured VOF schemes, quadratic reconstruction has also been achieved to approximate interface in quadrilateral and hexahedral elements. For numerical tests, canonical Zalesak and shear vortex problem in 2D and 3D are carried out to verify its performance. It is shown that no matter accuracy or convergence behavior, UMTHINC method demonstrated superior to most PLIC type schemes. Besides, compared with results of Cartesian grid, this accuracy on unstructured grid is entirely maintained with negligible error increasing. Since UMTHINC keeps remarkable capability in accuracy, efficiency and robustness, this scheme is seen to be the most practical and promising interface capturing scheme which can be used for simulations of multi-phase interfacial flows in the presence of complex geometrical configuration where unstructured grid is preferred.

Chapter 5

Numerical model for incompressible interfacial multiphase flow

5.1 Governing equations

In this paper, the framework for incompressible multiphase flow is developed based on one-fluid model on fixed arbitrary unstructured grid. In order to identify two immiscibe fluid, we employ volume of fluid (VOF) method to track or capture the moving interface. Considering the computational domain filled with fluid 1 and fluid 2, then a indicator function is defined as

$$\phi = \begin{cases} 1 & \text{fluid 1} \\ 0 & \text{fluid 2} \\ 0 < \phi < 1 & \text{interface} \end{cases} \tag{5.1}$$

A transition layer with finite thickness between two fluid is defined as interface and transported by flow velocity. Then, the time evolution of indicator function is solved by following advection equation:

$$\frac{\partial \phi}{\partial t} + \nabla \cdot (\mathbf{u}\phi) - \phi \nabla \cdot \mathbf{u} = 0 \tag{5.2}$$

After the indicator function is updated, we can redefine the fluid property for density and viscosity:

$$\begin{aligned} \rho &= \rho_1 \phi + \rho_2 (1 - \phi) \\ \mu &= \mu_1 \phi + \mu_2 (1 - \phi) \end{aligned} \tag{5.3}$$

With density and viscosity determined, governing equations of incompressible interfacial multiphase flow then can be developed straightforwardly based on unsteady incompresisble Navies-Stokes equations,

$$\nabla \cdot \mathbf{u} = 0 \tag{5.4}$$

$$\frac{\partial \mathbf{u}}{\partial t} + \nabla \cdot (\mathbf{u} \otimes \mathbf{u}) = -\frac{1}{\rho}\nabla p + \frac{1}{\rho}\nabla \cdot (\mu \nabla \mathbf{u}) + \frac{1}{\rho}\mathbf{F}_s + \mathbf{g} \tag{5.5}$$

where $\mathbf{u} = (u, v, w)$ is the velocity vector with components u, v and w in x, y and z directions respectively. p is the pressure, $\mathbf{g}$ the acceleration of gravity, ρ the density and μ the viscosity. $\mathbf{F}_s$ is surface tension computed by Blackball's CSF model[15] which represents the surface tension effects as a continuous volumetric force acting within the transition region $\sigma\kappa\nabla\phi$. The κ is the curvature of the interface, given by $\kappa = \nabla \cdot \left(\frac{\nabla\phi}{|\phi|}\right)$ and σ the fluid surface tension coefficient.

In order to simplify the specification of boundary condition, a modified pressure[131] is used instead: $p^* = p - \rho\mathbf{g} \cdot \mathbf{x}$. p^* represents a modified pressure obtained by removing hydrostatic pressure from the total pressure. Take gradient of both side of the equation, then we can obtain:

$$\nabla p^* = \nabla p - \nabla (\rho\mathbf{g} \cdot \mathbf{x}) = \nabla p - \rho\mathbf{g} - \mathbf{g} \cdot \mathbf{x}\nabla\rho \tag{5.6}$$

Substituting these formulations into momentum equation, we can assemble the final form:

$$\frac{\partial \mathbf{u}}{\partial t} + \nabla \cdot (\mathbf{u} \otimes \mathbf{u}) = -\frac{1}{\rho}\nabla p^* + \frac{1}{\rho}\nabla \cdot (\mu \nabla \mathbf{u}) + \frac{\sigma\kappa}{\rho}\nabla\phi - \mathbf{g} \cdot \mathbf{x}\nabla\rho \tag{5.7}$$

5.2 Smoothed volume fraction and fluid property

There is always contradiction between accuracy of interface capturing and computational stability. From view of interface tracking, sharper interface is required for higher accuracy while wider interface thickness is demanded for stability since the density varies rapidly near narrow interface region. For this purpose, we retain compact interface thickness by specifying larger β in THINC formulation while compute density as well as viscosity with smoothed VOF value.

As shown in Fig. 5.1, Once the reconstruction function of THINC formulation (4.7) is determined, the location of jump center $\widetilde{x}$ will be identified internally in the form of $\left(\mathcal{P}_i(x, y, z) + \hat{d}_i\right) = 0$. With parameter β specified, the thickness of jump transition can be effectively controlled as larger β value corresponds to steeper interface jump. Thus smoothed volume fraction φ can be obtained in following steps:

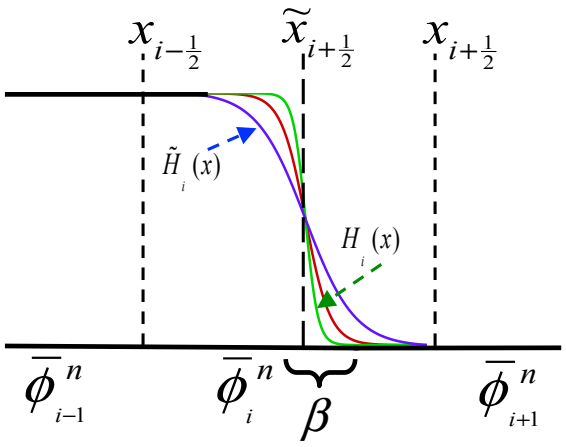


Figure 5.1: Thickness of jump transition can be effectively controlled by parameter β.

1. Construct reconstruction function of volume fraction by using hyperbolic tangent function as
$$H_i(\mathbf{x}) = \frac{1}{2}\left(1 + \tanh\left(\hat{\beta}\left(\mathcal{P}_i(x,y,z) + \hat{d}_i\right)\right)\right).$$
In order to sharp the interface, the larger $\widehat{\beta}$ value is desirable. In this study, we use 4.0 in practice.

2. The smoothed function is constructed as $\widetilde{H}_i(\mathbf{x}) = \frac{1}{2}\left(1 + \tanh\left(\widetilde{\beta}\left(\mathcal{P}_i(x,y,z) + \hat{d}_i\right)\right)\right)$ by using smaller $\widetilde{\beta}$ value. In this study, we choose it as 2.0.

3. Numerical integration is implemented for each cell by the formulation as
$$\varphi = \int_\Omega \widetilde{H}_i(\mathbf{x})\mathrm{d}\Omega = \sum \omega_{ij}\widetilde{H}_i(\mathbf{x}_{ij})$$
where $\mathbf{x}_{ij}$ and ω_{ij} indicates coordinate and weight for Gaussian quadrature.

4. With smoothed volume fraction φ determined, we update density and viscosity straightforwardly
$$\begin{aligned} \rho &= \rho_1\varphi + \rho_2\left(1-\varphi\right), \\ \mu &= \mu_1\varphi + \mu_2\left(1-\varphi\right). \end{aligned} \tag{5.8}$$

5.3 Surface tension formulation

According to balanced continuum surface force (CSF) model [15, 37], the surface tension force can be represented as

$$
\begin{aligned}
F_{ij}^{CSF} &= \sigma \kappa_{ij} \left(\nabla \phi\right)_{ij} \\
\kappa_i &= \nabla \cdot \mathbf{n}_{ij} \\
\mathbf{n}_{ij} &= \frac{\left(\nabla \phi\right)_{ij}}{\left|\left(\nabla \phi\right)_{ij}\right|}
\end{aligned}
\tag{5.9}
$$

where σ is surface tension coefficient, κ_i is interfacial curvature and $\left(\nabla \phi\right)_{ij}$ is face gradient of volume fraction. The curvature κ_i is computed from unit normal vector of cell boundary $\mathbf{n}_{ij}$ which obtained from face gradient of volume fraction $\left(\nabla \phi\right)_{ij}$. The crucial for balanced force formulation is to ensure the exactly same discretization implemented for face gradient of pressure $\left(\nabla p\right)_{ij}$ and volume fraction $\left(\nabla \phi\right)_{ij}$. In this study, we employ (2.42) and (2.43) for discretization of $\left(\nabla p\right)_{ij}$ and $\left(\nabla \phi\right)_{ij}$ which minimizes the error of non-orthogonality. For more details, refer to section 2.5.3.

Much of research can be found for pursuing higher accuracy and better representations of geometrical information of interface[82, 40, 187, 188, 146, 124]. Particularly, the calculation of curvature was paid the most attention as it is quite difficult to accurately evaluate unit normal vector $\left(\nabla \phi\right)_{ij}$ from nearly discontinuous volume fraction distribution (ϕ) across the interface. The available CLSVOF [187, 188], PROST[124] and K_8 kernel[37] require pseudo time iteration or topological manipulation which are complicated and inefficient to implement on unstructured grid. As a remedy, we proposed an efficient and accurate solution procedure based on least square method on arbitrary unstructured grid. $\left(\nabla \phi\right)_{ij}$ on cell boundary is evaluated followed by

1. From given VOF value ϕ in each cell, first order derivative at cell vertices $\left(\nabla \phi\right)_{ik}$ $(k = 1 \ldots K)$ is computed by least square method.

2. First derivative at cell boundary is approximated by formulation of

$$
\left(\nabla \phi\right)_{ij} = \frac{1}{2} \left(\sum_{k=1}^{k=K} \left(\nabla \phi\right)_{ik} + \sum_{k=1}^{k=K} \left(\nabla \phi\right)_{jk} \right).
$$

After $\left(\nabla \phi\right)_{ij}$ is determined, curvature κ_i at cell center is computed by (5.9) and interpolation should be implemented to estimate curvature at cell boundary κ_{ij}. As discussed in [187], the simple interpolation $\kappa_{ij} = \frac{1}{2}\left(\kappa_i + \kappa_j\right)$ will cause overestimation or underestimation of curvature, thus a sophisticated method is used to interpolates curvature κ_{ij} from curvature κ_i at nearest liquid interface by solving the following equations[60, 187, 188]:

$$
\frac{\partial \kappa}{\partial \tau} \pm \mathbf{n} \cdot \nabla \kappa = 0 \tag{5.10}
$$

where '+' sign is for value of κ located at the region of $\psi > 0$, '-' is for κ that ψ is less than 0, τ is the artificial time and $\mathbf{n}$ is unit normal vector of interface. The discretization of (5.10) on structured grid has been clarified in [187], however, it is not a trivial work

Element Type	Reconstruction function
Triangular element	$\Theta(\xi,\eta) = c_{00} + c_{10}\xi + c_{01}\eta$
Quadrilateral element	$\Theta(\xi,\eta) = c_{00} + c_{10}\xi + c_{01}\eta + c_{11}\xi\eta$
Tetrahedral element	$\Theta(\xi,\eta,\zeta) = c_{000} + c_{100}\xi + c_{010}\eta + c_{001}\zeta$
Hexahedral element	$\Theta(\xi,\eta,\zeta) = c_{000} + c_{100}\xi + c_{010}\eta + c_{001}\zeta + c_{110}\xi\eta + c_{011}\eta\zeta + c_{101}\xi\zeta + c_{111}\xi\eta\zeta$
Prismatic element	$\Theta(\xi,\eta,\zeta) = c_{000} + c_{100}\xi + c_{010}\eta + c_{001}\zeta + +c_{011}\eta\zeta + c_{101}\xi\zeta$
Pyramidal element	$\Theta(\xi,\eta,\zeta) = c_{000} + c_{100}\xi + c_{010}\eta + c_{001}\zeta + c_{111}\xi\eta\zeta$

Table 5.1: Reconstruction function for calculation of nodal curvature κ_{ik}.

to solve on hybrid unstructured grid. In this study, we employ following procedure for obtaining κ_{ij}.

1. Based on least-square interpolation method as denoted in Appendix 1, we initialize the curvature κ_{ik} and unit normal vector at vertex $\mathbf{n}_{ik}$ on vertex from surrounding curvature κ_i and VOF ϕ_i at cell center respectively.

2. Using nodal curvature κ_{ik} of each cell, canonical piecewise finite element formulation is constructed on local coordinate as denoted in Table 5.1.

3. First order derivative of curvature at vertex $(\nabla\kappa)_{ik}$ is determined from reconstruction function and weighed by

$$\omega_k = \frac{\max\left(0, \pm\mathbf{n}_{ij}\cdot\overrightarrow{\theta_{kc}\theta_{ik}}\right)}{\sum_{k=1}^{K}\max\left(0, \pm\mathbf{n}_{ij}\cdot\overrightarrow{\theta_{kc}\theta_{ik}}\right)}$$

   in the same manner with (3.44).

4. Update κ_{ik} using explicit Euler scheme as $\kappa_{ik}^{n+1} = \kappa_{ik}^{n} \mp \mathbf{n}_{ik}\cdot(\nabla\kappa)_{ik}^{n}$ until residual is satisfied. In present study, the residual is assumed as $\left|\kappa_{ik}^{n+1} - \kappa_{ik}^{n}\right| < 10^{-6}$.

5. The curvature at cell boundary is averaged as $\kappa_{ij} = \frac{1}{K}\sum_{k=1}^{K}\kappa_{ijk}$ where κ_{ijk} represents nodal curvature value belonged to each cell boundary.

5.4 Solution procedure for equation system

These governing equations are solved by fractional step approach[174, 175, 83] and the solution procedure is summarized as following for brevity.

1. Given the initial VOF field ϕ^n at time level n, predict time evolution of interface by advection equation (5.2).

2. From VOF field at time level $n+1$, smoothed volume fraction φ^{n+1} is obtained through changing parameter of UMTHINC formulation. For more detail, refer to section 5.2.

3. With φ^{n+1} determined, fluid property in term of density ρ and viscosity μ are updated straightforwardly,

$$\begin{aligned} \rho &= \rho_1 \varphi^{n+1} + \rho_2 \left(1 - \varphi^{n+1}\right), \\ \mu &= \mu_1 \varphi^{n+1} + \mu_2 \left(1 - \varphi^{n+1}\right). \end{aligned} \tag{5.11}$$

4. Curvature κ at surface is computed directly from ϕ^{n+1} field. Some techniques are developed as denoted in section 5.3.

5. Predict intermediate velocity by advection-diffuson equations under the effect of gravity and surface tension force,

$$\frac{\partial \mathbf{u}}{\partial t} = -\nabla \cdot (\mathbf{u} \otimes \mathbf{u}) + \frac{1}{\rho} \nabla \cdot (\mu \nabla \mathbf{u}) + \frac{\sigma \kappa}{\rho} \nabla \phi - \mathbf{g} \cdot \mathbf{x} \nabla \rho. \tag{5.12}$$

6. Formulate the Poisson equation by using intermediate velocity $\mathbf{u}^*$,

$$\nabla \cdot \left(\frac{1}{\rho} \nabla p^{n+1} \right) = \frac{1}{\Delta t} \nabla \cdot \mathbf{u}^*. \tag{5.13}$$

7. Correct velocity to ensure divergence free condition (projection step),

$$\frac{\mathbf{u}^{n+1} - \mathbf{u}^*}{\Delta t} = -\frac{1}{\rho} \nabla p^{n+1}. \tag{5.14}$$

The VOF equation is solved by UMTHINC scheme and Navier-Stokes equations are discretized and solved based on VPM/MCV scheme. The second order Runge-Kutta method is used for time integration for semi-discrete equations in the form of $d\phi/dt$.

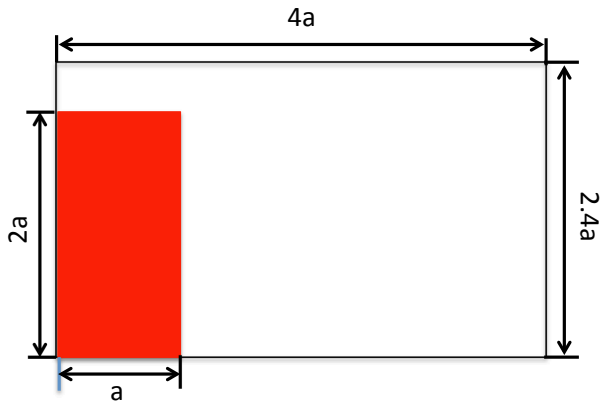


Figure 5.2: Definition of two dimensional dambreak test without obstacle.

5.5 Validation tests

5.5.1 2D Dambreak without obstacle

In order to verify the interfacial multiphase flow code, we conduct the simulation of collapse of a water column which is well know for its physical simplicity. A water column of $a \times 2a$ is set up in a tank of $4a \times a$ where a is specified with 0.146m as show in Fig. 5.2. Free-slip boundary conditions are imposed on the walls of tank and zero tangential velocity is specified on the open top wall. The density and dynamics viscosity for water are set to 1000kg/m^3 and $0.01\text{kg/}(\text{m}\cdot\text{s})$ while for air are set to 1kg/m^3 and $0.0001\text{kg/}(\text{m}\cdot\text{s})$ respectively. The water column collapses under the effect of gravity force and surface tension force is ignored in this case. Our results are compared with reference numerical solution in [32, 82] and experiment data of [88]. The evolution of free surface at the time of 0.1, 0.2, 0.3 and 0.4 computed on the mesh of 2160 triangular elements are shown in Fig. 5.3 and 5.4. We can find the interface is clearly captured and resolved, which is are visibly in good agreement with the result of [32, 82]. More quantitatively, the interface position on the bottom and left wall of tank is plotted in function of time as Fig. 5.5. We also investigated the convergence behavior with a refined mesh of 8636 elements. It is seen that present study shows full agreement with reference numerical results while slightly slower moving speed with time increasing. The discrepancy as mentioned in [82] is thought as consequence of deviation in boundary condition which is not possible to reproduce experimentally.

5.5.2 A circular droplet in static fluid

To validate surface tension model, we conduct a simple benchmark test which is called equilibrium drop[187]. In this benchmark test, a static droplet with a radius of $R = 0.25$ is located at center of the domain $[0, 4]^2$ in the absence of viscosity and gravitational force. A

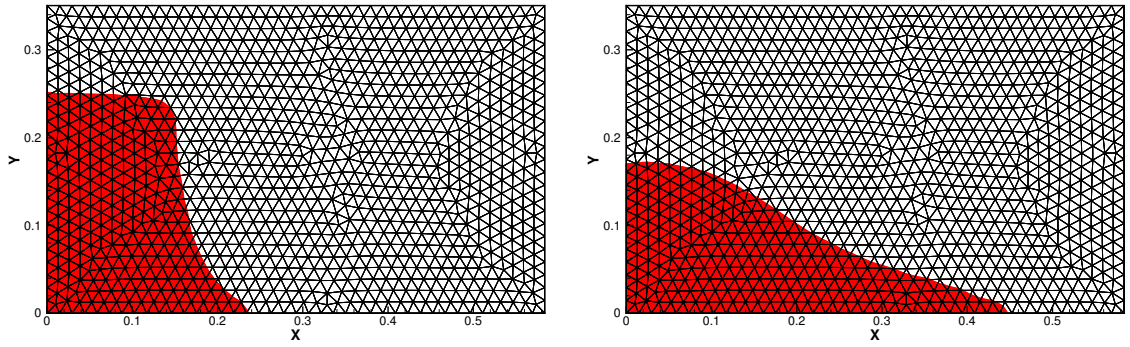


Figure 5.3: Snapshots of the water column for time 0.1(left) and 0.2(right).

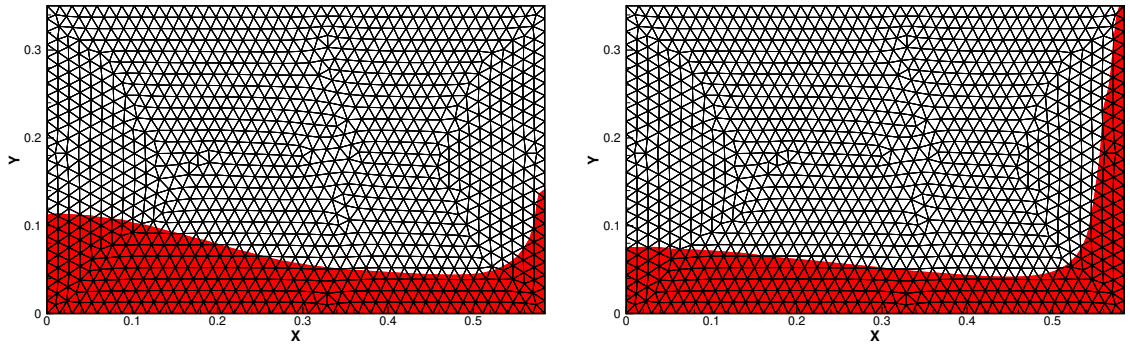


Figure 5.4: Snapshots of the water column for time 0.3(left) and 0.4(right).

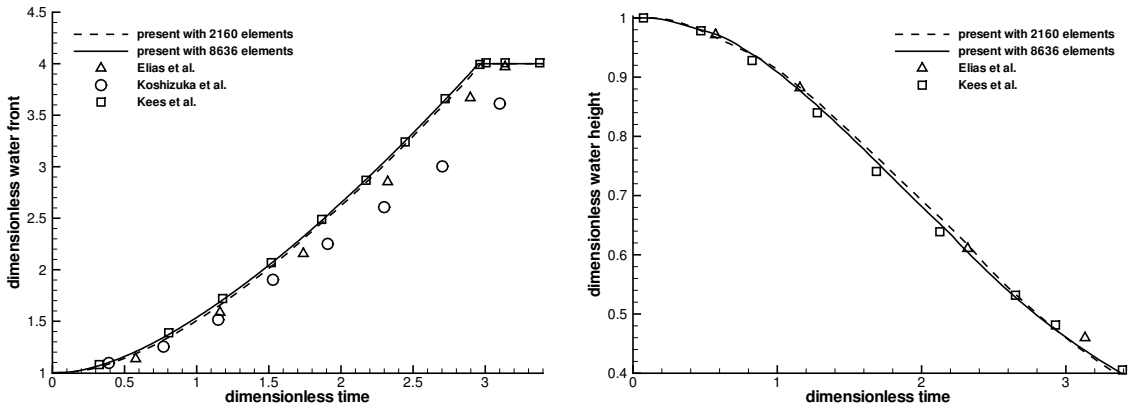


Figure 5.5: Air-water interface horizontal(left) and vertical(right) positions as a function of time in non-dimensional units.

circular droplet with radius of 1 keeps static under the effect of surface tension force. The fluids inside and outside of the droplet is specified as liquid with density of 1 and air with density of 0.001 respectively. The surface tension coefficient σ is set to 1. We impose the boundary as periodic condition and compute one time step with $\triangle t = 10^{-5}$. We measure the numerical errors of pressure jump by using exact pressure difference $E(\triangle P_{\text{total}})$ and pressure jump $\|E_p\|$ as reported in [37, 66]:

$$
\begin{aligned}
&P_{\text{exact}} = \sigma / R \\
&E(\triangle P_{\text{total}}) = ((P_{\text{in}} - P_{\text{out}}) - P_{\text{exact}}) / P_{\text{exact}} \\
&\|E_p\| = \left(\left(\frac{\sum \phi_i p_i}{\sum \phi_i} - \frac{\sum (1-\phi_i) p_i}{\sum (1-\phi_i)} \right) - P_{\text{exact}} \right) / P_{\text{exact}}
\end{aligned}
$$

where P_{exact} is exact pressure jump and P_{in}, P_{out} indicate the average pressure inside the drop (cells with $r \leq R$) and outside the drop (cells with $r > R$). In order to investigate the convergence behavior of pressure jump, we compute $E(\triangle P_{\text{total}})$ and $\|E_p\|$ on different grid resolution. We also compare the results computed by exact curvature($\kappa = 4$) and numerical curvature evaluated by least square method. Tolerance of pressure Poisson equation $\varepsilon_{\text{pressure}}$ is given as nearly 10^{-9}. From Table. 5.2 and Fig. 5.6, we can find the numerical error of pressure jump converges within nearly one order and the error with exact curvature shows to be little lower than result of numerical curvature. The pressure jump computed with numerical curvature on different resolution is plotted from bird's eye views in Fig. 5.7 and in form of profile along x axis as Fig. 5.8. We can find the pressure jump owing to surface tension force is adequately resolved and converges rapidly with mesh refinement. Due to employment of the balance force model, neither oscillation nor smearing of pressure jump is observed near the interface. Following [188], we defined numerical errors to estimate the sensitivity of spurious current affected by tolerance $\varepsilon_{\text{pressure}}$ of pressure Poisson equation as

$$
\begin{aligned}
&|\mathbf{u}_{\max}| = \max(|\mathbf{u}_i|), \\
&|\mathbf{u}|_{\text{avg}} = \textstyle\sum_i^{\text{N}} |\mathbf{u}_i| / \text{N} .
\end{aligned}
$$

We can find that with exact curvature, the spurious current mainly comes from tolerance $\varepsilon_{\text{pressure}}$ of pressure Poisson equation while with numerical curvature, the spurious current mostly comes from error of curvature evaluation. The method for curvature calculation with higher accuracy will be consider as future study.

To further verify the surface tension model, oscillation behavior of drop without gravity effect is investigated in the same computational condition with [37]. The computational domain of $[0, 20]^2$ is splitted into 14412 and 57518 triangular elements respectively. The drop interface is initially specified as elliptic shape given by the formulation of $(x-10)^2 / a^2 + (y-10)^2 / b^2 = 1 \, (a = 3, \, b = 2)$. The density and viscosity inside the

Elements	exact curvature(κ)		numerical curvature(κ)	
	$E(\triangle P_{\text{total}})$	$\|E_p\|$	$E(\triangle P_{\text{total}})$	$\|E_p\|$
894	1.351×10^{-2}	6.081×10^{-2}	1.504×10^{-2}	5.424×10^{-2}
3588	7.457×10^{-3}	3.333×10^{-2}	8.586×10^{-3}	2.709×10^{-2}
14412	3.629×10^{-3}	1.551×10^{-2}	3.910×10^{-3}	1.479×10^{-2}
57518	1.778×10^{-3}	7.649×10^{-3}	1.917×10^{-3}	7.258×10^{-3}

Table 5.2: Convergence behavior for pressure jump after one time step with exact curvature($\kappa = 4$) and numerical curvature.

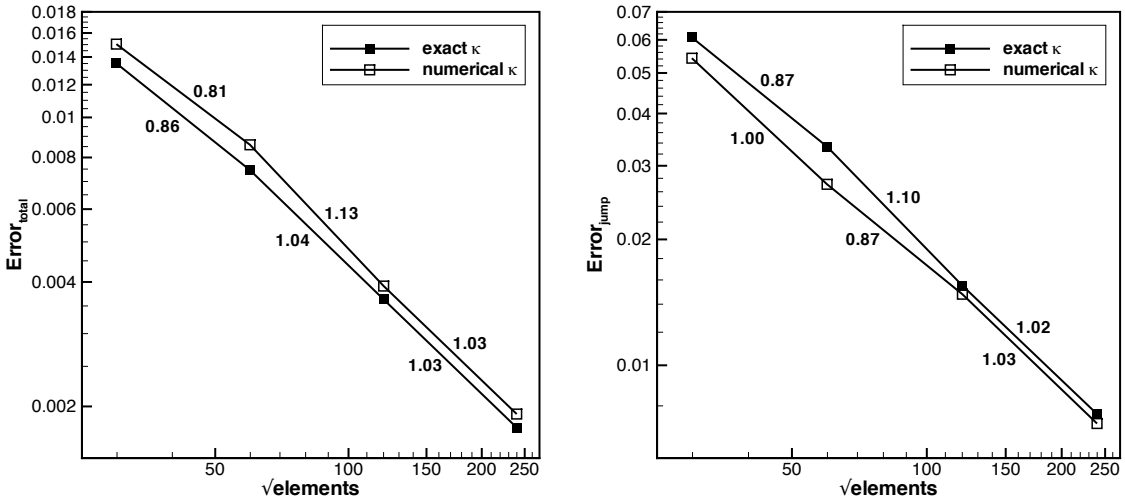


Figure 5.6: Convergence behavior for pressure jump after one time step with exact curvature($\kappa = 4$) and numerical curvature.

$\varepsilon_{\text{pressure}}$	exact curvature(κ)		numerical curvature(κ)	
	$\|\mathbf{u}\|_{max}$	$\|\mathbf{u}\|_{avg}$	$\|\mathbf{u}\|_{max}$	$\|\mathbf{u}\|_{avg}$
7.876×10^{-9}	6.832×10^{-10}	8.738×10^{-11}	4.007×10^{-5}	1.448×10^{-6}
1.812×10^{-9}	1.822×10^{-10}	2.220×10^{-11}		
3.753×10^{-10}	5.245×10^{-11}	3.549×10^{-12}		

Table 5.3: Sensitivity for spurious current with different tolerance $\varepsilon_{\text{pressure}}$ in pressure Poison equation after one time step.

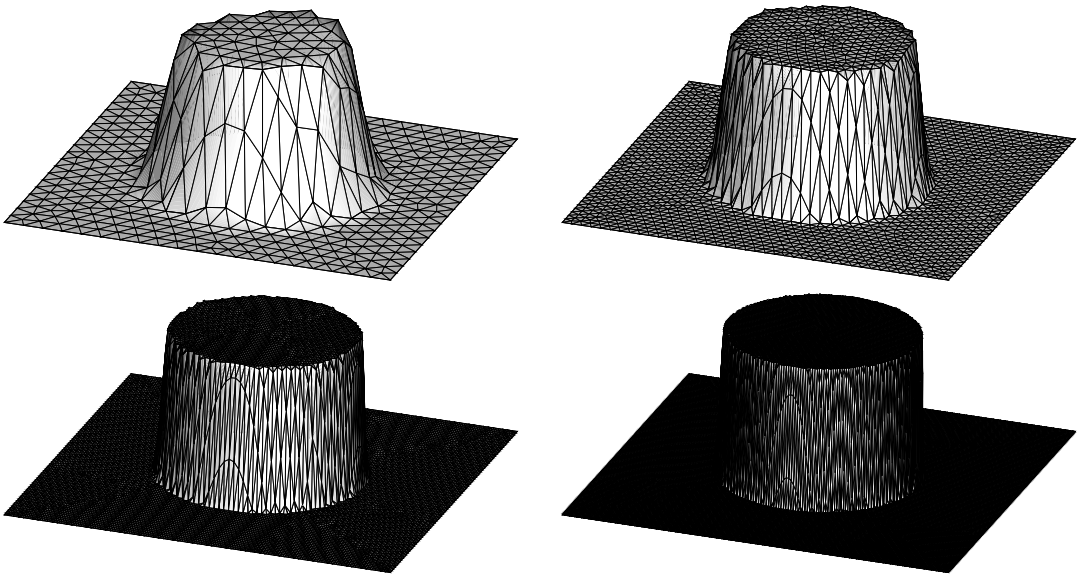


Figure 5.7: Bird's eye views of pressure jump computed with numerical curvature on different grid resolution.

drop are set as 1 and 0.01, and outside drop are 0.01 and 0.00005 respectively. The surface tension coefficient σ is 1. The drop oscillates periodically and eventually reaches static circular shape with radius of $R = \sqrt{ab} = \sqrt{6}$ under the effect of surface tension and viscosity. The parasitic currents estimated by kinetic energy $\left(\frac{1}{2}\sum_i \rho_i \left|\mathbf{u}_i\right|^2 \triangle\Omega\right)$ is shown in Fig. 5.9. Compared with results in [151], without any particular treatment, the parasitic currents is quite effectively suppressed which indicates the surface tension force is accurately balanced with viscosity. We also plot profile of VOF value($\phi = 0.05, 0.5, 0.95$) and pressure distribution when drop reaches steady state at instant of time 250 in Fig. 5.10. It is seen that the steady drop interface coincides well with analytical circle plotted by red solid line and pressure jump across the interface is adequately resolved.

5.5.3 Two dimensional bubble rising

The accuracy of present model is verified by this two-dimensional bubble rising benchmark test. The initial configuration is based on [58] as described in Fig. 5.11(left). The bubble is initially centered at $(0.5, 0.5)$ with 0.25 as the initial radius. The viscosity and density of fluid 1(Ω_1) and fluid 2(Ω_2) are defined as (1000:10) and (100:1) respectively. The domain is fully enclosed by no-slip walls at the top and the bottom, as well as free slip walls on the left and the right side. The gravity vector $\mathbf{g}$ points towards the bottom of the domain with magnitude of 0.98 and the coefficient of surface tension is given as 24.5. The bubble rises for 3s and the interface indicated by $\phi = 0.5$ is shown in Fig. 5.11(right). The time history of bubble position and rising velocity is plotted in Fig. 5.12. We can see, the present results show good agreement with results computed by FreeLIFE and TP2D[58]

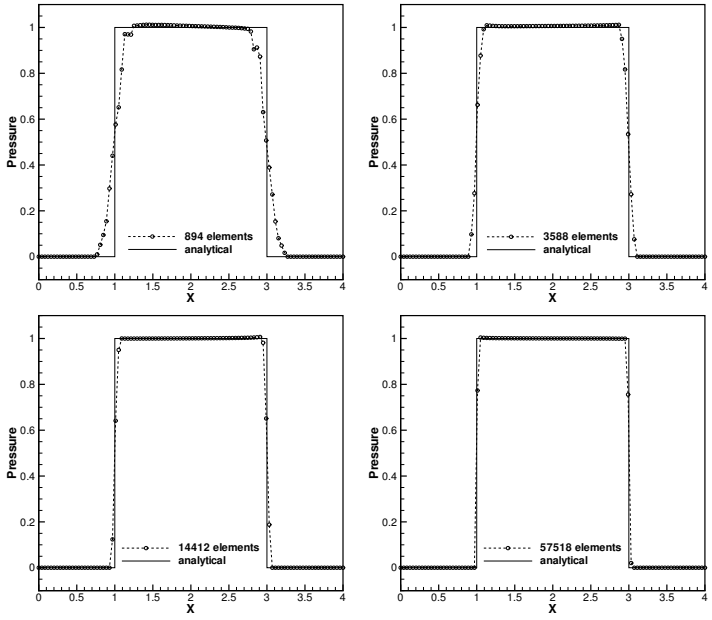


Figure 5.8: Profile along x axis of pressure jump computed with numerical curvature on different grid resolution.

quantity	good mesh	bad mesh	degradation rate
terminal rising position	1.55124	1.55165	0.0264%
terminal rising velocity	0.18245	0.18244	0.0055%
terminal perimeter of bubble	1.73416	1.72877	0.3108%

Table 5.4: Quantitative comparison for results computed on good mesh and bad mesh.

codes on finest structured grid of 1/320.

In order to determine the capability of present model to deal with nonorthogonality which often encounters in engineering problem, we generate another grid with a region where the mesh elements are distorted with large skewness and high aspect ratio. After bubble rises for 5.5s, we plot the shape interface comparing with results of uniform Cartesian grid as Fig. 5.13(right). More quantitative comparisons are measured by terminal position, velocity and perimeter of bubble tabulated in Table 5.4 and we can find the present scheme has gained adequate robustness and stability to ensure accuracy even on heavily distorted grid.

5.5.4 Three dimensional dambreak problem with obstacle

We verify capability of the numerical model to predict the pressure impacts caused by interfacial multiphase flows generated by a dam break. The experimental work was conducted at the Maritime Research Institute Netherlands (MARIN)[85]. A large tank of 3.22 by 1 by 1 meter is used with an open roof. The right part of the tank is first closed

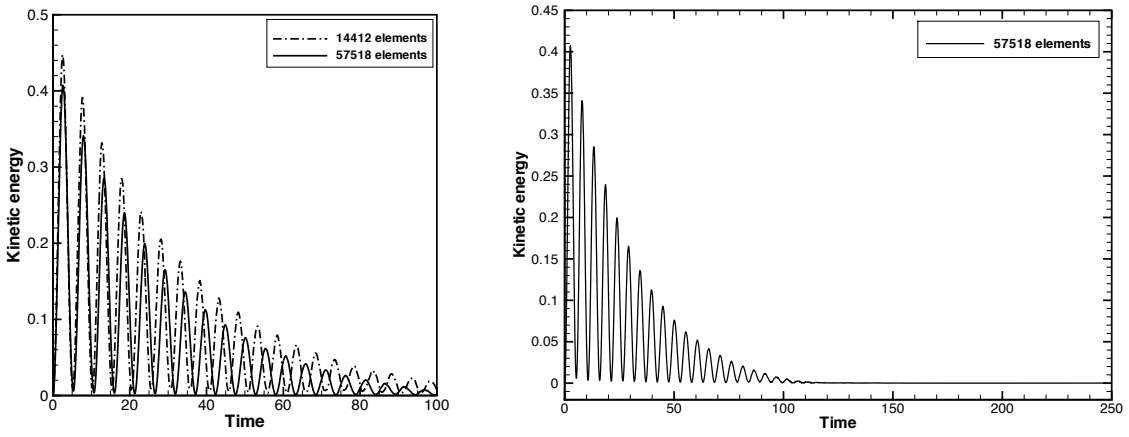


Figure 5.9: The evolution of the total kinetic energy in the drop oscillation problem. The left figure shows the results on grid of 14412 elements and 57518 elements for time [1,100]. The right figure shows the convergence behavior on grid of 57518 elements for long time computation.

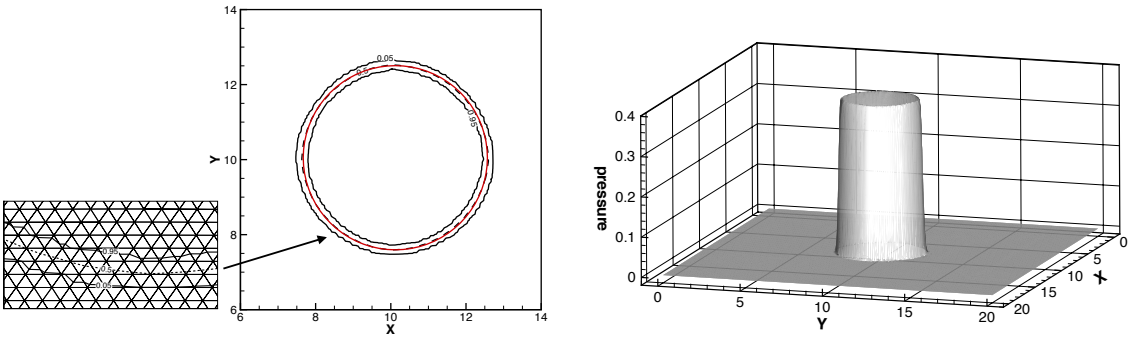


Figure 5.10: The VOF reaches steady state at time of $t = 250$. The left figure shows the profile of VOF value(ϕ) of 0.05, 0.5 and 0.95 and exact interface($\phi = 0.5$) is also plotted by red line. The right figure shows the pressure distribution in bird's eye views.

by a door (located at $x = 2m$). Behind the door 1.22 by 0.55 meter of water is waiting to flow into the tank when the door is opened. In the tank a box has been placed that represents the submerged obstacle in the water. The configuration of the tank is shown in Fig. 5.14.

The location of the obstacle box size is ($x$min / $x$max, $y$min / $y$max, $z$min / $z$max) = (0.67 / 0.83, -0.2 / 0.2, 0.0 / 0.16) .

Four pressure sensors are locate on the surface of the submerged box as follows:

P1: (x, y, z) = (0.831, -0.026, 0.025),

P3: (x, y, z) = (0.831, -0.026, 0.099),

P5: (x, y, z) = (0.806, 0.026, 0.165),

P7: (x, y, z) = (0.733, 0.026, 0.165).

The initial configuration of the simulation is evaluated accurately by local refinement approach to compute the cell average of volume fraction in each grid element. The fluid

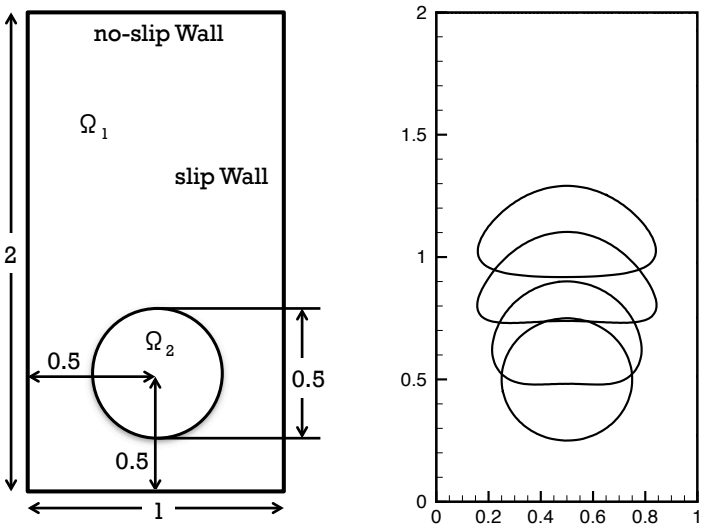


Figure 5.11: Left: initial condition; Right: bubble shape indicated by $\phi = 0.5$ for time 0s and 3s.

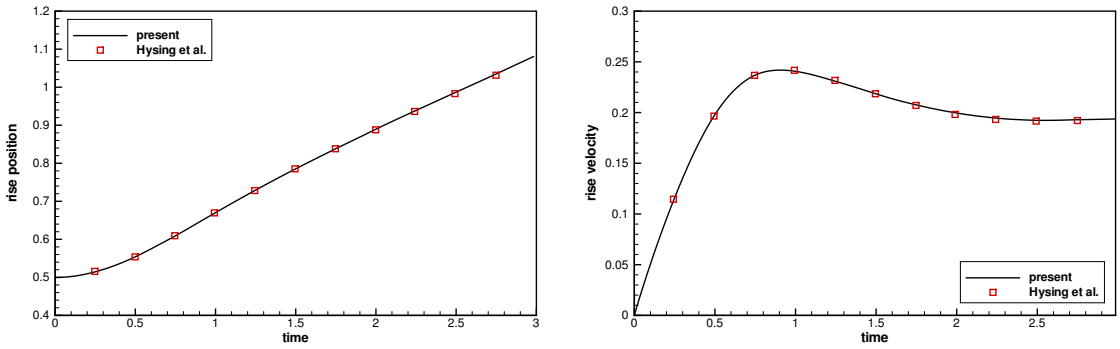


Figure 5.12: Time history of rising position and velocity for bubble.

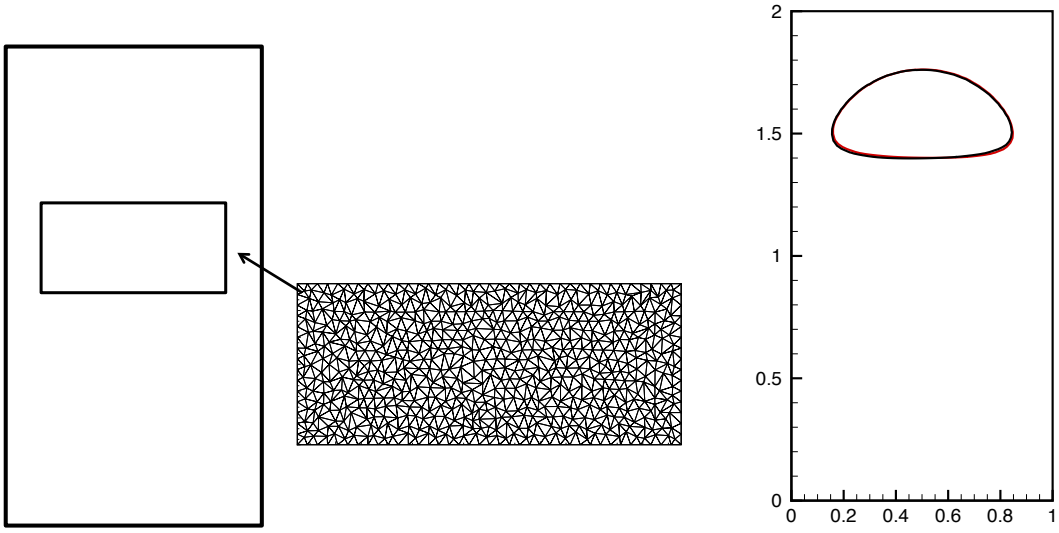


Figure 5.13: Left: the region filled with bad mesh elements. Right: bubble shape at end time for good mesh(black line) and bad mesh(red line).

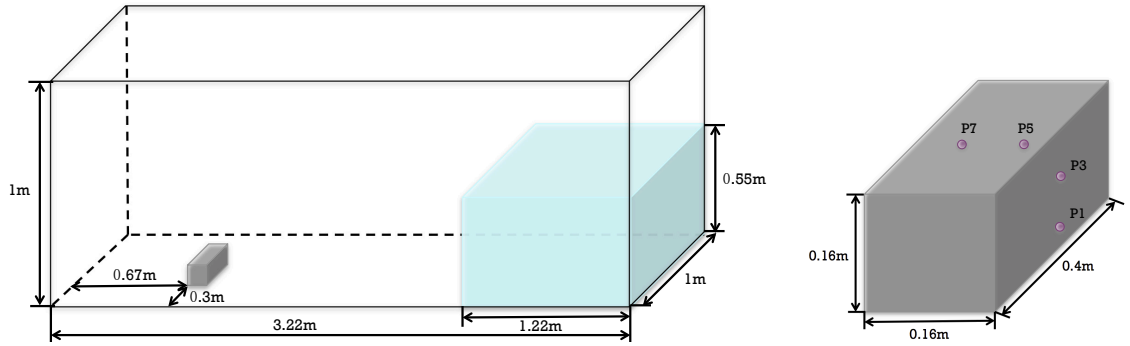


Figure 5.14: Configuration of the dam-break test (left), the measurement position for pressure(right).

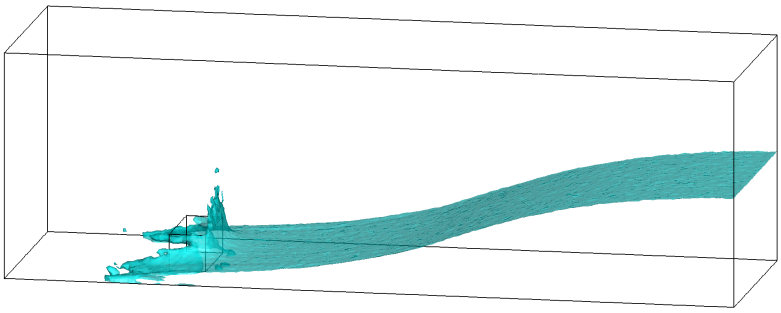
property of two phase is given as $\rho_l = 998\text{kg/m}^3$, $u_l = 1.0 \times 10^{-3}\text{Pa} \cdot \text{s}$ for water, $\rho_g = 1.2\text{kg/m}^3$, $u_g = 1.8 \times 10^{-5}\text{Pa} \cdot \text{s}$ for air and $\sigma = 0.072$ for interfacial surface tension coefficient. When the simulation is started, due to gravity the water begins to flow into the empty part of the tank. The simulation is continued for 6s with an automatically adapted time step using maximum CFL-numbers of 0.5, resulting in a time step of the order of 10^{-4}s.

In Fig. 5.15 the snapshots of water flow hitting the obstacle in the simulation are shown together for instants of time 0.48s, 0.96s, 1.92s, 2.4s. The results indicate that present scheme can clearly capture the moving interface involving extremely complicated deformation and distortion without any smearing or oscillation problem. The small rising bubbles and breaking droplets due to violent striking are also delicately resolved as well as the water motion.

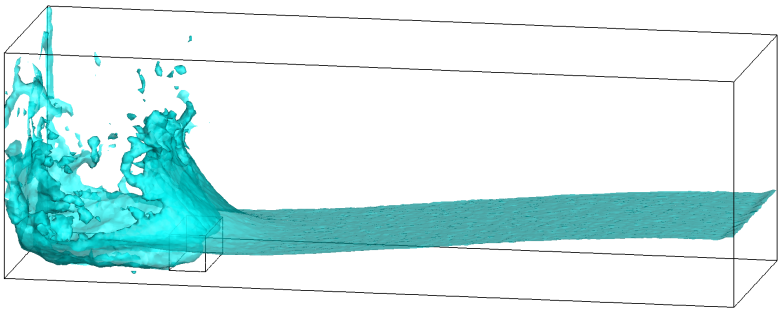
From Fig. 5.16, we can find that the instant when the wave hits the obstacle box is well captured by both probes and peak pressure caused by the wave impact is simulated in good consistency with experiment. From the pressure evolution history sampled at probe P5,P7 shown in Fig. 5.17, it is also evident that the present multiphase model is significantly more reliable than comFlow's results reported in [85], and shows the capability to accurately predict the fluid motion involving extremely complex interface changes.

5.5.5 Single bubble rising in a wide range of Reynolds and Bond number

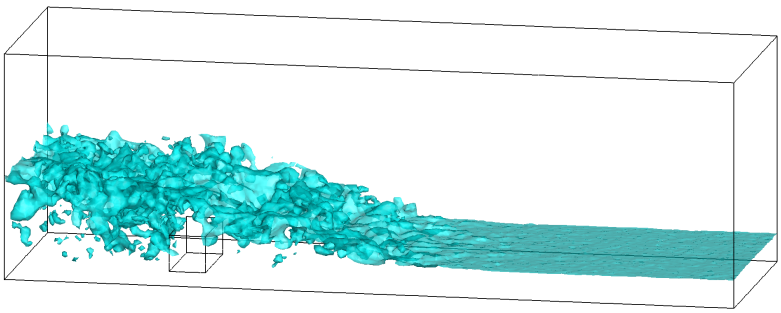
In this case, we present the numerical results for a single bubble rising in a viscous fluid under the effect of surface tension. Following Hnat and Buckmaster's experiment[57], one of the cases is with physical parameter given by $\rho = 1, \mu = 0.001$ for gas inside the bubble, $\rho = 875.5, \mu = 0.118$ for the outside liquid, $\sigma = 0.0322$ and $g = 9.81$. Under this condition, the terminal rising velocity V_∞ is proven to be 0.215. Referring to paper[66], the computational domain as large as $[0, 6D] \times [0, 6D] \times [0, 12D]$ is divided with unstructured hexahedral elements as shown in Fig. 5.18(left). At first, we plot bubble shapes



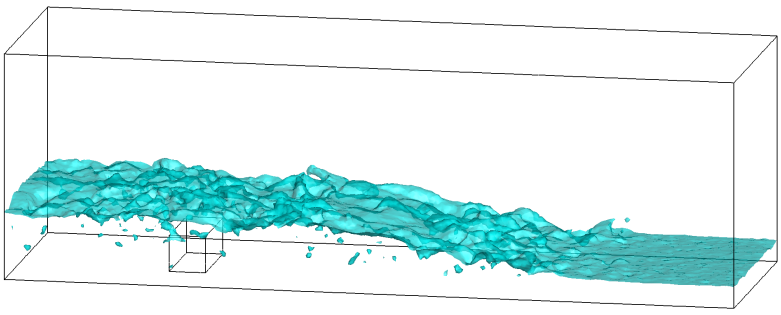
(a) t=0.48s



(b) t=0.96s



(c) t=1.92s



(d) t=2.4s

Figure 5.15: Snapshot of simulation for dambreak with an obstacle at instant of time 0.48s, 0.96s, 1.92s and 2.4s.

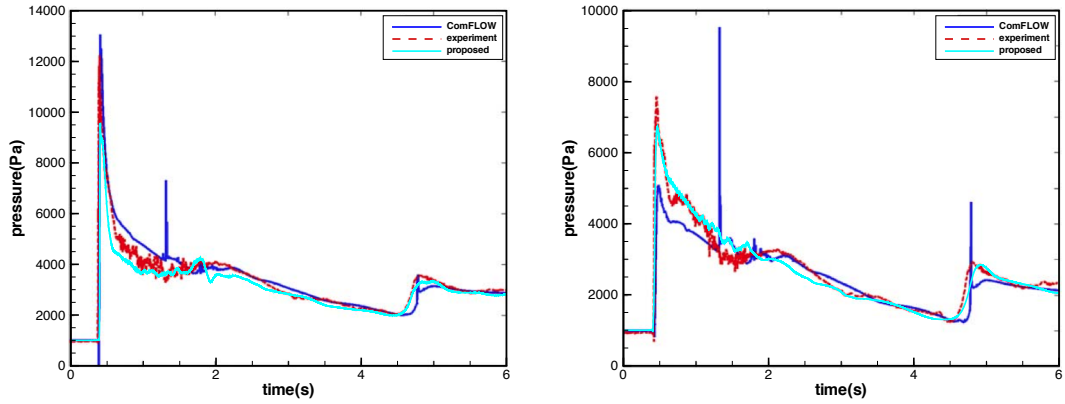


Figure 5.16: Pressure time histories at probe P1 and P3 on the vertical boundary of obstacle.

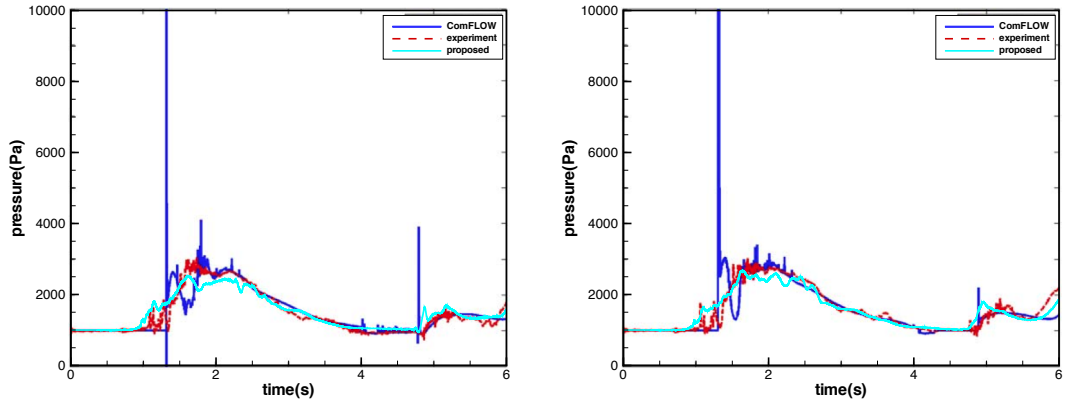


Figure 5.17: Pressure time histories at probe P5 and P7 on the horizontal boundary of obstacle.

and wake structures shown in Fig. 5.18(right) and compare the present results with available experiment/simulation results such as Hnat and Buckmaster[57](left), Gueyffier et al.[42](middle) and Ii et al.[66](right). Next, we investigate the bubble rising velocity and compare the bubble position history with experiments. We can find the present results agree well with existed both experimental and numerical researches. From Fig. 5.20, we can find the present model can accurately predict the bubble rising velocity and positions compared with experiment data. After validation, the numerical model is applied to reproduce bubble rising phenomenon under wide range of Reynolds and Bond number. As shown in Table 5.5, bubble shape is sufficiently resolved and terminal velocity is predicted with competitive accuracy.

5.5.6 Motion of microdropelet passing through ratchet structure

Ratchet structures with opening angle have been widely used as a flow rectification element for pumping application in microfluidics and micro process engineering. In order to

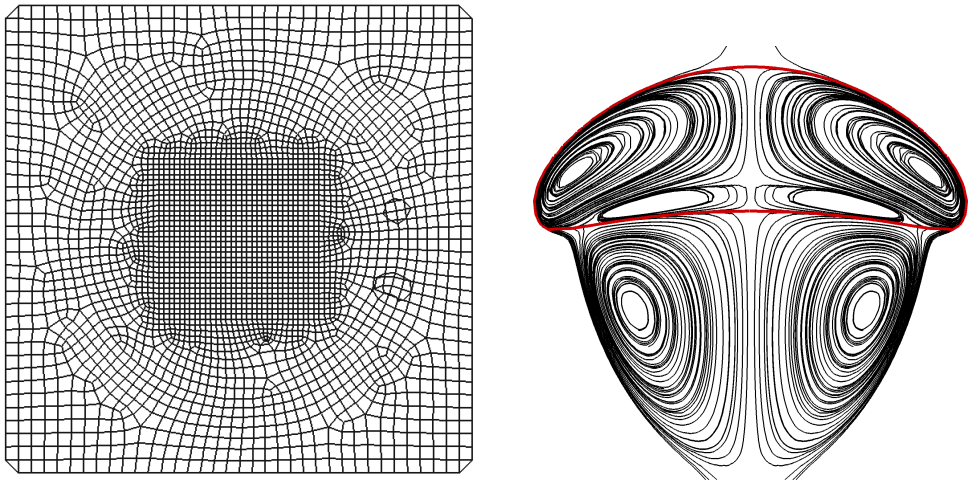


Figure 5.18: Computational grid across section(left) and bubble shape as well as streamline based on the bubble rise velocity(right).

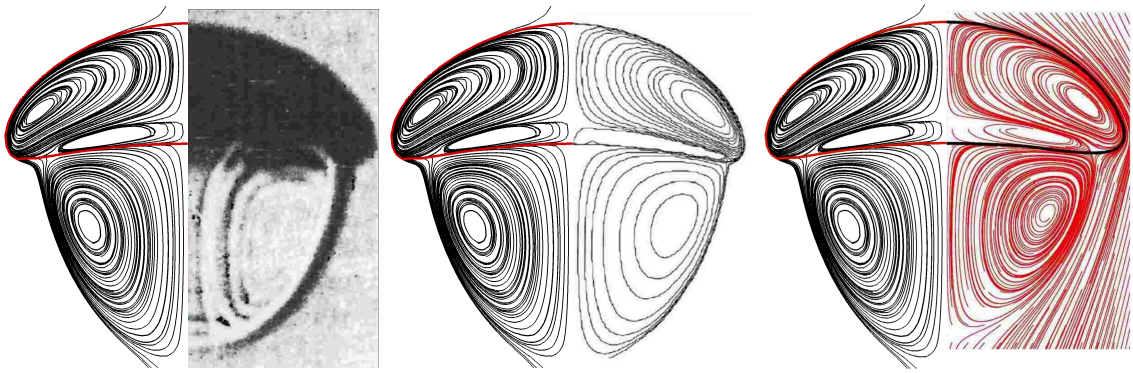


Figure 5.19: Comparisons of the bubble shape and streamline based on the bubble rise velocity. The left side and right side of each panel indicate the present result and experiment/other simulation results as Hnat and Buckmaster[57](left), Gueyffier et al.[42](middle) and Ii et al.[66](right).

investigate the behavior of a single droplet through the structure, numerical simulation is carried out within a three dimensional geometrical model as shown in Fig. 5.21. Refferring to [102], the geometrical configuration is designed with opening angle $\alpha = 45^{\circ}$ and width of 150 μm as the straight microchannels across the section.

The density and viscosity for two phase are $\left(800\text{kg/m}^3, 2.98\text{m}^2/\text{s}\right)$ for mineral oil as the carried fluid and $\left(998.57\text{kg/m}^3, 8.95\text{m}^2/\text{s}\right)$ for dispersed water. The interfacial tension between these two inmmiscible liquids is measured as 3.65mN/m. As the water is always surrounded by oil film, the contact angle at the wall is neglected. The No-slip boundary condition is enforced at the surrounding wall.

The droplet shape captured during the simulation is firstly compared with experiment results. From Table 5.6, we can realize the present scheme accurately simulated droplet passing through the ratchet involving complex structure. Since the Reynolds number is

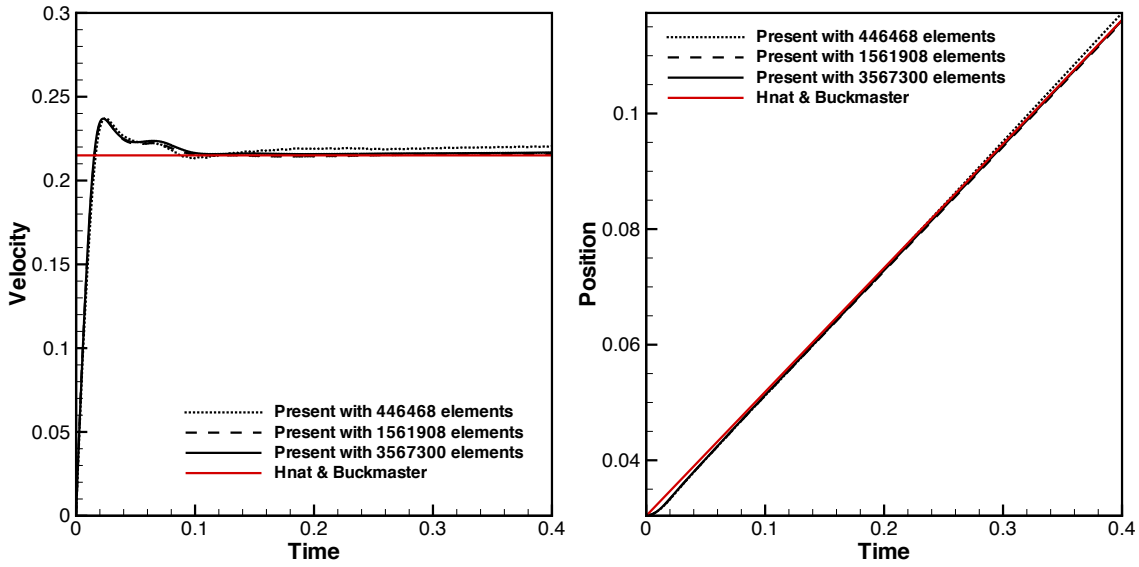


Figure 5.20: Time histories of bubble rising velocity(left) and position(right).

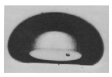
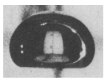
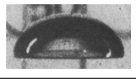
Experiment		Simulation				Error
Test condition	bubble shape	Modeling conditions	bubble shape	terminal velocity U^*	$Re = U^* \times Re^*$	$\frac{Re - Re_{exact}}{Re_{exact}} \times 100$
E = 243 M = 266 Re = 7.77		Bo* = 243 Re* = 15.24		0.5244	7.9921	1.196
E = 339 M = 43.1 Re = 18.3		Bo* = 339 Re* = 30.83		0.5616	17.316	5.538
E = 116 M = 226 Re = 3.57		Bo* = 116 Re* = 8.748		0.4472	3.8896	8.952
E = 116 M = 41.1 Re = 7.16		Bo* = 116 Re* = 13.95		0.5282	7.3677	2.819
E = 116 M = 5.51 Re = 13.3		Bo* = 116 Re* = 23.06		0.5588	12.885	3.120
E = 116 M = 1.31 Re = 20.4		Bo* = 116 Re* = 33.02		0.6032	19.917	2.366

Table 5.5: Comparison of terminal bubble shapes observed in experiments and predicted in simulation under Reynolds and Bond number.

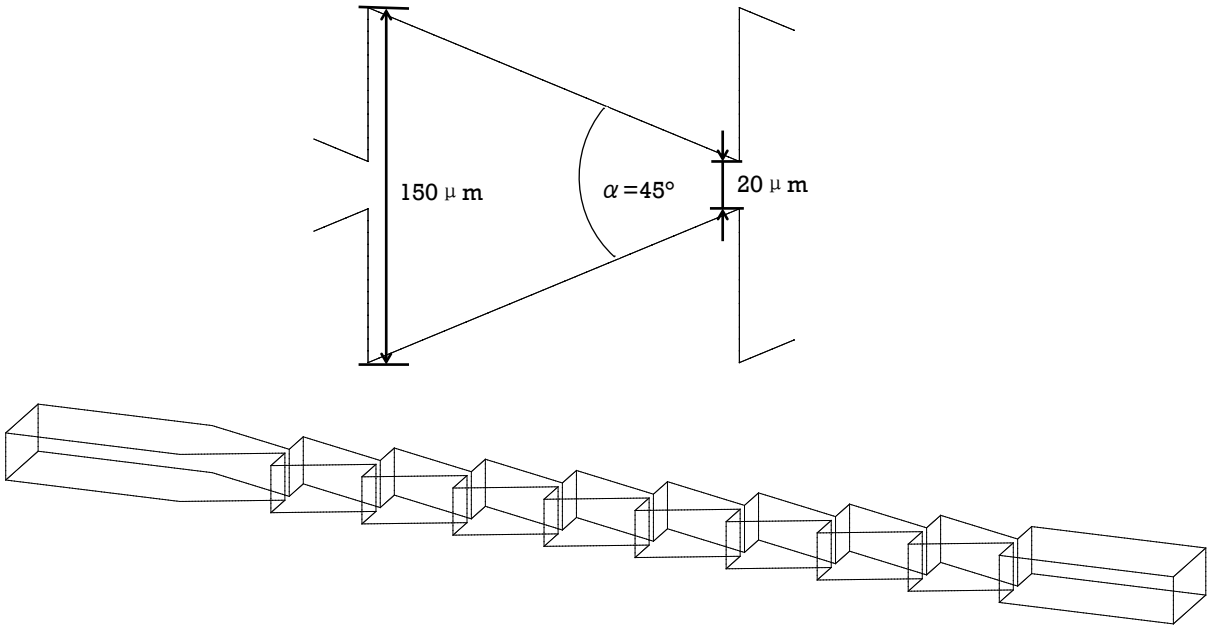


Figure 5.21: Schematic of investigated microfluidic ratchet structure.

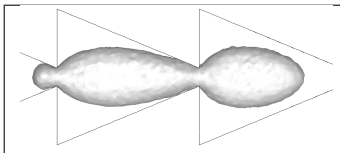
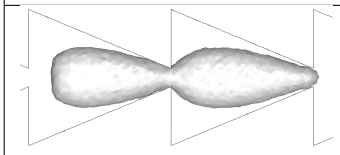
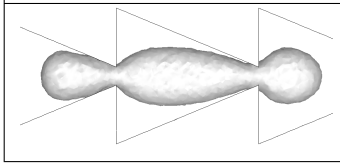
numerical data	experiment data
	
	
	

Table 5.6: Comparison of droplet shape between the present numerical solution and referred experimental data [102].

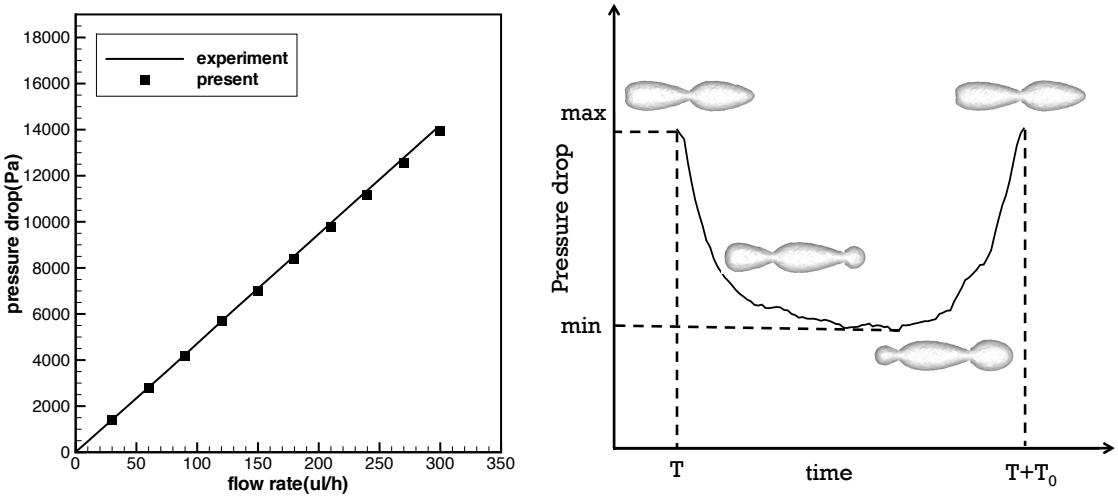


Figure 5.22: Comparison of pressure drop under different flow rate between numerical solution and experimental data(left). Periodical behavior of pressure drop as well as bubble shapes(right).

much smaller than 1, the pressure drop should be linear to the oil flow rate. In order to check this quality, we measure the pressure drop for different volumetric flow rate varied from from 30ul/h to 300ul/h. From Fig. 5.22(left), we can find the pressure drop in the simulation is in good agreement with the experimental data. When droplet passes through ratchet element, the pressure drop changes periodically with the variation of droplet shape and the characteristic is concluded in Fig. 5.22(right).

5.6 Summary of chapter 5

Using VPM/MCV method for incompressible fluid dynamics and UMTHINC scheme for interface capturing, we have developed numerical model for interfacial multiphase flow on arbitrary unstructured grid. In the framework of one-fluid model, VOF value is defined to represent the volume fraction of a specific fluid in each grid and updated by advection function based on finite volume method. In order to exactly evaluate numerical flux at cell boundary, UMTHINC scheme is required to reconstruct interface in each grid cell. Once VOF value resolved, density and viscosity can be updated straightforwardly and incompressible Navier-Stokes equation is solved by VPM/MCV scheme. In order to accurately reproduce phenomenon under the effect of surface tension force, spurious current is minimized by the effort in which (1) balanced surface tension model is adopted; (2) THINC formulation based smoothing function is proposed; (3) sophisticated interpolation method is utilized for curvature estimation instead of simple arithmetical average. As clarified in relevant studies, balanced force formulation is required to keep exact equilibrium between surface tension force and viscous force for collocated moment arrangement. For large density ratio flow, for instance $\rho_{\text{water}}/\rho_{\text{air}} = 1000$, smoothed VOF value is achieved through changing jump thickness with smaller parameter β of THINC formulation. The curvature at cell boundary is interpolated from center values closest to interface which alleviates unphysical oscillation caused by conventional arithmetical average method. The surface tension of present model is verified by equilibrium drop test under different grid resolution.

The numerical results for multiphase flow demonstrates remarkable performance in accuracy, generality and robustness. Ranging from extremely complicated interface changing involving in dambreak test to challenging surface tension dominant flow in micro-channel problem, all the phenomena are sufficiently recovered by present numerical model. Robustness is also verified and found that seriously distorted element can not perturb the results no matter qualitatively or quantitatively. The developed multiphase model shows great potential as one of the most practical and attractive choices to compute moving interfaces in the simulations of multiphase flows involving complex geometries.

Chapter 6

Conclusions and future work

In this study, I proposed novel VPM and MCV reconstruction formulations based on multi-moments as well as multi-moment constraints on unstructured grids. Unlike conventional FVM, piecewise incomplete quadratic polynomials are piecewisely constructed for VPM formulation based on VIA and PVs of a single grid cell as well as the derivatives at the cell center. These derivatives are approximated from the VIA and PVs of the cells sharing the boundary edges with the target cell. VPM can be equivalently expressed in form of MCV through the constraint conditions which approximate VIA in term of PVs at cell centroid and vertices. With VPM or MCV constructed, all sort of PVs, integrated averages and the derivative variables are derived in a straightforward and efficient manner.

Based on VPM/MCV scheme, I developed a Mach uniform solver for flows of different compressibility on unstructured grids. This model is realized by a sequence of decoupled partial differential equations and linked with pressure projected solution procedure. Detailedly, in first predictor step, advection and diffusion equation are solved to obtain intermediate variables. Next, the pressure Poisson equation is formulated by enforcing momentum equation to satisfy corresponding conditions for closed-form solution, i.e. continuity equation for incompressible flow and state equation as well as the first law of thermodynamics for Mach uniform compressible flow. As last correction step, the resulting pressure is used to update intermediate variables to reach next time level. TVD limiter is also devised to suppress oscillation and simultaneously retain high order accuracy. With all above devoted effort, the numerical model is verified to achieve significant improvements regarding accuracy and robustness with mildest extra cost.

I proposed UMTHINC scheme for interface capturing on unstructured grids. In order to make the computation efficient, the exact integration of the hyperbolic tangent function is made in the principal direction and the integration in other two directions is computed by numerical quadrature. The principal direction is determined from the major component of normal direction of the interface. The tests verified by canonical Zalesak and shear vortex flow problems demonstrate that numerical results of UMTHINC are among the

most accurate solutions and competitive with PLIC type VOF scheme.

I developed multiphase model on unstructured grids by integrating VPM/MCV based incompressible solver with UMTHINC based interface capturing scheme. In order to resolve high density ratio flow, THINC formulation based smoothing technique for VOF value is proposed and used to determine fluid property like density and viscosity. Using updated density and viscosity, the Navier-Stokes equation is solved by VPM/MCV schemes following incompressible solution procedure. For the purpose of surface tension dominant flow, I make improvements in calculation of geometrical property of interface like curvature and unit normal vector which result in a superior solution of balanced surface tension model. The present model is verified and validated by various benchmark tests and the results are in excellent agreement with existing experimental and numerical data.

6.1 Major contributions of present study

The numerical model developed in this study is able to provide high quality solutions for a wide range of complex flows from interfacial multiphase flow to high speed compressible flow. It is of high practicality and can be viewed as a promising new numerical framework for industrial applications due to following facts:

1. The present numerical model is as flexible as FVM to adopt arbitrary unstructured grid including triangular, quadrilateral elements for 2D and tetrahedral, hexahedral, prismatic and pyramidal elements for 3D. In order to resolve complex flow on domain involving complicated geometry, mixed type grid is required particularly for the turbulent flow which needs intensive mesh resolution for boundary layer. This capability significantly facilitate grid generation which is highly laboring task and most time consuming work in real application.

2. Based on conserved variables and finite volume method, conservativeness is rigorously ensured by the current numerical model in simulations of various complex flows including incompressible flow, multiphase flow and compressible flow of different Mach numbers. This essential property is not provided by many popular approaches like level-set method(LS), finite element method(FEM) as well as most pressure based compressible models.

3. Using DOFs defined on the cell vertices, VPM/MCV scheme of present numerical model can construct higher order reconstruction with compact stencil which is only associated with direct neighboring cells. The compactness eliminates the uncertainty in stencil selection and eases the difficulties with boundary specification and parallel implementation.

4. As shown in the verification tests, accuracy of present numerical model is substantially improved in both error and convergence compared with the conventional FVM models. Advection term in VPM/MCV scheme was verified as third order and error of Navier-Stokes equation turned out to be only 1% of FVM at the same computational condition. The UMTHINC scheme provided sufficient accuracy competitive to PLIC type VOF schemes.

5. Despite of remarkable accuracy improvement, the present VPM/MCV scheme only causes about $30 \sim 40\%$ increase in the memory consumption and $40 \sim 50\%$ increase in CPU time. Compared with other compact high order schemes like DG, SV, SD or CPR, the additional DOFs located on cell vertices are shared by surrounding cells which effectively alleviate requirement in memory usage. Compared with other wide stencil FVM schemes, the reconstruction is determined on reference element at local coordinate which avoids solving large matrix systems in each cell. The present model is devised to minimized the increase in computational cost. Efficiency in UMTHINC scheme is also realized through straightforward algebraic calculation instead of complicated geometrical reconstruction.

6. The robustness of present model is verified by investigating degradation of numerical solution on distorted grid. The robustness of VPM or MCV scheme is shown to be much superior to conventional FVM schemes. The UMTHINC is verified to be robust and of much less mesh dependency. And robustness of the multiphase model is shown to be sufficient to resolve applications involving complicated geometries.

The present numerical model provides overall optimized performance in aspects of flexibility, conservativeness, accuracy, efficiency, complexity and robustness, which makes it of great potential as a reliable and efficient numerical platform applicable in scientific and engineering fields, such as mechanical engineering, chemical engineering, civil engineering, nuclear engineering and aerospace engineering among others.

6.2 Impact of present study on related research field

The finite volume method (FVM) still remains the most popular and fundamental unstructured platform in CFD field and is adopted by almost all commercial CFD codes despite of the unresolved problems in accuracy and robustness. Although significant progress has been made in high order methods, like k-exact least-squares, ENO, WENO, DG, SV, SD, CPR etc, no clear sign appears that any of these will replace the dominant popularity of conventional second-order FVM paradigm. This is mainly because of the complexity and computational expensiveness of high order schemes. For instance, k-exact least-squares, or ENO/WENO type methods have to be reconstructed on wide stencils, which raises

difficulties in stencil selection, treatment of boundary condition and parallel computing. On the other hand, the spectral-like schemes represented by DG, SV, SD, CPR that use more locally defined DOFs in each grid cell to realize high order over compact stencils, require significant increase in CPU cost and memory usage. It makes these methods prohibitive for many real problems where computational efficiency and robustness are of more importance.

Being a methodology which lies between the conventional FVM and high-order local reconstruction based methods, the MCV and VPM presented in this thesis provide a numerical framework that is a better trade-off between accuracy and efficiency, and thus of more practical significance for real-case industrial applications. Using additional DOFs defined at cell vertices, the accuracy is remarkably improved with only 30∼40% increasing in both CPU time and memory consumption. As shown in the thesis, this basic platform demonstrates great potential to apply to various real problems in different fields

The proposed UMTHINC scheme follows the previous work of [173, 176, 186, 66] based on the concept that approximates the moving interface by using hyperbolic tangent function. Without explicitly reconstructing interface in each grid cell, the present method is easy to implement on unstructured grids. The scheme gives solutions comparable to PLIC VOF scheme, and shows adequate accuracy and robustness to resolve moving interface in presence of complex geometry. This scheme again achieved great success with balanced performance between the accuracy and efficiency which makes the method practical for industrial applications. The emergence of present scheme as well as integrated multiphase solver will significantly promote the related researches and facilitate the development of various applications particularly involving microflow, phase change and chemical reactions in the future.

The Mach uniform unstructured solver is developed for resolving fluid dynamics ranging from incompressible flow to high speed flow. Without any precondition treatment, the present model is proven to be capable of reproducing physically realistic result with sufficient accuracy for wide range of Mach number. The development of present solver substantially increase applicable scope under present multi-moment framework. With further improvement, the present unstructured Mach uniform solver and multi-moment framework can be developed to solve compressible multiphase flow which is one of the most challenging issues in related fields.

6.3 Future work

Although the present numerical model have enjoyed successes in various verifications and applications, the optimal solution still need to be investigated to make improvement in several aspects mainly in the area of oscillation limitation approach and pressure based

Mach uniform model in compressible fluid dynamics. In addition, based on present fundamental platform, new functions and models need to be incorporated to facilitate the model for wider applications, such as dynamic meshing for fluid-solid interactions, large eddy simulation (LES) model for turbulent flows and coupling models for particular applications.

Our oscillation limiter is devised based on the concept of TVD criteria. It is efficient and effective to control oscillation but insufficient in accuracy. As shown in verification tests, this limiter leads to degradation in both numerical error and convergence rate. On the other hand, remarkable progresses has been made for ENO[53, 1, 143], CENO[73], WENO[36, 59, 76, 30, 153], and MLP[119] limiting procedures which remove the oscillation near solution discontinuities and keep exact accuracy in the smooth region automatically. As the future studies, we will devised more sophisticated limiting procedure suitable for VPM or MCV schemes to improve the accuracy. The devised scheme should be not only sufficient in accuracy but also efficient and easy to implement on arbitrary unstructured grids. This work will contribute to improve resolution in high speed flow so as to identify more detailed structure near region of discontinuities.

The pressure based Mach uniform model is shown to be accurate and robust in various numerical tests however spurious oscillation is still observed in several cases involving shock wave. On the other hand, density based method has gained remarkable success for high Mach flows, where the Riemann solvers play a key role in finding the numerical fluxes. As one of the successful Riemann solver, the advection upstream splitting method (AUSM)[99, 100, 101] separates advection and pressure waves. More recently, in order to improve the performance of pressure based compressible solver, Xisto[179] proposed a hybrid pressure-density based method by using $\mathrm{AUSM}^{+}-\mathrm{up}$ to reformulate the flux at cell boundary which improves the resolution of shock wave without the occurrence of wiggles under supersonic flow the and produces accurate and physically realistic results in low Mach number flow. As the future studies, we will investigate to combine density-based AUSM type scheme to improve the performance in high Mach flow for present pressure based Mach uniform solver.

Appendix 1: Interpolation from cell center to vertex by least square method

Given the value at cell center, the quantities at cell vertex is required for many approaches in this study. Although the interpolation from value at cell center to cell vertex can be implemented by dozen of approaches, the least square method is employed as that it can provide arbitrary order quantities by using corresponding reconstruction function with enough number of DOFs. Here, for implicitly, we only consider linear reconstruction. Considering a small vicinity region that value ϕ_i at vertex θ_i is surrounded by value ϕ_{ik}, $k = 1, 2, \cdots, K$ at cells center. A linear interpolation function $\omega(x, y)$ defined on global coordinate system is formulated as followings:

$$\omega(x, y) = \phi_i + \phi_{xi}x + \phi_{yi}y$$

The three unknown coefficients is determined by the least squares method, i.e. minimizing the following quadratic function

$$L_P(\omega) = \sum_k \left(\phi_{ik} - \omega(x_{ik},\, y_{ik})\right)^2$$

which results in linear equations system as

$$\begin{bmatrix} K & \sum_k x_k & \sum_k y_k \\ \sum_k x_k & \sum_k x_k^2 & \sum_k x_k y_k \\ \sum_k y_k & \sum_k x_k y_k & \sum_k y_k^2 \end{bmatrix} \begin{bmatrix} \phi_i \\ \phi_{xi} \\ \phi_{yi} \end{bmatrix} = \begin{bmatrix} \sum_k \phi_{ik} \\ \sum_k \phi_{ik} x_{ik} \\ \sum_k \phi_{ik} y_{ik} \end{bmatrix} \tag{6.1}$$

This can also be formulated in term of

$$\begin{bmatrix} K & R_x & R_y \\ R_x & I_{xx} & I_{xy} \\ R_y & I_{xy} & I_{yy} \end{bmatrix} \begin{bmatrix} \phi_i \\ \phi_{xi} \\ \phi_{yi} \end{bmatrix} = \begin{bmatrix} \sum_k \phi_{ik} \\ \sum_k \phi_{ik} x_{ik} \\ \sum_k \phi_{ik} y_{ik} \end{bmatrix}$$

Then the unknown quantities including value ϕ_i and first order derivative (ϕ_{xi}, ϕ_{yi}) at cell vertex is yielded as

$$\begin{aligned} \phi_i &= \frac{\left(I_{xx}I_{yy}-I_{xy}^2\right)\sum_k \phi_{ik}+(R_yI_{xy}-R_xI_{yy})\sum_k \phi_{ik}x_{ik}+(R_xI_{xy}-R_yI_{xx})\sum_k \phi_{ik}y_{ik}}{2R_xR_yI_{xy}-R_y^2I_{xx}-R_x^2I_{yy}+K\cdot I_{xx}I_{yy}-K\cdot I_{xy}^2} \\ \phi_{xi} &= \frac{(R_yI_{xy}-R_xI_{yy})\sum_k \phi_{ik}+\left(K\cdot I_{yy}-R_y^2\right)\sum_k \phi_{ik}x_{ik}+(R_xR_y-K\cdot I_{xy})\sum_k \phi_{ik}y_{ik}}{2R_xR_yI_{xy}-R_y^2I_{xx}-R_x^2I_{yy}+K\cdot I_{xx}I_{yy}-K\cdot I_{xy}^2} \\ \phi_{yi} &= \frac{(R_xI_{xy}-R_yI_{xx})\sum_k \phi_{ik}+(R_xR_y-K\cdot I_{xy})\sum_k \phi_{ik}x_{ik}+\left(K\cdot I_{xx}-I_{xy}^2\right)\sum_k \phi_{ik}y_{ik}}{2R_xR_yI_{xy}-R_y^2I_{xx}-R_x^2I_{yy}+K\cdot I_{xx}I_{yy}-K\cdot I_{xy}^2} \end{aligned} \tag{6.2}$$

Appendix 2: Analytical expression for a quartic equation in the present method

The analytical solution for quartic equaiton in THINC reconstruction has been given in [66]. A quartic equation is defined as

$$a_4x^4 + a_3x^3 + a_2x^2 + a_1x + a_0 = 0. \tag{6.3}$$

For simplicity, (6.3) is replaced by dividing a_4,

$$x^4 + b_3x^3 + b_2x^2 + b_1x + b_0 = 0 \tag{6.4}$$

where $b_3 = a_3/a_4$, $b_2 = a_2/a_4$, $b_1 = a_1/a_4$, and $b_0 = a_0/a_4$. (6.4) then is further expressed as

$$\left(x^2 + Ax + B\right)^2 - (Cx + D)^2 = 0. \tag{6.5}$$

Here, the following relationship is obtained from identity (6.4) and (6.5).

$$\begin{cases} 2A = b_3, \\ A^2 + 2B - C^2 = b_2, \\ 2AB - 2CD = b_1, \\ B^2 - D^2 = b_0. \end{cases} \tag{6.6}$$

Supposing $z = 2B$, we can eliminate A, C and D by a cubic equation for z given by

$$z^3 + c_2z^2 + c_1z + c_0 = 0. \tag{6.7}$$

$$\begin{cases} c_2 = -b_2 \\ c_1 = b_1 b_2 - 4b_0 \\ c_0 = b_0\left(4b_2 - b_3^2\right) - b_1^2 \end{cases} \tag{6.8}$$

According to Cardano's formula, one real solution z_1 to the cubic equation (6.7) is obtained as

$$\begin{cases} \sqrt[3]{\frac{-b+\sqrt{b^2+4a^3}}{2}} - \sqrt[3]{\frac{b+\sqrt{b^2+4a^3}}{2}} - \frac{c_2}{3} & \text{for } b^2+4a^3 \geq 0 \\ 2\sqrt{-b}\cos\left(\frac{1}{3}\tan^{-1}\left(\frac{\sqrt{-(b^2+4a^3)}}{-b}\right)\right) - \frac{c_2}{3} & \text{for } b^2+4a^3 < 0 \end{cases} \tag{6.9}$$

where,

$$a = -\frac{c_2^2}{9} + \frac{c_1}{3},\ b = \frac{2c_2^3}{27} - \frac{c_1 c_2}{3} + c_0. \tag{6.10}$$

According to Brown's formula, when one real number solution z_1 to solution (6.7) is known, the coefficients A, B, C and D in (6.6) are determined as follows:

$$\begin{cases} A = \frac{b_1}{2} \\ B = \frac{z_1}{2} \\ D = \sqrt{B^2 - b_0} \\ C = \frac{-b_1/2 + AB}{D} \end{cases} \tag{6.11}$$

It remains possible that D becomes imaginary when $B^2 - b_0$ becomes negative in (6.10). Fortunately for the present method, it never becomes negative from our numerical experiments. Therefore, the above relations hold. Finally, four solutions to (6.3) are obtained by solving the two quadratic equations from (6.5) as follows,

$$\begin{aligned} x^2 + (A - C)\, x + (B - D) = 0 \\ x^2 + (A + C)\, x + (B + D) = 0 \end{aligned} \tag{6.12}$$

In practice, we choose the solution given by

$$x = \frac{-(A - C) + \sqrt{(A - C)^2 + 4\,(B - D)}}{2} \tag{6.13}$$

from the physical requirements, and it is easily found that (6.12) truly works as the solution to (6.3) in all cases.

Bibliography

[1] R. Abgrall, On essentially non-oscillatory schemes on unstructured meshes: analysis and implementation, J. Comput. Phys. 144 (1994) 45–58.

[2] M. Ahmed, H. C. Kuhlmann, Flow instability in triangular lid-driven cavities with wall motion away from a rectangular corner, Fluid Dyn Res, 44 (2012) 025501.

[3] R. Akoh, S. Ii, F. Xiao, A CIP/multi-moment finite volume method for shallow water equations with source terms, Int. J. Numer. Methods Fluids 56 (2008) 2245–2270.

[4] R.Akoh, S.Ii and F. Xiao: A multi-moment finite volume formulation for shallow water equations on unstructured mesh, J. Comput. Phys., 229 (2010) 4567-4590.

[5] S. Albensoeder, H. Kuhlmann, Accurate three-dimensional lid-driven cavity flow, J Comp. Phys. 206 (2005) 536–558.

[6] T. Aoki, Interpolated differential operator (IDO) scheme for solving partial differential equations, Comput. Phys. Commun., 102 (1997), 132.

[7] A. Ashgriz, J.P Poo, FLAIR: flux line-segment model for adevction and interface reconstruction, J. Comput. Phys. 93 (1991) 449–468.

[8] E. Aulisa, S. Manservisi, R. Scardovelli, S. Zaleski, A geometrical area-preserving Volume-of-Fluid advection method, J. Comput. Phys. 192 (2003) 355–364.

[9] E. Barragy, G.F. Carey, Stream function-vorticity driven cavity solutions using p finite elements, Comput. and Fluids, 26 (1997), 453–468.

[10] T.J. Barth and P.O. Frederickson, High-Order Solution of the Euler Equations on Unstructured Grids using Quadratic Reconstruction, AIAA (1990) 90-0013 .

[11] T.J. Barth, Recent developments in high order K-exact reconstruction on unstructured meshes, AIAA (1993) 93-0668.

[12] A.S Benjamin, V.E. Denny, On the convergence of numerical solutions for 2-D flows in a cavity at large Re, J. Comput. Phys., 33 (1979), 340–358.

[13] H. Bijl, P. Wesseling, A unified method for computing incompressible and compressible flows in boundary-fitted coordinates, J. Comput. Phys. 141 (1998) 153.

[14] O. Botella, R. Peyret, Benchmark spectral results on the lid-driven cavity flow, Comput. and Fluids, 27 (1998), 421– 433.

[15] J.U. Brackbill, D.B. Kothe, and C. Zemach. A continuum method for modelling surface tension. J. Comp. Phys., 100 (1992) 335–354.

[16] C. H. Bruneau, M. Saad, The 2D lid-driven cavity problem revisited, Comput. and Fluids **35** (2006) 326-348.

[17] A. Cervone, S. Manservisi, R. Scardovelli, S. Zaleski, A geometrical predictor-corrector advection scheme and its application to the volume fraction function, J. Comput. Phys. 228 (2009) 406–419.

[18] S.R. Chakravarthy, S. Osher, High resolution applications of the OSHER upwind scheme for the Euler equations, AIAA (1983) 83-1943.

[19] A. Chorin, Numerical solution of the Navier–Stokes equations, Math. Comput. 22 (1968) 745-762.

[20] C.G. Chen, F. Xiao, Shallow water model on spherical-cubic grid by multi-moment finite volume method, J. Comput. Phys. 227 (2008) 5019–5044.

[21] B. Cockburn and C.W. Shu, TVB Runge-Kutta local projection discontinuous Galerkin finite element method for conservation laws II: General framework, Math. Comput. **52** (1989) 411-435.

[22] B. Cockburn, S.Y. Lin and C.-W. Shu, TVB Runge-Kutta local projection discontinuous Galerkin finite element method for conservation laws III: One-dimensional systems, J. Comput. Phys. **84** (1989) 90-113.

[23] B. Cockburn, S. Hou and C.W. Shu, TVB Runge-Kutta local projection discontinuous Galerkin finite element method for conservation laws IV: The multidimensional case, Math. Comput. **54** (1990) 545-581.

[24] B. Cockburn, C.W. Shu, The Runge-Kutta discontinuous Galerkin method for conservation laws V: The multidimensional systems, J. Comput. Phys. **141** (1998) 199-224.

[25] G.S. Constantinescuandm, K.D. Squires, LES and DES investigations of turbulent Flow overa sphere, AIAA (2000) 2000–0540.

[26] M.S. Darwish, F. Moukalled, TVD schemes for unstructured grids, Int. J. Heat Mass Transfer 46 (4) (2003) 599–611.

[27] Demirdzic, Z. Lilek, M. Peric, Fluid flow and heat transfer test problems for non-orthogonal grids: bench-mark solutions, Int. J. Numer. Methods Fluids 15 (1992) 329–354.

[28] A. Deliceoğlu, S.H. Aydın, Flow bifurcation and eddy genesis in an L-shaped cavity, Comp. Fluids, 73 (2013) 24–46.

[29] S. Dong, G.E. Karniadakis, A. Ekmekci, and D. Rockwell, A combined direct numerical simulation-particle image velocimetry study of the turbulent near wake, J. Fluid Mech. 569 (2006), 185.

[30] M. Dumbser, M. Kaser, Arbitrary high order non-oscillatory finite volume schemes on unstructured meshes for linear hyperbolic systems, J. Comput. Phys. 221 (2007) 693–723.

[31] S. Eckert, H. Baaser, D. Gross, O. Scherf, A BDF2 integration method with step size control for elasto-plasticity, Computational Mechanics 34 (2004) 377–386.

[32] R.N. Elias and A.L.G.A. Coutinho, Stabilized edge-based finite element simulation of free-surface flows, Int. J. Numer. Meth. Fluids 54 (2007) 965–993.

[33] E. Erturk, T.C. Corke et.al, Numerical solutions of 2-D steady incompressible driven cavity flow at high Reynolds numbers, Int. J. Numer. Meth. Fluids, 48 (2005) 747-774.

[34] E. Erturk and O. Gokcol, Fine grid numerical solutions of triangular cavity flow, Eur. Phys. J. Appl. Phys. 38 (2007), 97–105.

[35] E. Ferrer and R. Willden, A high order discontinuous Galerkin finite element solver for the incompressible Navier-Stokes equations, Comput. and Fluids **46** (2011) 224-230.

[36] O. Friedrich, Weighted essentially non-oscillatory schemes for the interpolation of mean values on unstructured grids, J. Comput. Phys. **144** (1998) 194-212.

[37] M.M. Francois, S.J. Cummins, E.D. Dendy, D.B. Kothe, J.M. Sicilian, M.W. Williams, A balanced-force algorithm for continuous and sharp interfacial surface tension models within a volume tracking framework, J. Comput. Phys. 213 (2006) 141–173.

[38] D. Gartling, A test problem for outflow boundary conditions-flow over a backward-facing step, Int. J. Numer. Methods Fluids 11 (1990) 953–67.

[39] P.H. Gaskell, H.M. Thompson, M.D. Savage, and J.B. Ikin, Steady recirculating flow near static contact lines, Chem. Eng. Sci. 54(1999) 819.

[40] D. Gerlach, G. Tomar, G. Biswas and F. Durst, Comparison of volume-of-fluid methods for surface tension-dominant two-phase flows, Int. J. Heat and Mass Transfer 49 (2006) 740–754.

[41] U. Ghia, K.N. Ghia, C.T. Shin, High-Re solutions for incompressible flow using the Navier–Stokes equations and a multigrid method, J. Comput. Phys., 48 (1982), 387–411.

[42] D. Gueyffier, J. Li, A. Nadim, R. Scardovelli, S. Zaleski, Volume-of-fluid interface tracking with smoothed surface stress methods for three-dimensional flows, J. Comput. Phys. 152 (1999) 423–456.

[43] R. Glowinski, G. Guidoboni, T.W. Pan, Wall-driven incompressible viscous flow in a two-dimensional semi-circular cavity, J. Comput. Phys. 216 (2006) 76–91.

[44] L.M. Gonzalez, M. Ahmed et. al, Three-dimensional flow instability in a lid-driven isosceles triangular cavity, J. Fluid Mech. 675 (2011), 369–396.

[45] C.O. Gooch and M.V. Altena, A high-order-accurate unstructured mesh finite-volume scheme for the advection–diffusion equation, J. Comput. Phys. 181 (2002) 729–752.

[46] H. Guillard, C. Viozat, On the behavior of upwind schemes in the low Mach number limit, Comput. Fluids 28 (1999) 63.

[47] M.M. Gupta, R.P. Manohar, Boundary approximations and accuracy in viscous flow computations. J. Comput. Phys. 31(1979) 265–288.

[48] E. Hachem, B. Rivaux, T. Kloczko, H. Digonnet, T. Coupez, Stabilized finite element method for incompressible flows with high Reynolds number, J Comput Phys 229 (2010) 8643–8665.

[49] F.H. Harlow, J.E. Welch, Numerical calculation of time-dependent viscous incompressible flow of fluid with free surface, Phys. Fluids, 8 (1965) 2182–2189.

[50] F. Harlow, A. Amsden, Numerical calculation of almost incompressible flows, J. Comput. Phys. 3 (1968) 80.

[51] F. Harlow, A. Amsden, A numerical fluid dynamics calculation method for all flow speeds, J. Comput. Phys. 8 (1971) 197.

[52] A. Harten, High resolution schemes for hyperbolic con- servation laws, J. Comput. Phys. 49 (1983) 357–393.

[53] A. Harten, B. Enquist, S. Osher, S.R. Chakravarthy, Uniformly high order accurate essentially non-oscillatory schemes, III, J. Comput. Phys. 71 (1987) 231–303.

[54] D.J.E. Harvie, D.F. Fletcher, A new volume of fluid advection algorithm: the stream scheme, J. Comput. Phys. 162 (2000) 1–32.

[55] D.J.E. Harvie, D.F. Fletcher, A new volume of fluid advection algorithm: the defined donating region scheme, Int. J. Numer. Methods Fluids 35 (2001) 151–172.

[56] J. Hernandez, J. Lopez, P. Gomez, C. Zanzi, F. Faura, A new volume of fluid method in three dimensions – Part I: multidimensional advection method with face-matched flux polyhedra, Int. J. Numer. Methods Fluids 58 (2008) 897–921.

[57] J.G. Hnat, J.D. Buckmaster, Spherical cap bubbles and skirt formation, Phys. Fluids, 19 (1976) 182–194.

[58] S. Hysing, S. Turek, D. Kuzmin, N. Parolini, E. Burman, S. Ganesan, L. Tobiska, Quantitative benchmark computations of two-dimensional bubble dynamics, Int. J. Numer. Meth Fluids, 60 (2008) 1259–1288.

[59] C. Hu and C.W. Shu, Weighted essentially non-oscillatory schemes on triangular meshes, J. Comput. Phys. **150** (1999) 97-127.

[60] M. Herrmann, A balanced force refined level set grid method for two-phase flows on unstructured flow solver grids, J. Comput. Phys. 227 (2008) 2674–2706

[61] C.W. Hirt, B.D. Nichols, Volume of fluid (VOF) method for the dynamics of free boundaries, J. Comput. Phys. 39 (1981) 201–225.

[62] S. Hou, Q. Zou, S. Chen, G. Doolen, A.C. Cogley, Simulation of cavity flow by the lattice Boltzmann method, J. Comput. Phys., 118(1995), 329–347.

[63] S. Ii, M. Shimuta, F. Xiao, A 4th-order and single-cell-based advection scheme on unstructured grids using multi-moments, Comput. Phys. Commun. 173 (2005) 17–33.

[64] S. Ii, F. Xiao, CIP/multi-moment finite volume method for Euler equations: a semi-Lagrangian characteristic formulation, J. Comput. Phys. 222 (2007) 849–871.

[65] S.Ii and F. Xiao: A global shallow water model using high order multi-moment constrained finite volume method and icosahedral grid, J. Comput. Phys., 229 (2010), 1774-1796.

[66] S. Ii, K. Sugiyama, S. Takeuchi, S. Takagi, Y. Matsumoto, F. Xiao, An interface capturing method with a continuous function: the THINC method with multi-dimensional reconstruction, J. Comput. Phys. 231 (2012) 2328–2358.

[67] S. Ii, B. Xie, F. Xiao, An interface capturing method with a continuous function: The THINC method on unstructured triangular and tetrahedral meshes, J. Comput. Phys. 259 (2014) 260–269.

[68] A. Ikebata, Y. Muraoka, F. Xiao, Multiphase fluid simulations on a multiple GP-GPU PC using unsplit time integration VSIAM3. Progress in Nuclear Science and Technology, 2 (2001) 491–497.

[69] A. Ikebata, F. Xiao, Development of conservative front capturing scheme and applications to multi-fluid simulations. Proc. 2002 Annual Conference of Japan Society of Mechanical Engineering, Tokyo, Japan (2002) 301–302 (in Japanese).

[70] Y. Imai and T. Aoki, Stable coupling between vector and scalar variables for the IDO scheme on collocated grids, J. Comput. Phys. 215 (2006) 81.

[71] Y. Imai, T. Aoki and K. Takizawa, Conservative form of interpolated differential operator scheme for compressible and incompressible fluid dyanmics, J. Comput. Phys. 227 (2008) 2263.

[72] R. Issa, D. Gosman, A. Watkins, The computation of compressible and incompressible flows by a non-iterative implicit scheme, J. Comput. Phys. 62 (1986) 66.

[73] L. Ivan, C.P.T. Groth, High-order solution-adaptive central essentially non-oscillatory (CENO) method for viscous flows, J. Comput. Phys. 257 (2014) 830–862.

[74] A. Jagannathan, R. Mohan, M. Dhanak, A spectral method for the triangular cavity flow, Comput. and Fluids **95** (2014), 40-48.

[75] H. Jasak, OpenFOAM: Open source CFD in research and industry, Int. J. Naval Archit. and Ocean Engin. **1** (2009) 89-94.

[76] G.S. Jiang, C.W. Shu, Efficient implementation of weighted ENO schemes, J. Comput. Phys. 126 (1996) 202–228.

[77] L. Jofre, O. Lehmkuhl, J. Castro, A. Oliva, A 3-D volume-of-fluid advection method based on cell-vertex velocities for unstructured meshes, Computers & Fluids, 94 (2014) 14–29.

[78] T.A. Johnson and V.C. Patel, Flow past a sphere up to a Reynolds number of 300, J. Fluid Mech. 378 (1999) 19-70.

[79] F. Juretić and A.D. Gosman, Error analysis of the finite-volume method with respect to mesh type, Numerical Heat Transfer (Part B), **57** (2010) 414-439.

[80] C. Karki, S. Patankar, Pressure based calculation procedure for viscous flows at all speed in arbitrary configurations, AIAA 27 (1989) 1167.

[81] T. Kariya and H. Kurata, Generalized Least Squares, Wiley, New York, 2004.

[82] C.E. Kees, I. Akkerman, M.W. Farthing, A conservative level set method suitable for variable-order approximations and unstructured meshes, J. Comput. Phys. 230 (2011) 4536-4558.

[83] J. Kim, P. Moin, Applicaiton of a fractional-step method to incompressible Navier–Stokes equations, J. Comput. Phys. 59 (1985) 308–323.

[84] J. Kim, D. Kim, H. Choi, An immersed-boundary finite-volume method for simulations of flow in complex geometries, J. Comput. Phys. 171 (2001) 132–150.

[85] K.M.T. Kleefsman, G. Fekken, A Volume-of-Fluid based simulation method for wave imacpt problems, J. Comput. Phys., 206 (2005) 363-393.

[86] H. Kohno and K.J. Bathe, A flow-condition-based interpolation finite element procedure for triangular grids, Int. J. Numer. Meth. Fluids, 51 (2006) 673-699.

[87] B. Koren, B. van Leer, Analysis of preconditioning and multigrid for Euler flows with low-subsonic regions, Adv. Comput. Methods 4 (1995) 127–144.

[88] S. Koshizuka, H. Tamako, Y. Oka, A particle method for incompressible viscous flow with fluid fragmentation, Computational Fluid Mechanics Journal 113 (1995) 134–147.

[89] G. Kravchenko and P. Moin, Numerical studies of flow over a circular cylinder at Re=3900, Phys. Fluids 12(2), (2000) 403-417.

[90] E.J. Kubatko, C. Dawson, J.J. Westerink, Time step restrictions for Runge–Kutta discontinuous Galerkin methods on triangular grids, J. Comput. Phys. 227 (2008) 9697–9710.

[91] N. Kwatra, J. Su, J.T. Grétarsson, R. Fedkiw, A method for avoiding the acoustic time step restriction in compressible flow, J. Comput. Phys. 228 (2009) 4146-4161.

[92] B.V. Leer, Towards the ultimate conservative difference scheme. V. A second-order sequel to GodunovÕs method, J. Comput. Phys. 32 (1979) 101–136.

[93] M. Lentine, J.T. Grétarsson, R. Fedkiw, An unconditionally stable fully conservative semi-Lagrangian method, J. Comput. Phys. 230 (2011) 2857-2879.

[94] B.P. Leonard, A stable and accurate convective modelling procedure based on quadratic upstream interpolation, Comput. Methods Appl. Mech. Eng. 19 (1979) 59–98.

[95] R. LeVeque, High-resolution conservative algorithms for advection in incompressible flow, SIAM Journal on Numerical Analysis, 33 (1996) 627–665.

[96] M. Li, T. Tang, B. Fornberg, A compact fourth-order finite difference scheme for the steady incompressible Navier–Stokes equations, Int. J. Numer. Meth. Fluids, 20 (1995), 1137–1151.

[97] M. Li and T. Tang, Steady viscous flow in a triangular cavity by efficient numerical techniques, 31(1996) 55-65.

[98] S.J. Liao, J. M. Zhu, A short note on higher-order streamfunction-vorticity formulation of 2-D steady state Navier–Stokes equations, Int. J. Numer. Meth. Fluids, 22 (1996), 1–9.

[99] M.S. Liou, C.J. Steffen, A new flux splitting scheme, J. Comput. Phys. 107 (1993) 23–39.

[100] M.S. Liou. A sequel to AUSM: AUSM(+), J. Comput. Phys. 129 (1996) 364–382.

[101] M.S. Liou, A sequel to AUSM, PART II: AUSM$^+$ – up for all speeds, J. Comput. Phys. 214 (2006) 137–170.

[102] J. Liu, Y.F. Yap, N.T. Nguyen, Behavior of microdroplets in diffuser/nozzle structures, Microfluid Nanofluid 6 (2009) 835–846.

[103] Y. Liu, M. Vinokur, Z. Wang, Discontinuous spectral difference method for conservation laws on unstructured grids, in: Proceedings of the 3rd Inter- national Conference on Computational Fluid Dynamics, Toronto, Canada, July 2004, 12–16.

[104] L.M. Lourenco, C. Shih, Characteristics of the the plane turbulent near wake of a circular cylinder – a particle image velocimetry study, private communication, 1993.

[105] X. Ma, G.S. Karamanos and G.E. Karniadakis, Dynamics and low-dimensionality of a turbulent near wake, J. Fluid. Mech 410 (2000), 29-65.

[106] K. Mahesh, G. Constantinescu, P. Moin, A numerical method for large-eddy simulation in complex geometries, J. Comput. Phys. 197 (2004) 215–240.

[107] J. McGuirk, J. Page, Shock capturing using a pressure correction method, AIAA 28 (1990) 1751.

[108] W.D. McQuain, C.J. Ribbens, C.Y. Wang and L.T. Watson, Steady viscous flow in a trapezoidal cavity, Comput. Fluids 23 (1994) 613-626.

[109] H. Mercan, K. Atalik, Vortex formation in lid-driven arc-shape cavity flows at high reynolds numbers. Euro J Mech B/Fluids 28 (2009) 61–71.

[110] K. Michalak, C.F. Ollivier-Gooch, Accuracy preserving limiter for the high-order accurate solution of the Euler equations, J. Comput. Phys. 228 (2009) 8693–8711.

[111] R. Mittal, P. Moin, Suitability of upwind biased schemes for large-eddy simulation, AIAA 30(8) (1997) 1415–1417.

[112] A. Nejat, C.F. Ollivier-Gooch, A high-order accurate unstructured finite volume Newton–Krylov algorithm for inviscid compressible flows, J. Comput. Phys. 227 (2008) 2582–2609.

[113] H. Nishida, N. Satofuka, Higher-order solutions of square driven cavity flow using a variable-order multi-grid method, Int. J. Numer. Meth. Fluids, 34 (1992), 637–653.

[114] C.F. Ollivier-Gooch, High-order ENO schemes for unstructured meshes based on least-squares reconstruction, AIAA (1997) 97-0540.

[115] C.F. Ollivier-Gooch, Quasi-ENO schemes for unstructured meshes based on unlimited data-dependent least-squares reconstruction, J. Comput. Phys. 133 (1997) 6–17.

[116] E. Olsson, G. Kreiss, A conservative level set method for two phase flow, J. Comput. Phys. 210 (2005) 225–246.

[117] C.W. Oosterlee, P. Wesseling, E. Brakkee, Benchmark solutions for the incompressible Navier–Stokes equations in general co-ordinates on staggered grids, Int. J. Numer. Methods Fluids 17 (1993) 301–321.

[118] D. Pan, C.H. Chang, The capturing of free surfaces in incompressible multi-fluid flows, Int. J. Numer. Methods Fluids 30 (2000) 203–222.

[119] J.S. Park, S.H. Yoon, C. Kim, Multi-dimensional limiting process for hyperbolic conservation laws on unstructured grids, J. Comput. Phys. 229 (2010) 788-812.

[120] P. Parnaudeau, J. Carlier, D. Heitz and E. Lamballais, Experimental and numerical studies of the flow over a cylinder at Reynolds number 3900, Phys. Fluids 20 (2008) 085101.

[121] A. Prasad, C.H.K. Williamson, The instability of the separated shear layer from a bluff body, Phys. Fluids 8 (1999) 1347.

[122] J.E. Pilliod Jr., E.G. Puckett, Second-order accurate volume-of-fluid algorithms for tracking material interfaces, J. Comput. Phys. 199 (2004) 465–502.

[123] E.G. Puckett, A.S. Almgren, J.B. Bell, D.L. Marcus, W.J. Rider, A high-order projection method for tracking fluid interfaces in variable density incompressible flows, J. Comput. Phys. 130 (1997) 269–282.

[124] Y. Renardy, M. Renardy, PROST: a parabolic reconstruction of surface tension for the volume-of-fluid method, J. Comput. Phys. 183 (2002) 400–421.

[125] C.J. Ribbens, L.T. Watson and C.Y. Wang, Steady viscous flow in a triangular cavity, J. Comput. Phys. 112 (1994) 173-181.

[126] W.J. Rider, D.B. Kothe, Reconstructing volume tracking, J. Comput. Phys. 141 (1998) 112–152.

[127] P.L. Roe, Some contributions to the modeling of discontinuous flows, Proceedings of the AMS/SIAM Seminar, San Diego, 1983.

[128] P.L. Roe, Some contributions to the modeling of discontinuous flows, Lect. Appl. Math. 22 (1985) 163–193.

[129] R. Rossi, Direct numerical simulation of scalar transport using unstructured finite-volume schemes, J. Comput. Phys **229** (2009) 1639-1657.

[130] M. Rudman, Volume-tracking methods for interfacial flow calculations, Int. J. Numer. Methods Fluids, 24 (1997) 671–691.

[131] H. Rusche, Computational Fluid Dynamics of Dispersed Two-Phase Flows at High Phase Fractions, thesis of doctor degree for University of London and Diploma of Imperial College.

[132] Y. Sato, B. Niceno, A conservative local interface sharpening scheme for the constrained interpolation profile method, Int. J. Numer. Methods Fluids, 70 (2012) 441–467.

[133] R. Scardovelli, S. Zaleski, Analytical relations connecting linear interfaces and volume fractions in rectangular grids, J. Comput. Phys. 164 (2000) 228–237.

[134] R. Scardovelli, S. Zaleski, Interface reconstruction with least-square fit and split Eulerian Lagrangian advection, Int. J. Numer. Methods Fluids 41 (2003) 251–274.

[135] R. Schreiber, H.B. Keller, Driven cavity flows by efficient numerical techniques, J. Comput. Phys., 49 (1983), 310–333.

[136] K. Shahbazi, P. Fischer and C. Ethier, A high-order discontinuous Galerkin method for the unsteady incompressible Navier-Stokes equations, J. Comput. Phys., **222** (2007) 391-407.

[137] K. Shahbazi, M. Paraschivoiu, J. Mostaghimi, Second order accurate volume tracking based on remapping for triangular meshes, J. Comput. Phys. 188 (2003) 100–122.

[138] P.N. Shankar and M. D. Deshpande, Fluid Mechanics in the driven cavity, Annu. Rev. Fluid Mech. 32 (2000) 93–136.

[139] T. Sheu, S. Tsai, Flow topology in a steady three-dimensional lid-driven cavity, Comp Fluids 31 (2002) 911–934.

[140] C.W. Shu, Total-variation-diminishing time discretizations, SIAM J. Sci. Stat. Comput. **9** (1988) 1073-1084.

[141] W. Shyy, E. Braaten, Adaptive grid computation for inviscid compressible flows using a pressure correction method, AIAA (1988) 88-3566.

[142] K.K. So, X.Y. Hu, N.A. Adams, Anti-diffusion method for interface steepening in two-phase incompressible flow, J. Comput. Phys. 230 (2011) 5155–5177.

[143] T. Sonar, On the construction of essentially non-oscillatory finite volume approximations to hyperbolic conservation laws on general triangulations: polynomial recovery, accuracy and stencil selection, Comput. Methods Appl. Mech. Eng. 140 (1997) 157-181.

[144] L. Sun, S.R. Mathur and J.T. Murthy, An unstructured finite-volume method for incompressible flows with complex immersed boundaries, Numerical Heat Transfer (Part B), **58** (2010) 217-241.

[145] M. Sussman, P. Smereka, S. Osher, A level set approach for capturing solution to incompressible two-phase flow, J. Comput. Phys. 114 (1994) 146.

[146] M. Sussman, E.G. Puckett, A coupled level set and volume-of-fluid method for computing 3D and axisymmetric incompressible two-phase flows, J. Comput. Phys. 162 (2000) 301–337.

[147] P.K. Sweby, High resolution schemes using flux limiters for hyperbolic conservation laws, SIAM J. Numer. Analysis, 21 (1984) 995–1011.

[148] K. Tanaka, T. Nakamura and T. Yabe: Constructing exactly conservative scheme in a non-conservative form, Comput. Phys. Commum 126 (2000) 232.

[149] J.J. Thibert, M. Grandjacques, L.H. Ohman, Experimental data base for computer program assessment: NACA 0012 Airfoil, AGARD Advisory Report 138, 1979.

[150] E. Toro, Riemann Solvers and Numerical Methods for Fluid Dynamics, Springer, Berlin, 1997.

[151] D.J. Torres, J.U. Brackbill, The point-set method: front-tracking without connectivity, J. Comput. Phys. 165 (2000) 620–644.

[152] G. Tryggvason, R. Scardovelli, S. Zaleski, Direct Numerical Simulations of Gas–Liquid Multiphase Flows, Cambridge University Press, 2011.

[153] P. Tsoutsanis, V.A. Titarev, D. Drikakis, WENO schemes on arbitrary mixed-element unstructured meshes in three space dimensions, J. Comput. Phys. 230 (2011) 1585–1601.

[154] S. Tu, S. Aliabadi, Development of a hybrid finite volume/element solver for incompressible flows, Int. J. Numer. Meth. Fluids. **55** (2007), 177-203.

[155] S. Turek, M. Schafer, Benchmark computations of laminar flows around a cylinder, in: E.H. Hirschel (Ed.), Flow Simulation with High-Performance Computers II, in: Notes on Numerical Fluid Mechanics, 52 (1996) 547–566.

[156] E. Turkel, Preconditioned methods for solving the incompressible and low speed compressible equations. J. Comput. Phys. 72 (1987) 277–298.

[157] E. Turkel, Review of preconditioning techniques for fluid dynamics, Appl. Numer. Math. 21 (1993) 385-416.

[158] C. Ubink, R.I. Issa, A method for capturing sharp fluid interfaces on arbitrary meshes, J. Comput. Phys. 153 (1999) 26–50.

[159] B. VanLeer, Towards the ultimate conservative difference scheme. IV. A new approach to numerical convection, J. Comput. Phys., **23** (1977) 276-299.

[160] B. VanLeer, Towards the ultimate conservative difference scheme, V. A second order sequel to Godunov's Method, J. Comp. Phys., **32**(1979) 101-136.

[161] S.P. Vanka, Block-implicit multigrid solution of Navier–Stokes equations in primitive variables, J. Comput. Phys., 65 (1986), 138–158.

[162] Z.J. Wang, Spectral (finite) volume method for conservation laws on unstructured grids: basic formulation, J. Comput. Phys. **178** (2002) 210-251.

[163] Z.J. Wang, Y. Liu, Spectral (finite) volume method for conservation laws on unstructured grids II: extension to two-dimensional scalar equation, J. Comput. Phys. **179** (2002) 665-697.

[164] Z.J. Wang, Y. Liu, G. May, A. Jameson, Spectral difference method for unstructured grids II: Extension to the Euler equations, J. Sci. Comput. 32 (1) (2007) 45–71.

[165] M. Weiss, A. Smith, Preconditioning applied to variable and constant density flows, AIAA 22 (1995) 2050-2057.

[166] H.G. Weller, G. Tabor, H. Jasak, C. Fureby, A tensorial approach to computational continuum mechanics using object-oriented techniques, Comput. Phys. 12 (1998) 620–631.

[167] P. Woodward, P. Colella, The numerical simulation of two-dimensional fluid flow with strong shocks, J. Comput. Phys. 54 (1984) 115-173.

[168] N.G. Wright, P.H. Gaskell, An efficient multigrid approach to solving highly recirculating flows, Comput. and Fluids, 24 (1995), 63–79.

[169] F. Xiao and T. Yabe, Completely conservative and oscillation-less semi-Lagrangian schemes for advection transportation, J. Comput. Phys. **170** (2001) 498-522.

[170] F. Xiao, T. Yabe, X. Peng and H. Kobayashi, Conservative and oscillaiton-less atmospheric transport schemes based on rational functions, J. Geophysical Research-Atomsphere, 107, (2002) 4609.

[171] F. Xiao, A. Ikebata, An efficient method for capturing free boundaries in multi-fluid simulations, Int. J. Numer. Methods Fluids, 42 (2003) 187–210.

[172] F. Xiao, Unified formulation for compressible and incompressible flows by using multi integrated moment method: one-dimensional inviscid compressible flow, J. Comput. Phys. **195** (2004) 629-654.

[173] F. Xiao, Y. Honma, K. Kono, A simple algebraic interface capturing scheme using hyperbolic tangent function, Int. J. Numer. Methods Fluids 48 (2005) 1023–1040.

[174] F. Xiao, A. Ikebata, T. Hasegawa, Numerical simulations of free-interface fluids by a multi integrated moment method, Comput. Struct. **83** (2005) 409-423.

[175] F. Xiao, R. Akoh and S. Ii, Unified formulation for compressible and incompressible flows by using multi-integrated moments II: Multi-dimensional version for compressible and incompressible flows, J. Comput. Phys. **213** (2006) 31-56.

[176] F. Xiao, S. Ii, C.G. Chen, Revisit to the THINC scheme: a simple algebraic VOF algorithm, J. Comput. Phys. 230 (2011) 7086–7092.

[177] B. Xie, S. Ii, A. Ikebata, F. Xiao, A multi-moment finite volume method for incompressible Navier–Stokes equations on unstructured grids: Volume-average/point-value formulation, J. Comput. Phys. **227** (2014) 138-162.

[178] B. Xie, S. Ii and F. Xiao, An efficient and accurate algebraic interface capturing method for unstructured grids in 2 and 3 dimensions: The THINC method with quadratic surface representation, Int. J. Numer. Methods Fluids 76 (2014) 1025–1042.

[179] C.M. Xisto, J. C. Pascoa, P. J. Olivera and D. A. Nicolini, A hybrid pressure-density based algorithm for the Euler equations at all Mach number regimes, Int. J. Numer. Methods Fluids 70 (2012) 961–976.

[180] T. Yabe and T. Aoki, A universal solver for hyperbolic-equations by cubic-polynomial interpolation. 1. One-dimensional solver, Comput. Phys. Commun. **66** (1991) 219-232.

[181] T. Yabe and P.Y. Wang, Unified numerical procedure for compressible and incompressible fluid, J. Phys. Soc. Japan, 60, (1991) 2105-2108.

[182] T. Yabe, F. Xiao, T. Utsumi, The constrained interpolation profile method for multiphase analysis, J. Comput. Phys. **169** (2001) 556-593.

[183] T. Yabe, R. Tanaka, T. Nakamura, and F. Xiao, An Exactly Conservative Semi-Lagrangian Scheme (CIP–CSL) in One Dimension, Monthly Weather Review, 129 (2001), 332.

[184] J.Y. Yang, S.C. Yang, Y.N. Chen, C.A. Hsu, Implicit weighted ENO schemes for the three-dimensional incompressible Navier-Stokes equations, J Comput Phys, 146 (1998) 464–487.

[185] X. Yang, A.J. James, Analytic relations for reconstructing piecewise linear interfaces in triangular and tetrahedral grids, J. Comput. Phys. 214 (2006) 41–54.

[186] K. Yokoi, Efficient implementation of THINC scheme: A simple and practical smoothed VOF algorithm, J. Comput. Phys. 226 (2007) 1985–2002.

[187] K. Yokoi, A practical numerical framework for free surface flows based on CLS-VOF method, multi-moment methods and density-scaled CSF model: Numerical simulations of droplet splashing, J. Comput. Phys. 232 (2013) 252-271.

[188] K. Yokoi, A density-scaled continuum surface force model within a balanced force formulation, J. Comput. Phys. 278 (2014) 221-228.

[189] D.L. Youngs, Time-dependent multi-material flow with large fluid distortion, in: K.W. Morton, M.J. Baines (Eds.), Numerical Methods for Fluid Dynamics, Academic Press (1982) 273–285.

[190] D.L. Youngs, An interface tracking method for a 3D Eulerian hydrodynamics code, Technical Report 44/92/35, AWRE, 1984.

[191] S.T. Zalesak, Fully multi-dimensional flux corrected transport algorithm for fluid flow. J. Comput. Phys. 31 (1979) 335–362.